공학박사학위논문

Standardization of Split Hopkinson Pressure Bar Test Procedure for Concrete

콘크리트 Split Hopkinson Pressure Bar 실험절차의 표준화

2023 년 2 월

서울대학교 대학원

건설환경공학부

김 경 민

Standardization of Split Hopkinson Pressure Bar Test Procedure for Concrete

콘크리트 **Split Hopkinson Pressure Bar**
실험절차의 표준화

지도 교수 조 재 열

이 논문을 공학박사 학위논문으로 제출함
2022 년 11 월

서울대학교 대학원
건설환경공학부
김 경 민

김경민의 공학박사 학위논문을 인준함
2022 년 12 월

위 원 장 _____ (인)

부위원장 _____ (인)

위 원 _____ (인)

위 원 _____ (인)

위 원 _____ (인)

ABSTRACT

Standardization of Split Hopkinson Pressure Bar Test Procedure for Concrete

Kim, Kyoung-Min

Department of Civil & Environmental Engineering

The Graduate School

Seoul National University

Recently, extreme events such as the explosion of plants, collision of vehicles, rockfall, and impact of aircraft or missiles have frequently occurred. Accordingly, the necessity of research on extreme loadings such as impact-resistant performance evaluation of structures subjected to extreme loading has increased for the safety of social infrastructures. Concrete, which is the most widely used material for the construction of social infrastructures, has rate-dependent properties. The compressive strength of concrete is enhanced as the strain rate increases due to the strain-rate effect and shows different behavior compared to that under general static loadings. Therefore, it is necessary to investigate the dynamic material properties of the concrete for accurate evaluation and economical design of the structures under extreme loadings. In particular, the dynamic compressive strength of concrete can be obtained through various dynamic material tests and the split Hopkinson pressure bar (SHPB) test has been chiefly performed.

However, the main limitation of the concrete SHPB test is the absence of the standard test method. Since concrete is non-homogeneous material

consisting of various components with different particle sizes such as coarse and fine aggregates, the dispersion of the test results is more severe than in homogenous materials such as metals. In addition, the frictional effect in the SHPB test might result in the overestimation of the dynamic compressive strength due to the strain-rate effect. For this reason, it is difficult to consistently and accurately evaluate the dynamic compressive strength through the SHPB test without a standardized guideline. Therefore, a standardized test method should be established covering from the specimen preparation to acquisition process of test results to obtain accurate and consistent dynamic compressive strength of concrete through SHPB tests.

The main objective of this study is to develop an SHPB test procedure to improve the consistency of the dynamic compressive strength evaluation. For this objective, the contents which should be included in the SHPB test method were drawn. Among the contents, three main subjects were selected; specimen dimension, lubrication method, and loading condition. To suggest proper guidelines for each subject, previous experimental and numerical studies were reviewed and a series of experimental and numerical works were conducted.

At first, SHPB tests were performed for 240 specimens to suggest a guideline to decide the concrete specimen dimension. To this end, maximum coarse aggregate sizes and specimen dimensions were selected as the main variables. In particular, the maximum coarse aggregate sizes used in the actual construction site were included. The size of coarse aggregate may affect the dispersion of test results because concrete is non-homogeneous material. Therefore, the effect of maximum coarse aggregate size on the dispersion of

the test results was investigated and the dynamic increase factor (DIF) for each size of maximum coarse aggregate through the SHPB test was obtained and compared. Based on the test results, a guideline for the determination of the specimen dimension was suggested to secure consistent test results: (1) specimen dimension should be at least three times G_{max}, and (2) actual G_{max} should be used in the concrete SHPB test.

Secondly, numerical and experimental studies were carried out to propose an appropriate lubricating technique. In the concrete SHPB test, the friction on the interfaces between specimen and bars induces confining effect. This effect additionally enhances the dynamic compressive strength in the increased strength by the strain-rate effect, which results in the overestimation of the dynamic compressive strength. Accordingly, an adequate lubricating technique to minimize the frictional effect is essential for the accurate evaluation of the dynamic compressive strength of concrete. For necessity, this study conducted concrete SHPB tests for 52 specimens with the main variables of lubricant type and amount of lubricant to suggest a proper lubrication method. Then the proposed method was thoroughly verified through a follow-up SHPB test for 75 concrete specimens with various specimen dimensions. Based on the tests, the lubrication method was suggested to eliminate the frictional effect in the concrete SHPB test: the specimens should be lubricated with the amount of 12 mg/cm^2 or more with one of the lubricants, high vacuum grease, petroleum jelly, or Teflon.

Lastly, the study on the determination method of the incident stress wave to secure valid test results was performed. In order to obtain valid results, the dynamic stress equilibrium of the specimen should be achieved

during the SHPB test. The dynamic stress equilibrium of the specimen is influenced by the specimen properties and the incident stress waves of the test. Therefore, an available range of the incident stress wave should be defined considering the specimen properties. This study proposed the range of the incident wave rate using the previous concrete SHPB test results which makes the specimen satisfy the dynamic stress equilibrium considering the specimen properties. The suggested range was verified through the concrete SHPB test for 184 specimens with various properties such as the dimension and the static compressive strength. Then the suggested range was modified using additional test results obtained in this study.

Finally, a test procedure for the concrete SHPB test to obtain consistent results was developed based on each experimental result conducted in this study. In addition, the applicability of the developed test method was verified.

The developed test method of the concrete SHPB test can provide a high-quality database of concrete dynamic material properties under extreme loadings. Furthermore, the suggested test procedure can be used as a standard test method for the concrete SHPB test and improve the reliability of the impact-resistant performance evaluation of materials.

Keywords: concrete dynamic compressive strength, split Hopkinson pressure bar, standard specimen making method, standard test method, dynamic material test

Student Number: 2018-31976

TABLE OF CONTENTS

LIST OF TABLES

LIST OF FIGURES

NOTATIONS

Symbol	Definition and description
A_b	Cross-section area of bar components
A_s	Cross-section area of a specimen
a_0 , a_1 , a_2	Maximum failure surface parameters in Karagozian and Case concrete model
a_{0y} , a_{1y} , a_{2y}	Yield failure surface parameters in Karagozian and Case concrete model
a_{1f} , a_{2f}	Residual failure surface parameters in Karagozian and Case concrete model
b_1 , b_2 , b_3	Damage scaling factors in Karagozian and Case concrete model
$c_{1,b}$	Elastic wave velocity of bar components
$c_{1,s}$	Elastic wave velocity of a specimen
D	Nominal diameter of a specimen
d_s	Initial diameter of a specimen
E_b	Elastic modulus of bar components
E_s	Elastic modulus of a specimen
$\dot{e}_0$	Reference deviatoric strain rate
$\dot{e}_{eff}$	Effective deviatoric strain rate
f_c	Static compressive strength of a specimen
f_d	Dynamic compressive strength of a specimen

$f_{d,FEA}$	Dynamic compressive strength obtained from the finite element analysis
$f_{d,TEST}$	Dynamic compressive strength obtained from the test
f_t	Uniaxial tensile strength
G_{max}	The maximum coarse aggregate size
K_{cal}	Threshold value of the constant related to dynamic stress equilibrium
K_u	Unloading bulk modulus
k	Constant related to dynamic stress equilibrium
k_1	Coefficient related to the strain-rate effect
k_2	Coefficient related to the lateral inertial effect
k_3	Coefficient related to the axial inertial effect
L	Nominal length of a specimen
l_s	Initial length of a specimen
p	Pressure
P_1	Front force
P_2	Back force
R	R-value (an indicator of dynamic stress equilibrium)
R_{reg}	Regression curve related to dynamic stress equilibrium
R_{AS}	Apparent strength ratio
t	Time
t_0	Transit time
t_{peak}	Time at peak stress
t_t	Traveling time of stress wave

v_{back}	Particle velocity on the interface between a transmitted bar and a specimen
v_{front}	Particle velocity on the interface between an incident bar and a specimen
w_{lz}	Localization width in Karagozian and Case concrete model
α	Coefficient related to relationship between incident and reflected stress wave rates
γ_{app}	Apparent dynamic increase factor
γ_{rate}	Pure rate dynamic increase factor
$\varepsilon_{incident}$	Incident strain wave
ε_r^{eng}	Engineering radial strain of a specimen
$\varepsilon_{reflected}$	Reflected strain wave
$\varepsilon_{transmitted}$	Transmitted strain wave
ε_v	Volumetric strain
ε_x	Axial strain of a specimen
ε_x^{eng}	Engineering axial strain of a specimen
$\dot{\varepsilon}_0$	Reference strain rate
$\dot{\varepsilon}_r^t$	True radial strain rate of a specimen
$\dot{\varepsilon}_x^{eng}$	Engineering axial strain rate of a specimen
$\dot{\varepsilon}_x^t$	True axial strain rate of a specimen
$\ddot{\varepsilon}_x^{eng}$	Engineering axial strain acceleration of a specimen
η	Yield scale factor in Karagozian and Case concrete model
λ	Damage function in Karagozian and Case concrete model

μ	Friction coefficient
$\boldsymbol{\mu}$	Mean vector of the apparent dynamic increase factor and the corresponding engineering axial strain rate
ν_s	Poisson's ratio of a specimen
ρ_s	Density of a specimen
$\boldsymbol{\Sigma}$	Covariance matrix of the apparent dynamic increase factor and the corresponding engineering axial strain rate
$\sigma_{incident}$	Incident stress wave
$\sigma_{reflected}$	Reflected stress wave
$\sigma_{transmitted}$	Transmitted stress wave
σ_x	Engineering axial stress of a specimen
$\sigma_{x,back}$	Axial stress on the interface between a transmitted bar and a specimen (back stress)
$\sigma_{x,front}$	Axial stress on the interface between an incident bar and a specimen (front stress)
$\dot{\sigma}_{incident}$	Incident stress wave rate
$\dot{\sigma}_{reflected}$	Reflected stress wave rate
$\dot{\sigma}_{transmitted}$	Transmitted stress wave rate
$\dot{\sigma}_x$	Engineering axial stress rate
ω	Associativity parameter

1. Introduction

1.1. Research background

Recently, the occurrence frequency of extreme events such as explosion of plants, collision of vehicles, rockfall, and missile or aircraft impacts has increased worldwide. These extreme events cause impact or blast loadings on social infrastructures and threaten the safety of society. The most distinguishing characteristic of these impact or blast loadings is that they apply tremendous loading in a very short time duration compared to the typical static loadings. These extreme loadings make structures deform at a high strain rate range over 10 s^{-1}, while the strain rate of static loading is in the range of 10^{-8}–10^{-4} s^{-1} as presented in Figure 1.1 (fib Bulletin 66, 2012). Therefore, the structures subjected to extreme loadings show different behaviors compared to those under static loadings. Because of these features, the dynamic behavior of structures over 10 s^{-1} should be understood for the safety and the accurate evaluation and design of the structures. For a better understanding, the dynamic properties of construction materials should be primarily investigated.

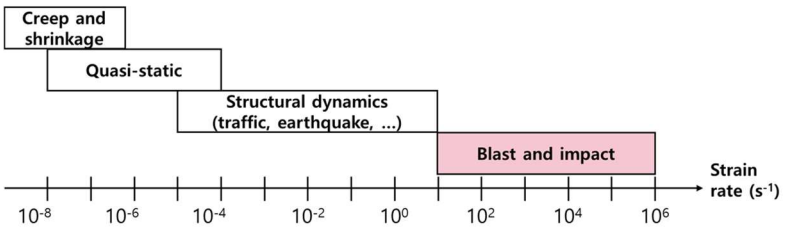

Figure 1.1 Strain rate range for various loadings (fib Bulletin 66, 2012)

Concrete is a representative material for construction, so it is widely used for social infrastructures. Since concrete has rate-dependent properties, the compressive strength of concrete is enhanced as the strain rate increases under extreme loadings. Figure 1.2 shows typical axial stress–strain relationships of concrete after the static and dynamic compressive strength tests.

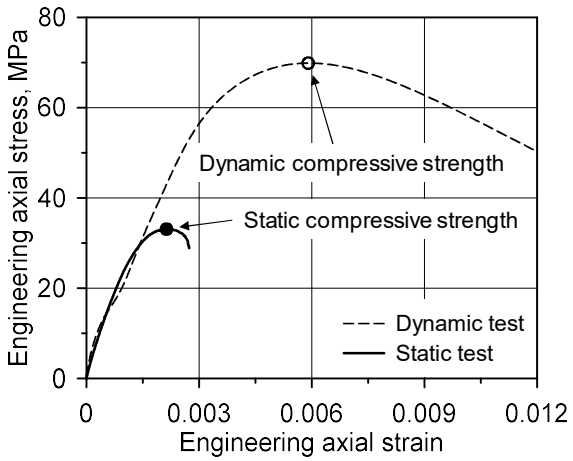

Figure 1.2 Typical axial stress–strain relationship of concrete under static and dynamic compressive strength test

In order to consider the strength enhancement of concrete, the dynamic increase factor (DIF), the ratio of dynamic compressive strength to static compressive strength, has been used in the construction engineering field. Since the dynamic compressive strength is increased along with the strain rate, the strain-rate effect of concrete can be considered as a relationship between DIF and strain rate. The DIF models can be acquired through dynamic material tests, and the representative test method is the split Hopkinson pressure bar (SHPB) test. Figure 1.3 shows a typical schematic SHPB system. After the SHPB test technique was devised (Kolsky, 1949), numerous studies

have been conducted with cementitious composites to explore the dynamic compressive behaviors of the material (Bhargava and Rehnström, 1977; Tang et al., 1984; Ross and Tedesco, 1989; Ross et al., 1995; Grote et al., 2001; Zhang et al., 2009; Wang et al., 2011; Hao et al., 2013a; Guo et al., 2017; Lee et al., 2018; Kim et al., 2019; Kim et al., 2022).

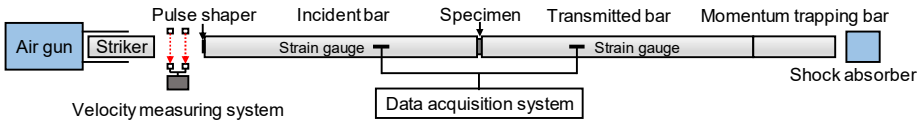

Figure 1.3 Typical schematic SHPB testing system

However, although the SHPB test technique has been applied to cementitious composites for a long time, the standard test method has not been established. The absence of a standardized test procedure makes researchers difficult to compare and combine the test results with others because every researcher performed the test in different methods. Therefore, the development of a standard test method for concrete SHPB test is mandatory for the accurate and consistent evaluation of dynamic material properties of concrete and the safe and economical design of social infrastructures including nuclear power plants and protective facilities.

Concrete is a non-homogeneous material consisting of several components with different particle sizes such as coarse and fine aggregates. Because of this characteristic, the test results can be relatively dispersive compared to homogeneous materials such as metals. The dispersion of the test results of concrete can be influenced by several factors such as the particle

sizes of aggregates, the strength difference between the aggregates and the cement paste. In particular, the aggregates affect the interfacial transition zone (ITZ) distribution between the aggregates and the cement pastes. Therefore, the specimen dimension for the concrete SHPB test should be carefully decided considering the aggregate sizes before the test. Then the concrete specimens can be fabricated following consistent guidelines such as ASTM C192 to minimize unnecessary differences among specimens in the same testing group. After the specimen preparation, the test conditions have to be decided: lubrication method and loading condition.

The specimen is sandwiched between the incident and transmitted bars in the SHPB test, and there is friction on the interfaces between the specimen and bars. The friction between the specimen and bars induces the confining effect on the specimen and it additionally enhances the compressive strength to the increased strength by strain-rate effect. Therefore, an appropriate lubricating technique should be established to prevent the frictional effect and to evaluate the genuine strain-rate effect through the SHPB test. In addition, the specimen has to satisfy the dynamic stress equilibrium state during the test to be valid in the concrete SHPB test. The dynamic stress equilibrium is mainly affected by the incident stress wave. Accordingly, the loading condition which determines the incident stress wave should be carefully decided. In particular, it is necessary to restrict the incident stress wave range which allows the specimen to achieve a dynamic stress equilibrium state for the efficiency of the test. Therefore, the development of a standard test method covering from the specimen preparation to the data acquisition for concrete SHPB test is an indispensable assignment.

The aim of this study is to establish a concrete SHPB test procedure to improve the consistency of the test results. To accomplish the objective, this study conducted numerous SHPB tests. Then, the guidelines for specimen preparation and determination of test conditions were proposed based on the test results. Eventually, the concrete SHPB test method for consistent evaluation of the dynamic compressive strength was developed.

1.2. Research objective and scope

There is one biggest objective in this study: the development of a test method for concrete SHPB tests to improve the consistency of the test results.

This study consists of four parts. The first part is about the specimen preparation procedure. Experimental work was carried out to investigate the effect of maximum coarse aggregate size on the dispersion of test results. Based on the test results, a guideline for the determination of the specimen dimension was suggested.

In the second part, an appropriate lubrication method for the concrete SHPB test was established through a series of SHPB tests. The main variables for the test were the type and the amount of lubricant.

The third part covers analytical and experimental works about the incident stress wave. A proper incident stress wave rate range was suggested based on the previous concrete SHPB test results and the range was verified through the concrete SHPB test. From the results, an available stress wave rate range was derived.

In the last part, the test procedure for the concrete SHPB test was developed by organizing each finding of the previous parts and the applicability of the developed method was verified.

1.3. Outline

Chapter 1 provides the introduction of this study including the research background, objective, scope, and outline.

Chapter 2 presents the review of previous research. The previous studies are divided into three parts: (1) specimen dimension, (2) lubrication method, and (3) loading condition. Limitations of the studies are discussed and the importance of this study is explained.

From Chapters 3 to 5, the main experimental works are described. Each chapter contains the details of the SHPB test program and the test results. In Chapter 3, the effect of maximum coarse aggregate size is presented. Chapter 4 shows the effect of friction in the SHPB test and Chapter 5 presents the effect of incident wave rate in the SHPB test. Guidelines were drawn based on each SHPB test and explained in each chapter.

Chapter 6 provides details of the established test method for concrete SHPB test through the test covered in Chapters 3 to 5. Examples of test results following the developed test method are also presented and the applicability was verified.

Chapter 7 summarizes this study and explains the conclusion. In addition, recommendations for further studies are described in the chapter.

Appendix A presents the developed test procedure for the concrete SHPB test. Appendices B to D show all test results of Chapters 3 to 5, respectively.

2. Literature Review

The main objective of this study is to establish a test method for the concrete SHPB test for consistent evaluation of dynamic compressive strength. Therefore, it is necessary to understand the basic principle of the SHPB test and figure out the parameters which need to be established. This section contains a brief explanation of the concrete SHPB test and the literature review on three subjects: specimen dimension, lubrication method, and loading condition.

2.1. Principle of split Hopkinson pressure bar test

Kolsky (1949) devised the SHPB test technique through modification of the Hopkinson pressure bar developed by Hopkinson (1914) to investigate the mechanical properties of materials at a high strain rate. The SHPB test method can be applied to both homogeneous and non-homogeneous solid materials. Therefore, numerous experimental studies have been carried out with the SHPB test method for cementitious composites (Bhargava and Rehnström, 1977; Tang et al., 1984; Ross and Tedesco, 1989; Ross et al., 1995; Grote et al., 2001; Zhang et al., 2009; Wang et al., 2011; Hao et al., 2013a; Guo et al., 2017; Lee et al., 2018; Kim et al., 2019; Kim et al., 2022).

The general SHPB test system is shown in Figure 1.3. The SHPB test system mainly consists of three bar components made of steel: striker, incident, and transmitted bars. The lubricated specimen is sandwiched between the incident and transmitted bars for the test. After placing the

specimen, the SHPB test can be conducted by launching the striker with the pressurized air gun. When the striker impacts one end of the incident bar, a compressive stress wave is generated and propagated along the incident bar. In this procedure, the pulse shaper is widely used to prevent wave dispersion and help the specimen satisfy the dynamic stress equilibrium state. At the interface between the incident bar and specimen, the part of the compressive stress wave is transmitted to the specimen. The rest of the stress wave is reflected as a tensile stress wave due to the difference in impedance of the steel and the specimen. Then the compressive stress wave keeps traveling along the specimen and the transmitted bar. At the end of the transmitted bar, the stress wave is transmitted to the momentum trapping bar and then dissipated through the shock absorber. The whole traveling time histories of the stress waves are measured with the strain gauges on the incident and transmitted bars as the incident, reflected, and transmitted strain waves.

The engineering axial stress–strain relationship of material can be calculated through one-dimensional stress wave theory from the measured strain histories (Chen and Song, 2010). Figure 2.1 shows the details of the testing section.

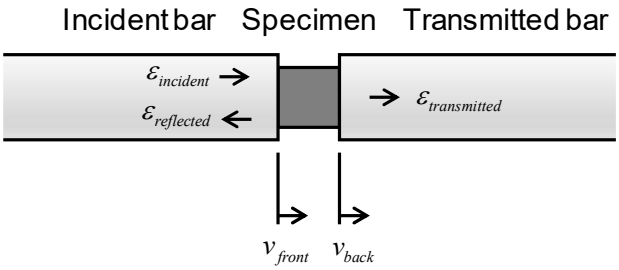

Figure 2.1 Details of the testing section

The particle velocities on the interfaces, v_{front} and v_{back}, can be obtained following Equations (2.1) and (2.2), where $c_{1,b}$ is the elastic wave velocity of bar components; $\varepsilon_{incident}$, $\varepsilon_{reflected}$, and $\varepsilon_{transmitted}$ denote the incident, reflected, and transmitted strain waves, respectively.

$$v_{front} = c_{1,b}\left(\varepsilon_{incident} - \varepsilon_{reflected}\right) \tag{2.1}$$

$$v_{back} = c_{1,b}\varepsilon_{transmitted} \tag{2.2}$$

Then the engineering axial strain rate, engineering axial strain, and the axial stresses of the specimen on the interfaces can be calculated as follows;

$$\dot{\varepsilon}_x^{eng} = \frac{v_{front} - v_{back}}{l_s} \tag{2.3}$$

$$\varepsilon_x^{eng} = \int_0^t \dot{\varepsilon}_x^{eng}(\tau)\, d\tau \tag{2.4}$$

$$\sigma_{x,front} = \frac{A_b}{A_s} E_b\left(\varepsilon_{incident} + \varepsilon_{reflected}\right) \tag{2.5}$$

$$\sigma_{x,back} = \frac{A_b}{A_s} E_b \varepsilon_{transmitted} \tag{2.6}$$

where $\dot{\varepsilon}_x^{eng}$ and ε_x^{eng} describe the engineering axial strain rate and the engineering axial strain, respectively; $\sigma_{x,front}$ and $\sigma_{x,back}$ denote the front stress (the stress on the interface between the incident bar and the specimen) and the back stress (the stress on the interface between the specimen and the

transmitted bar), respectively; l_s means the initial length of the specimen; t describes the time; A_b and A_s denote the cross-section area of the bar components and the specimen, respectively; E_b means the elastic modulus of the bar components. Then, the dynamic engineering axial stress of the specimen (σ_x) can be acquired as the average stress of the front and back stresses following Equation (2.7).

$$\sigma_x = \frac{\sigma_{x,front} + \sigma_{x,back}}{2} \tag{2.7}$$

Finally, the dynamic axial stress–strain relationship is obtained and the dynamic compressive strength of the material can be acquired at the maximum stress. In addition, the axial strain rate–strain relationship and the corresponding strain rate at the maximum stress can be obtained. Therefore, the relationship between the DIF and the corresponding axial strain rate can be described as the SHPB test results.

In order to obtain the relationship between the DIF and the corresponding axial strain rate in a wide range of strain rates, the SHPB tests should be conducted for several specimens under various strain rates. Also, it is important to achieve reproducibility and obtain consistent test results during the test. Therefore, the SHPB test method should be standardized to reduce the dispersion of the test data and to suggest a reliable relationship between the DIF and the strain rate.

Based on the basic principle of the SHPB test, three main issues can be drawn which have to be established: specimen dimension, lubrication method, and loading condition. Before the SHPB test, the specimen dimension should be determined. In particular, the dimension of concrete must be decided considering the aggregate sizes for the accurate evaluation of the dynamic compressive strength. In addition, the appropriate lubrication method has to be applied to the specimen to prevent the frictional effect in the SHPB test and the loading condition should be carefully determined to make the specimen satisfy the dynamic stress equilibrium state as well. Therefore, it is necessary to review the previous studies about each subject: specimen dimension, lubrication method, and loading condition to suggest appropriate guidelines for the concrete SHPB test.

2.2. Previous studies on concrete SHPB test

As mentioned in Section 2.1, numerous experimental studies have been conducted with the SHPB testing system for cementitious composites. However, the previous research performed the SHPB tests without a consistent method because the standard test method has not been established for the test. The previous studies were reviewed in terms of three subjects–specimen dimension, lubrication method, and loading condition–to figure out factors that have to be considered for the standardization.

2.2.1. Specimen dimension

Table 2.1 shows the previous studies which conducted SHPB tests for cementitious composites such as mortar and concrete, where f_c, D, and L denote the static compressive strength, the nominal diameter, and the nominal length of the specimen, respectively. As shown in Table 2.1, most of the research performed the test with small size specimens under 100 mm diameter due to the restriction of the apparatus size. Moreover, most of the studies for concrete specimens used the maximum coarse aggregate sizes (G_{max}) smaller than 19 mm except for a few studies due to the small-dimension of the specimen. However, commonly used G_{max} in construction sites is larger than 25 mm. Therefore, it is questionable whether the DIF obtained from the mortar or concrete with small G_{max} represents the actual strength enhancement of the concrete with large G_{max} used in practice. To resolve the uncertainty about the specimen dimension, the effect of G_{max} and the specimen dimension on the DIF obtained from the SHPB test should be thoroughly investigated.

Table 2.1 Previous experimental studies of the SHPB tests for cementitious composites

Reference	SHPB diameter, mm	Pulse shaping	Material	G_{max}, mm	f_c, MPa	Specimen size, mm	Strain rate, s^{-1}
Bhargava and Rehnström, 1977	100	Not used	Concrete	12	30	D100×L200	30
Fagerlund and Larsson, 1979	-	Not used	Concrete	10–32	46	D100×L100	30
Tang et al., 1984	19.05	Not used	Mortar	-	-	-	200–800
Malvern et al., 1985	-	Not used	Concrete	13 9.5	60–110	D76×L76 D76×L66	59–118
Ross et al., 1989	51	Not used	Concrete	19	60	D51×L51	20–190
Tang et al., 1992	76.2	Not used	Concrete	9.5	97	D76.2×L76.2 D76.2×L38.1	5–230
Ross et al., 1995	51	Not used	Concrete	9.5	48.3	D51×L51	1–300
Tedesco and Ross, 1998	-	Not used	Cement paste	-	30–55	D51×L51	130–370
Grote et al., 2001	12.7 19.05	Not used	Mortar	-	29.7	D: 10.1–18.8 L: 4.8–16.0	250–1700
Zhang et al., 2009	-	Rubber ring shaper	Mortar	-	44.9 51	D37×L18 D50×L25 D74×L21	50–400
Wang et al., 2011	80	Aluminum shaper	Concrete	10	86	D77×L38	10–300
Chen et al., 2013	-	Copper shaper	Concrete	9	44	D74×L37	20–150
Hao and Hao, 2013	75	Varied cross-section striker	Concrete	10	35.5	D75×L37.5	50–200

Reference	SHPB diameter, mm	Pulse shaping	Material	G_{max}, mm	f_c, MPa	Specimen size, mm	Strain rate, s^{-1}
Hao et al., 2013a	40	Varied cross-section striker	Concrete	8	37.6	D32×L16	80–300
Xiao et al., 2015	74	Copper shaper	Concrete	12.5	25–35	D70×L35	10–100
Shemirani et al., 2016	63	Copper shaper	Concrete	10	48.5	D62×L93	43–82
Guo et al., 2017	80	Brass shaper	Concrete	10	60–110	D77×L40	30–110
Lee et al., 2018	76.2	Copper shaper	Concrete	13	51.9 61.35 85.10	D50×L25 D50×L50 D75×L37 D75×L75	37–364
Liu et al., 2018	100	Not used	Mortar	-	32.5 52.5	D90×L45	110–260
Li et al., 2018	75	Not used	Concrete	7.5	High-strength Regular-strength	50 mm cubic D50×L50 D50×L25	20–100
Kim et al., 2019	76.2	Copper shaper	Mortar Concrete	13, 19, 25	53.2 66.4	D50×L50 D75×L75	20–200
Sun et al., 2020	-	Not used	Concrete	15	25	D74×L37	100
Zhang et al., 2021	100	Copper shaper	Mortar	-	5.2	D100×L50	43–220
Hu et al., 2021	74	Simple waveform shaper	Concrete	16	49.34	D70×L35	46.6–95.4
Kim et al., 2022	76.2	Copper shaper	Concrete	13, 25	26.7 28.1 33.6	D50×L40, L50 D75×L45, L60, L75	30–300

2.2.1.1. Hao and Hao (2011)

Hao and Hao (2011) evaluated the effect of coarse aggregate on the dynamic compressive strength of concrete through numerical work. Concrete specimens with different volume fractions of the coarse aggregate were modeled for finite element analysis and the dimension of the specimen was D12×L6 mm. The G_{max} considered in the study was 1.5 mm.

Figure 2.2 exhibits the DIF–strain rate relationship of the analysis cases and the DIF suggested in CEB-FIP model code 1990 for comparison. The analysis result showed that the DIF varies with the volume fraction of the coarse aggregate. Hao and Hao (2011) insisted that the compressive strength of the concrete with more aggregates is higher than others because the crack propagates through the aggregates under a high strain rate. Therefore, they concluded that the aggregate should be considered to avoid the underestimation of the concrete DIF.

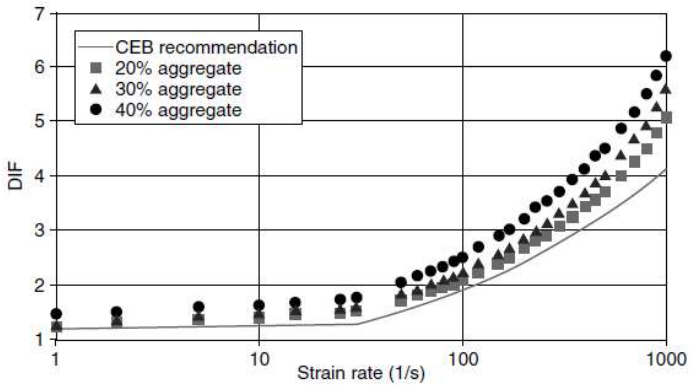

Figure 2.2 Analysis results of Hao and Hao (2011)

2.2.1.2. Chen et al. (2013)

Chen et al. (2013) conducted experimental studies on cementitious composites to investigate the dynamic response of the materials such as failure mechanisms and crack patterns under high strain rates. The SHPB test technique using a pulse shaper was adopted for the experiments and the results of the tests were used to modify an existing dynamic constitutive model of the materials. The SHPB test was performed with cement paste, mortar, and concrete with a G_{max} of 9 mm. The same water-cement ratio was used for the cement paste, mortar, and concrete. The diameter of the specimen was 74 mm and the length was 37 mm.

Figure 2.3 shows the failure modes of the materials at different strain rates. As shown in Figure 2.3, the failure modes were obviously different among the materials. Since the coarse aggregate is not included in the cement paste and the mortar specimens, they have relatively homogeneous cross-sections. However, the cross-section of the concrete is relatively heterogeneous due to the coarse aggregates. Accordingly, the cement paste and mortar showed straight and clean failure cracks while the cracks of the concrete specimen propagated along with the ITZ, between the cement paste and the coarse aggregate, under the lower strain rate range in the test (under 68 s^{-1}).

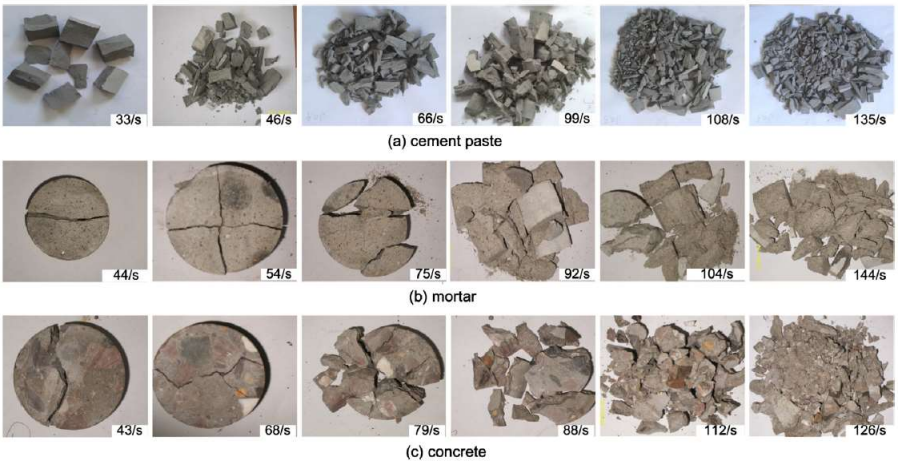

Figure 2.3 Fracture patterns of Chen et al. (2013)

Figure 2.4 shows the relationship between the DIF and the strain rate for cement paste, mortar, concrete, and other studies (Zhou and Hao, 2008, Tedesco et al., 1997, CEB-FIP model code 1990). As depicted in Figure 2.4, the cement paste presented the highest DIF and the concrete showed the lowest DIF. Therefore, it was revealed that the DIF is influenced by the aggregate sizes.

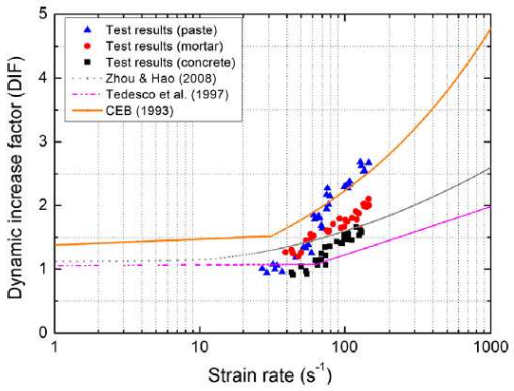

Figure 2.4 Test results of Chen et al. (2013)

2.2.1.3. Hao et al. (2013a)

Hao et al. (2013a) carried out experimental studies to figure out the influence of coarse aggregate in terms of the size and the volume fraction under the impact loading. For the investigation, the SHPB test method was applied. The prepared specimens for the test were mortar matrix and concrete with G_{max} of 4 and 8 mm. The diameter and the length of the test specimen were 32 and 16 mm, respectively. The diameter of the SHPB test apparatus used in the study was 40 mm.

Figure 2.5 presents the DIF–strain rate relationship of the mortar matrix and the concrete specimens with different G_{max}. As shown in Figure 2.5, the DIF is varied with the G_{max}. The mortar matrix which didn't contain the aggregate showed the lowest DIF. In the case of the concrete specimens, the DIF decreases as the increase of G_{max}. Also, the test results of the concrete with a G_{max} of 8 mm were relatively dispersive to others. Hao et al. (2013a) insisted that the dispersion of the test results was induced by the heterogeneity of the concrete specimen due to the large coarse aggregate. Accordingly, Hao et al. (2013a) concluded that the concrete with small coarse aggregate showed better performance under high strain rates. In addition, Hao et al. (2013a) discussed the influence of the volume fraction of the coarse aggregates by suggesting the results depicted in Figure 2.6. The results showed that the volume fraction of the coarse aggregate also affected the DIF. Therefore, it can be concluded that the effect of the coarse aggregate on the DIF of concrete is obvious.

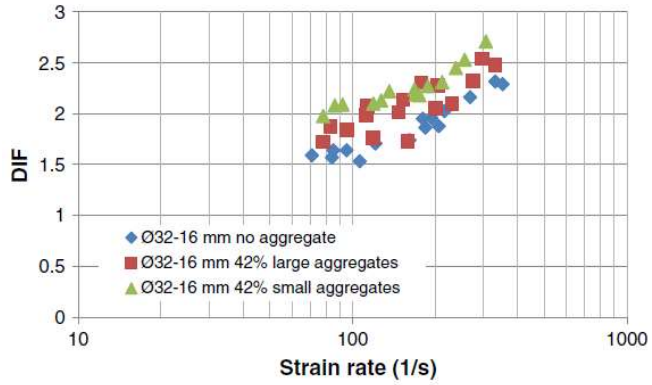

Figure 2.5 DIF–strain rate relationship of mortar matrix and concrete specimens with different G_{max} (Hao et al., 2013a)

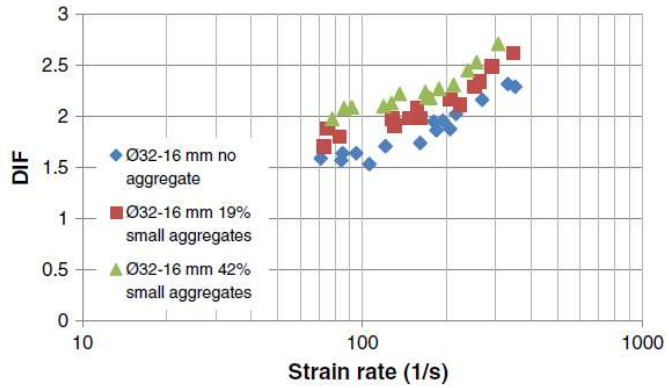

Figure 2.6 DIF of concrete specimen with different volume fractions of coarse aggregate (Hao et al., 2013a)

However, the test of Hao et al. (2013a) only covered the G_{max} under 8 mm which is smaller than the G_{max} used in the actual construction site. Therefore, it is necessary to investigate the effect of G_{max} with larger coarse aggregates to understand the effect of G_{max} in real concrete.

2.2.1.4. Kim et al. (2019)

Kim et al. (2019) perceived the effect of coarse aggregate on concrete DIF through previous studies. Nevertheless, most of the previous experimental studies were conducted for small size specimens with small coarse aggregates because of the diameter restriction of the SHPB test apparatus. Therefore, Kim et al. (2019) conducted a series of SHPB tests for high-strength concrete specimens (static compressive strengths ranging from 50 to 70 MPa) with the actual size coarse aggregates to thoroughly figure out the effect of G_{max} and to suggest a guideline about specimen dimension for the concrete SHPB test. For the SHPB test, the concrete specimens with G_{max} of 13, 19, and 25 mm were prepared. Mortar specimens were also tested for comparison. The specimen dimension was set to D50×L50 and D75×L75 mm considering the G_{max}, referring to ASTM C192, the standard method for making concrete specimens for the static test.

In order to investigate the effect of heterogeneity induced by the coarse aggregate, the dispersion of the test results was evaluated as a multivariate coefficient of variation (COV) about the DIF and the strain rate as shown in Figure 2.7. The severe dispersion of test results was observed for the smaller specimens (D50×L50), especially for the specimen with G_{max} of 19 and 25 mm, which has a smaller dimension than three times G_{max}. However, D75×L75 specimens for all G_{max} presented relatively consistent results. Based on the results, Kim et al. (2019) insisted that the specimen dimension should be at least three times G_{max} to avoid heterogeneity which results in data dispersion.

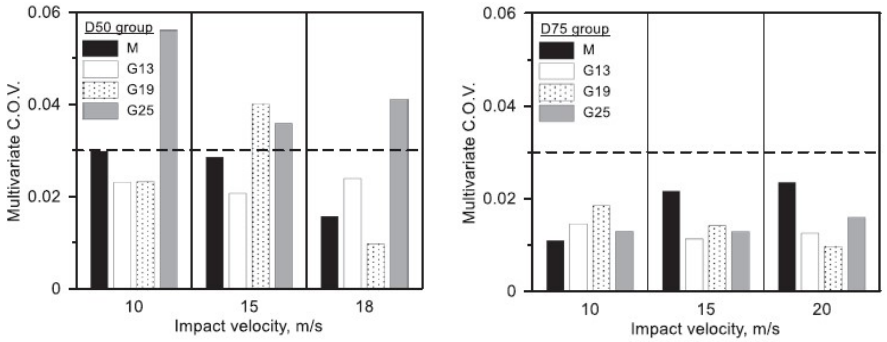

(a) (b)

Figure 2.7 Multivariate COV of Kim et al. (2019); (a) D50 group; (b) D75 group

In addition, the pure rate DIFs for each G_{max} were obtained by eliminating the inertial effect from the DIF obtained through the SHPB test. Figure 2.8 depicts the pure rate DIFs along with the strain rate. As presented in Figure 2.8, the pure rate DIFs were definitely different for each G_{max}. Moreover, there was no specific tendency between the pure rate DIF and the G_{max}. These observations supported the point that the DIF obtained from the specimen with small aggregates cannot represent the DIF of real concrete with large aggregates. Therefore, it is necessary to consider the coarse aggregate size used in practice, and the specimen dimension should be decided carefully considering the coarse aggregate to acquire consistent results.

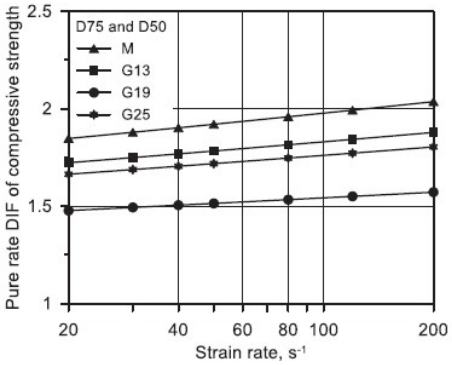

Figure 2.8 Pure rate DIF with different G_{max} (Kim et al., 2019)

2.2.2. Lubrication method

In the concrete SHPB test, the concrete specimen is sandwiched between the incident and the transmitted bars. When the test is performed after setting up the specimen, the concrete specimen is fractured by the incident stress wave. In this procedure, friction on the interfaces between the specimen and the bars confines the lateral deformation of the specimen and enhances the dynamic compressive strength additionally to the strength increment by the strain-rate effect. In other words, the friction overestimates the dynamic compressive strength and makes it difficult to accurately evaluate the pure strain-rate effect under high strain rates. Figure 2.9 shows the engineering stress and engineering strain relationship of an alumina-filled epoxy presented in Chen and Song (2010). As depicted in Figure 2.9, there is a significant difference between non-lubricated and lubricated cases. Therefore, Chen and Song (2010) emphasized that appropriate lubrication should be applied to the interfaces between the specimen and the bars to eliminate the frictional effect.

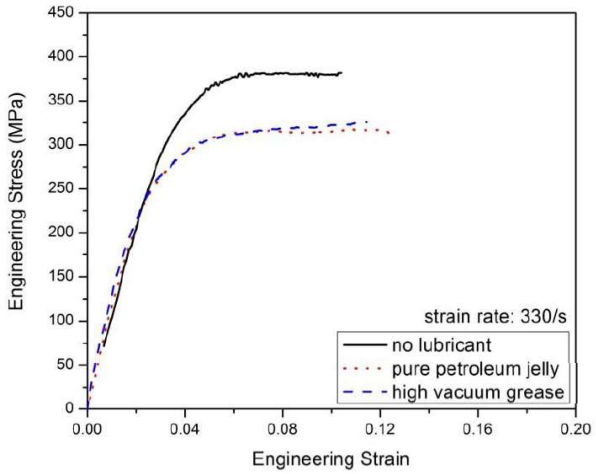

Figure 2.9 Lubrication effect presented in Chen and Song (2010)

For this, a number of previous studies have used lubricants such as petroleum jelly and grease. Table 2.2 presents the previous studies of the SHPB test with lubrication for cementitious composites. As listed in Table 2.2, various experimental works applied lubrication to remove the frictional effect in the SHPB tests.

However, none of the research explained the details of the lubrication method including the type and amount of lubricant. Therefore, it is necessary to investigate the frictional effect on the concrete SHPB test and the effect of lubrication on the frictional effect. Moreover, a standardized lubrication method has to be established to accurately evaluate the pure strain-rate effect of concrete under high strain rates.

Table 2.2 Previous studies about SHPB test with lubrication

Reference	Specimen	Lubricant	Lubrication details
Wang et al., 2011	Concrete	Grease	A thin layer of grease was applied.
Hao et al., 2013a	Concrete Mortar	Grease	Grease was applied at the specimen-bar interfaces.
Heard et al., 2014	Concrete	High-pressure MoS_2 paste	Lubricant was applied at the specimen-bar interfaces.
Shemirani et al., 2016	Concrete	Grease	Specimens were attached with a very thin layer of grease.
Guo et al., 2017	Concrete	Not mentioned	Surface treatment and lubrication were applied.
Lee et al., 2018	Concrete	Petroleum jelly	Petroleum jelly was applied to the surfaces of the specimen.
Kim et al., 2019	Concrete	Petroleum jelly	Petroleum jelly lubricant was applied.
Hu et al., 2021	Polyvinyl chloride coarse aggregate concrete	Vaseline (Petroleum jelly)	Vaseline was coated on both ends of the specimens.

2.2.2.1. Li and Meng (2003)

Li and Meng (2003) attempted to verify the validity of SHPB tests on cementitious composites by analyzing previous studies. Li and Meng (2003) insisted that the strength enhancement of cementitious composites under high strain rates includes not only the strain-rate effect but also the lateral confinement induced by the frictional effect and the lateral inertial effect. In addition, Li and Meng (2003) explained that the frictional effect at the contact between the specimen and the bars is normally ignored for metal specimens if

the specimen is lubricated because the metal is hydrostatic-stress-independent. However, the frictional effect in cementitious composites may not be neglected due to the hydrostatic-stress-dependency of the material according to Li and Meng (2003).

Therefore, it is necessary to develop an optimized lubrication method for the concrete SHPB test.

2.2.2.2. Li et al. (2009)

Li et al. (2009) conducted numerical work to investigate the non-strain-rate effects on the DIF of cementitious composites through the SHPB test. For this purpose, Li et al. (2009) modeled mortar specimens, and the frictional effect of the DIF was considered by inputting constant friction coefficients (μ) ranging from 0 to 0.7. According to Li et al (2009), the dynamic compressive strength of the mortar increases significantly when μ is higher than 0.2. However, the frictional effect is negligible for the cases when $\mu \leq 0.1$. Li et al. (2009) insisted that proper lubrication can reduce the frictional coefficient.

2.2.2.3. Kim et al. (2010)

Kim et al. (2010) figured out the effect of friction on DIF through numerical analysis. Figure 2.10 shows the simulation results of Kim et al. (2010) and the SHPB test results of Grote et al. (2001). As presented in Figure 2.10, the friction at the specimen and the bar interfaces significantly influenced the DIF.

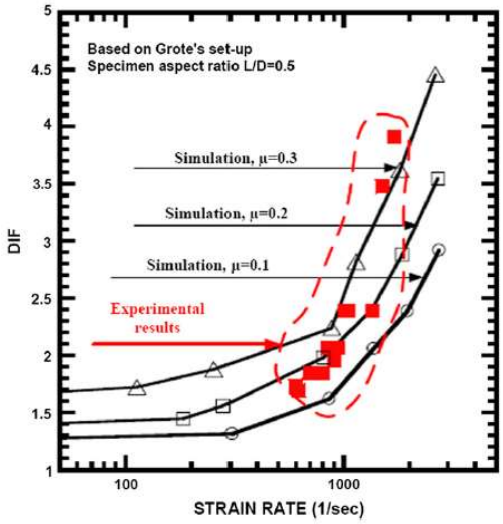

Figure 2.10 Frictional effect investigated in the study of Kim et al. (2010)

2.2.2.4. Hao et al. (2013a)

Hao et al. (2013a) carried out an SHPB test for cementitious composites to investigate the influencing factors on DIF. In particular, the concrete specimens with a G_{max} of 4 mm were tested for different L/D ratios (D32×L30, D32×L20, and D32×L10) to explore the effect of friction at the specimen and the bar interfaces. In the test, lubricant was not applied to the specimen and the apparatus. Figure 2.11 presents the DIF and the strain rate relationship of the specimens. Through Figure 2.11, it was observed that the frictional effect was influenced by the L/D ratio of the specimens.

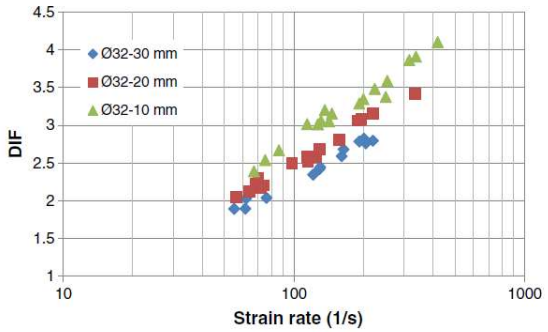

Figure 2.11 Test results of Hao et al. (2013a)

Accordingly, Hao et al. (2013a) tried to correct the frictional effect using numerical simulation and the static friction coefficient. However, the corrected DIF showed a slight difference from the reference DIF curve. Hao et al. (2013a) explained that the difference was caused by the discrepancy between the static and the dynamic friction coefficient since the dynamic friction coefficient is applied during the SHPB test rather than the static friction coefficient. Also, they stated that the determination of the dynamic friction coefficient is difficult in the test.

Therefore, an effective lubrication method should be developed to overcome the uncertainty of correcting the frictional effect after the test.

2.2.2.5. Hao et al. (2013b)

Hao et al. (2013b) investigated the frictional effect on DIF through a series of numerical analyses. The finite element analyses were carried out for concrete specimens with L/D ratios of 0.5, 1.0, and 2.0. In order to compare the frictional effect, friction coefficients ranging from 0.0 to 0.5 were applied. Figure 2.12 presents the analysis results for different L/D ratios and frictional

coefficients. As shown in Figure 2.12, the effect of friction was more critical for the specimens with low L/D ratios. Moreover, the frictional effect became severe as the strain rate increased. However, there was no effect of the L/D ratio when the friction did not exist as depicted in Figure 2.13.

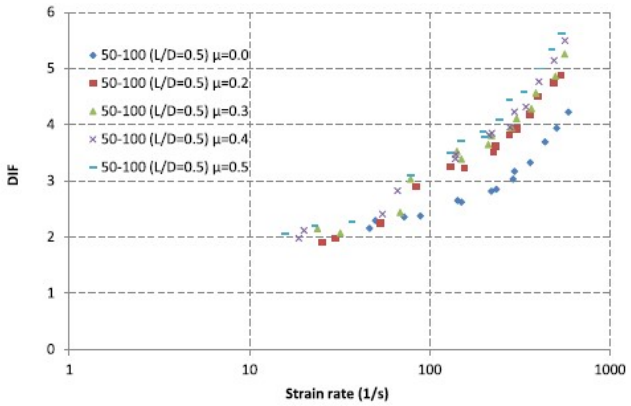

(a)

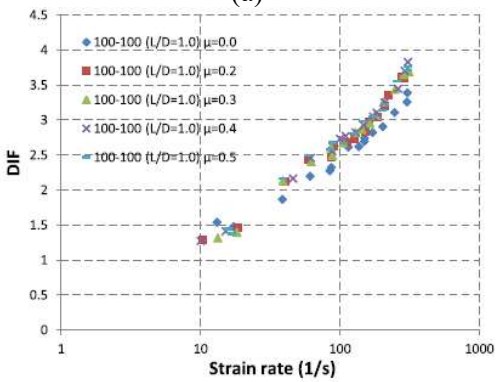

(b)

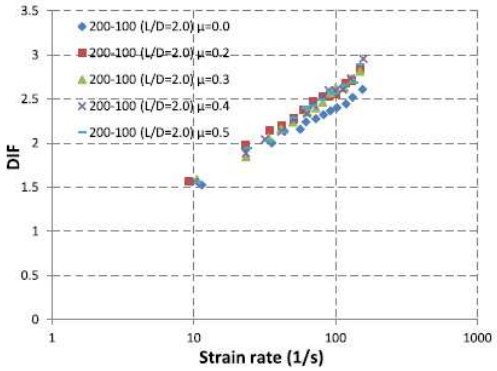

(c)

Figure 2.12 Analysis results of Hao et al. (2013b); (a) L/D = 0.5; (b) L/D = 1.0; (c) L/D = 2.0

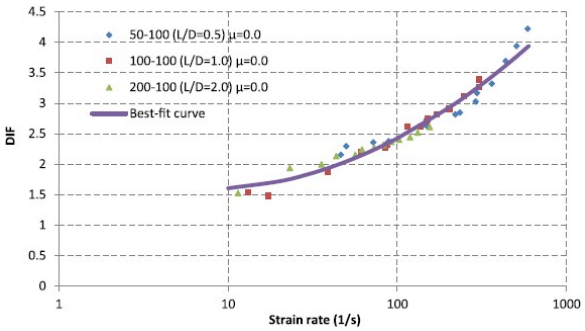

Figure 2.13 Analysis results without frictional effect of Hao et al. (2013b)

Therefore, the frictional effect should be considered or thoroughly removed for the reliable evaluation of the strength enhancement of the cementitious composites through the SHPB test.

2.2.2.6. Liu et al. (2018)

Liu et al. (2018) performed an SHPB test for mortar specimens to investigate the interfacial effect in the SHPB test: interfacial friction

coefficient, specimen diameter, and specimen non-parallelism. Liu et al. (2018) repeated the test to compare the consistency of the test results since the prepared specimens had individual differences in the interfacial contact conditions. The consistency of the test results was evaluated using stress waves of repeated tests, and the results showed slight differences from each other. Therefore, Liu et al. (2018) inferred that the discrepancy of the test results in the repeated tests was caused by the interfacial effect.

In addition, Liu et al. (2018) conducted numerical analyses to compare the interfacial effects–interfacial friction coefficient, specimen diameter, and specimen non-parallelism–on normal-strength cement mortar (NSCM) and high-strength cement mortar (HSCM). Figure 2.14 presents the analysis results, where the y-axis indicates the sensitivity of the parameter. Through the analysis, it was revealed that the interfacial friction coefficient was a dominant parameter of the interfacial effects.

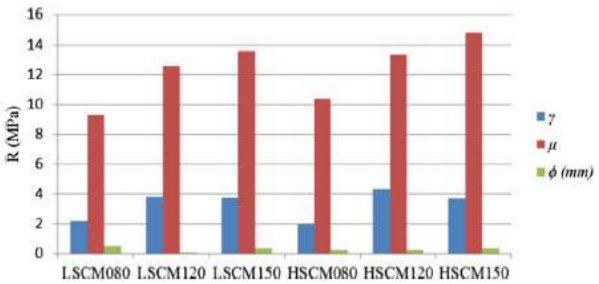

Figure 2.14 Analysis results of Liu et al. (2018)

Therefore, it can be concluded that the most important thing to obtaining an accurate and reliable DIF of concrete through SHPB is a minimization of the frictional effect.

2.2.3. Loading condition

In the concrete SHPB test, the result of the experiment is only valid when the specimen satisfies the dynamic stress equilibrium state during the test. The dynamic stress equilibrium of the specimen is significantly affected by the loading which corresponds to the incident stress wave in the SHPB test technique. The dynamic stress equilibrium is achieved when the front stress and back stress of the specimen are similar. In other words, sufficient time is needed to evenly distribute the stress in the specimen after the incident stress wave arrived at the specimen. For this, the incident stress wave should be gradually imposed on the specimen. However, the incident stress wave generated by the collision of the striker on the incident bar shows the rectangular pulse as presented in Figure 2.15.

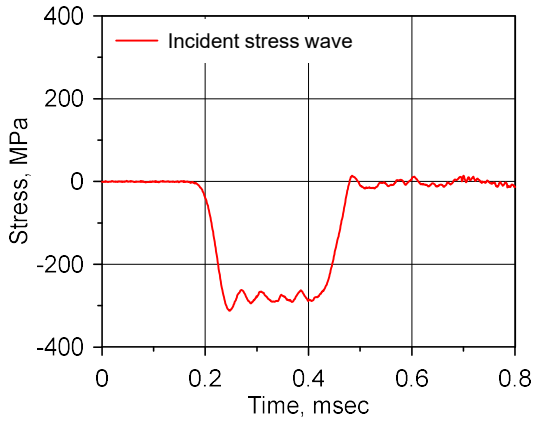

Figure 2.15 Typical incident stress wave in SHPB test

Therefore, previous researchers have made efforts to generate gradually increasing incident stress waves by changing the form of the striker (Lok et al., 2002) or using a pulse shaper (Lu and Li, 2010, Heard et al., 2014, Shemirani

et al., 2016, Xu and Wille, 2016, Hassan and Wille, 2017). In this study, the pulse shaping technique was adopted. In the pulse shaping technique, a pulse shaper is attached to the impact end of the incident bar as described in Figure 1.3. Figure 2.16 shows the typical incident stress wave using a pulse shaper made of C1020 copper.

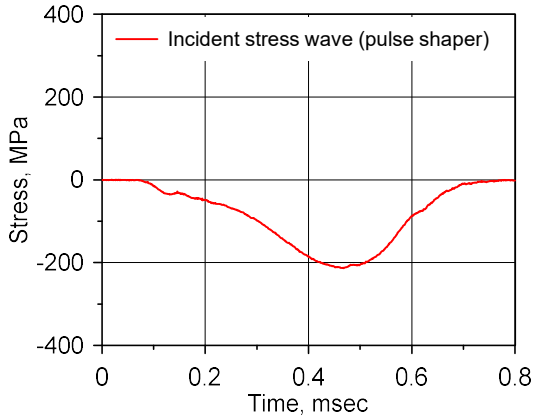

Figure 2.16 Typical incident stress wave using a pulse shaper made of copper

Moreover, the pulse shaper is effective to alleviate wave dispersion of the incident stress wave. Since the incident stress wave consists of various frequencies and the SHPB apparatus for testing cementitious composites has a relatively large diameter, it shows wave dispersion. However, the pulse shaper is helpful to alleviate wave dispersion because the pulse shaper filters out the high-frequency components. For these reasons, the pulse shaping technique has been widely used for a number of studies on the SHPB test.

Therefore, the previous studies on the pulse shaping technique for the SHPB test on cementitious composites should be reviewed to suggest an organized method for the loading condition.

2.2.3.1. Lu and Li (2010)

Lu and Li (2010) conducted numerical analyses to appraise the pulse shaping SHPB test on mortar specimens. The SHPB apparatus having diameters of 20, 74, and 100 mm was modeled for the analyses. The input incident stress waves using pulse shaper were assumed as half-sine, bell-like, triangular, and trapezium for the SHPB system with a diameter of 74 mm as shown in Figure 2.17. The incident stress wave without pulse shaper was additionally considered for the 74 and 100-mm-diameter-SHPB system for comparison. Also, an isosceles trapezium shape wave was used for the SHPB apparatus with a 20 mm diameter.

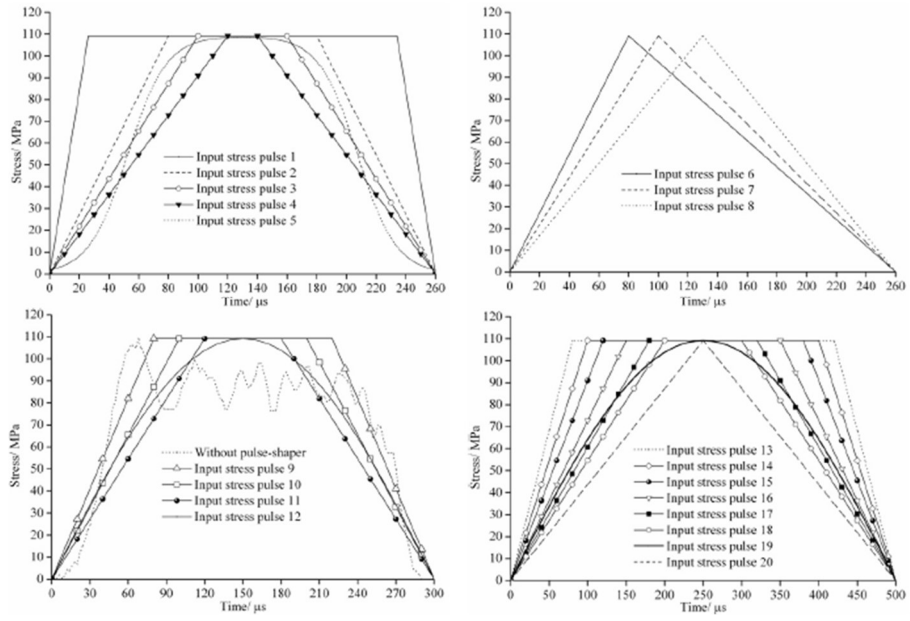

Figure 2.17 Applied incident stress waves for 74-mm-diameter-SHPB system of Lu and Li (2010)

Figure 2.18 shows the analysis results of Lu and Li (2010), where P_1 and P_2 denote the front force, force on the interface between the incident bar and the specimen, and the back force, stress on the interface between the specimen and the transmitted bar, respectively; t and t_0 mean the time and the transit time, respectively. The front force, back force, and transit time can be calculated with Equations (2.8)–(2.10), where $c_{1,s}$ denotes the elastic wave velocity of the specimen (Lu and Li, 2010). When the ratio of the front force and the back force is similar to 1.0, the dynamic stress equilibrium state is achieved. As presented in Figures 2.18 (a) and (b), the dynamic stress equilibrium was hardly satisfied without a pulse shaper. Also, a 100 mm-SHPB system was relatively more difficult to achieve the dynamic stress equilibrium than a 74-mm-SHPB system.

$$P_1 = A_b E_b \left(\varepsilon_{incident} + \varepsilon_{reflected} \right) \tag{2.8}$$

$$P_2 = A_b E_b \varepsilon_{transmitted} \tag{2.9}$$

$$t_0 = \frac{l_s}{c_{1,s}} \tag{2.10}$$

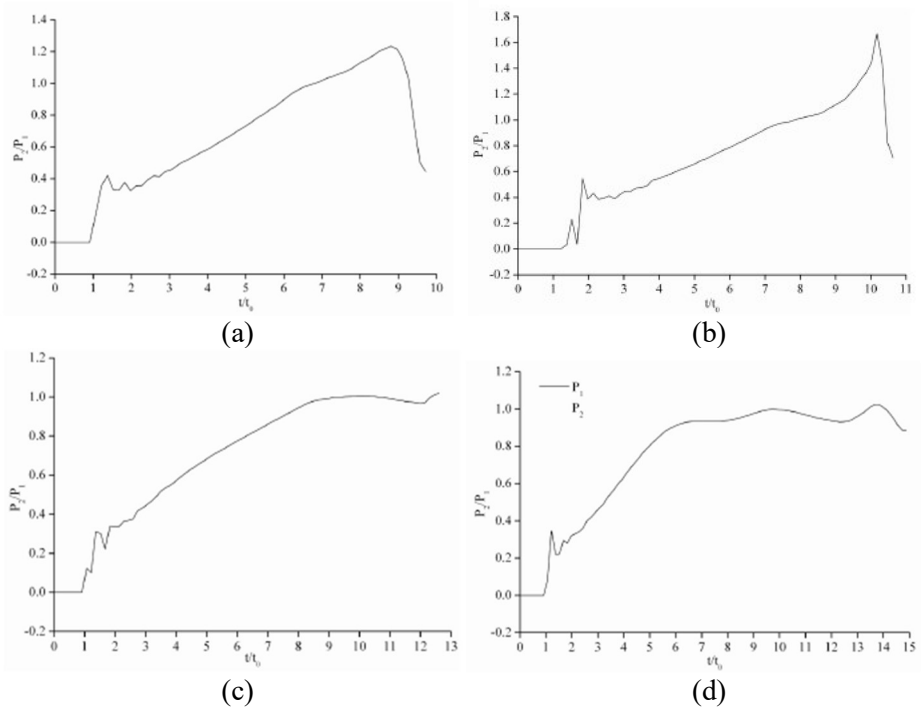

Figure 2.18 Analysis results of Lu and Li (2010); (a) 74-mm-SHPB test without pulse shaper; (b) 100-mm-SHPB test without pulse shaper; (c) 74-mm-SHPB test with pulse 5; (d) 74-mm-SHPB test with pulse 16

Figure 2.19 presents the time histories of the dynamic stress equilibrium index (R(t)) for several incident stress waves used in the numerical analysis. If R(t) is close to 0.0, it can be said that the dynamic stress equilibrium is satisfied. As shown in Figure 2.19, R(t) was quickly decreased after four reverberations except for the cases without pulse shaper and pulse 1 which has a short rising time.

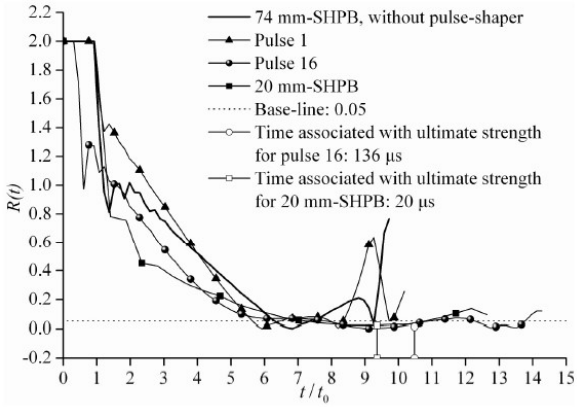

Figure 2.19 Analysis result on dynamic stress equilibrium of Lu and Li (2010)

Therefore, Lu and Li (2010) concluded that the dynamic stress equilibrium is difficult to achieve without using a proper pulse shaper which helps to extend the rising time of the incident stress wave.

2.2.3.2. Heard et al. (2014)

Heard et al. (2014) developed a novel pulse shaping technique for a large-diameter SHPB test system. Heard et al. (2014) explained that the large solid pulse shaper for the large diameter SHPB test apparatus generates noise-like oscillations on the incident stress wave because of the radial inertia in the solid pulse shaper. Therefore, Heard et al. (2014) devised an annular shape pulse shaper.

Figure 2.20 illustrates the incident wave with different types of copper pulse shapers presented in Heard et al. (2014). As shown in Figure 2.20, the solid pulse shaper with a large diameter (25.4-mm-diameter and 1.5-mm-thickness) included oscillation while the annular pulse shaper (25.4-mm-outer-diameter and 14.4-mm-inner-diameter) didn't. In addition, Heard et al.

(2014) applied the developed annular pulse shaper for the SHPB test of self-consolidating high-strength concrete, and the results showed that the dynamic stress equilibrium of the specimen was satisfied. Therefore, Heard et al. (2014) recommended that the annular pulse shaper is suitable for the SHPB test system with a large diameter for cementitious composites.

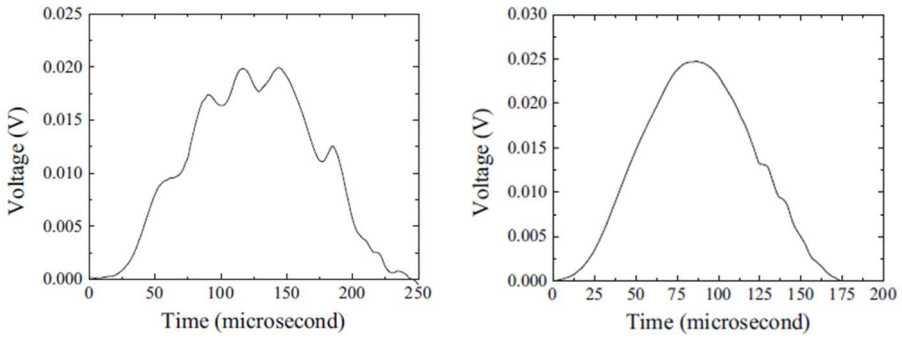

(a) (b)

Figure 2.20 Incident stress waves presented in Heard et al. (2014);
(a) Solid pulse shaper; (b) Annular pulse shaper

2.2.3.3. Shemirani et al. (2016)

Shemirani et al. (2016) conducted experimental and numerical studies to investigate effective pulse shaping parameters such as the diameter and length of the pulse shaper. The SHPB tests were performed for concrete specimens, and the solid copper pulse shapers with three dimensions were used: 12 and 24 mm diameters for a thickness of 1 mm and 12 mm diameter for a thickness of 2 mm.

Figure 2.21 shows the test results on the dynamic stress equilibrium of Shemirani et al. (2016) for different pulse shaping conditions. For the

dynamic stress equilibrium state, the sum of the incident and the reflected stress wave should be similar to the transmitted stress wave. As presented in Figure 2.21, the thicker pulse shapers showed better results with a proper rising time of the waves. Therefore, Shemirani et al. (2016) insisted that using an improper pulse shaper makes the specimen difficult to achieve the dynamic stress equilibrium state. They also insisted that the pulse shaper with a large thickness is needed for the dynamic stress equilibrium state. Moreover, Shemirani et al. (2016) recommended changing the dimension of the pulse shaper for each strain rate considering the velocity of the striker.

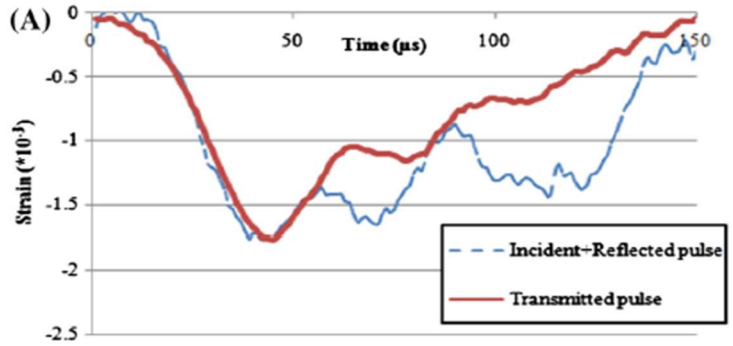

(a)

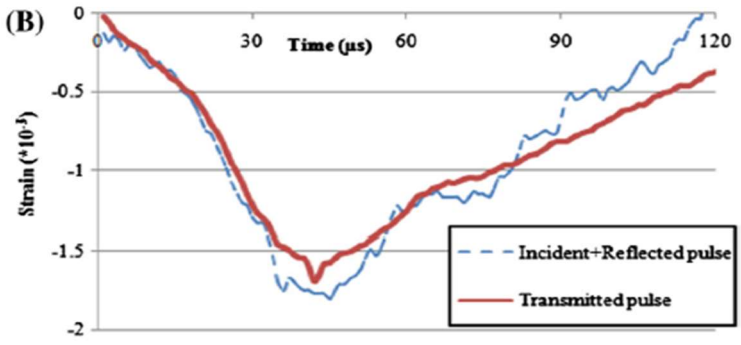

(b)

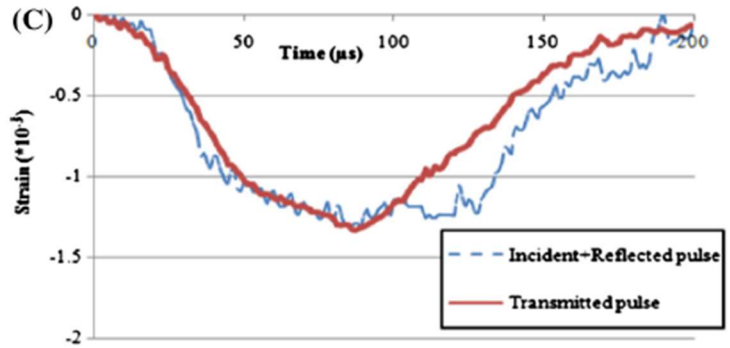

(c)

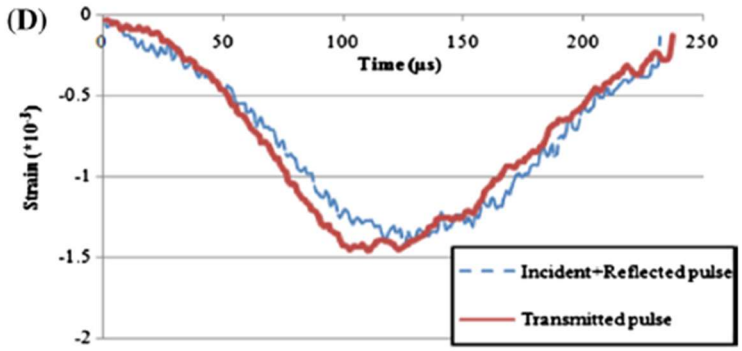

(d)

Figure 2.21 Test results of Shemirani et al. (2016); (a) Without pulse shaper; (b) Using pulse shaper of 12-mm-diameter and 1-mm-thickness; (c) Using pulse shaper of 24-mm-diameter and 1-mm-thickness; (d) Using pulse shaper of 12-mm-diameter and 2-mm-thickness

2.2.3.4. Xu and Wille (2016)

Xu and Wille (2016) conducted numerical analyses to examine the effect of the material and dimension of pulse shaper in the SHPB test for ultra-high-performance fiber-reinforced concrete. Various pulse shapers were considered in the numerical analyses. The material used for the pulse shapers were copper,

brass, and aluminum alloy. Four diameters and five thicknesses were applied for the modeling of the pulse shapers.

Figure 2.22 shows the incident stress waves and dynamic stress equilibrium results for different pulse shapers with the same thickness presented in Xu and Wille (2016). The effect of the material and diameter of the pulse shaper can be compared in Figure 2.22. As presented in Figure 2.22, the pulse shaper made of the aluminum alloy performed stably in terms of the dynamic stress equilibrium. Moreover, it was revealed that the increase in the diameter of the pulse shaper induced wave oscillations but the diameter did not affect the rising time of the incident stress wave.

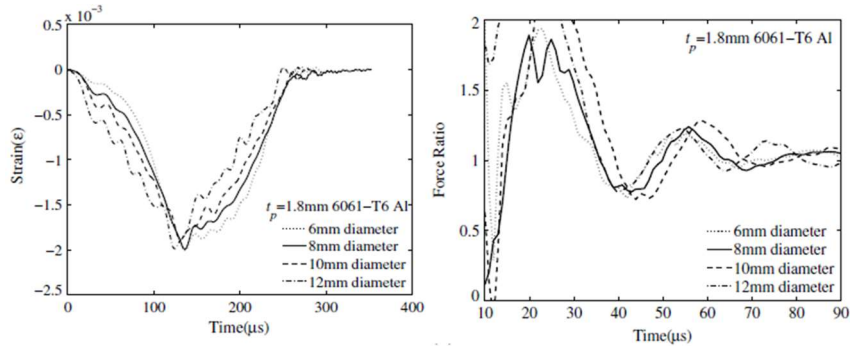

(a)

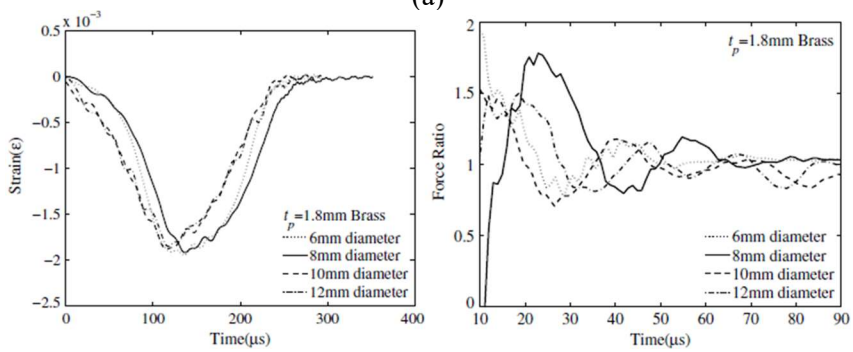

(b)

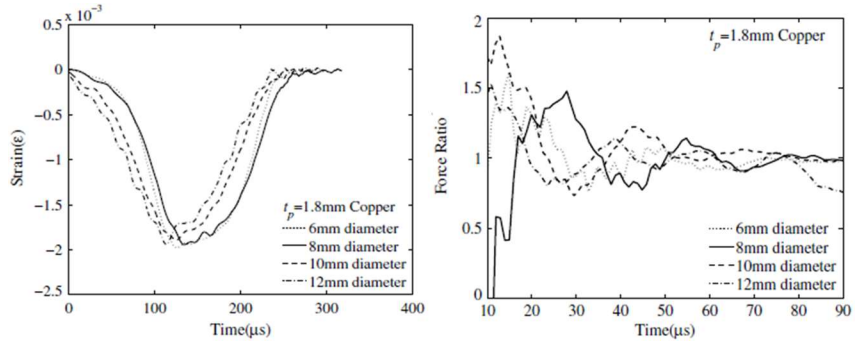

(c)

Figure 2.22 Analysis results of Xu and Wille (2016) for the same thickness of the pulse shaper; (a) Aluminum alloy; (b) Brass; (c) Copper

Figure 2.23 presents the analysis results of Xu and Wille (2016) for different pulse shapers with the same diameter. Through Figure 2.23, it was clearly seen that the increase in the thickness of the pulse shaper extended the rising time of the incident stress wave. In addition, Xu and Wille (2016) insisted that the dimension of the pulse shaper should be changed according to the impact velocity of the striker for the valid SHPB test.

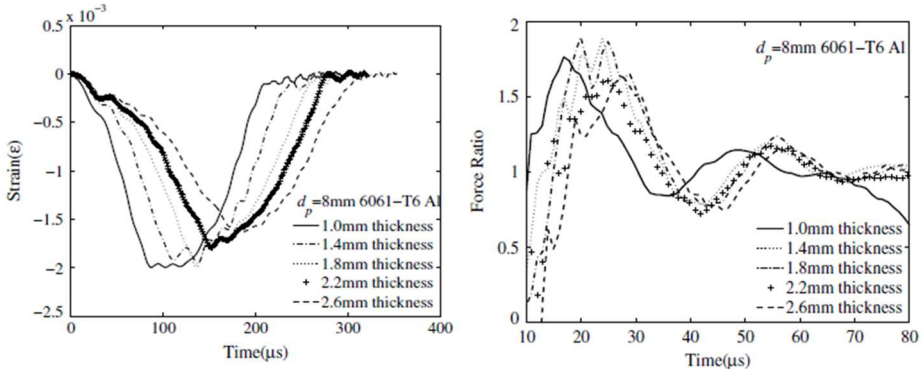

(a)

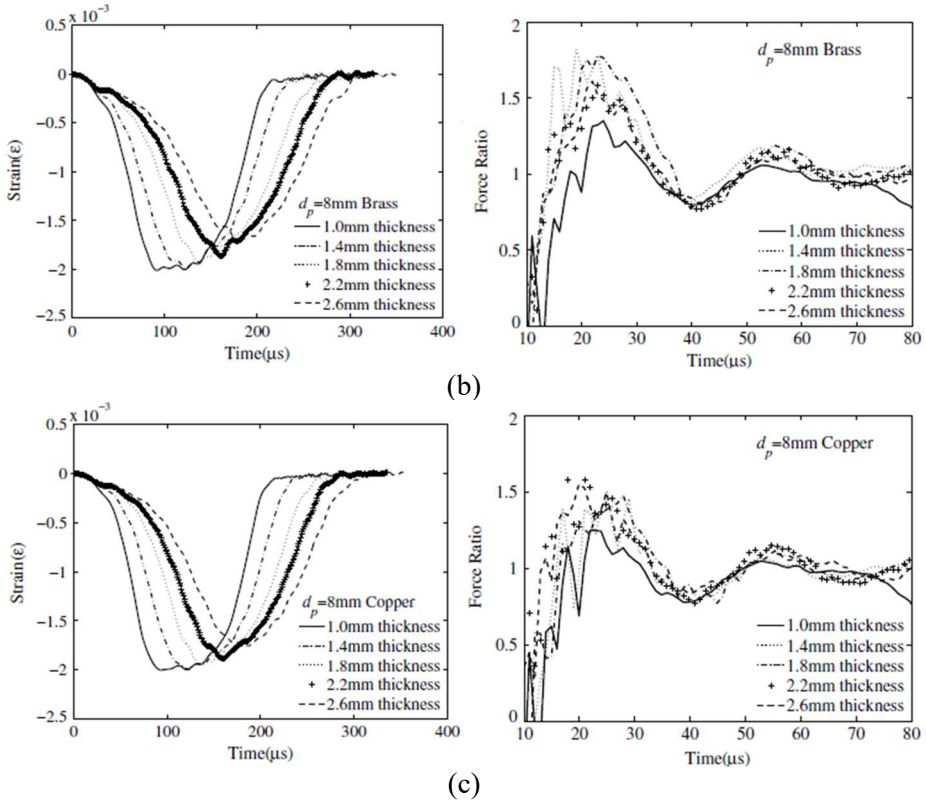

Figure 2.23 Analysis results of Xu and Wille (2016) for the same diameter of the pulse shaper; (a) Aluminum alloy; (b) Brass; (c) Copper

2.2.3.5. Hassan and Wille (2017)

Hassan and Wille (2017) carried out SHPB tests for ultra-high performance concrete with different pulse shapers. Copper and aluminum pulse shapers were applied with three diameters and four thicknesses.

The incident stress waves generated with different pulse shapers are illustrated in Figure 2.24. As shown in Figure 2.24, the rising time of the incident stress wave increased as the thickness of the pulse shapers increased.

Moreover, the incident stress wave increased steeply and decreased shallowly for the smaller diameter of the pulse shaper regardless of the material.

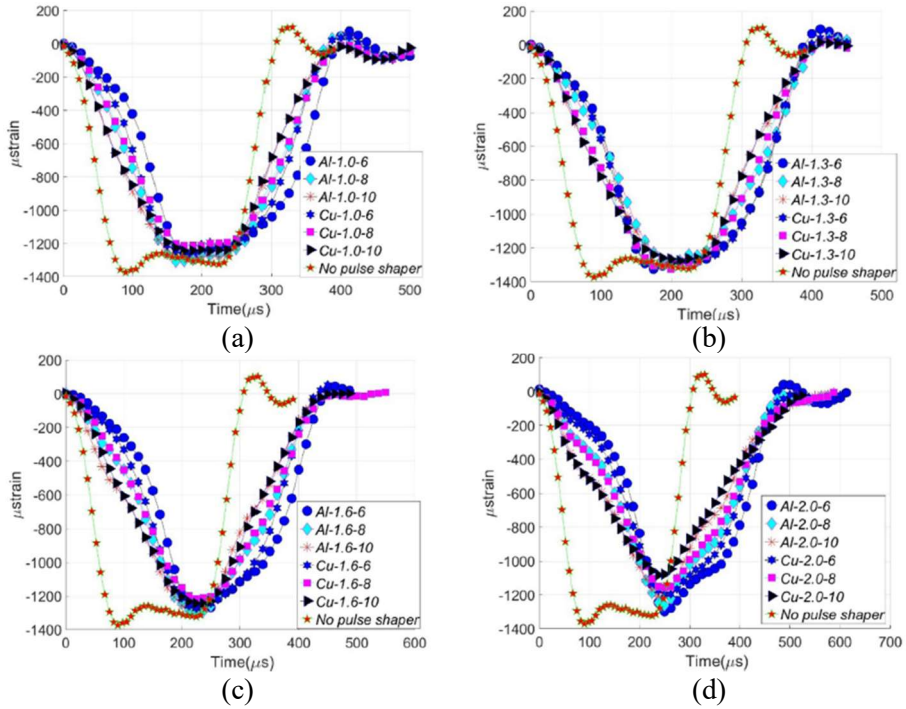

Figure 2.24 Test results of Hassan and Wille (2017) for different thickness of pulse shaper; (a) 1.0 mm; (b) 1.3 mm; (c) 1.6 mm; (d) 2.0 mm

In addition, Hassan and Wille (2017) discussed the dynamic stress equilibrium of the tested specimens with different pulse shapers and they concluded that the pulse shaper is essential for the dynamic stress equilibrium of the specimen in the SHPB test.

2.3. Concluding remarks

As mentioned in Section 2.1, it is required to establish a test method for the concrete SHPB test because the dynamic material properties of the concrete can be obtained as a DIF–strain rate relationship based on several test results through the SHPB test. The test method should include major contents such as specimen dimension, lubrication method, and loading condition. Therefore, previous studies on each issue were reviewed in Section 2.2 to draw important factors to organize and establish the test method.

Firstly, previous research on the specimen dimension was reviewed. Since the general concrete consists of cement, water, fine aggregate, and coarse aggregate, the specimen dimension should be decided considering the size of the aggregates. In particular, the specimen dimension is restricted by the diameter of the SHPB apparatus. Therefore, a guideline to determine the specimen dimension is necessary. To this end, several researchers conducted numerical and experimental studies to investigate the effect of aggregates in terms of size and volume fraction. It was revealed that the dynamic compressive behavior of the concrete was influenced by the size and volume fraction of the aggregates from the studies. Moreover, the heterogeneity of the concrete specimen resulted in dispersive results. However, most of the G_{max} used in previous studies were quite smaller than 25 mm which is the widely used G_{max} in actual construction sites. Although there was an experimental study that used a large G_{max} (Kim et al., 2019), only high-strength concrete specimens with static compressive strengths ranging from 50 to 70 MPa were covered. Therefore, an additional investigation on the effect of the G_{max} for

normal-strength concrete is required to suggest a standardized guideline for the determination of the specimen dimension for the concrete SHPB test.

Secondly, previous studies on the effect of friction in the SHPB test for cementitious composites were reviewed to figure out the necessity of lubrication and to suggest a proper lubrication method. Most of the researchers conducting the SHPB test recognized the frictional effect in the test and applied lubricants on the specimen to avoid the frictional effect. According to the previous research introduced in Section 2.2.2, the friction on the specimen-bar interfaces significantly enhances the dynamic compressive strength of the cementitious composites in the SHPB test and results in the overestimation of the strain-rate effect. However, researchers insisted that the frictional effect can be minimized with the proper lubrication method. Nevertheless, the standard lubrication method for the concrete SHPB test covering the type and amount of the lubricant has not been established. Therefore, it is essential to develop a standardized lubrication method to improve the accuracy of the dynamic behavior evaluation of the concrete in the SHPB test.

Lastly, previous research related to the loading condition of the SHPB test for cementitious composites was reviewed to understand the loading condition of the SHPB test and to suggest a guideline for the determination of the loading condition. As explained in Section 2.2.3, the test results acquired from the SHPB test are only valid when the dynamic stress equilibrium state of the specimen is satisfied. However, it is difficult to achieve the dynamic stress equilibrium when the typical incident stress waves are applied to the

specimen due to steeply rising pulses in a very short time duration. In particular, the SHPB apparatus for testing cementitious composites has a relatively large diameter to the system for metallic materials. Therefore, the incident wave of the apparatus for the cementitious composites shows wave dispersion. To resolve these problems, some researchers adopted the pulse shaping technique. In the pulse shaping SHPB test, the pulse shaper extends the rising time of the incident stress wave and filters out the high-frequency components so it helps the specimen to satisfy the dynamic stress equilibrium. However, the dimension and material of the pulse shaper and the combination of the pulse shaper and the impact velocity of the striker generates different incident stress waves so it produces different results. Moreover, the test results may differ for specimens with different material properties. Therefore, a specific guideline to decide the loading condition considering the material properties of the specimen is necessary to improve the efficiency of the SHPB test.

Therefore, the major contents of the concrete SHPB test method for consistent evaluation of the dynamic compressive strength were drawn as listed in Table 2.3 through the reviewing of the principle of SHPB test and previous studies. This study conducted a series of SHPB tests focusing on the contents presented in Table 2.3 to establish the test method for the concrete SHPB test. The details of the experiment program and results will be explained and discussed in the following chapters.

Table 2.3 Contents of the test method for concrete SHPB test

Test method for concrete SHPB test							
	Specimen preparation		SHPB test program				
	Specimen dimension	Specimen fabrication	Test condition		Data acquisition		Report
			Loading	Lubrication	Measurement	Data processing	
Contents	・Diameter ・Length	・Fabrication program ・Dimension measurement	・Available incident wave rate range	・Lubricant ・Amount of lubricant	・Strain gauge for SHPB ・Strain gauge for concrete ・Impact velocity of striker	・Dynamic stress–strain relationship ・Dynamic compressive strength ・Strain rate ・Strain acceleration ・Dynamic stress equilibrium	・Specimen dimension ・Loading condition ・Static compressive strength ・Dynamic compressive strength ・Strain rate ・Strain acceleration ・Dynamic stress equilibrium

3. Effect of Maximum Coarse Aggregate Size in Concrete SHPB Test

In Chapter 3, details of the SHPB test for investigation of the effect of maximum coarse aggregate size on concrete dynamic material properties are described.

3.1. SHPB test program

3.1.1. Test variables

The most crucial test variable is the maximum coarse aggregate size. In order to figure out the effect of G_{max}, three sizes of G_{max} were used: 13, 19, and 25 mm. In addition, mortar specimens were prepared to compare the effect of coarse aggregate. According to ASTM C192, the diameter of the cylindrical specimen should be at least three times G_{max}. Thus, the specimen dimension was determined to be D75×L75 mm which satisfies three times the largest G_{max}, 25 mm. In concrete, the cross-section is heterogeneous due to the coarse aggregate and the heterogeneity differs according to the specimen dimension for the same G_{max}. The heterogeneity over the cross-section may affect the dispersion of the test results. Therefore, D50×L50 mm specimens were also prepared to compare the effect of G_{max} in terms of the heterogeneity over the specimen cross-section. Three impact velocities for each specimen dimension were applied to the test to acquire the test results in a wide range of strain rates (10, 13, and 15 m/s for the D50 specimen group and 10, 15, and 18 m/s for the D75 specimen group). Annular pulse shapers made of C1020

copper were used for the dynamic stress equilibrium of the specimen. The dimensions of the pulse shapers were selected through preliminary tests. The pulse shaper with the dimension of 52×48×4 mm was used for the tests with the impact velocities of 10 and 15 m/s, and a 51×47×3 mm pulse shaper was applied to the tests of 13 and 18 m/s. The static compressive strength for the test was aimed to be normal strength, 30 MPa. The SHPB tests were repeated ten times for each specimen group to estimate the dispersion of the test results. Therefore, a total of 240 tests were conducted (120 tests for D50 and 120 tests for D75). Table 3.1 lists the test variables, and each test group's designation is shown in Figure 3.1.

Table 3.1 Details of SHPB test to investigate the effect of G_{max}

Parameter	Value
G_{max}, mm	Mortar, 13, 19, 25
Specimen dimension, mm	D50×L50, D75×L75
Static compressive strength, MPa	30
Impact velocity, m/s	10, 13, 15 for D50×L50 10, 15, 18 for D75×L75
Pulse shaper material	C1020 copper
Pulse shaper dimension, mm	52×48×4 for 10 and 15 m/s 51×47×3 for 13 and 18 m/s

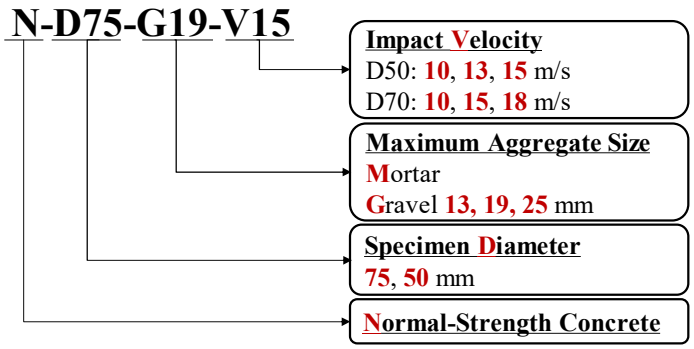

Figure 3.1 Designation of specimen group

3.1.2. Specimen preparation

Cylindrical molds of D50×L100 and D75×L150 mm were used for specimen fabrication. Table 3.2 presents mix proportions for the mortar and concrete specimens. Only the G_{max} was replaced for the same unit weight of the coarse aggregate. The specimens were prepared and cured referring to ASTM C192. After curing, the cylindrical specimens were cut into D50×L50 and D75×L75 mm for the SHPB test. The middle part of the specimens was obtained by cutting out both ends. The actual lengths of the specimens were obtained as an average value of lengths measured at six locations spaced evenly around the circumference. In addition, a maximum difference of the length was calculated as a difference between the maximum and the minimum lengths. Then the error of the perpendicularity to the axis was evaluated as the ratio of the maximum difference of length to the diameter of the specimen. The maximum error of perpendicularity to the axis among all of the specimens was 0.41º which is lower than the value suggested in ASTM C39, 0.5º. Figure 3.2 shows the prepared specimens for the SHPB test (G19) and Figure 3.3 illustrates how the specimen length and the error of the perpendicularity to the axis were evaluated.

Table 3.2 Mix proportions

Target strength, MPa	G_{max}, mm	Unit weight, kg/m^3			
		Cement	Water	Fine aggregate	Coarse aggregate
30	Mortar	390	180	810	-
	13, 19, 25	390	180	810	988

Figure 3.2 Prepared SHPB specimens for G19

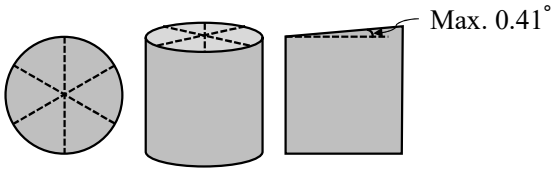

Figure 3.3 Specimen length measurement and error of the perpendicularity to the axis

Before performing the SHPB test, a static compressive strength test was conducted for D50×L100 and D75×L150 mm cylindrical specimens. Table 3.3 shows the static compressive strength of each specimen, average compressive strength, and average density of the specimens.

Table 3.3 Static compressive strength of mortar and concrete specimens

Specimen		Static compressive strength, MPa				Average strength, MPa	Average density, kg/m^3
		#1	#2	#3	#4		
D50×L100	M	19.0	20.1	-	-	19.6	2014
	G13	21.5	23.5	22.2	-	22.4	2286
	G19	23.7	24.1	23.8	23.1	23.7	2330
	G25	22.2	20.1	18.5	19.7	20.1	2304
D75×L150	M	23.6	21.1	21.2	-	22.0	2014
	G13	24.4	25.5	26.9	-	25.6	2286
	G19	28.2	27.3	28.7	30.7	28.7	2330
	G25	27.8	23.4	23.4	26.9	25.4	2304

3.1.3. Test procedure

The SHPB tests were performed in Extreme Performance Testing Center at Seoul National University. Figure 3.4 shows the SHPB system and the characteristics of the SHPB system are listed in Table 3.4.

Figure 3.4 The SHPB system in Extreme Performance Testing Center

Table 3.4 Characteristics of the SHPB system

	Properties	Value
Geometrical properties	Diameter, mm	76.2
	Length of incident bar, mm	5500
	Length of transmitted bar, mm	5500
Material properties	Density, kg/m^3	7800
	Elastic modulus, GPa	210
	Poisson's ratio	0.29

As mentioned in Section 3.1.1, two different pulse shapers were used for the SHPB test as shown in Table 3.1. The pulse shaper was attached to the impact end of the incident bar as presented in Figure 3.5. To prevent the frictional effect on the pulse shaper and bar interfaces, the pulse shaper was lubricated with petroleum jelly. The striker length was 600 mm for V10 and 300 mm for V13, V15, and V18. The air pressure for each impact velocity was determined through preliminary tests.

Figure 3.5 Pulse shaper attachment

The specimen was also lubricated with petroleum jelly for both ends. The lubricated specimen was sandwiched between the incident and transmitted bars. Figure 3.6 presents test specimens for each dimension before and after the test.

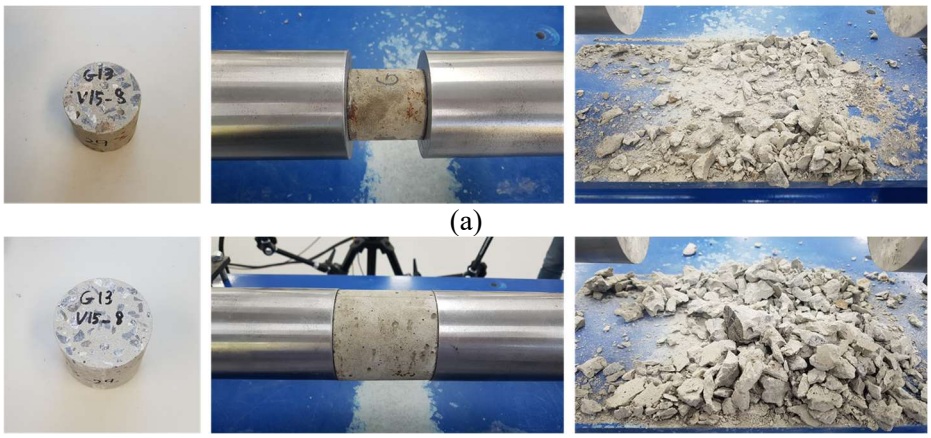

Figure 3.6 Test specimens for each dimension; (a) D50×L50; (b) D75×L75

3.1.4. Data acquisition and processing

In order to obtain the axial stress and strain relationship of the specimen, strain gauges were attached to the incident and transmitted bars. Time histories of the incident, reflected, and transmitted strain waves were measured from gauges with a 2 MHz sampling rate. The waves were filtered with a low-pass filter and the cut-off frequency was 20 kHz referring to Lee et al. (2018) and Kim et al. (2019). Then the stress waves were calculated through Hook's law as described in Equations (3.1)–(3.3). Figure 3.7 shows one of the time histories of each wave after the filtering.

$$\sigma_{incident} = E_b \varepsilon_{incident} \tag{3.1}$$

$$\sigma_{reflected} = E_b \varepsilon_{reflected} \tag{3.2}$$

$$\sigma_{transmitted} = E_b \varepsilon_{transmitted} \tag{3.3}$$

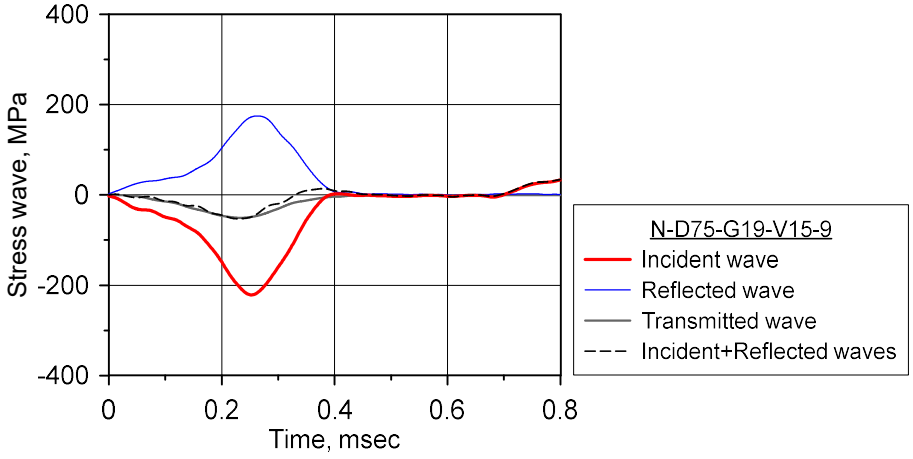

Figure 3.7 Stress waves measured in SHPB test (N-D75-G19-V15-9)

The dynamic engineering axial stress and strain relationship can be obtained through one-dimensional stress wave theory as explained in Section 2.1. Figure 3.8 shows the dynamic engineering axial stress–strain and engineering axial strain rate–strain relationships. The dynamic compressive strength (f_d) of the specimen was obtained as the maximum average stress and the corresponding engineering axial strain rate ($\dot{\varepsilon}_x^{eng}$) was determined at the same strain as the maximum average stress as marked in Figure 3.8.

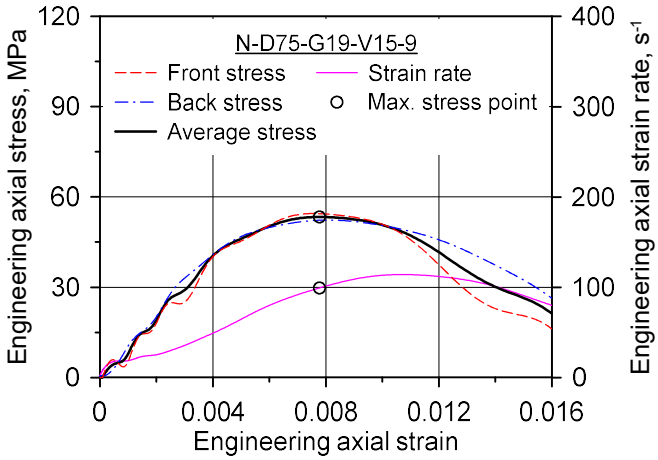

Figure 3.8 Dynamic engineering axial stress–strain and engineering axial strain rate–strain relationships (N-D75-G19-V15-9)

In addition, a high-speed camera was used to check the test normality. Figure 3.9 presents the still shots of the video of two representative cases (N-D50-M-V10-5 and N-D75-G19-V15-9).

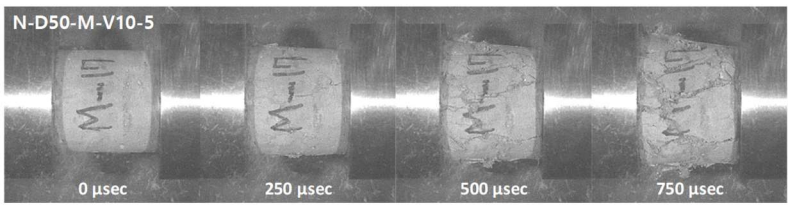

(a)

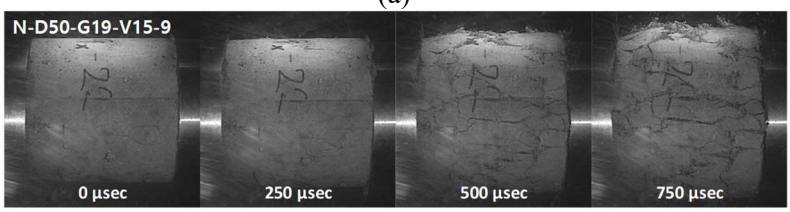

(b)

Figure 3.9 Still shots of high-speed camera video; (a) N-D50-M-V10-5; (b) N-D75-G19-V15-9

3.1.5. Test results

3.1.5.1. Dynamic stress equilibrium

In the SHPB test, the results are valid when the dynamic stress equilibrium of the specimen is satisfied. Therefore, this study evaluated the dynamic stress equilibrium of each specimen with an R-value (Flores-Johnson and Li, 2017; Kim et al., 2019, Kim et al., 2022) at the maximum average stress as shown in Equation (3.4). Figure 3.10 shows R-value for all test cases and Figure 3.11 presents dynamic engineering axial stress–strain and engineering axial strain rate–strain relationships with different R-values (4, 9, and 15%) in the same test group. As shown in Figure 3.11, the dynamic compressive strengths and the corresponding engineering axial strain rates were similar to each other when the R-value was not greater than 15%. Therefore, the test cases which have R-value under 15% were considered as in the dynamic stress equilibrium state in this test, and others were excluded from the test results. During the test, it was difficult to satisfy the dynamic stress equilibrium for most of the V18 cases (N-D75-G13-V18, N-D75-G19-V18, N-D75-G25-V18) because the high impact velocity imposed steeply rising incident waves which have insufficient time to evenly distribute the stress waves in the specimen. Therefore, a total of 148 out of 240 results were included. Table 3.5 lists the number of used test results for each specimen group. Here, the test groups having few results (one or two results) were excluded for the evaluation of the data dispersion, but those were included for the calculation of pure rate DIF.

$$R = \left| \frac{\sigma_{x,front} - \sigma_{x,back}}{\sigma_x} \right|_{\text{at maximum average stress}} \quad (3.4)$$

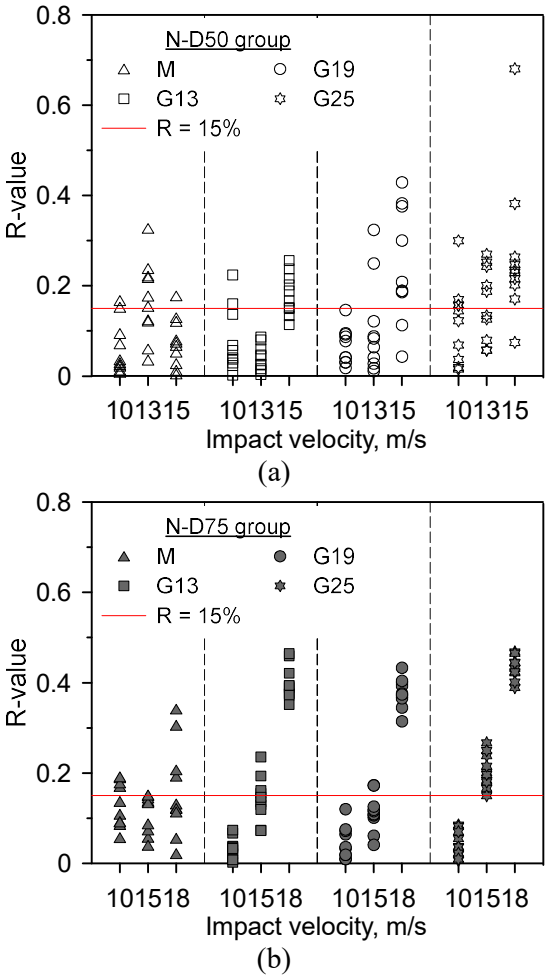

Figure 3.10 R-values of all test results; (a) N-D50 group; (b) N- D75 group

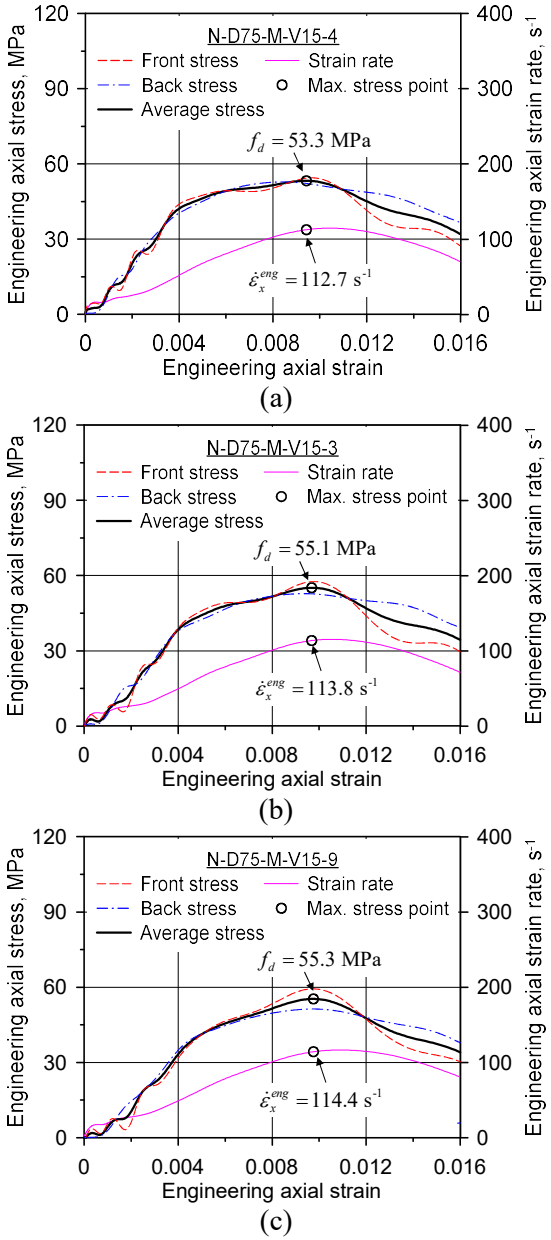

Figure 3.11 Dynamic engineering axial stress–strain and engineering axial strain rate strain relationships with different R-values; (a) N-D75-M-V15-4 (R = 4%); (b) N-D75-M-V15-3 (R = 9%); (c) N-D75-M-V15-9 (R = 15%)

Table 3.5 The number of valid test results

D50					D75				
	M	G13	G19	G25		M	G13	G19	G25
V10	9	9	10	6	V10	6	10	10	10
V13	6	10	8	5	V15	10	7	8	1
V15	10	4	2	1	V18	6	-	-	-

3.1.5.2. Reproducibility of test

As mentioned in Section 3.1.1, the SHPB tests were repeated ten times for each test group to figure out the dispersion of test results caused by the heterogeneity of the specimen. Therefore, it is important to achieve reproducibility without other influences on data dispersion except for the effect of G_{max}. The reproducibility of tests was evaluated in terms of two factors: specimen length and incident stress wave. As presented in Equation (2.3), the specimen length is dominant in the engineering axial strain rate. Therefore, the difference in lengths among the specimens in the same test group may result in dispersive test data. In addition, the difference in incident stress wave also affects the test results because the incident stress wave is the most influencing factor in the SHPB test.

In order to evaluate the effect of the difference in specimen length, the coefficient of variation (COV) was calculated for each specimen group. Figure 3.12 illustrates the COV of specimen length. As shown in Figure 3.12, all of the COVs of specimen length was very low and similar to each other. Therefore, the effect of the difference in specimen length was negligible in the repeated test. The difference in the incident stress wave was evaluated as the difference in the maximum value of the incident stress wave in the same test

group. Figure 3.13 shows the COV of maximum incident stress waves for each group. Although the difference in the incident stress wave was relatively higher than the difference in the specimen length as presented in Figure 3.13, the COVs were similar in concrete specimens so the difference in the incident stress wave was also negligible for the concrete specimens. As a result, those two influencing factors didn't affect the dispersion of test results and the reproducibility of the test was satisfied. Therefore, the dispersion of the test results can be discussed in terms of the effect of G_{max}.

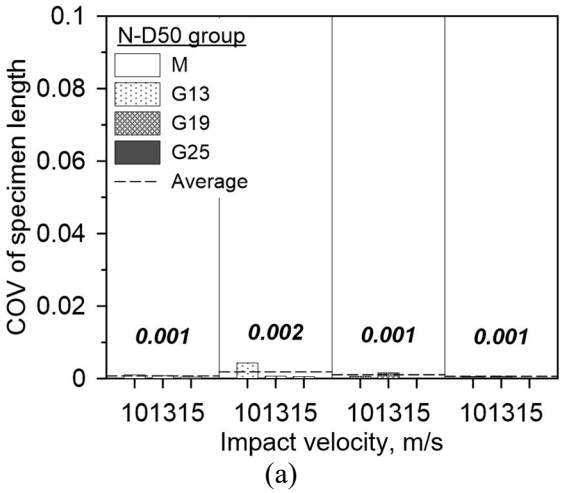

(a)

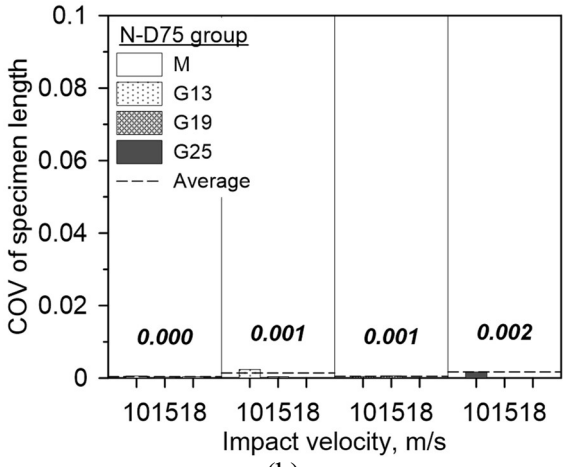

(b)

Figure 3.12 COV of specimen length; (a) N-D50 group; (b) N-D75 group

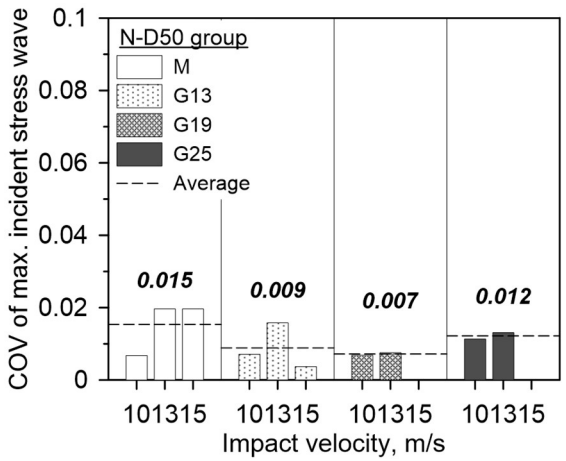

(a)

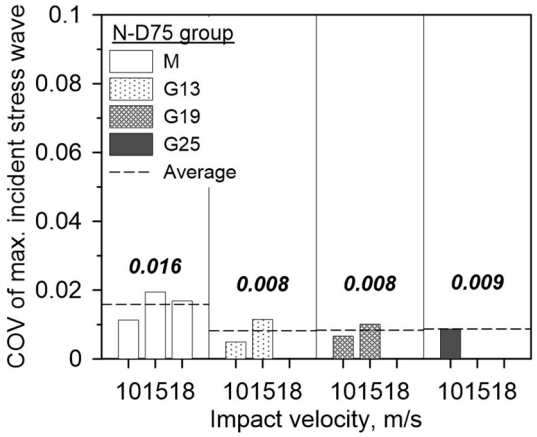

(b)

Figure 3.13 COV of maximum incident stress wave; (a) N-D50 group; (b) N-D75 group

3.1.5.3. Apparent DIF

The apparent DIF (γ_{app}) can be calculated as a ratio of the dynamic compressive strength obtained from the SHPB test to the static compressive strength acquired from the static compressive strength test as shown in Equation (3.5), where f_c denotes the average static compressive strength of the specimen. In this test, the static compressive strength of the cylindrical specimen with the same diameter and G_{max} of the SHPB test specimen was used for the apparent DIF. For example, the apparent DIF of N-D75-M-V15-4 presented in Figure 3.11 (a) was calculated by dividing the dynamic compressive strength, 53.1 MPa, by the average static compressive strength of the D75×L150 mm mortar specimen (22.0 MPa). Figure 3.14 presents the apparent DIF along with the corresponding engineering axial strain rate for

the test cases satisfying the dynamic stress equilibrium as explained in Section 3.1.4.1.

$$\gamma_{app}\left(\dot{\varepsilon}_x^{eng}\right)=\frac{f_d\left(\dot{\varepsilon}_x^{eng}\right)}{f_c} \tag{3.5}$$

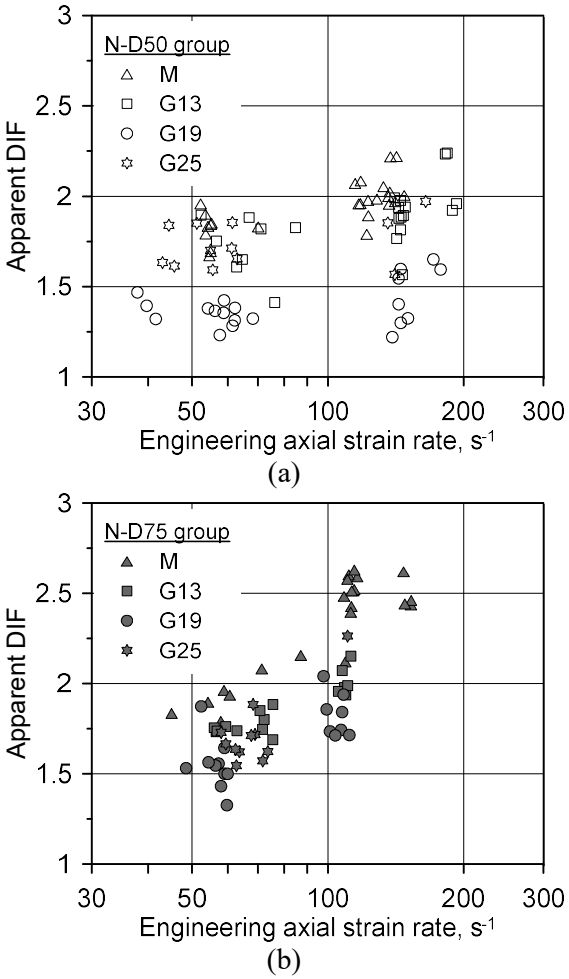

Figure 3.14 Apparent DIF–engineering axial strain rate relationship;

(a) N-D50 group; (b) N-D75 group

3.2. Effect of maximum coarse aggregate size

3.2.1. Dispersion of test results

Concrete is non-homogeneous material because it contains coarse aggregate which has relatively large particle sizes. The heterogeneity of the specimen is intensified as the particle size increases in the same dimension as shown in Figure 3.15 (Kim et al., 2019). In other words, the heterogeneity of the concrete specimen is more severe when the G_{max} is relatively larger than the other specimen. In a concrete SHPB test, the heterogeneity of the specimen may result in dispersive test results. Therefore, the dispersion of the test results should be compared to figure out the effect of G_{max} in the concrete SHPB test. To evaluate the dispersion of the test results, multivariate COV (Albert and Zhang, 2010) between the apparent DIF and the corresponding engineering axial strain rate as described in Equation (3.6) was used in this study, where $\boldsymbol{\mu}$ and $\boldsymbol{\Sigma}$ are the mean vector and covariance matrix of the apparent DIF and corresponding engineering axial strain rate, respectively. Figure 3.16 presents the multivariate COV for each test group. In Figure 3.16, the label values are the average multivariate COV for the same G_{max}.

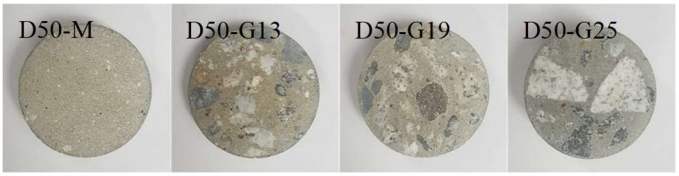

Figure 3.15 Heterogeneity of mortar and concrete specimen along with the G_{max} (Kim et al., 2019)

$$\text{Multivariate COV} = \sqrt{\frac{\boldsymbol{\mu}^T \boldsymbol{\Sigma} \boldsymbol{\mu}}{\left(\boldsymbol{\mu}^T \boldsymbol{\mu}\right)^2}} \tag{3.5}$$

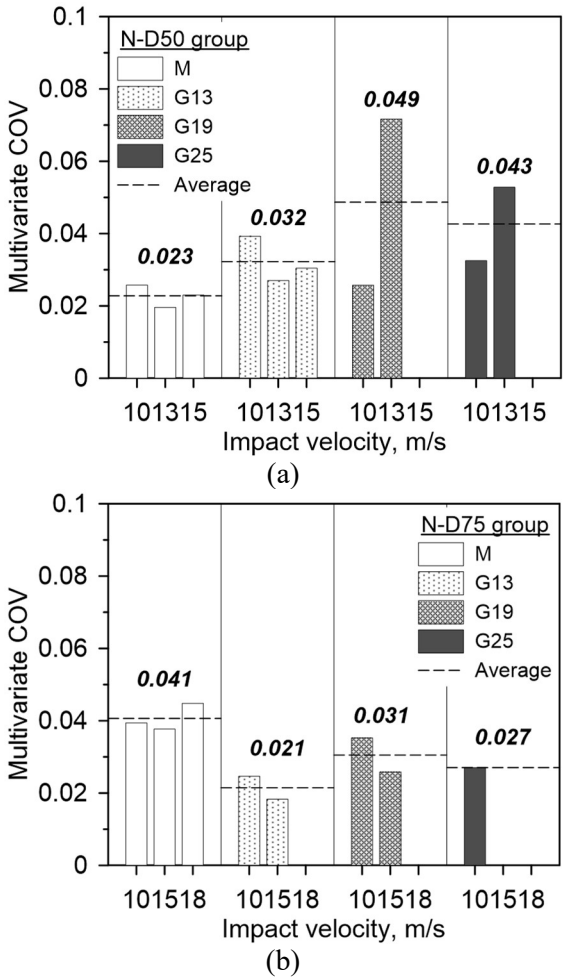

Figure 3.16 Multivariate COV of the SHPB test results; (a) N-D50 group; (b) N-D75 group

Here, the average multivariate COV of the mortar specimens for both specimen dimensions (N-D50-M and N-D75-M) can be used as a reference

value to evaluate the dispersion induced by the coarse aggregate in concrete specimens because the mortar specimen didn't contain coarse aggregate. In other words, the average multivariate COV of mortar was induced by the effect of two factors described in the previous section: the difference in the specimen length and that in the incident stress wave. Therefore, the dispersions of the concrete test results due to the coarse aggregate were quantitatively obtained by subtracting the average multivariate COV of mortar (0.032) from each multivariate COVs as listed in Table 3.6.

Table 3.6 Dispersion of concrete test results due to coarse aggregate

	Average multivariate COV due to coarse aggregate	
	N-D50 group	N-D75 group
G13	0	*(-0.011)*
G19	0.017	*(-0.001)*
G25	0.011	*(-0.005)*

As shown in Figure 3.16 and Table 3.6, the dispersion of the test results of concrete in the N-D50 group is relatively more severe than in the N-D75 group. This may be caused by the relatively small dimension (D50) than D75 for the same G_{max}. In particular, the specimens which didn't satisfy the condition described in ASTM C192 that the specimen diameter should be at least three times G_{max} (N-D50-G19 and N-D50-G25) presented excessive multivariate COVs. Therefore, it can be concluded that the specimen dimension must be at least three times G_{max} to neglect the effect of heterogeneity on the dispersion of the test results for the normal-strength concrete.

3.2.2. Pure rate DIF

In order to investigate the effect of G_{max} on the strain-rate effect of the concrete specimens, a comparison of each DIF is necessary. However, the apparent DIF obtained through the SHPB test includes an inertial effect (Lee et al., 2018). The inertial effect overestimates the strength enhancement by the strain-rate effect. In general, the inertial effect is already considered in the constitutive equation of the material. Therefore, it is necessary to obtain pure rate DIF excluding the inertial effect from the apparent DIF to consider the pure strain-rate effect in FEA. For this reason, the pure rate DIF (Lee et al., 2018) was adopted in this study for each G_{max}. Since it was revealed that the specimen dimension has to satisfy at least three times G_{max} as explained in Section 3.2.1, the test results satisfying the criterion were used in this section: N-D50-M, N-D50-G13, N-D75-M, N-D75-G13, N-D75-G19, and N-D75-G25.

The apparent DIF including the inertial effects can be presented as Equation (3.6) (Lee et al., 2018), where k_2 and k_3 denote the lateral and axial inertial effect parameters, respectively; ρ_s, d_s, and l_s are the density, initial diameter, and initial length of the specimen, respectively; $\ddot{\varepsilon}_x^{eng}$ and f_c mean the engineering axial strain acceleration and static compressive strength of the specimen, respectively. And the pure rate DIF (γ_{rate}) can be calculated by regression analysis as presented in Equations (3.7) (Lee et al., 2018), where $\dot{\varepsilon}_x^{eng}$, $\dot{\varepsilon}_0$, and k_1 denote the engineering axial strain rate of the specimen, reference strain rate, and rate effect parameter, respectively. In

this test, the reference strain rate $\dot{\varepsilon}_0$ was 10^{-5} s^{-1} to ensure DIF equal to 1 at static state. Figure 3.17 shows the pure rate DIF for each G_{max} and corresponding k_1. In Figure 3.17, ALL-M denotes the pure rate DIF obtained from the test results of N-D50-M and N-D75-M; ALL-G13 denotes the pure rate DIF obtained from the test results of N-D50-G13 and N-D75-G13; and D75-G19 and D75-G25 represent the pure rate DIFs calculated from N-D75-G19 and N-D75-G25, respectively.

$$\gamma_{app} = \gamma_{rate} + k_2 \frac{\rho_s d_s^2 \ddot{\varepsilon}_x^{eng}}{f_c} + k_3 \frac{\rho_s l_s^2 \ddot{\varepsilon}_x^{eng}}{f_c} \tag{3.6}$$

$$\gamma_{rate} = \left(\frac{\dot{\varepsilon}_x^{eng}}{\dot{\varepsilon}_0} \right)^{k_1} \tag{3.7}$$

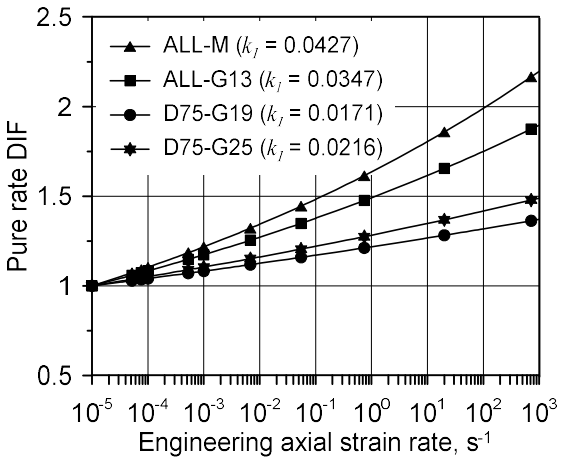

Figure 3.17 Pure rate DIF for each G_{max}

As presented in Figure 3.17, the pure rate DIF varies with the G_{max} and the specific tendency was not observed according to the G_{max}. In particular,

the DIF of mortar shows the highest increment of the dynamic compressive strength. Therefore, it is dangerous to apply the DIF of mortar specimens to the concrete since it leads to an overestimation of the dynamic compressive strength of concrete. In other words, the previous test results acquired from the SHPB test for the mortar specimen or the concrete specimen with small size coarse aggregate listed in Table 2.1 are difficult to use for the actual concrete with G_{max} larger than 19 mm. As a result, the coarse aggregate used on a real construction site should be applied to the concrete SHPB test to accurately investigate the strain-rate effect of the concrete. In addition, the specimen dimension for the concrete SHPB test should consider the G_{max} as mentioned in Section 3.2.1. The identical findings were drawn in the previous study on high-strength concrete of 53.2 and 66.4 MPa (Kim et al., 2019). In conclusion, these criteria were thoroughly verified for concrete specimens in the range of static compressive strength from 20 to 70 MPa.

3.3. Concluding remarks

In this chapter, a series of SHPB tests were described for mortar and concrete with various sizes of coarse aggregate to identify the effect of the G_{max} in the concrete SHPB test. The effect of G_{max} was investigated in two main aspects: dispersion of test results and pure rate DIF. To this end, the main variables of the SHPB test were determined as the G_{max} (mortar, 13, 19, and 25 mm) and the specimen dimension (D50×L50 and D75×L75 mm). The SHPB tests were conducted in a wide range of strain rates (30–200 s^{-1}) and the tests were repeated ten times for each specimen group.

Before analyzing the results about the effect of G_{max}, the dynamic stress equilibrium state of the test results was evaluated for validity. In addition, the reproducibility of the test was checked on two influencing factors: the difference in specimen length and that of the incident stress wave. It was confirmed that the test was well-repeated and the influences of the two factors were similar in concrete specimen groups which indicates that those factors were negligible. Therefore, it was possible to compare the effect of G_{max} through the test results.

The test results were described as a relationship between the apparent DIF and the engineering axial strain rate. In order to figure out the effect of G_{max} in terms of the dispersion of test results, multivariate COV was calculated and compared. It was observed that the dispersion of the test results is negligible when the specimen dimension satisfies at least three times the G_{max} as presented in ASTM C192. In addition, the pure rate DIF was obtained

and compared for each G_{max} to identify the effect of G_{max} on the pure strain-rate effect excluding the inertial effect. From the comparison of the pure rate DIF, it was revealed that the DIF varies with the G_{max} without a certain tendency. Therefore, the real G_{max} used in practice should be considered in concrete SHPB to ensure the accurate and safe evaluation of the dynamic compressive strength of the concrete. In conclusion, two important guidelines are drawn: (1) specimen dimension should be at least three times G_{max}, and (2) actual G_{max} should be used in the concrete SHPB test. These guidelines have been verified in normal and high-strength concrete (20–70 MPa). The suggested guidelines can be adopted as a standard method to determine the specimen dimension for the concrete SHPB test. Moreover, it is expected to improve the consistency and accuracy of the test results by applying the suggested guidelines.

In the following chapter, the experimental work on the frictional effect in the concrete SHPB test is described to suggest a proper lubrication method.

4. Effect of Friction in Concrete SHPB Test

In Chapter 4, details of the concrete SHPB test to investigate the effect of friction are described (Kim et al., 2022). The final objective of Chapter 4 is to suggest a proper lubrication method for the concrete SHPB test. To this end, two series of concrete SHPB test was conducted. Firstly, the lubrication method was suggested through the SHPB test with various lubricants and various amounts of lubricant. Secondly, the suggested lubrication method was verified for concrete specimens with various dimensions. Based on these experimental works, the proper lubrication method for the concrete SHPB test was established.

4.1. SHPB test program for suggestion of lubrication method

4.1.1. Test variables

In order to investigate the frictional effect and suggest a lubrication method, three lubricants widely used for the SHPB test were considered: high vacuum grease, petroleum jelly, and Teflon (polytetrafluoroethylene, PTFE). The amounts of lubricant for the test were also set as variables to compare the lubrication effect. The SHPB test was performed for D75×L75 mm specimens with a G_{max} of 25 mm. The amount of lubricant was considered for the D75×L75 mm specimens as 0.0, 0.1, 0.5, 1.0, 1.5 g (none, 2.3, 11.3, 22.6, and 34.0 mg/cm^2). The impact velocities were 10, 13, 16, and 18 m/s, and the target strain rate range was 30–120 s^{-1} which covers the impact and blast

loadings (Daudeville and Malécot, 2011). The annular pulse shaper made of C1020 copper was applied and the dimension of the pulse shaper was 52×48×4 mm. The target static compressive strength of the concrete was 30 MPa. Table 4.1 lists the details of the test condition and Figure 4.1 shows the designation of test specimens. A total of 52 tests were conducted.

Table 4.1 Details of SHPB test to investigate the frictional effect

Parameter	Value
G_{max}, mm	25
Specimen dimension, mm	D75×L75
Lubricant	High vacuum grease Petroleum jelly Teflon (Polytetrafluoroethylene, PTFE)
Amount of lubricant, mg/cm^2	None, 2.3, 11.3, 22.6, 34.0
Static compressive strength, MPa	30
Impact velocity, m/s	10, 13, 16, 18
Pulse shaper material	C1020 copper
Pulse shaper dimension, mm	52×48×4

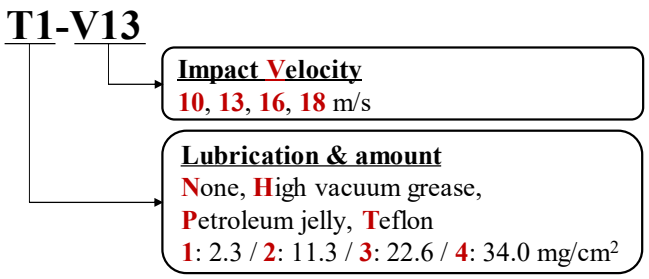

Figure 4.1 Designation of test specimen

4.1.2. Specimen preparation

A cylindrical mold of D75×L150 mm was used for specimen fabrication. Table 4.2 presents the mix proportion. Specimens were prepared in a similar procedure explained in Chapter 3.1.2. The maximum error of perpendicularity to the axis was 0.38º. Figure 4.2 shows a part of the SHPB test specimens. The static compressive strength test was conducted for four D75×L150 mm cylindrical specimens and the average compressive strength was 28.1 MPa. Table 4.3 lists the static compressive strength test results.

Table 4.2 Mix proportion

Target strength, MPa	G_{max}, mm	Unit weight, kg/m^3			
		Cement	Water	Fine aggregate	Coarse aggregate
30	25	459	170	661	1037

(a)

(b)

Figure 4.2 Prepared SHPB specimens; (a) V10; (b) V20

Table 4.3 Static compressive strength test results

Static compressive strength, MPa				Average strength, MPa	Average density, kg/m^3
#1	#2	#3	#4		
26.7	31.5	26.7	27.6	28.1	2365

4.1.3. Test procedure

The SHPB test system described in Section 3.1.3 was used for the test and the overall test procedure was similar to Section 3.1.3 except for the striker length and the lubrication method. The striker lengths were 600 mm for V10 and V13 cases, and 300 mm for V16 and V18 cases. The lubricants were carefully applied to both ends of the specimen using wood sticks to evenly spread the lubricant with the lubrication condition prescribed in Table 4.1. The wood sticks with the same dimension were used for all specimens and the applicable area of the wood sticks was carefully controlled to minimize the difference in the lubrication with different conditions. Figure 4.3

shows the lubricating process with a wood stick and Figure 4.4 presents the lubricated specimens with Teflon for each amount of the lubricant. Figure 4.5 shows some of the test specimens before and after the test.

Figure 4.3 Lubricating process with wood stick

Figure 4.4 Lubricated specimens with Teflon for each amount of the lubricant

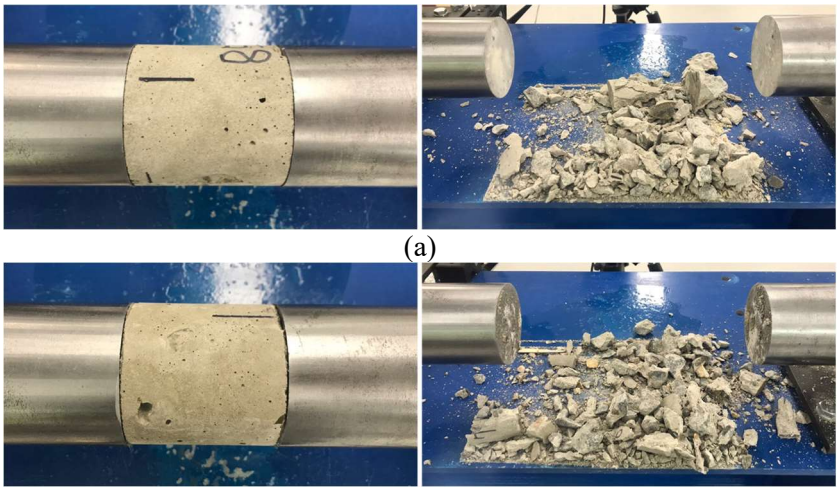

(a)

(b)

Figure 4.5 Test specimens before and after the test; (a) T1-V10; (b) T4-V10

4.1.4. Data acquisition and processing

The stress waves of the tests were measured through the strain gauges as described in Section 3.1.4. The sampling rate of the waves was 2 MHz and the cut-off frequency for the filtering was 20 kHz. Then, the dynamic engineering axial stress–strain and engineering axial strain rate–strain relationships were obtained through one-dimensional stress wave theory. The dynamic compressive strength (f_d) and the corresponding engineering axial strain rate ($\dot{\varepsilon}_x^{eng}$) were determined at the same axial strain for the maximum average stress. Figure 4.6 and Figure 4.7 show one of the stress waves and the dynamic engineering axial stress–strain and engineering axial strain rate–strain relationships, respectively.

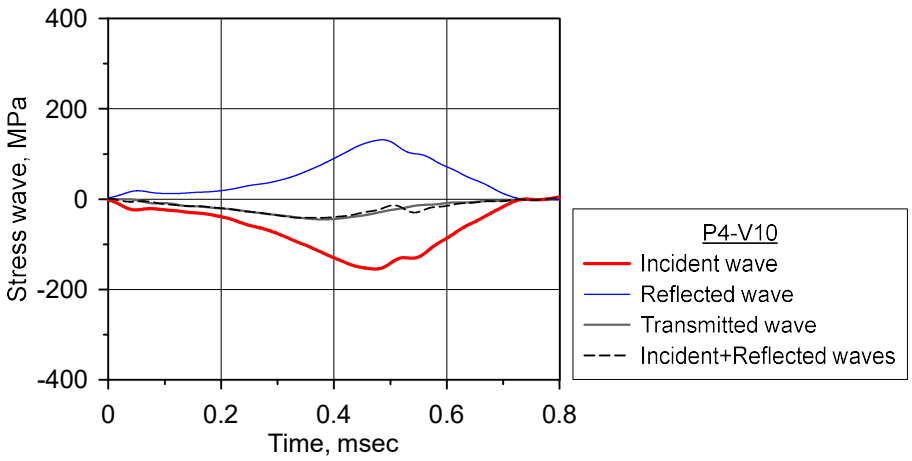

Figure 4.6 Stress waves of the SHPB test (P4-V10)

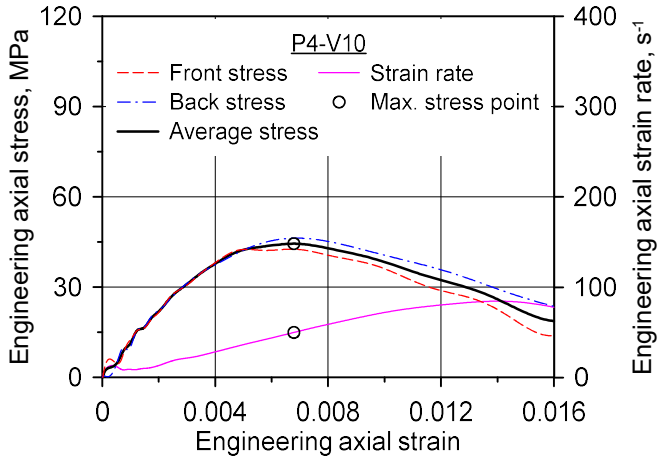

Figure 4.7 Dynamic engineering axial stress–strain and engineering axial strain rate–strain relationships (P4-V10)

A high-speed camera was used in the SHPB test and the crack patterns of the specimens were compared for each lubrication condition. The details of the crack patterns are described in the next section.

4.1.5. Test results

4.1.5.1. Dynamic stress equilibrium

The dynamic stress equilibrium of the specimens was evaluated in the same method explained in Section 3.1.5.1. Figure 4.8 illustrates the R-value for all of the specimens. In this test, 10% was used as a threshold value for the dynamic stress equilibrium state of the specimen. Figure 4.9 shows the representative cases with different R-values (5% and 10%) for the same lubrication condition (T1-V10 and T1-V16). In accordance, whole test cases of V18 and several cases of V13 and V16 were excluded for the reliability of the test results. A total of 31 results were included.

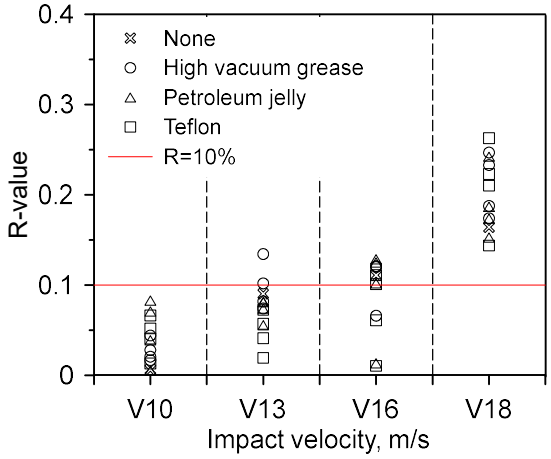

Figure 4.8 R-value of test specimens

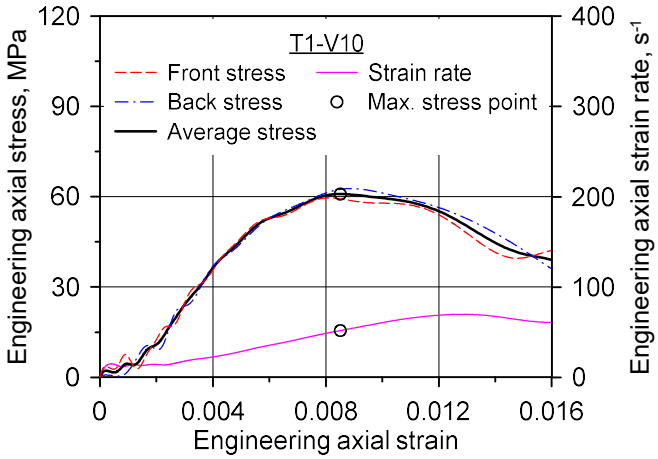

(a)

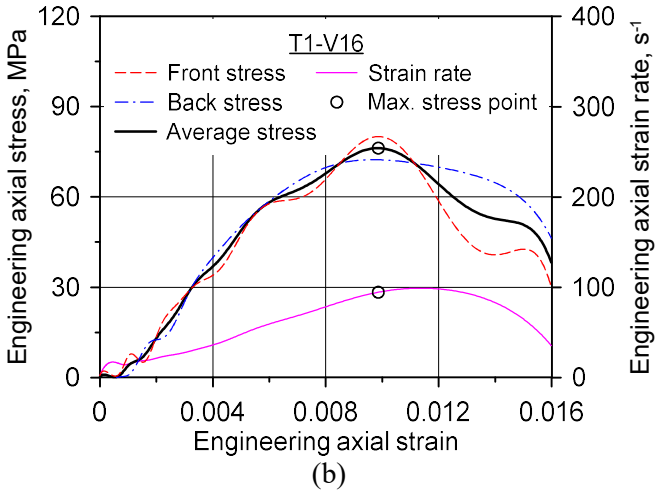

(b)

Figure 4.9 Dynamic engineering axial stress–strain and engineering axial strain rate–strain relationships with different R-values; (a) T1-V10; (b) T1-V16

4.1.5.2. Apparent DIF

The relationship between the apparent DIF and the corresponding engineering axial strain rate was obtained following the same procedure described in Section 3.1.5.3. Figure 4.10 presents the apparent DIF–engineering axial strain rate relationship of the test cases satisfying the dynamic stress equilibrium.

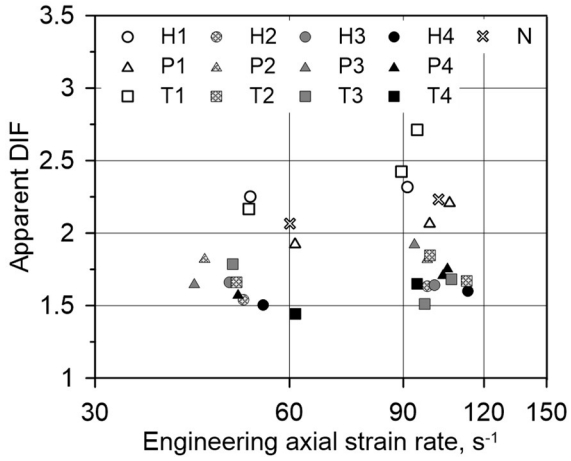

Figure 4.10 Apparent DIF–engineering axial strain rate relationship

4.1.6. Effect of friction along lubrication condition

4.1.6.1. Apparent DIF according to the amount of lubricant

Figure 4.11 illustrates the apparent DIF according to the lubrication condition. Since the apparent DIF did not shows a significant difference according to the impact velocities, the apparent DIFs were averaged for the same lubricant amount. Accordingly, the average apparent DIFs are depicted in each plot (see Figure 4.11). Also, the label values in Figure 4.11 indicate the ratio of the average apparent DIF to that of non-lubricated cases (0.0 mg/cm^2), and the COV of the apparent DIFs with the same lubricant amount is described in brackets. As mentioned previously, the impact velocity didn't show a noticeable effect on the apparent DIF so the COV was low. Moreover, as clearly seen in Figure 4.11, the apparent DIFs are significantly reduced when the lubricants were applied with an amount of over 11.3 mg/cm^2 for all

lubricants. In addition, the apparent DIFs lubricated over the lubricant amount of 11.3 mg/cm^2 were similar regardless of the lubricant amount.

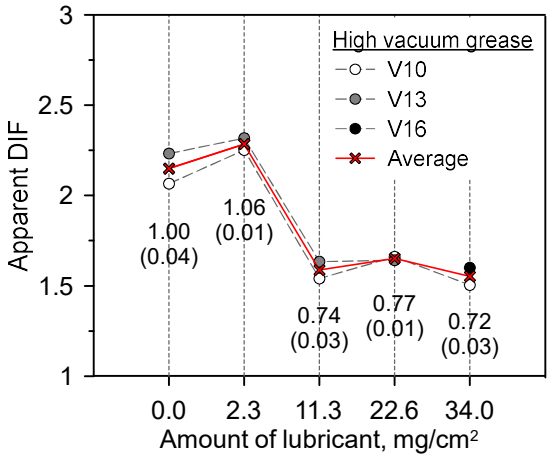

(a)

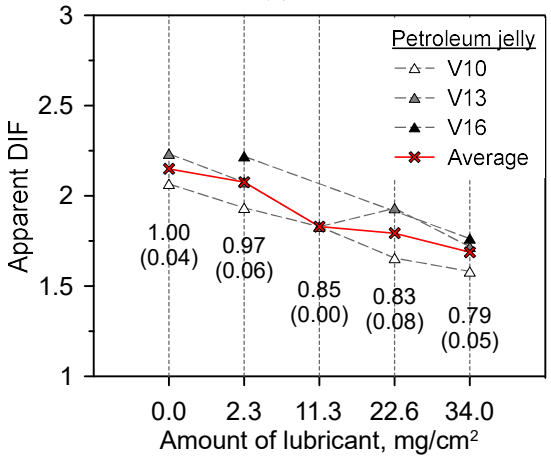

(b)

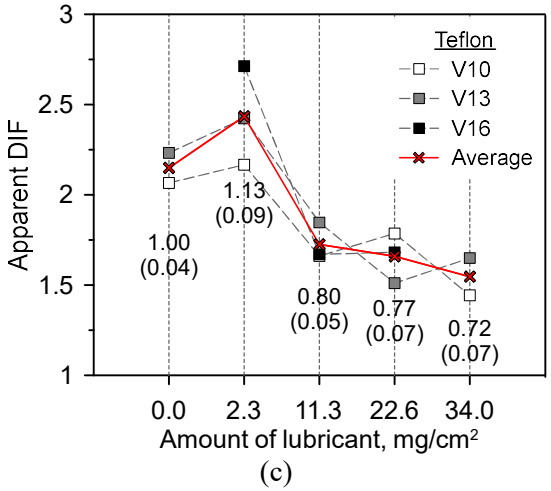

(c)

Figure 4.11 Apparent DIFs according to the amount of lubricant for each lubricant; (a) High vacuum grease; (b) Petroleum jelly; (c) Teflon

In order to compare the apparent DIF for lubricant type, all results were plotted at once as presented in Figure 4.12. In Figure 4.12, the label values are the average apparent DIF and the values in the bracket indicate the COV of the apparent DIFs. The low COVs for the lubricated cases over the lubricant amount of 11.3 mg/cm^2 (under 7%) indicate that the lubrication effect was similar regardless of the lubricant type. In addition, the apparent DIFs were similar to each other as 78% of the apparent DIF of non-lubricated cases. This indicates that the frictional effect in the concrete SHPB test can additionally increase the dynamic compressive strength by about 22% when the specimen is not lubricated. In other words, the frictional effect significantly overestimates the dynamic compressive strength of concrete specimens in the concrete SHPB test. Therefore, it is important to remove the frictional effect through proper lubrication for the accurate evaluation of the strain-rate effect.

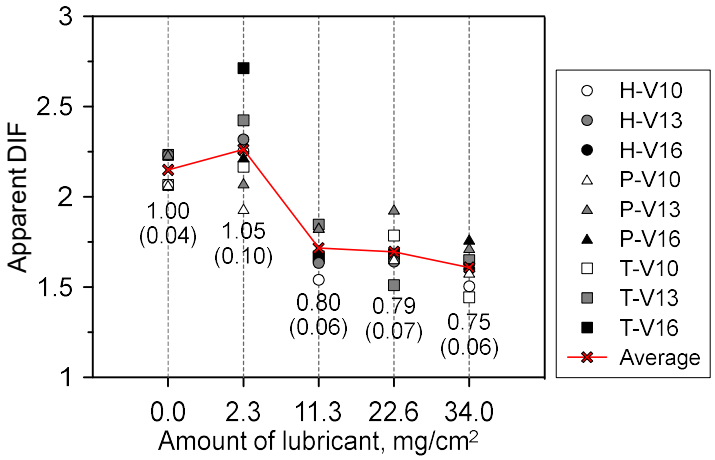

Figure 4.12 All apparent DIFs along with lubricant amount

Based on the comparison of the apparent DIF according to the lubrication condition, a proper lubrication method can be proposed: over the amount of 11.3 mg/cm^2 should be applied to both ends of the specimen using one of the lubricants among high vacuum grease, petroleum jelly, and Teflon. However, this lubrication method was suggested by the sole specimen dimension, D75×L75, in spite that the specimen dimension influences the frictional effect. Therefore, additional verification is necessary for various specimen dimensions to adopt the suggested lubrication technique as a standard method.

4.1.6.2. Crack patterns according to lubrication

The effect of lubrication also can be investigated by comparing the crack patterns between non-lubricated cases and sufficiently-lubricated cases. Figure 4.13 shows the crack patterns of non-lubricated cases (N) and sufficiently-lubricated cases (T2 and T3) at different impact velocities. The major cracks were illustrated with white dashed lines. In Figure 4.13, the

similar crack patterns at different impact velocities in the same lubrication condition supported that the effect of the impact velocity was insignificant. However, the difference in the crack patterns was observed following the amount of lubricant. As shown in Figure 4.13 (a), the crack patterns of non-lubricated cases were intertwined. On the other hand, the crack patterns of sufficiently-lubricated cases (T2 and T3) were relatively straight. This implies that the frictional effect of T2 and T3 cases was minimized. Therefore, the suggested lubricated method was validated through the comparison of the crack patterns.

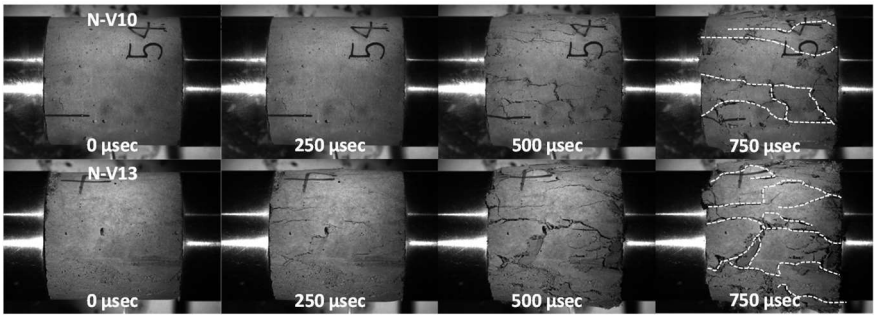

(a)

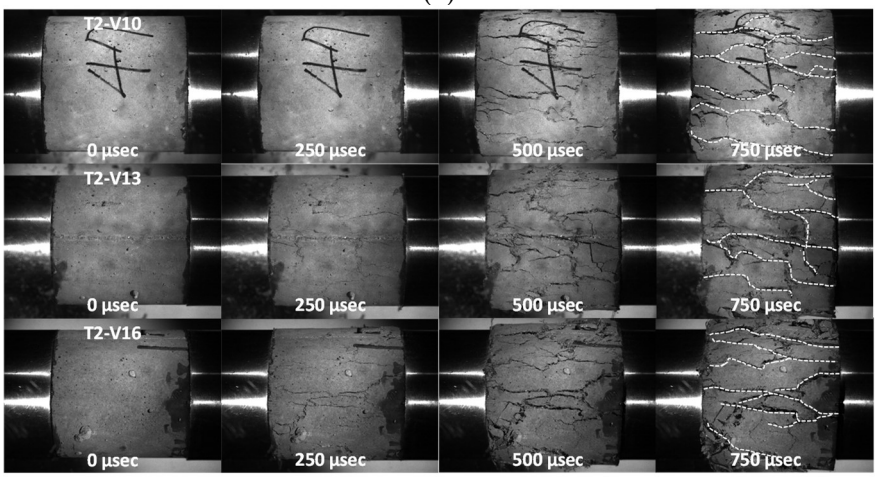

(b)

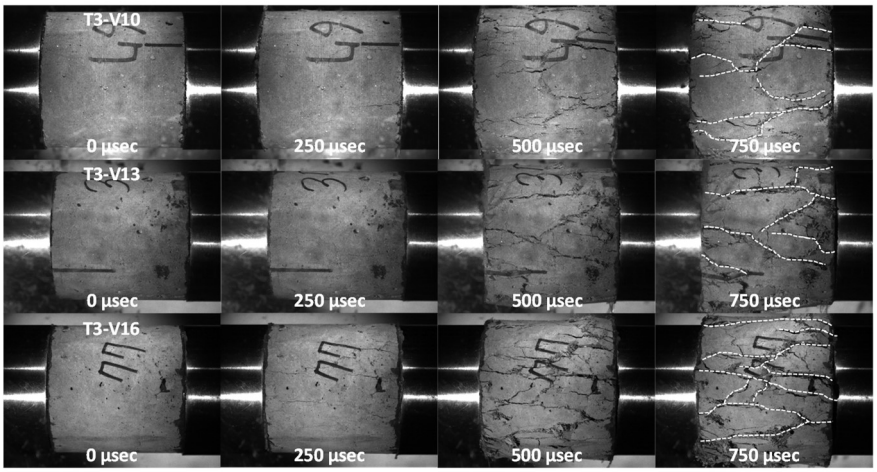

(c)

Figure 4.13 Crack patterns at different impact velocities; (a) N; (b) T2; (c) T3

4.2. SHPB test program for verification of lubrication method

In this section, the concrete SHPB test for various specimen dimensions is described. The main purpose of this test was to verify the lubrication method suggested in the previous section.

4.2.1. Test variables

Before the determination of the test variables, a numerical analysis was conducted to investigate the influence of specimen dimensions on the frictional effect in the concrete SHPB test. The numerical analysis conditions are listed in Table 4.4 and the results are shown in Figure 4.14, where μ denotes the frictional coefficient. As presented in Figure 4.14, the frictional effect definitely increases the apparent DIF. In particular, the apparent DIF was increased as the L/D ratio decreased when the frictional effect existed. This is because the friction at the interfaces constrains the lateral deformation of the specimen. As the L/D ratio decreases, the influenced section by the frictional effect increases which severely enhances the dynamic compressive strength of the specimen. However, there was no effect of the L/D ratio on the apparent DIF when the frictional coefficient was zero. These findings were applied to the following test.

Table 4.4 Numerical analysis conditions

Parameter	Value
G_{max}, mm	13
Specimen dimension, mm (L/D ratio)	D75×L45 (0.6) D50×L40 (0.8) D75×L60 (0.8) D50×L50 (1.0) D75×L75 (1.0)
Frictional coefficient	0.0 0.2
Static compressive strength, MPa	40

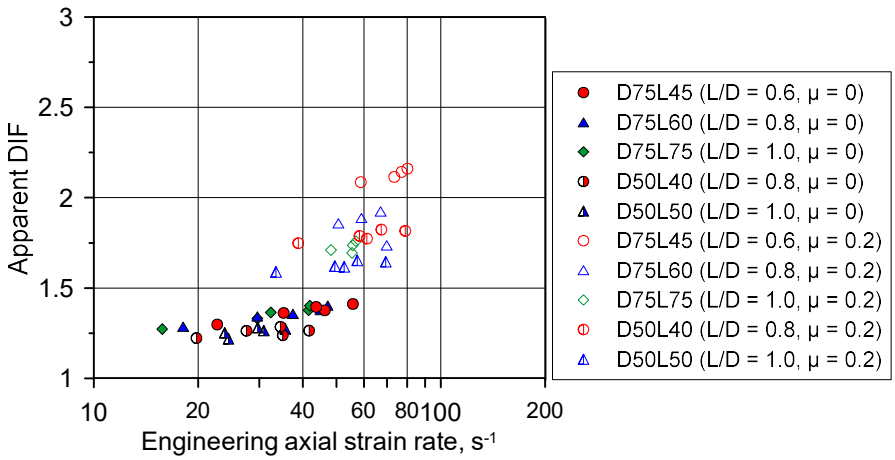

Figure 4.14 Numerical analysis result on frictional effect

The most important variable for this test was the specimen dimension. Therefore, five dimensions for the specimen were considered: D75×L45, D75×L60, D75×L75, D50×L40, and D50×L50 mm. Teflon was used for the follow-up test because the lubrication effect was similar to each other for three types of lubricants in the previous test. The amount of lubricant was determined to be 0, 12, and 35 mg/cm^2 considering the suggested lubrication method (over 11.3 mg/cm^2). The target compressive strength of the concrete specimen was 30 MPa and G_{max} was decided as 13 mm considering the

specimen dimension. Impact velocities were 10, 11, 12, 13, and 15 m/s and the C1020 copper pulse shaper dimension was 52×48×4 mm. The maximum impact velocity was decreased because it was observed that the dynamic stress equilibrium of the concrete specimen is difficult to achieve under high impact velocity. Table 4.5 lists the details of the test condition and the designation of the specimen is illustrated in Figure 4.15. A total of 75 tests were performed.

Table 4.5 Details of SHPB test to verify the suggested lubrication method

Parameter	Value
G_{max}, mm	13
Specimen dimension, mm (L/D ratio)	D75×L45 (0.6) D50×L40 (0.8) D75×L60 (0.8) D50×L50 (1.0) D75×L75 (1.0)
Lubricant	Teflon
Amount of lubricant, mg/cm^2	None, 12, 35
Static compressive strength, MPa	30
Impact velocity, m/s	10, 11, 12, 13, 15
Pulse shaper material	C1020 copper
Pulse shaper dimension, mm	52×48×4

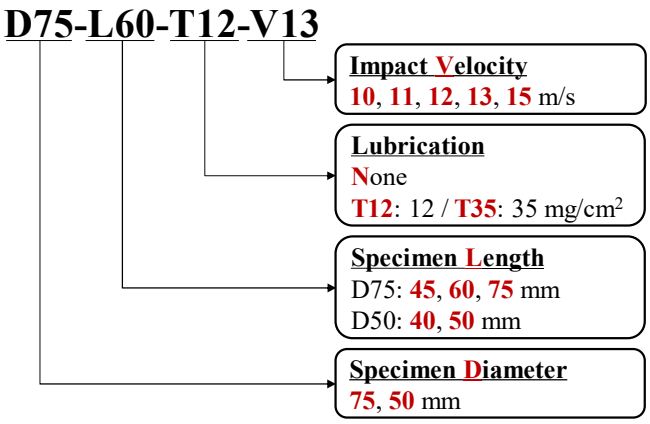

Figure 4.15 Designation of test specimen

4.2.2. Specimen preparation

As same as the previous test conducted in this study, cylindrical molds of D50×L100 and D75×L150 mm were used for the specimen fabrication. Table 4.5 shows the mix proportion. The specimens were fabricated and cured referring to ASTM 192 and cut into the desired dimensions for the SHPB test. The maximum error of perpendicularity to the axis was 0.31º. Figure 4.16 shows the prepared specimens with different dimensions. The static compressive strength tests were conducted for D50×L100 and D75×L150 mm specimens referring to ASTM C39 and the results are listed in Table 4.6.

Figure 4.16 Prepared specimens for the concrete SHPB test

Table 4.6 Static compressive strength test results

Specimen	Static compressive strength, MPa						Average strength, MPa	Average density, kg/m^3
	#1	#2	#3	#4	#5	#6		
D50×L100	28.9	24.3	27.2	26.4	35.0	-	26.7	2340
D75×L150	37.5	34.0	34.6	35.6	28.7	31.4	33.6	

4.2.3. Test procedure

In this test, three strikers were used to properly implement the target impact velocities (600 mm striker for V10, V11, and V 12 cases, 400 mm striker for V13 cases, and 300 mm striker for V15 cases). The pulse shaper was lubricated as same as the previous tests. The lubricant was applied to both ends of the specimen with wood sticks as described in Section 4.1.3. Figure 4.17 shows the D75×L45 specimens before and after the test for different lubrication conditions. In Figure 4.17 (a), the specimen was hardly fractured due to the frictional effect that increases the dynamic compressive strength.

(a) (b) (c)

Figure 4.17 Test specimens before and after the test; (a) D75-L45-N-V12; (b) D75-L45-T12-V12; (c) D75-L45-T35-V12

4.2.4. Data acquisition and processing

Most material models for the concrete consider the strain-rate effect with the relationship between DIF and effective strain rate or effective deviatoric strain rate. In the concrete SHPB test, the effective deviatoric strain rate ($\dot{e}_{eff}$) can be obtained from the radial strain of the specimen as presented in Equation (4.1) by assuming that the radial strain is identical to the circumferential strain, where $\dot{\varepsilon}_x^t$ and $\dot{\varepsilon}_r^t$ denote the true axial strain rate and true radial strain rate of the specimen, respectively (Kim et al., 2022). The true axial strain rate and true radial strain rate can be calculated from the engineering axial strain (ε_x^{eng}) and engineering radial strain (ε_r^{eng}) as shown in Equations (4.2) and (4.3), where t denotes the time. Since the radial strain was assumed to be the same as the circumferential strain of the specimen, a strain gauge was additionally attached to the concrete specimen to measure the circumferential strain of the specimen as shown in Figure 4.16.

$$\dot{e}_{eff} = \frac{2}{3}\left(\dot{\varepsilon}_x^t - \dot{\varepsilon}_r^t\right) \tag{4.1}$$

$$\dot{\varepsilon}_x^t = -\frac{d}{dt}\left\{\ln\left(1-\varepsilon_x^{eng}\right)\right\} \tag{4.2}$$

$$\dot{\varepsilon}_r^t = -\frac{d}{dt}\left\{\ln\left(1-\varepsilon_r^{eng}\right)\right\} \tag{4.3}$$

As same as in Section 4.1.4, the strain waves were acquired with a 2 MHz sampling rate and filtered with a cut-off frequency of 20 kHz. Then the dynamic engineering axial stress–strain relationship was obtained. The

circumferential strain of the specimen was also measured with a 2 MHz sampling rate and filtered using a low-pass filter with a cut-off frequency of 50 kHz. Figure 4.18 shows the representative engineering axial and circumferential strain of the specimen (D75-L75-T35-V11) and Figure 4.19 presents the dynamic engineering axial stress–strain and the engineering axial strain rate–strain relationships of the same test case. As same as the previous SHPB test, the dynamic compressive strength was obtained at the peak average stress and the corresponding engineering axial strain rate was decided at the same strain of the peak stress. The engineering circumferential strain was also obtained at the same strain as marked in Figure 4.18.

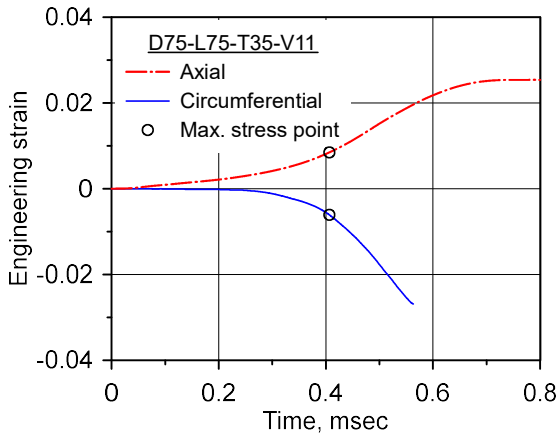

Figure 4.18 Engineering axial and circumferential strain

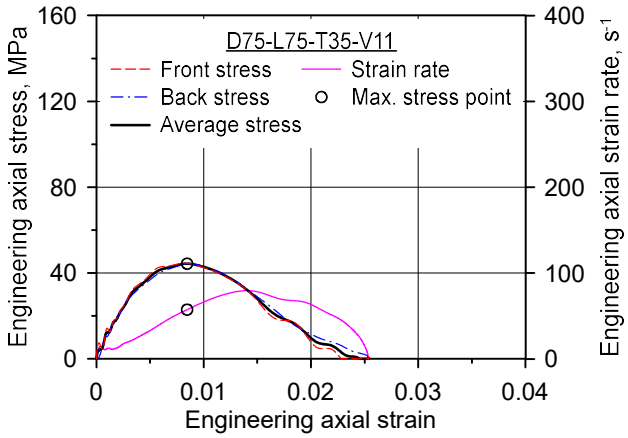

Figure 4.19 Dynamic engineering axial stress–strain and engineering axial strain rate–strain relationships (D75-L75-T35-V11)

The high-speed camera was also used for the same purpose described in Section 4.1.4. The details of the crack patterns observed through the high-speed camera are explained in the next section.

4.2.5. Test results

4.2.5.1. Dynamic stress equilibrium

The dynamic stress equilibrium of the specimens was evaluated following the same procedure in Section 4.1.5.1 and presented in Figure 4.20. In the same manner, 10% was set as a threshold value. Therefore, a total of 60 results were included.

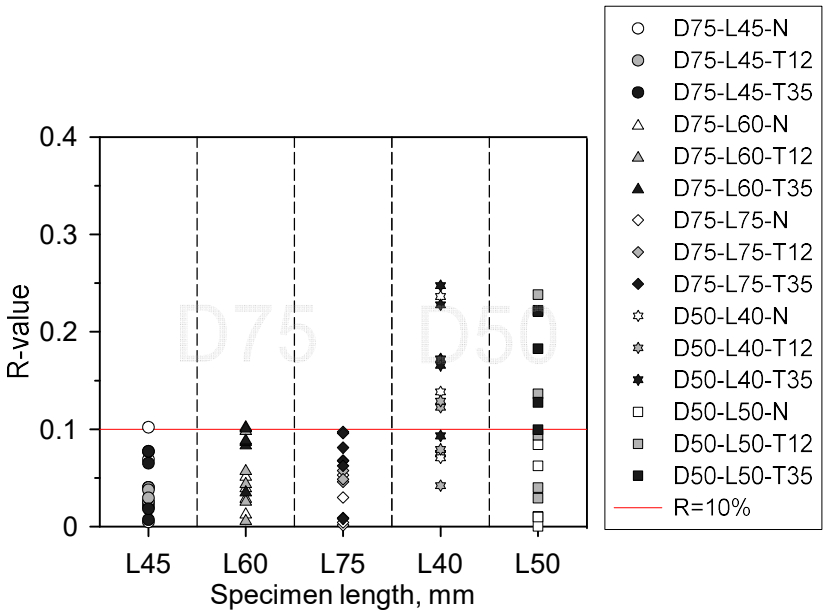

Figure 4.20 R-value of test specimens

4.2.5.2. Apparent DIF

The apparent DIF was calculated in the same procedure described in Section 4.1.5.2. However, the effective deviatoric strain rate was used rather than the engineering axial strain rate to illustrate the strain-rate effect in this test. During the test, eight specimens among the specimens which achieved the dynamic stress equilibrium could not obtain the circumferential strain. Therefore, the results of eight specimens were excluded. Figure 4.21 shows the relationship between the apparent DIF and the effective deviatoric strain rate of the specimens.

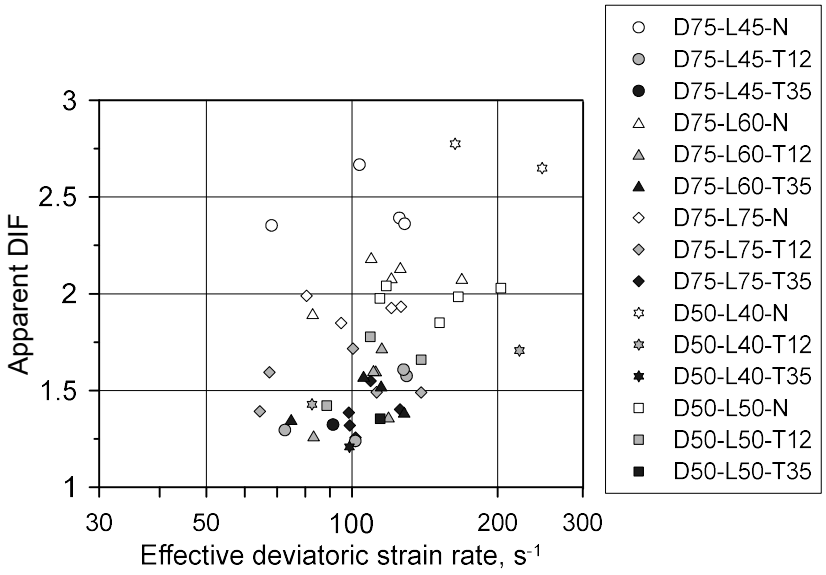

Figure 4.21 Apparent DIF–effective deviatoric strain rate relationship

4.2.6. Verification of suggested lubrication method

4.2.6.1. Apparent DIF according to lubrication

According to the numerical analysis in Section 4.2.1, the apparent DIF was not affected by the L/D ratio of the specimen when the frictional effect didn't exist. By using this point, the effect of lubrication can be evaluated whether the friction was eliminated through lubrication or not. To this end, the apparent DIF–effective deviatoric strain rate relationship was exhibited for each specimen diameter (D75 and D50) as shown in Figure 4.22.

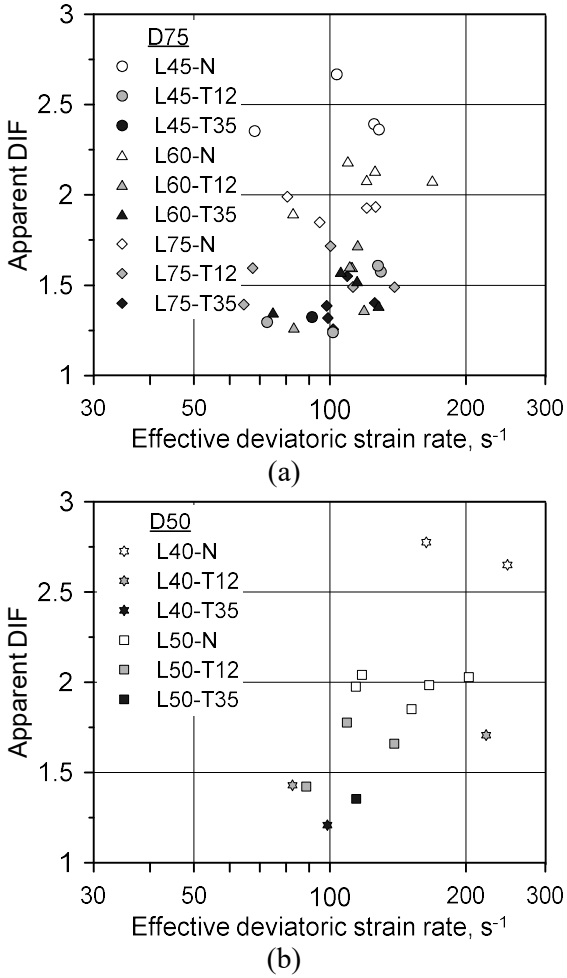

Figure 4.22 Apparent DIF–effective deviatoric strain rate; (a) D75; (b) D50

As presented in Figure 4.22 (a), the remarkable effect of the L/D ratio was observed in the N cases. Since there was a frictional effect in the N cases, the apparent DIF was increased as the specimen length decreased. On the other hand, the apparent DIFs of T12 and T35 cases were all similar regardless of the specimen length. It indicates that there was no frictional effect in the T12 and T35 cases. The same tendency was also shown in the

D50 specimen as presented in Figure 4.22 (b). Therefore, it can be concluded that the frictional in the concrete SHPB test can be removed when the lubricant such as high vacuum grease, petroleum jelly, and Teflon is applied to both ends of the specimens with the amount of 12 mg/cm^2 or more.

4.2.6.2. Crack patterns according to lubrication

Figure 4.23 shows the crack patterns of the specimens with different lubrication conditions at different impact velocities. The same findings explained in Section 4.1.6.2 were drawn. In the N cases, the cracks were propagated in both axial and diagonal directions, while the axial cracks were mainly propagated in sufficiently-lubricated cases (T12 and T35 cases). In particular, barreling was observed in the N cases since the friction restricted the radial deformation at the interfaces between the specimen and the bars. Therefore, the lubrication method of the T12 and T35 cases was also validated through the comparison of crack patterns of the specimens.

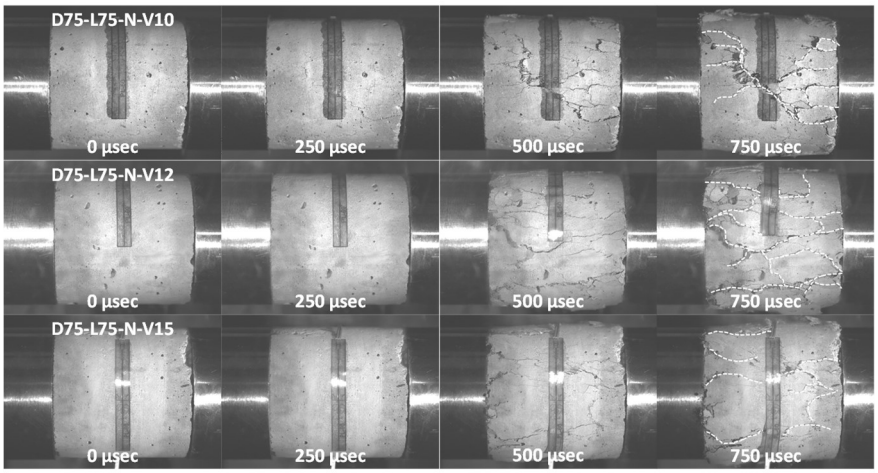

(a)

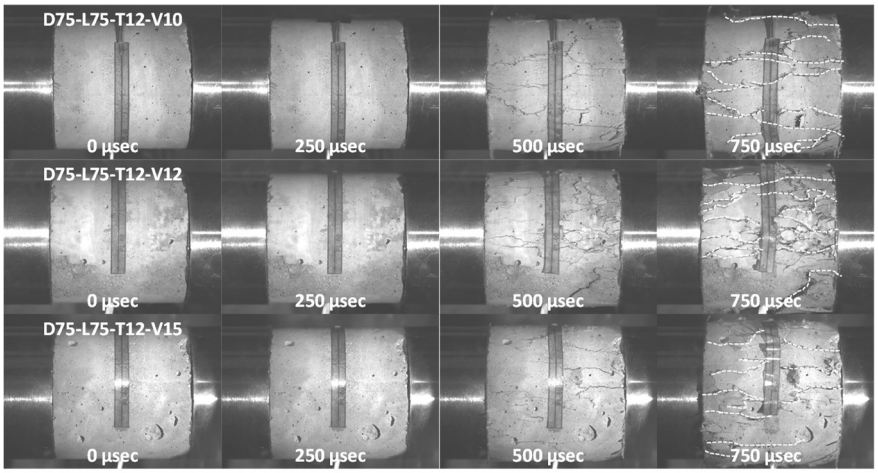

(b)

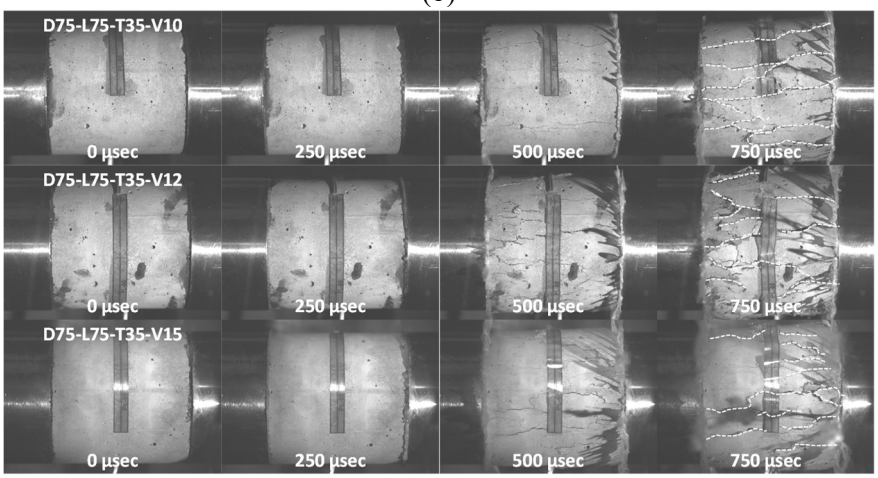

(c)

Figure 4.23 Crack patterns at different impact velocities; (a) N; (b) T12; (c) T35

4.3. Effect of friction

4.3.1. Pure rate DIF

In Section 4.2, the proposed lubrication method in Section 4.1 was verified through the concrete SHPB test for the specimens with various dimensions. Accordingly, the apparent DIF without the frictional effect was acquired (T12 and T35 cases). However, as explained in Section 3.2.2, there is an inertial effect in the apparent DIF. Although the frictional effect is eliminated in the apparent DIF, the inertial effect should be additionally removed to evaluate the pure strain-rate effect. Therefore, the pure rate DIF was calculated following Lee et al. (2018) as explained in Section 3.2.2 with the test results of T12 and T35 cases. Since the apparent DIF was presented along with the effective deviatoric strain rate in this section, the pure rate DIF was also obtained for the effective deviatoric strain rate as presented in Equation (4.4), where $\dot{e}_0$ denotes the reference effective deviatoric strain rate. In this section, 10^{-5} s^{-1} was used for $\dot{e}_0$. Figure 4.24 shows the pure rate DIF of frictionless cases.

$$\gamma_{rate} = \left(\frac{\dot{e}_{eff}}{\dot{e}_0} \right)^{k_1} \tag{4.4}$$

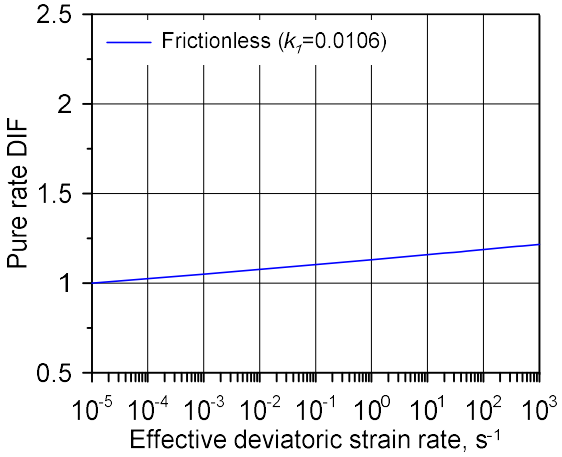

Figure 4.24 Pure rate DIF of frictionless case

4.3.2. Validation of lubrication method

In addition to the experimental verification of the suggested lubrication method, numerical analysis was conducted to validate the lubrication method. To this end, the pure rate DIF obtained in Section 4.3.1 was applied to the numerical analysis on the concrete SHPB test conducted in Section 4.2. For the analysis, the LS-DYNA program was used.

4.3.2.1. Analysis details

As mentioned previously, the concrete SHPB test performed in Section 4.2 was modeled. For the analysis, three parts were modeled: incident bar, specimen, and transmitted bar. The stress waves measured in the test were used to impose the identical loading instead of modeling the loading devices. The stress waves were input as nodal forces at the impact end of the incident bar. Eight-node solid element was used for the whole modeling with reduced integration (ELFORM = 1) and the mesh sizes were determined through the

mesh size test: 7.62×10 mm for bar components, 3.75×3.75 mm for D75 specimens, and 1.0×1.0 mm for D50 specimens. Figure 4.25 shows the part of modeling for each specimen dimension.

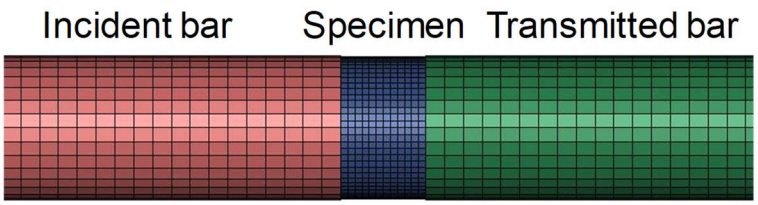

(a)

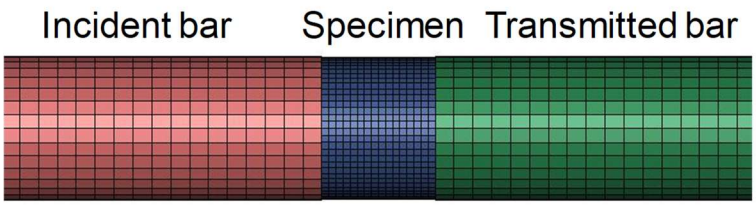

(b)

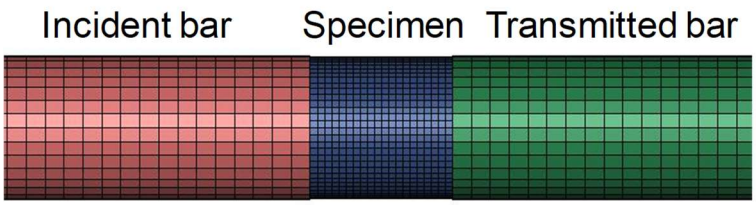

(c)

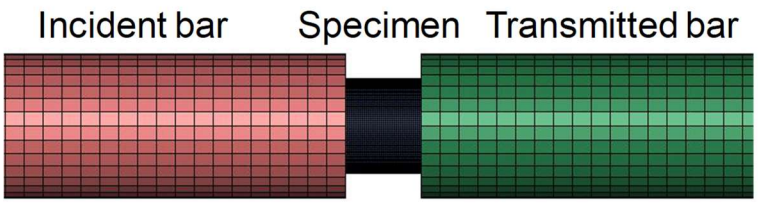

(d)

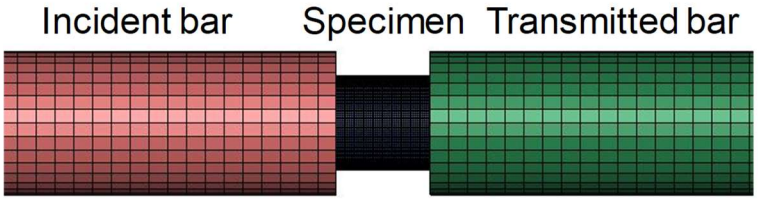

(e)

Figure 4.25 Numerical analysis models; (a) D75-L45; (b) D75-L60; (c) D75-L75; (d) D50-L40; (e) D50-L50

The linear elastic material model (MAT 001) was used for the bar components and the material parameters were inputted following Table 3.4. For the concrete specimens, the Karagozian & Case concrete model (K&C model, MAT 072R3) was selected to apply the pure rate DIF as a user-defined curve (Malvar et al., 1997). The material parameters such as strength surface parameters, damage function, and the equation of state (EOS) were determined based on the static compressive strength test results listed in Table 4.6 following Kong et al. (2017) and Wu and Crawford (2015). Table 4.7, Table 4.8, and Table 4.9 present the details of the material parameters of this study, where η and λ are the yield scale factor and damage function, respectively; ε_v, p, and K_u denote the volumetric strain, pressure, and unloading bulk modulus, respectively. In particular, EOS was determined by scaling the default EOS of the K&C model following Wu and Crawford (2015). The pure rate DIF of Figure 4.24 was inserted as a user-defined curve. The frictional coefficients of the contact surface were zero to simulate the frictionless condition.

Table 4.7 Details of concrete model parameters (unit: mm, sec, ton)

Description	Symbol	Value (D75)	Value (D50)
Density	ρ_s	2.340×10^{-9}	2.340×10^{-9}
Poisson's ratio	ν_s	0.14	0.14
Uniaxial tensile strength	f_t'	3.25	2.89
Maximum failure surface parameters (Kong et al., 2017)	a_0	14.88	11.83
	a_1	0.5698	0.5698
	a_2	0.000748	0.000942
Yield failure surface parameters (Kong et al., 2017)	a_{0y}	9.40	7.47
	a_{1y}	0.8989	0.8989
	a_{2y}	0.002037	0.002564
Residual failure surface parameters (Kong et al., 2017)	a_{1f}	0.5698	0.5698
	a_{2f}	0.000748	0.000942
Associativity parameter (Wu and Crawford, 2015)	ω	0.5	0.5
Localization width	w_{lz}	39	39
Damage scaling factors (Wu and Crawford, 2015)	b_1	0.841	0.504
	b_2	1.562	1.454
	b_3	1.15	1.15

Table 4.8 Relationship between η and λ proposed by Kong et al. (2017)

λ	η
0	0.0
2.5×10^{-5}	0.6203
5.0×10^{-5}	0.9231
7.0×10^{-5}	0.9925
8.7×10^{-5}	1.0
1.0×10^{-4}	0.9927
3.0×10^{-4}	0.6933
5.0×10^{-4}	0.5230
8.0×10^{-4}	0.3882
1.5×10^{-3}	0.2498
3.0×10^{-3}	0.1478
8.0×10^{-3}	0.0672
2.0×10^{-2}	0.0314

Table 4.9 Equation of state (EOS) (Wu and Crawford, 2015)

ε_v	p , MPa	K_u , MPa
0	0	14290
-0.0015	21	14290
-0.0043	47	14490
-0.0101	75	15215
-0.0305	143	18108
-0.0513	215	21001
-0.0726	305	23894
-0.0943	467	26078
-0.174	2724	58668
-0.208	4167	71448

4.3.2.2. Analysis results

The dynamic compressive strength was obtained as the analysis result in the same procedure as the actual test. To compare the SHPB test result of T12 and T35 cases to the analysis result, the apparent strength ratio (R_{AS}) was calculated as presented in Equation (4.5), where $f_{d,FEA}$ and $f_{d,TEST}$ denote the dynamic compressive strengths obtained from the analysis and test, respectively. Figure 4.26 shows the apparent strength ratio according to the impact velocity.

$$R_{AS} = \frac{f_{d,FEA}}{f_{d,TEST}} \tag{4.5}$$

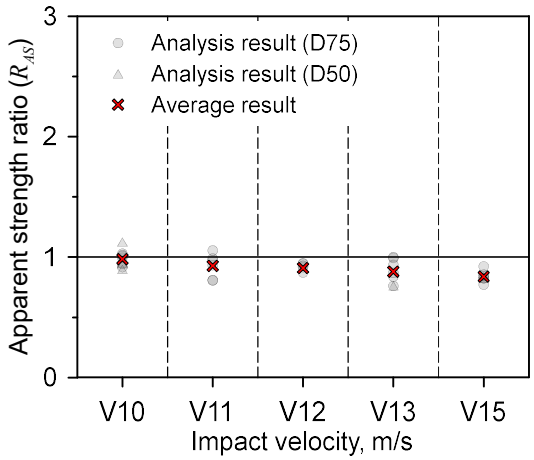

Figure 4.26 Apparent strength ratio according to the impact velocity

In Figure 4.26, the average of the apparent strength ratio at the same impact velocity was calculated and marked. The numerical analysis with the pure rate DIF predicted the dynamic compressive strength of the test within a 9% error on average, which indicates that the pure rate DIF showed a good prediction of the dynamic compressive strength of the concrete. Therefore, the pure rate DIF was verified through numerical analysis, and the lubrication method was also validated.

4.4. Concluding remarks

In this chapter, a series of concrete SHPB tests were described. First of all, the concrete SHPB test to propose a proper lubrication method was performed. Secondly, the concrete SHPB test to verify the suggested lubrication method was conducted. Lastly, the numerical analysis was implemented to verify the pure rate DIF obtained from the follow-up SHPB test and validated the suggested lubrication technique.

The main variables of the first SHPB test were the type and amounts of lubricant. The lubricants widely used for the SHPB test–high vacuum grease, petroleum jelly, and Teflon–were adopted. The test was carried out for D75×L75 mm specimens and the amount of lubricant was determined for D75×L75 mm specimens as 0.0, 0.1, 0.5, 1.0, and 1.5 g (none, 2.3, 11.3, 22.6, and 34.0 mg/cm^2). The test results indicated that the lubrication effect was similar for three types of lubricants and the frictional effect was effectively minimized when any lubricants were applied with the amount of 11.3 mg/cm^2 or more. In addition, it was found that the frictional effect may significantly increase the dynamic compressive strength by about 22 %. Therefore, it is mandatory to lubricate the specimen with a proper method as proposed in this test. However, verification of the suggested lubrication technique was necessary for various L/D ratios because the L/D ratio significantly influences the frictional effect.

To this end, a follow-up SHPB test was conducted for various specimen dimensions: D75×L45, D75×L60, D75×L75, D50×L40, and D50×L50 mm.

Since the lubrication effect of each lubricant used in the previous test was similar to each other, only Teflon was used in the follow-up test. The amount of lubricant was decided to be 0.0, 12, and 35 mg/cm^2 to consider non-lubricated, properly-lubricated, and excessively-lubricated cases. The apparent DIF was obtained to compare the frictional effect according to each lubrication condition. As a result, it was clearly shown that the frictional effect was eliminated when the Teflon of 12 mg/cm^2 or over was applied to both ends of the specimens because the apparent DIFs were similar regardless of the L/D ratio due to the frictionless state. From the frictionless apparent DIFs (test cases with lubricants over 12 mg/cm^2), the pure rate DIF was calculated by correcting the inertial effect.

In order to verify the pure rate DIF and validate the lubrication method, numerical analysis was carried out with the obtained pure rate DIF. The analysis was conducted on the follow-up SHPB test. The dynamic compressive strength was obtained following the same procedure as the test and compared with the dynamic compressive strength acquired from the test. The results showed good agreement with the test results, which indicates that the pure rate DIF is verified and the lubrication method is valid.

From these experimental and numerical studies, an appropriate lubrication method can be suggested: the specimens should be lubricated with the amount of 12 mg/cm^2 or more with one of the lubricants, high vacuum grease, petroleum jelly, or Teflon for the concrete SHPB test. The suggested lubrication method can be used as a standard lubrication method for the concrete SHPB test to improve the accuracy of the strain-rate effect evaluation.

In the following chapter, the analytical and experimental works to suggest the method to determine the loading condition in the concrete SHPB test are described.

5. Effect of Incident Wave Rate in Concrete SHPB Test

5.1. Suggestion of desirable incident wave rate

5.1.1. Characteristic of incident stress wave

In the concrete SHPB test, the incident stress wave is a critical factor in obtaining the dynamic compressive strength of the specimen. In addition, the dynamic stress equilibrium of the specimen highly depends on the incident stress wave. Therefore, it is necessary to establish a guideline to determine the available incident stress wave for the efficiency of the concrete SHPB test.

Figure 5.1 shows the examples of the incident stress wave with various loading conditions consisting of the impact velocity (V), pulse shaper (PS), and striker length (ST). Here, all of the pulse shapers were made of C1020 but the dimensions were varied. PS55-51-3 and PS52-48-4 indicate the dimension of the pulse shaper (outer diameter, inner diameter, and thickness in order). As shown in Figure 5.1 (a), the striker length is related to the loading duration while the rate of the incident wave is similar to each other by the combination of the impact velocity and pulse shaper. In Figures 5.2 (b) and (c), it was observed that the incident wave rates are varied with the pulse shaper or impact velocity. Therefore, it is obvious that the incident stress wave is decided by the combination of the three factors: impact velocity, pulse shaper, and striker length. In general, however, the specimen in the concrete SHPB test fractured before reaching the peak stress of the incident wave. This

indicates that a guideline to determine the loading condition should be suggested by the incident wave rate rather than proposing a single factor.

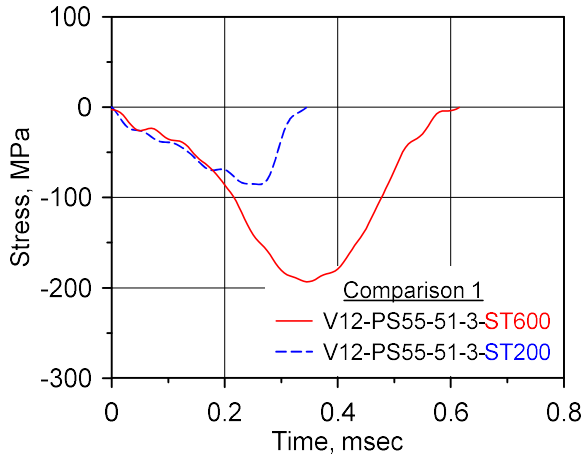

(a)

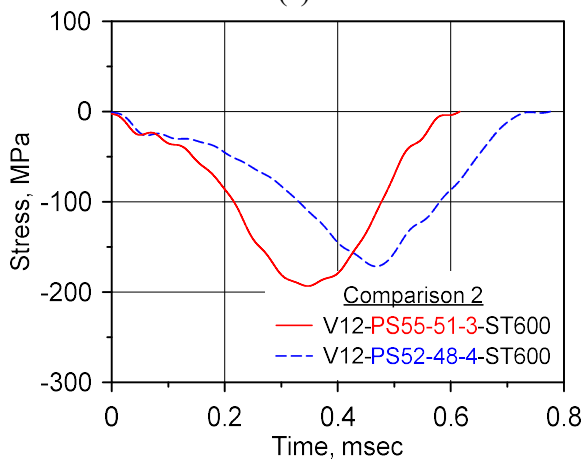

(b)

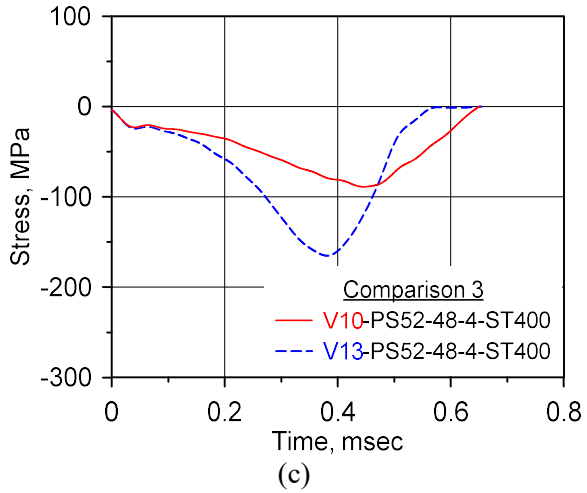

Figure 5.1 Examples of incident stress waves; (a) Different striker length; (b) Different pulse shaper; (c) Different impact velocity

5.1.2. Available incident wave rate

As mentioned previously, the dynamic stress equilibrium of the specimen is related to the incident stress wave. However, the material properties of the specimen also influence the dynamic stress equilibrium. In order to figure out the relationship between the material properties and the incident stress wave in terms of the dynamic stress equilibrium, the time history of the dynamic engineering axial stress was assumed as shown in Figure 5.2, where σ_x and $\dot{\sigma}_x$ denote the engineering axial stress and rate of the dynamic engineering axial stress, respectively; f_d is the dynamic compressive strength; t and t_{peak} mean the time and time at the peak stress, respectively.

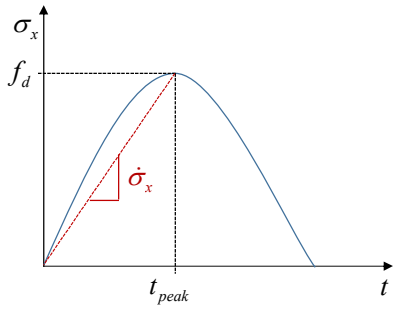

Figure 5.2 Assumption of time history of dynamic engineering axial stress

The dynamic compressive strength of concrete can be calculated with the apparent DIF (γ_{app}) and the static compressive strength (f_c) as presented in Equation (5.1).

$$f_d = \gamma_{app} f_c \tag{5.1}$$

Then, the time at the peak stress (t_{peak}) can be expressed as Equation (5.2), and the dynamic engineering axial stress rate ($\dot{\sigma}_x$) also can be expressed as presented in Equation (5.3).

$$t_{peak} = \frac{f_d}{\dot{\sigma}_x} = \frac{\gamma_{app} f_c}{\dot{\sigma}_x} \tag{5.2}$$

$$\dot{\sigma}_x = \frac{f_d}{t_{peak}} \tag{5.3}$$

The dynamic stress equilibrium of the specimen is satisfied when the imposed incident stress wave is evenly distributed in the specimens through to and fro motion of the wave during the sufficient time. Figure 5.3 illustrates

the specimen subjected to the incident stress wave ($\sigma_{incident}$) and the to and fro motion of the wave with k times, where k is constant; t_t denotes the traveling time of the stress wave; $c_{1,s}$ and l_s describe the elastic wave velocity and initial length of the specimen, respectively. The traveling time, t_t , can be calculated as shown in Equation (5.4).

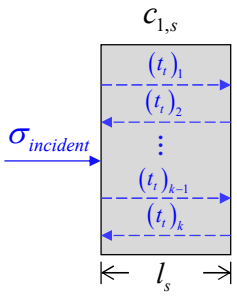

Figure 5.3 The specimen subjected to incident stress wave

$$t_t = \frac{l_s}{c_{1,s}} \tag{5.4}$$

To achieve the dynamic stress equilibrium, the condition presented in Equation (5.5) should be satisfied. Then Equation (5.5) can be expressed as shown in Equation (5.6) using Equations (5.2) and (5.4).

$$t_{peak} \geq kt_t \tag{5.5}$$

$$\frac{\gamma_{app} f_c}{\dot{\sigma}_x} \geq k \frac{l_s}{c_{1,s}} \tag{5.6}$$

In Equation (5.6), the dynamic engineering axial stress rate ($\dot{\sigma}_x$) when the dynamic stress equilibrium was satisfied can be obtained through one-dimensional stress wave theory explained in Section 2.1 as follows;

$$\sigma_x = \frac{A_b}{A_s}\left(\sigma_{incident} + \sigma_{reflected}\right) = \frac{A_b}{A_s}\sigma_{transmitted} \tag{5.7}$$

$$\dot{\sigma}_x = \frac{A_b}{A_s}\left(\dot{\sigma}_{incident} + \dot{\sigma}_{reflected}\right) = \frac{A_b}{A_s}\dot{\sigma}_{transmitted} \tag{5.8}$$

where A_b and A_s denote the cross-section area of bar components and specimen, respectively; $\sigma_{incident}$, $\sigma_{reflected}$, and $\sigma_{transmitted}$ describe the incident, reflected, and transmitted stress waves, respectively; $\dot{\sigma}_{incident}$, $\dot{\sigma}_{reflected}$, and $\dot{\sigma}_{transmitted}$ are the incident wave rate, reflected wave rate, and the transmitted wave rate, respectively. In this study, the average rate of change at the peak stress of the specimen was adopted for each stress wave rate ($\dot{\sigma}_{incident}$, $\dot{\sigma}_{reflected}$, and $\dot{\sigma}_{transmitted}$) as described in Figure 5.4 and Equations (5.9)–(5.11).

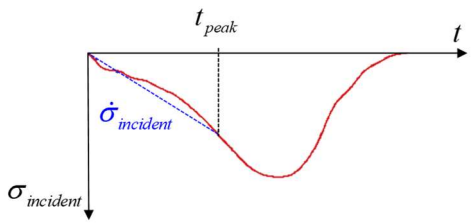

Figure 5.4 Illustration of the incident stress wave and incident wave rate

$$\dot{\sigma}_{incident} = \frac{\sigma_{incident}\left(t_{peak}\right)}{t_{peak}} \tag{5.9}$$

$$\dot{\sigma}_{reflected} = \frac{\sigma_{reflected}\left(t_{peak}\right)}{t_{peak}} \tag{5.10}$$

$$\dot{\sigma}_{transmitted} = \frac{\sigma_{transmitted}\left(t_{peak}\right)}{t_{peak}} \tag{5.11}$$

Then Equation (5.6) can be expressed as shown in Equation (5.12) using Equation (5.8).

$$\frac{A_b}{A_s}\left(\dot{\sigma}_{incident} + \dot{\sigma}_{reflected}\right) \le \frac{1}{k}\frac{c_{1,s}}{l_s}\gamma_{app} f_c \tag{5.12}$$

However, the reflected wave rate only can be obtained after the test. Therefore, the relationship between the incident wave rate and the reflected wave rate was investigated through linear regression analysis using the previous SHPB test data performed in the affiliated laboratory (90 data). Equations (5.13) and (5.14) present the linear regression model, and Figure 5.5 shows the previous SHPB test data and the regression curve. Table 5.1 lists the details of the previous SHPB test data used in the regression analysis.

$$\dot{\sigma}_{reflected} = \alpha \dot{\sigma}_{incident} \tag{5.13}$$

$$\alpha = 0.6365 \tag{5.14}$$

Figure 5.5 Previous SHPB test data and regression curve

Table 5.1 Details of previous SHPB test data used in regression analysis

d_s , mm	l_s , mm	f_c , MPa	$\dot{\sigma}_{incident}$, GPa/sec
50, 75	40–75	26.7–51.5	98.3–472.2

Then, Equation (5.12) can be expressed as Equation (5.15).

$$\frac{A_b}{A_s}(1+\alpha)\dot{\sigma}_{incident} \le \frac{1}{k}\frac{c_{1,s}}{l_s}\gamma_{app} f_c \tag{5.15}$$

From Equation (5.15), the available incident wave rate range for the dynamic stress equilibrium is acquired as shown in Equation (5.16).

$$\dot{\sigma}_{incident} \le \frac{A_s}{A_b}\frac{1}{k}\frac{1}{(1+\alpha)}\frac{c_{1,s}}{l_s}\gamma_{app} f_c \tag{5.16}$$

In Equation (5.16), k is the constant related to the dynamic stress equilibrium as shown in Equation (5.5). In order to obtain the value of k,

Equation (5.16) was expressed as Equations (5.17)–(5.19), where K_{cal} is a threshold value of k.

$$k \le \frac{A_s}{A_b} \frac{1}{(1+\alpha)\dot{\sigma}_{incident}} \frac{c_{1,s}}{l_s} \gamma_{app} f_c \tag{5.17}$$

$$K_{cal} = \frac{A_s}{A_b} \frac{1}{(1+\alpha)\dot{\sigma}_{incident}} \frac{c_{1,s}}{l_s} \gamma_{app} f_c \tag{5.18}$$

$$k \le K_{cal} \tag{5.19}$$

The relationship between K_{cal} and R-value was exhibited in Figure 5.6 using the previous SHPB test results in Figure 5.5 and Table 5.1.

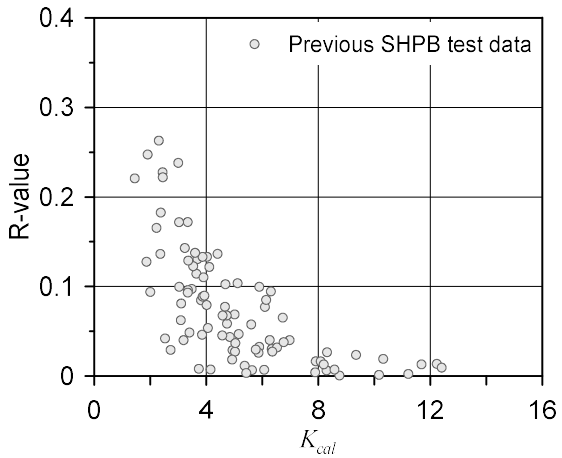

Figure 5.6 R-value according to K_{cal}

In order to obtain the relationship between the R-value and K_{cal}, the regression analysis was carried out. The regression model should satisfy two boundary conditions as presented in Equations (5.20) and (5.21).

$$K_{cal} \to \infty,\ \mathrm{R} \to 0 \tag{5.20}$$

$$K_{cal} = 0,\ \mathrm{R} = \left| \frac{\sigma_{x,front} - \sigma_{x,back}}{\sigma_x} \right| = 2 \left| \frac{\sigma_{x,front} - 0}{\sigma_{x,front} + 0} \right| = 2 \tag{5.21}$$

Therefore, the regression model (R_{reg}) was selected as follows;

$$\mathrm{R}_{reg} = -\frac{4}{\pi} \tan^{-1}\left(\beta K_{cal}\right) + 2 \tag{5.22}$$

Then, the regression curve was obtained through the regression analysis as presented in Equation (5.23), and the regression curve was depicted in Figure 5.7.

$$\mathrm{R}_{reg} = -\frac{4}{\pi} \tan^{-1}\left(3.7988 K_{cal}\right) + 2 \tag{5.23}$$

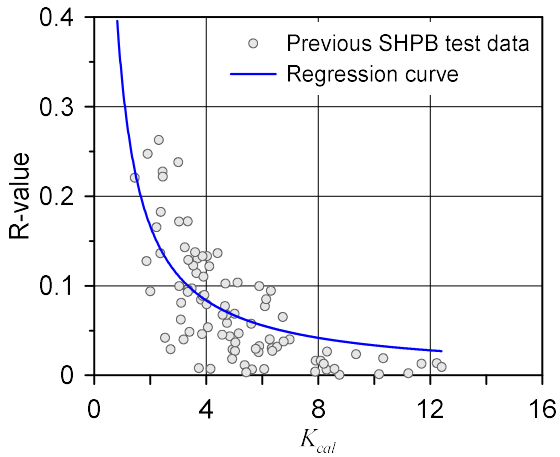

Figure 5.7 Regression curve and previous SHPB test data

By using Equation (5.23), a proper K_{cal} can be obtained for a specific R-value. For example, if 10% is selected as a threshold R-value, K_{cal} should satisfy the condition presented in Equation (5.24). The corresponding range is shaded in Figure 5.8. From Equations (5.19) and (5.24), k can be determined to satisfy the dynamic stress equilibrium in the range of the 10% of R-value as shown in Equation (5.25).

$$K_{cal} \geq 3.3397 \tag{5.24}$$

$$k = 3.3397 \text{ for } \mathrm{R} \leq 10\% \tag{5.25}$$

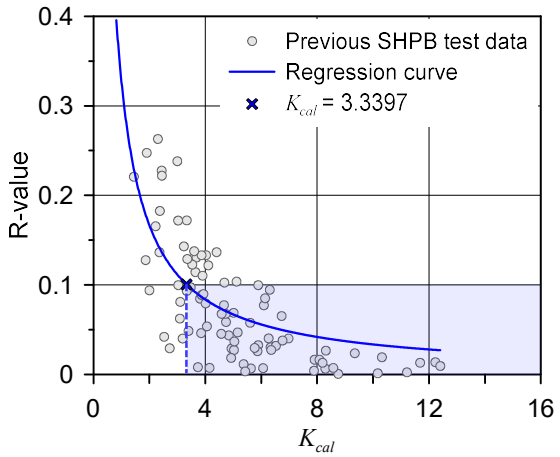

Figure 5.8 Corresponding range for specific range of K_{cal}

As a result, the available incident wave rate range to achieve the dynamic stress equilibrium at a specific level can be suggested as presented in Equation (5.16) considering the material properties such as specimen dimension, elastic wave velocity, static compressive strength, and apparent DIF. Since the apparent DIF is an unknown factor before the test, it is recommended to

assume the apparent DIF referring to the previous studies or use 1.0 for safety. However, experimental verification of the suggested range is necessary to adopt the equation as an organized test method to determine an appropriate loading condition.

In this chapter, the threshold value for the dynamic stress equilibrium was selected as 10% following Section 4.1.5. Therefore, Equations (5.14), (5.16), and (5.25) were adopted for the verification.

5.2. SHPB test program to verify incident wave rate

5.2.1. Test variables

In order to verify the suggested incident wave rate range considering the material properties of the specimen, the specimen dimension, static compressive strength, and incident stress wave were selected as main variables.

The specimen dimension was determined as D75×L50, D75×L75, D75×L120, and D50×L50 mm. In accordance, a G_{max} of 13 mm was used according to Chapter 3. The target static compressive strengths were 30, 40, and 50 MPa for D75×L75 and D50×L50 mm specimens. For the specimens of D75×L50 and D75×L120, the static compressive strength of 30 and 50 MPa were targeted.

Before the determination of the incident stress wave, the available incident wave rate was calculated using Equations (5.14), (5.16), and (5.25). The apparent DIF was assumed to be 1.5 referring to Figure 4.10 and Figure 4.21. The elastic wave velocity of the specimen ($c_{1,s}$) was calculated as in Equation (5.26). In Equation (5.26), the elastic modulus of the specimen (E_s) was assumed as presented in Equation (5.27) (ACI 318-19) and the density of the specimen (ρ_s) was assumed to be 2300 kg/m^3. Table 5.2 exhibits the calculated incident wave rate range for each specimen condition.

$$c_{1,s} = \sqrt{\frac{E_s}{\rho_s}} \tag{5.26}$$

$$E_s = 4700\sqrt{f_c} \tag{5.27}$$

Table 5.2 Available incident wave rate range according to specimen properties

Specimen dimension, mm	Target strength, MPa	$c_{1,s}$, m/s	Available incident wave rate, GPa/sec
D75×L75	30	3346	$\dot{\sigma}_{incident} \le 356$
	40	3595	$\dot{\sigma}_{incident} \le 510$
	50	3801	$\dot{\sigma}_{incident} \le 674$
D50×L50	30	3346	$\dot{\sigma}_{incident} \le 238$
	40	3595	$\dot{\sigma}_{incident} \le 340$
	50	3801	$\dot{\sigma}_{incident} \le 449$
D75×L50	30	3346	$\dot{\sigma}_{incident} \le 534$
	50	3801	$\dot{\sigma}_{incident} \le 1011$
D75×L120	30	3346	$\dot{\sigma}_{incident} \le 223$
	50	3801	$\dot{\sigma}_{incident} \le 421$

The incident stress waves were determined considering the available incident wave rate range listed in Table 5.2. The same striker length (600 mm) and pulse shaper (C1020 pulse shaper of 52×48×4 mm) were used, but the impact velocities were varied. The proper impact velocities for the verification of the suggested incident wave rate range were decided through preliminary tests. Table 5.3 shows the selected impact velocity for each specimen condition and the predicted R-value according to each incident wave rate and specimen characteristic. Figure 5.9 illustrates the time histories of the selected incident stress waves.

Table 5.3 The selected impact velocities and predicted R-value

Specimen condition	Impact velocity, m/s ($\dot{\sigma}_{incident}$, GPa/sec)	Predicted R-value		
		S30	S40	S50
D75-L75 S30: $\dot{\sigma}_{incident} \leq 356$ S40: $\dot{\sigma}_{incident} \leq 510$ S50: $\dot{\sigma}_{incident} \leq 674$	10 (250)	R ≤ 10%	R ≤ 10%	R ≤ 10%
	12 (394)	R ≈ 10%	R ≤ 10%	R ≤ 10%
	14 (543)	R > 10%	R ≈ 10%	R ≤ 10%
	15 (645)	R > 10%	R > 10%	R ≤ 10%
	17 (960)	R > 10%	R > 10%	R > 10%
D50-L50 S30: $\dot{\sigma}_{incident} \leq 238$ S40: $\dot{\sigma}_{incident} \leq 340$ S50: $\dot{\sigma}_{incident} \leq 449$	6 (134)	R ≤ 10%	R ≤ 10%	R ≤ 10%
	10 (230)	R ≈ 10%	R ≤ 10%	R ≤ 10%
	12 (308)	R > 10%	R ≈ 10%	R ≤ 10%
	14 (430)	R > 10%	R > 10%	R ≈ 10%
	17 (583)	R > 10%	R > 10%	R > 10%
D75-L50 S30: $\dot{\sigma}_{incident} \leq 534$ S50: $\dot{\sigma}_{incident} \leq 1011$	10 (250)	R ≤ 10%	-	R ≤ 10%
	12 (394)	R ≤ 10%	-	R ≤ 10%
D75-L120 S30: $\dot{\sigma}_{incident} \leq 223$ S50: $\dot{\sigma}_{incident} \leq 421$	10 (250)	R ≈ 10%	-	R ≤ 10%
	12 (394)	R > 10%	-	R ≈ 10%

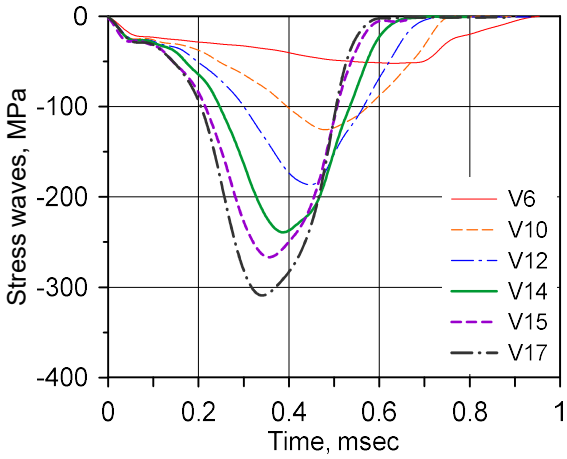

Figure 5.9 Time histories of selected incident stress waves

The overall test variables are presented in Table 5.5. Four or five specimens were tested with the same test condition, and a total of 184 tests were conducted. Figure 5.10 shows the designation of each specimen group.

Table 5.4 Details of SHPB test to verify the suggested incident wave rate

Parameter	Value
G_{max}, mm	13
Specimen dimension, mm	D75×L75 D50×L50 D75×L50 (For 30 and 50 MPa) D75×L120 (For 30 and 50 MPa)
Static compressive strength, MPa	30, 40, 50
Impact velocity, m/s	For D75: 10, 12, 14, 15, 17 For D50: 6, 10, 12, 14, 17
Pulse shaper material	C1020 copper
Pulse shaper dimension, mm	52×48×4

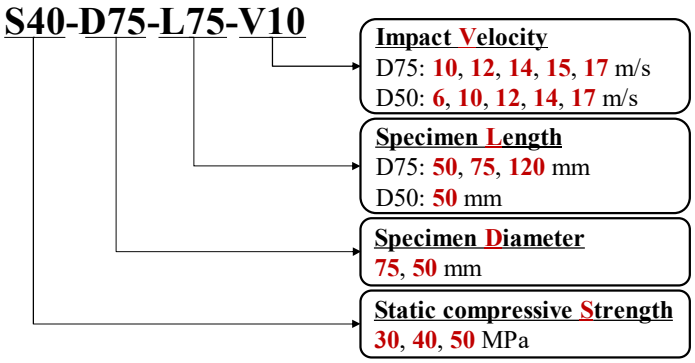

Figure 5.10 Designation of test specimen group

5.2.2. Specimen preparation

Specimens were prepared in a similar way to the previous sections. The cylindrical molds of D75×L150 and D50×L100 mm were used for specimen fabrication. Table 5.5 shows mix proportions for each target static compressive strength. In this test, dried standard sand was used as fine aggregate. The maximum error of the perpendicularity to the axis was 0.4º. Figure 5.11 shows representative specimens for each specimen dimension. The static compressive strength tests were also carried out for D75×L150 and D50×L100 mm specimens and the results are exhibited in Table 5.6.

Table 5.5 Mix proportions

Target strength, MPa	G_{max}, mm	Unit weight, kg/m^3			
		Cement	Water	Fine aggregate	Coarse aggregate
30	13	351	183	681	1144
40		390	220	810	988
50		459	207	661	1037

Figure 5.11 SHPB test specimens

Table 5.6 Static compressive strength test results

Specimen		Static compressive strength, MPa					Average strength, MPa	Average density, kg/m^3
		#1	#2	#3	#4	#5		
D75×L100	S30	33.1	35.1	30.4	33.2	-	33.0	2376
	S40	41.1	40.0	42.1	42.1	-	41.3	2292
	S50	53.3	53.4	50.5	51.7	55.2	52.8	2411
D50×L100	S30	34.5	32.0	36.4	38.5	-	35.4	2376
	S40	38.8	42.0	42.7	39.9	42.9	41.3	2292
	S50	55.3	53.1	53.7	53.4	50.1	53.1	2411

5.2.3. Test procedure

As mentioned in Section 5.2.1, the same striker (600 mm) and C1020 pulse shaper (52×48×4 mm) were used. The pulse shaper was lubricated with petroleum jelly, and the specimens were lubricated with Teflon of 12 mg/cm^2 following the findings in Chapter 4. Figure 5.12 exhibits the test specimens of D75 with different specimen lengths at the same impact velocity before and after the test.

(a)

(b)

(c)

Figure 5.12 Test specimens before and after the test; (a) D75-L50-V10-1; (b) D75-L75-V10-1; (c) D75-L120-V10-1

5.2.4. Data acquisition and processing

As same as the SHPB tests performed in this thesis, the strain gauges were attached to the SHPB bar components to obtain the dynamic axial stress and strain relationships and the high-speed camera was used to observe the specimens during the test. In addition to those measurements, a circumferential strain of the specimen was measured using strain gauges for the specimen. Two strain gauges were attached to the concrete specimen at diametrically opposite locations.

The sampling rate of all strain gauges attached to the bar components and the specimen was 1 MHz. The low-pass filter was also applied as same as in

Sections 3.1.4, 4.1.4, and 4.2.4. The cut-off frequency for the filtering was 15 and 50 kHz for the strains of bar components and concrete specimen, respectively. The dynamic compressive strength and the instantaneous strain rate were evaluated at the peak average stress. The circumferential strain history was obtained by averaging the strains measured from two gauges on the concrete specimen, and the instantaneous circumferential strain was acquired at the same strain with the peak stress. Then the effective deviatoric strain of the specimen ($\dot{e}_{eff}$) was calculated using Equations (4.1)–(4.3), by assuming that the engineering radial strain (ε_r^{eng}) is identical to the average circumferential strain. Figure 5.13 exhibits one of the time histories of the axial and average circumferential strain. The dynamic engineering axial stress–strain and engineering axial strain rate–strain relationships are presented in Figure 5.14 for the same test case (S50-D75-L75-V12-1).

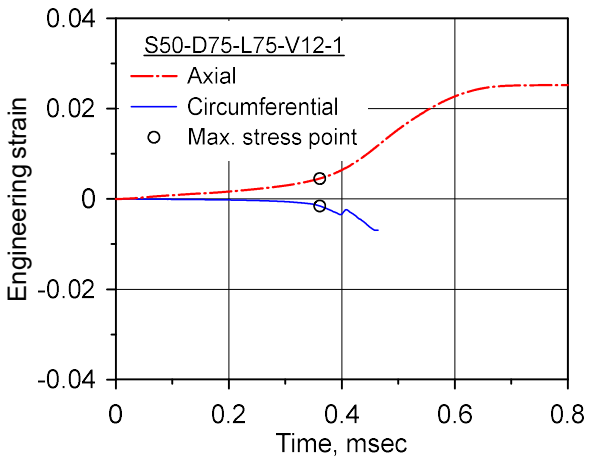

Figure 5.13 Engineering axial and circumferential strain

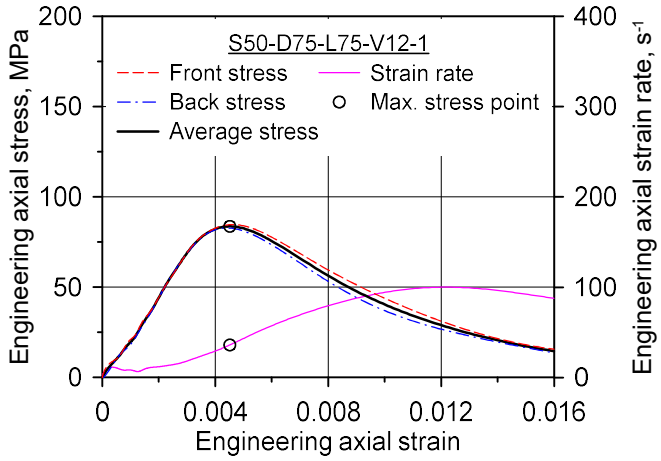

Figure 5.14 Dynamic engineering axial stress–strain and engineering axial strain rate–strain relationships (S50-D75-L75-V12-1)

5.2.5. Test results and discussions

5.2.5.1. Dynamic stress equilibrium according to incident wave rate

In order to verify the suggested available incident wave rate range in Section 5.2.1, the R-value was calculated following the same procedure in previous chapters.

Figure 5.15 shows the relationship between the R-value and the impact velocity for D75-L75 specimens. A distinct tendency, increasing R-value following the increasing impact velocity, was observed for all specimen groups of different static compressive strengths (S30, S40, and S50). The R-values were comparable as predicted in Table 5.3. Figure 5.16 was illustrated to compare the calculated available incident wave rate before the test (Table 5.2) and the actual results after the test. The predicted range of the R-value according to the incident wave rate was shaded by using the threshold value

calculated in Table 5.2. As presented in Figure 5.16, the suggested incident wave rate range in Equations (5.14), (5.16), and (5.25) well predicted the R-value.

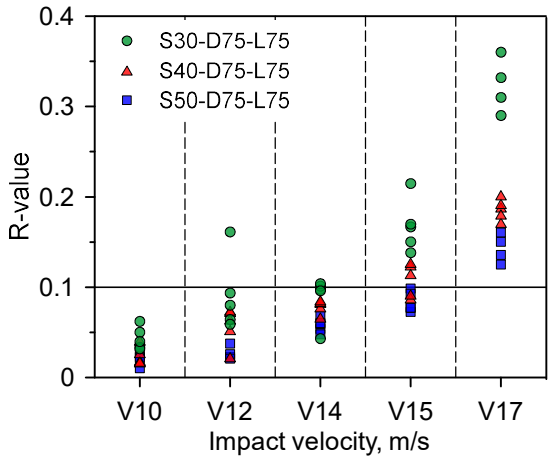

Figure 5.15 R-values according to impact velocities (D75-L75)

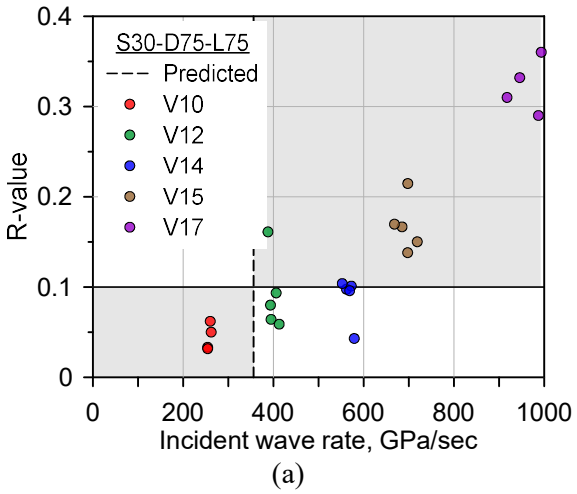

(a)

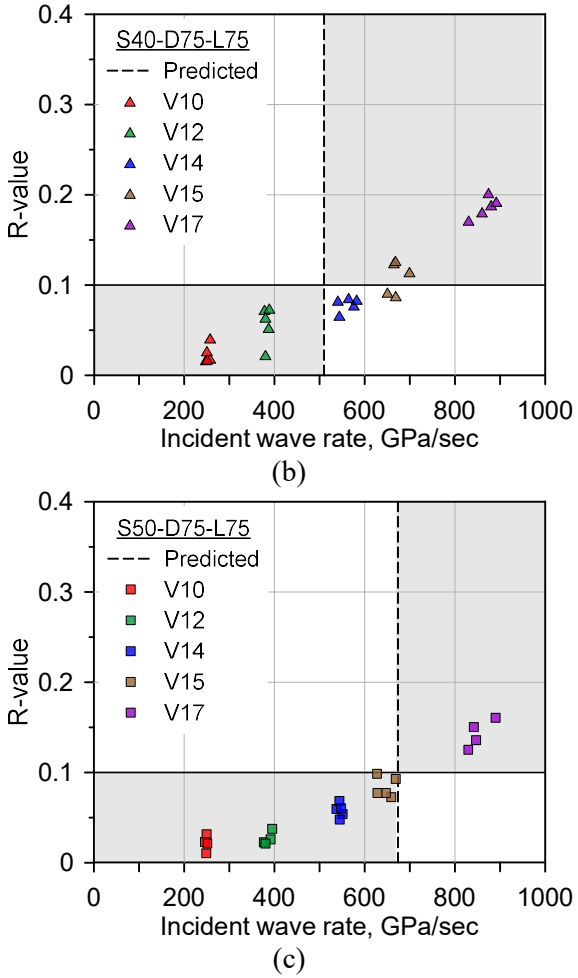

Figure 5.16 R-values according to incident wave rate range and predicted range of test results (D75-L75); (a) S30; (b) S40; (c) S50

In the same manner, the R-values according to the impact velocity and the incident wave rate were illustrated for D50-L50 specimens as shown in Figure 5.17 and Figure 5.18. Although better results with low R-values were obtained for the D50-L50 specimens of S40 and S50, the suggested incident wave rate range was applicable for the test.

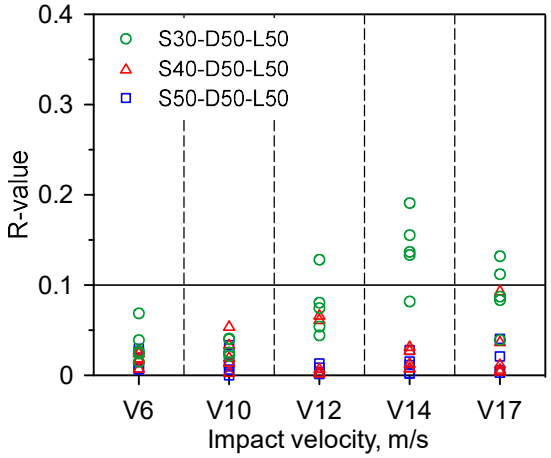

Figure 5.17 R-values according to impact velocities (D50-L50)

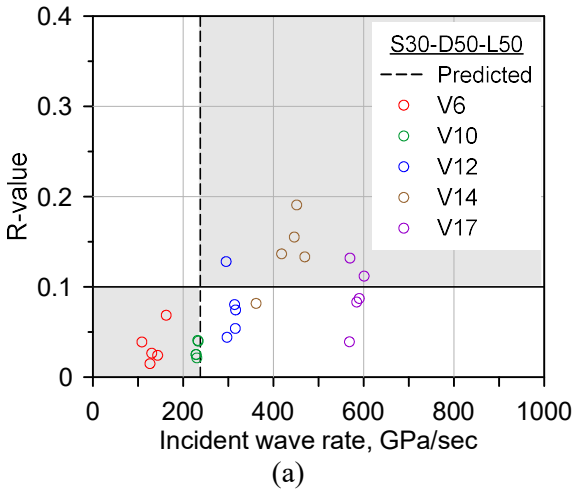

(a)

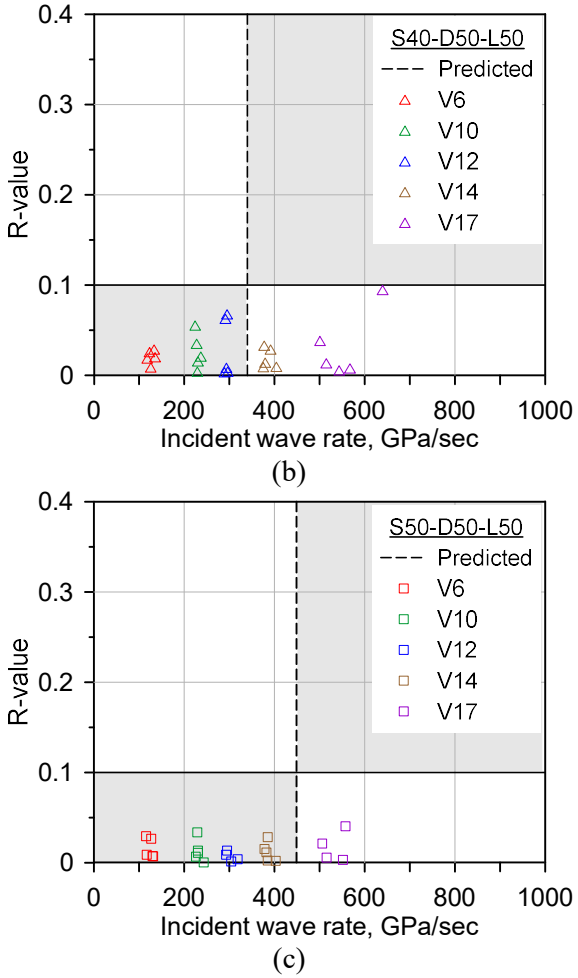

Figure 5.18 R-values according to incident wave rate range and predicted range of test results (D50-L50); (a) S30; (b) S40; (c) S50

For D75-L50 and D75-L120 specimens, the results were exhibited with D75-L75 specimens to compare the effect of specimen lengths on the dynamic stress equilibrium. Therefore, the R-values were described according to the specimen lengths and the impact velocity for each static compressive strength as shown in Figure 5.19. As clearly seen in Figure 5.19, the dynamic

stress equilibrium was relatively poor for the specimens with a longer length, lower compressive strength, and higher impact velocity. However, as presented in Figure 5.20, the results were exhibited in the predicted range. Therefore, the applicability of the suggested incident wave rate range was clearly verified through the test.

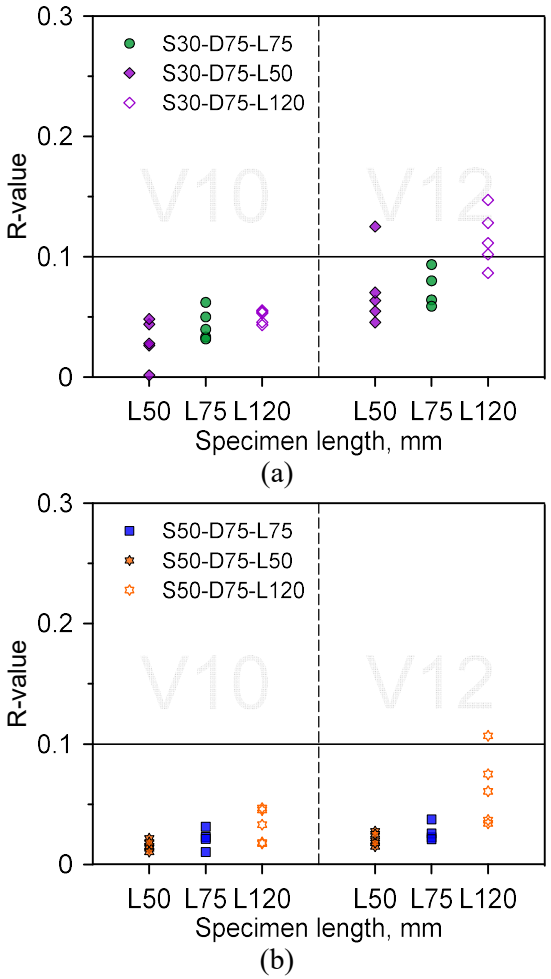

Figure 5.19 R-values according to specimen length and impact velocity (D75-L50 and D75-L120); (a) S30; (b) S50

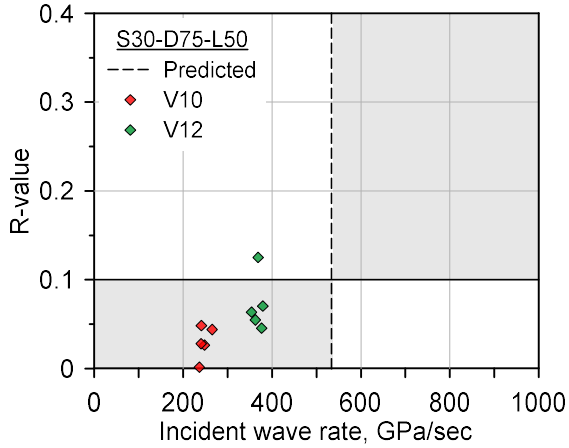
S30-D75-L50
Predicted
V10
V12
R-value
0.4
0.3
0.2
0.1
0
0
200
400
600
800
1000
Incident wave rate, GPa/sec

(a)

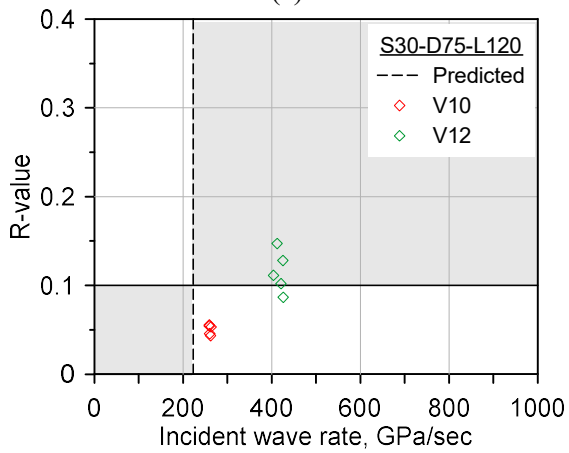
S30-D75-L120
Predicted
V10
V12
R-value
0.4
0.3
0.2
0.1
0
0
200
400
600
800
1000
Incident wave rate, GPa/sec

(b)

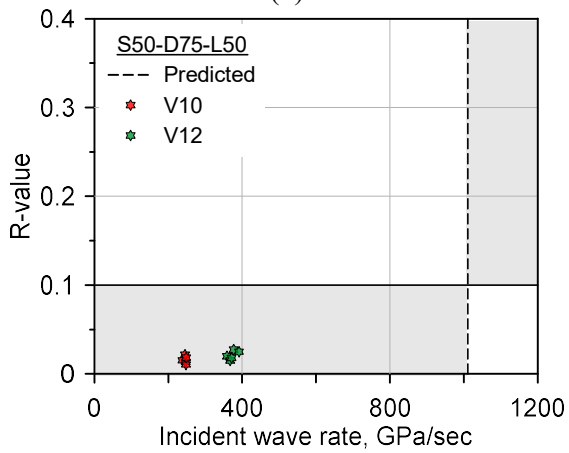
S50-D75-L50
Predicted
V10
V12
R-value
0.4
0.3
0.2
0.1
0
0
400
800
1200
Incident wave rate, GPa/sec

(c)

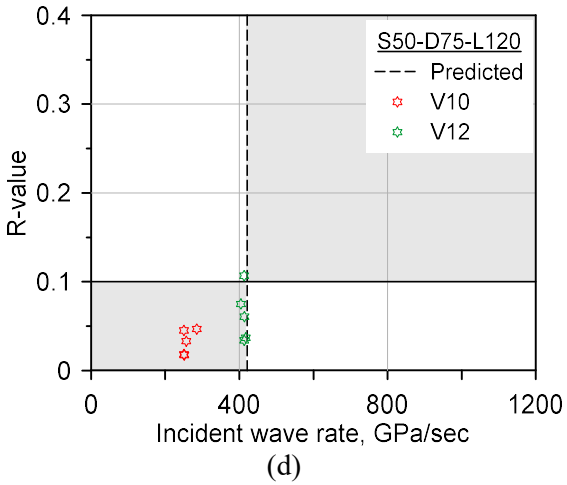

(d)

Figure 5.20 R-values according to incident wave rate range and predicted range of test results; (a) S30-D75-L50; (b) S30-D75-L120; (c) S50-D75-L50; (d) S50-D75-L120

5.2.5.2. Modification of the incident wave rate range

The proposed incident wave rate range in Section 5.2.1 was verified in the previous section. Meanwhile, the 184 test results were obtained through the verification test. Therefore, it is necessary to modify the suggested incident wave rate range to improve the predictability and test efficiency.

In Section 5.1.2, the relationship between the incident stress wave rate ($\dot{\sigma}_{incident}$) and the reflected stress wave rate ($\dot{\sigma}_{reflected}$) through linear regression analysis as presented in Equations (5.13)–(5.14) and Figure 5.5. Since the additional test results were acquired through the verification test conducted in this section, the relationship was updated as follows;

$$\dot{\sigma}_{reflected} = \alpha \dot{\sigma}_{incident} \tag{5.28}$$

$$\alpha = 0.5981 \tag{5.29}$$

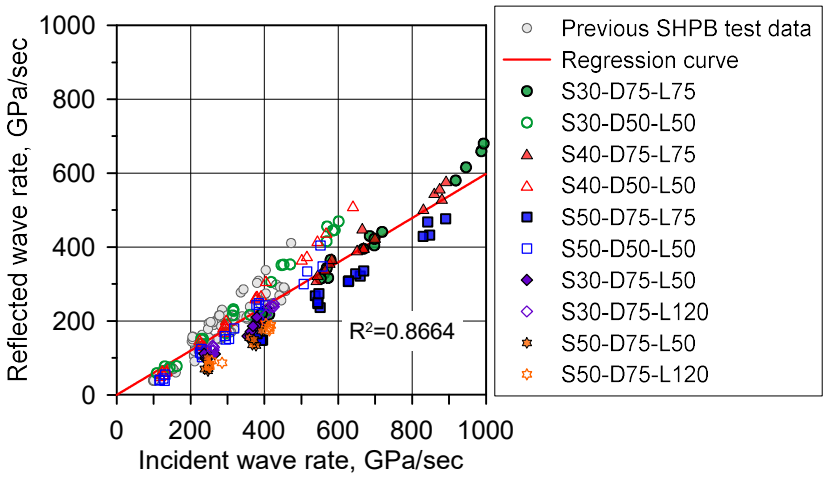

Figure 5.21 Modified relationship between the incident wave rate and the reflected wave rate

As presented in Figure 5.21, the modified regression curve was well-fitted for the previous SHPB test data and additional test results conducted in this section. Table 5.7 lists the range of the used test results for the regression analysis.

Table 5.7 Details of SHPB test data used in regression analysis

d_s , mm	l_s , mm	f_c , MPa	$\dot{\sigma}_{incident}$, GPa/sec
50, 75	40–120	26.7–53.1	98.3–993.7

In addition, the regression curve to determine the constant k for a specific range of R-values was modified through regression analysis as follows;

$$\mathrm{R}_{reg} = -\frac{4}{\pi}\tan^{-1}\left(4.4011K_{cal}\right) + 2 \tag{5.30}$$

$$k = 2.8774 \text{ for } \mathrm{R} \le 10\% \tag{5.31}$$

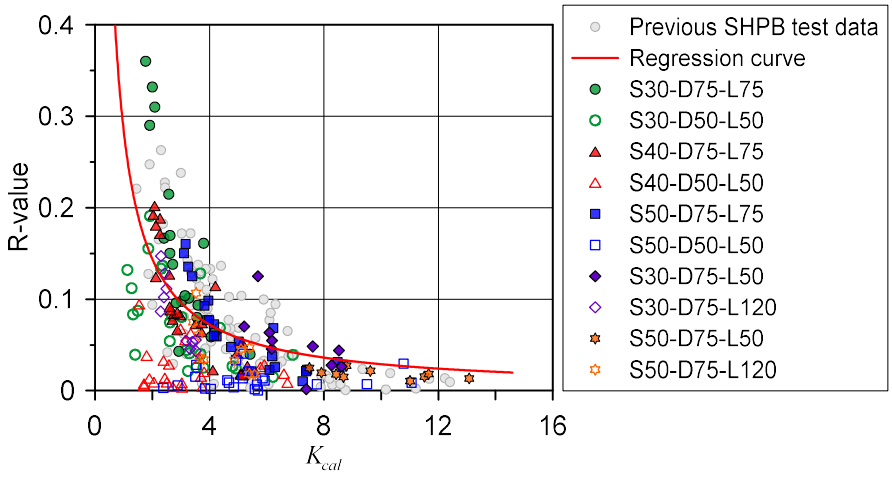

Figure 5.22 Modified regression curve and test results

Finally, the available incident stress wave rate range for the concrete specimen to satisfy the dynamic stress equilibrium at a specific level is presented in Equation (5.32), here, $\alpha = 0.5981$, and the constant k can be obtained from Equation (5.30) for a specific level of R-value. For example, $k = 2.8774$ for $\mathrm{R} \le 10\%$.

$$\dot{\sigma}_{incident} \le \frac{A_s}{A_b}\frac{1}{k}\frac{1}{(1+\alpha)}\frac{c_{1,s}}{l_s}\gamma_{app} f_c \tag{5.32}$$

The suggested incident wave rate range was verified for the specimen properties listed in Table 5.7.

5.3. Concluding remarks

In this chapter, the incident stress wave rate range was proposed for the concrete SHPB test. The suggested incident wave rate range provides the available incident wave rates to make the specimen achieve the dynamic stress equilibrium at a specific level considering the specimen properties such as specimen dimension, static compressive strength, and apparent DIF. The available incident wave rate range was suggested by using previous concrete SHPB test results.

In addition, a verification test was carried out to evaluate the applicability of the proposed incident wave rate range for the actual concrete SHPB test. The main variables were the specimen dimension (D75×L50, D75×L75, D75×L120, and D50×L50 mm), the static compressive strength (30, 40, and 50 MPa), and the incident stress wave rate (adjusted by the impact velocities of 6, 10, 12, 14, 15, 17 m/s). A total of 184 tests were conducted and the results showed that the suggested incident wave rate range appropriately predicted the dynamic stress equilibrium state. Moreover, the effect of the specimen length was investigated by comparing the results of D75×L50, D75×L75, and D75×L120 mm specimens. From the test, it was clearly shown that the dynamic stress equilibrium is difficult to be achieved as the length of the specimen increases. However, the proposed incident wave rate range was applicable for those specimens because the suggested range considers the specimen dimension.

Since the 184 test results were acquired, the suggested range was modified by using the added test data. Finally, the available incident stress wave rate range for the concrete SHPB test to make the specimen satisfy the dynamic stress equilibrium at a specific level was proposed. For clarity, the verified range of the specimen properties was also provided in Section 5.2.5.2.

The suggested incident stress wave rate range can be used as a guideline to determine the loading condition for the concrete SHPB test. Moreover, it is expected to highly improve the efficiency of the concrete SHPB test.

In the following chapter, the established test method for the concrete SHPB test is described. In addition, examples of the concrete SHPB test result after applying the established test method are provided.

6. Establishment of Test Method for Concrete Compressive SHPB Test

6.1. Establishment of test method

The test method for the concrete compressive SHPB test can be established based on the contents listed in Table 2.3 in Chapter 2. Among the contents, three major categories were proposed in this thesis: specimen dimension, lubrication method, and loading condition. The developed test method for the concrete compressive SHPB test is provided in Appendix A.

6.1.1. Specimen preparation

6.1.1.1. Determination of the specimen dimension

In general, the diameter of the SHPB test system is restricted because the length of each bar should be long enough to avoid the overlapping of stress waves, generally an L/D ratio over 20 (Chen and Song, 2010). In addition, the capacity of the loading device should be sufficiently high to implement the SHPB test with a large diameter (Chen and Song, 2010). Due to these limitations, previous experimental studies on cementitious composites were mainly conducted with a small diameter specimen. Accordingly, the coarse aggregates were excluded or replaced with small sizes under 12 mm. However, the coarse aggregates with the maximum coarse aggregate sizes of 19 and 25 mm are also widely used in the actual construction site. In addition, the coarse aggregate affects the dynamic compressive strength and the sizes of the coarse aggregate may influence the dispersion of test results. Therefore, it is

necessary to consider the coarse aggregate, and the specimen dimension should be determined considering the size of the coarse aggregate.

To this end, the effect of G_{max} was thoroughly investigated for high-strength concrete in Kim et al. (2019) and normal-strength concrete in Chapter 3 of this thesis. The test results were dispersive when the G_{max} was relatively large than the specimen dimension. Moreover, the pure rate DIF varied according to G_{max} without a specific tendency. From those observations, two guidelines were drawn: (1) specimen dimension should be at least three times G_{max}, and (2) actual G_{max} should be used in the concrete SHPB test. In addition, the diameter of the test specimen needs to be smaller than the diameter of the SHPB test system for the compressive SHPB test.

6.1.1.2. Measurement of specimen length and error of perpendicularity

In the SHPB test, the specimen length is closely related to the strain rate of the specimen, and the specimen should be parallel enough to be evenly loaded by the stress waves transferred along the bar components. Therefore, it is important to measure the specimen lengths and the error of perpendicularity to the axis after specimen fabrication. The specimen lengths can be measured at six locations evenly spaced around the circumference. Then the average length should be acquired by averaging six lengths. The error of the perpendicularity to the axis can be calculated as a ratio of the maximum difference of the lengths to the specimen diameter. The error of the perpendicularity to the axis should be lower than 0.5º following ASTM C39.

6.1.2. Lubrication method

In the concrete SHPB test, the frictional effect is unavoidable without lubrication. The friction on the interfaces between the bar components and the specimen restricts the radial deformation and confines the specimen. Then, the frictional effect significantly enhances the dynamic compressive strength of the specimen and overestimates the strain-rate effect. Therefore, the establishment of a standard lubrication method was necessary.

A series of concrete SHPB tests were carried out in Chapter 4 to investigate the frictional effect and suggest a proper lubrication method. Moreover, the proposed lubrication technique was verified through a follow-up concrete SHPB test. From the test, an efficient lubrication method was drawn: both ends of the specimen should be lubricated using one of the lubricants among high-vacuum grease, petroleum jelly, and Teflon, with the amount of 12 mg/cm^2 or more. By applying the lubrication, the frictional effect can be efficiently eliminated in the concrete SHPB test.

6.1.3. Loading condition

The loading condition should be carefully determined because the dynamic stress equilibrium of the specimen is highly affected by the loading condition and characteristics of the specimen. To this end, a method to decide the loading condition for the concrete SHPB test was suggested and verified in Chapter 5.

Since the incident stress wave is determined by a combination of the impact velocity, pulse shaper, and striker length, the loading condition should be selected based on the incident stress wave rate rather than changing a single factor. Therefore, the available incident stress wave rate range considering the material properties of the specimen was proposed based on the previous concrete SHPB test results in Section 5.1. Then, the suggested range was verified through the concrete SHPB test for the specimens with various properties. Finally, the incident wave rate range to make the specimen achieve the dynamic stress equilibrium at a specific level was modified with additional test results and suggested as presented in Equation (6.1). Here, $\alpha = 0.5981$, and the constant k can be selected considering the dynamic stress equilibrium level using Equations (6.2)–(6.4) and Figure 6.1. For example, $k = 2.8774$ for $\mathrm{R} \le 10\%$.

$$\dot{\sigma}_{incident} \le \frac{A_s}{A_b}\frac{1}{k}\frac{1}{(1+\alpha)}\frac{c_{1,s}}{l_s}\gamma_{app} f_c \tag{6.1}$$

$$K_{cal} = \frac{A_s}{A_b}\frac{1}{(1+\alpha)\dot{\sigma}_{incident}}\frac{c_{1,s}}{l_s}\gamma_{app} f_c \tag{6.2}$$

$$k \le K_{cal} \tag{6.3}$$

$$\mathrm{R}_{reg} = -\frac{4}{\pi}\tan^{-1}(4.4011 K_{cal}) + 2 \tag{6.4}$$

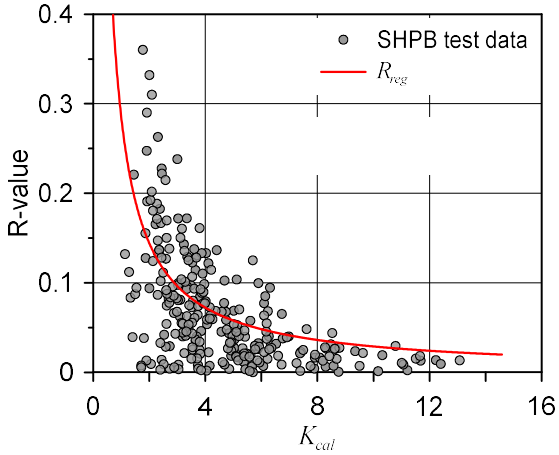

Figure 6.1 SHPB test results and regression curve

6.1.4. Data acquisition and processing

6.1.4.1. Data acquisition

The basic principle of the SHPB test is the one-dimensional stress wave theory. Therefore, the dynamic axial stress–strain and axial strain rate–strain relationships can be drawn from the strains of bar components. Accordingly, the strain gauges must be attached to the incident and transmitted bars.

In addition to the strain gauges on bar components, the strain gauges can be used for the specimen to measure the circumferential strain. Most of the material models for concrete consider the strain-rate effect as a relationship between the DIF and the effective deviatoric strain rate. The effective deviatoric strain rate can be calculated using the axial and radial strain of the specimen. In particular, the radial strain of the specimen can be assumed to be the same as the circumferential strain. Therefore, the circumferential strain of the specimen can be measured in need.

A high-speed camera is optional for the SHPB test. By using the high-speed camera, it is possible to observe the cracking process of the specimen during the test.

6.1.4.2. Data processing

The sampling rate of strain gauges on bar components and specimens should high enough to investigate the dynamic behavior of the specimen. Basically, 1 MHz was confirmed as sufficient to measure the dynamic behavior of the concrete specimen through the test performed in this study. In addition, the noises have to be filtered with a proper cut-off frequency, when the signals of the strain gauges include unnecessary noises.

The dynamic stress equilibrium can be evaluated using R-value (Flores-Johnson and Li, 2017, Lee et al., 2018, Kim et al., 2019, Kim et al., 2022). For the test reliability, a threshold R-value has to be determined at an appropriate level and the test cases that could not satisfy the level should be excluded.

6.1.5. Report

In general, the dynamic axial stress–strain and axial strain rate–strain relationships of the specimen can be acquired as SHPB test results. From those relationships, the dynamic compressive strength and the strain rate can be obtained, and the apparent DIF also can be drawn. In addition, the specimen dimension and the dynamic stress equilibrium have to be provided as results.

6.2. Examples of test results

In this section, examples of the concrete SHPB test results are provided. The test results were classified according to whether the developed test method was applied. Then the applicability of the test method was discussed. In addition, the pure rate DIFs of the concrete specimens were described.

6.2.1. Apparent DIF

Figure 6.2 shows the various DIF models suggested in design guidelines (fib MC2010, UFC 3-340-02, ACI 349-13, ACI 370R-14) and the test results of Chapter 4 and Chapter 5. The test results were categorized as whether the established test method described in Section 6.1 was applied or not. Not applied cases include the test results violating the standard lubrication method and/or available incident wave rate range. In addition, 10% was selected as a threshold R-value to evaluate the validity of the test results. Table 6.1 lists the number of test results for each condition and Figure 6.3 presents the DIF models and the test results of both applied and not applied cases. As presented in Table 6.1 and Figure 6.3, more valid results ($R \leq 10\%$) were obtained (90.9%) when the developed test method was applied than not applied cases (54.9%).

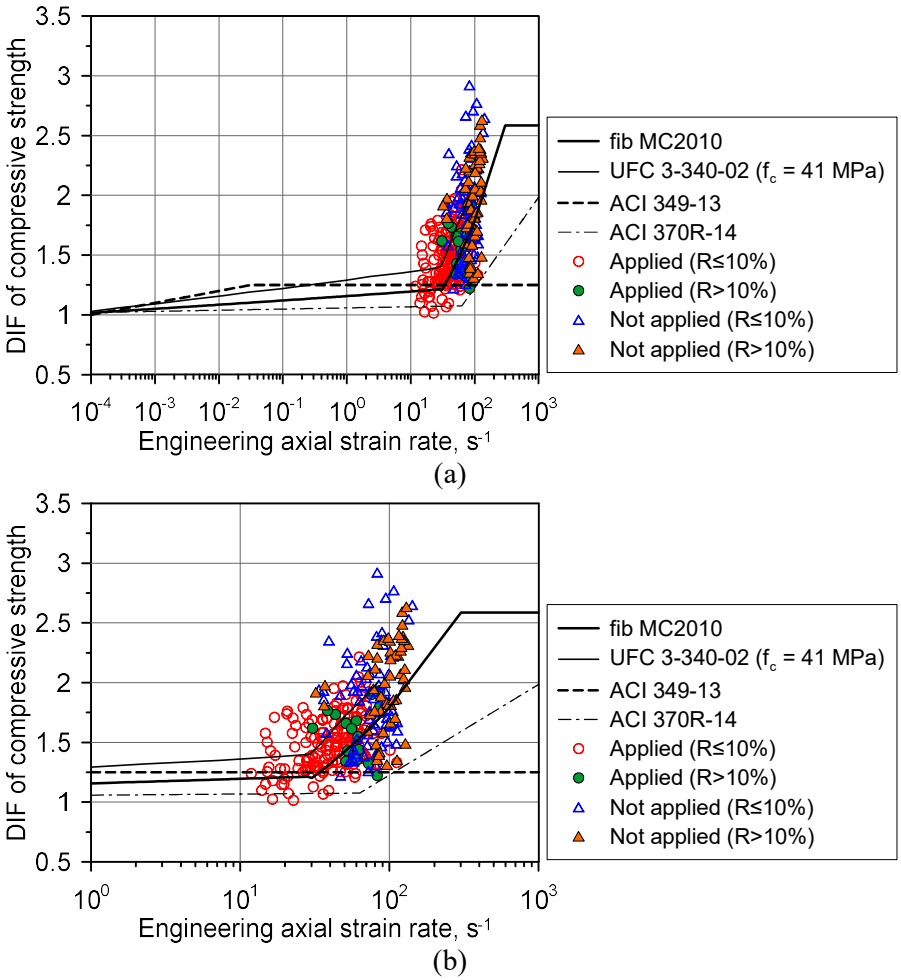

Figure 6.2 Various DIF models and SHPB test results;

(a) Strain rate range of 0.0001–1000; (b) Strain rate range of 1–1000

Table 6.1 The number of test data for each condition

Application of test method	R-value	The number of data	Ratio
Applied	R ≤10%	170	90.9%
	R > 10%	17	9.1%
	Total	187	-
Not applied	R ≤10%	71	57.3%
	R > 10%	53	42.7%
	Total	124	-

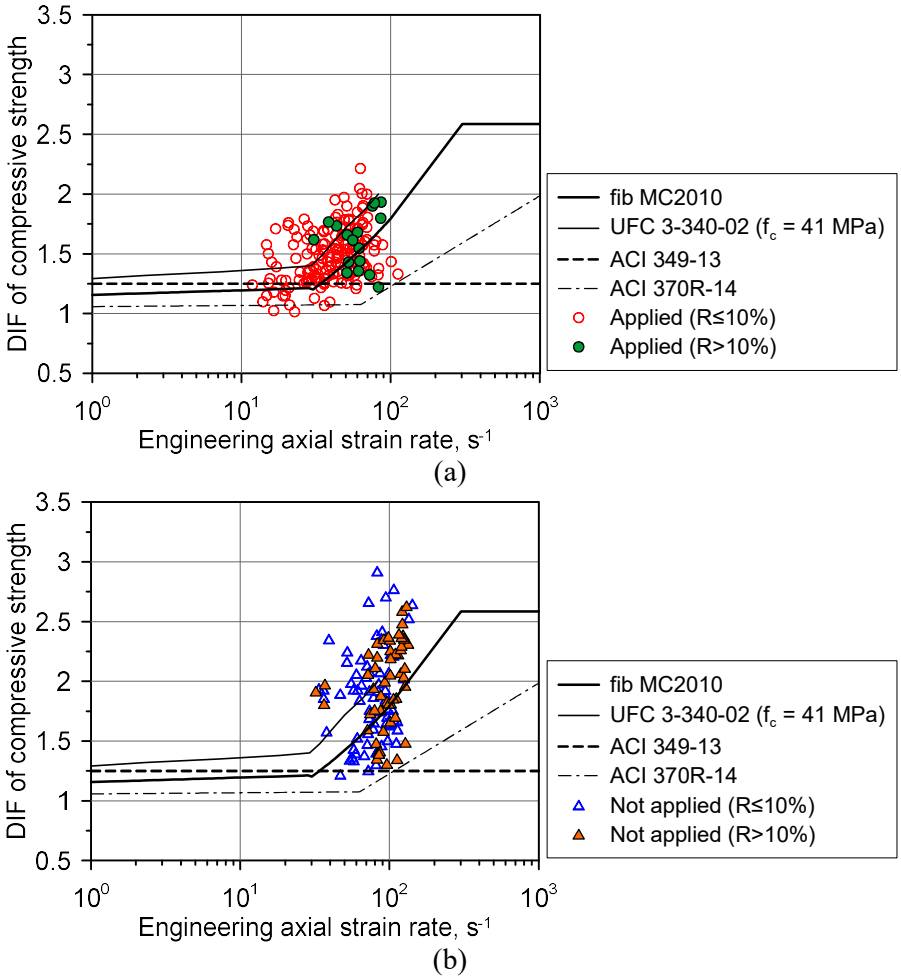

Figure 6.3 Various DIF models and test results; (a) Applied (b) Not applied

Figure 6.4 presents the test results satisfying $R \leq 10\%$ for both applying the test method and not applying cases. As depicted in Figure 6.4, the apparent DIFs were considerably different according to the application of the test method even if the test was conducted at the same time for the same test group. Therefore, it is very important to apply the established test method to obtain consistent test results and improve the accuracy of the strain-rate effect evaluation.

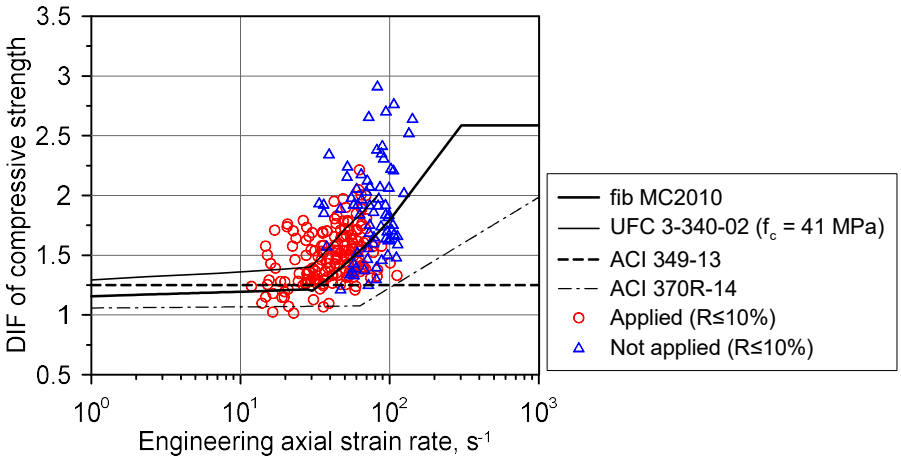

Figure 6.4 Various DIF models and test results satisfying $R \leq 10\%$

6.2.2. Pure rate DIF

In order to evaluate the pure strength enhancement induced by the strain-rate effect, the relationship between the pure rate DIF (Lee et al., 2018) and the effective deviatoric strain rate was obtained from valid results ($R \leq 10\%$) with the application of the developed test method using Eq. (4.4). In the process, a few test cases whose circumferential strain was not available were

excluded. The number of data and details used for the calculation are listed in Table 6.2 and Figure 6.5 exhibits the pure rate DIF.

Table 6.2 The number of test data and details used in pure rate DIF calculation

Pure rate DIF designation	Specimen dimension	G_{max}, mm	The number of data	Static compressive strength, MPa	Section
F2	D75-L75 D75-L60 D75-L45 D50-L50 D50-L40	13	29	33.6 (D75) 26.7 (D50)	4.2
S30	D75-L120 D75-L75 D75-L50 D50-L50	13	40	33.0 (D75) 35.4 (D50)	5.2
S40	D75-L120 D75-L75 D75-L50 D50-L50	13	27	41.3 (D75) 41.3 (D50)	5.2
S50	D75-L120 D75-L75 D75-L50 D50-L50	13	57	52.8 (D75) 53.1 (D50)	5.2
ALL	D: 50, 75 L: 45–120	13	153	26.7–53.1	-

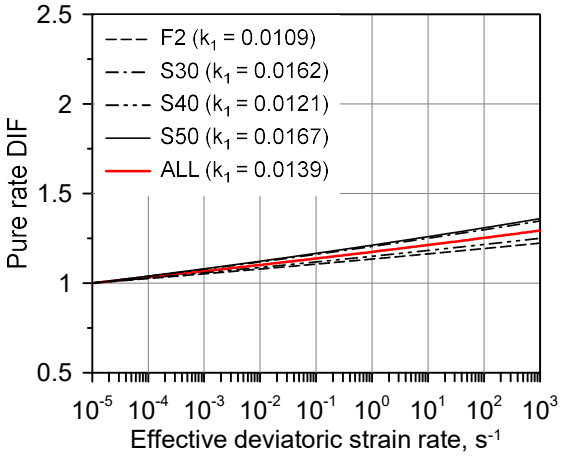

Figure 6.5 Pure rate DIF of valid results

As listed in Table 6.2, the compressive strengths of F2 and S30 were similar to each other. However, the pure rate DIFs were significantly different as presented in Figure 6.5. In addition, when comparing the pure rate DIFs of S30, S40, and S50, it was difficult to figure out the influence of the static compressive strength of the concrete on the pure rate DIF. Therefore, the pure rate DIF with all the available data (ALL) was also drawn as shown in Figure 6.5. The obtained pure rate DIF is applicable for the static compressive strength range 26.7–53.1 MPa and engineering axial strain rate range 10–100 s^{-1} (effective deviatoric strain rate range 10–170 s^{-1}).

As mentioned previously, it was difficult to identify a specific tendency of pure rate DIF according to the properties of the specimen such as the static compressive strength. Therefore, it is recommended to perform the SHPB test to accurately evaluate the pure strain-rate effect for each cementitious composite, and the test method established in this study must be applied to improve the consistency and accuracy of the test results.

6.3. Concluding remarks

In this chapter, the development of the test method for the concrete SHPB test was described. The contents of the test method were suggested and verified through a series of SHPB tests carried out in Chapters 3, 4, and 5.

In addition, the validity and applicability of the developed test method were verified through the comparison of test results. The test results of Chapters 4 and 5 were classified as whether the developed test method was applied or not (lubrication and loading conditions). The validity of the test results was evaluated with the dynamic stress equilibrium (R-value) at a level of 10%. Among the test results that did not satisfy the established test method, only 57.3 % satisfied the dynamic stress equilibrium. However, 90.9 % were valid when the developed test method was applied. Therefore, the validity of the test method was clearly confirmed since the efficiency of the test was highly improved by the application of the developed test method.

However, the available strain rate range might be limited when using the developed test method to obtain the test results satisfying the dynamic stress equilibrium state and it is the limitation of the SHPB test technique. Nevertheless, the developed test procedure can highly improve the consistency and efficiency of the concrete SHPB test in the verified strain rate range.

Lastly, the pure rate DIFs were calculated with the test results satisfying the developed test method. The pure rate DIFs for each test set and for whole results were obtained and compared. The pure rate DIFs varied for each test

set regardless of the static compressive strength. Therefore, it is recommended that each pure rate DIF should be obtained through the SHPB test for each cementitious composite.

In conclusion, the test method for the concrete SHPB test was developed and the applicability of the test method was validated. It is expected to improve the consistency and efficiency of the test results by applying the established test method. Moreover, the accuracy of the strain-rate effect evaluation can be enhanced. The developed test method for the concrete SHPB test can be used as a standard test method and it can contribute to constructing a high-quality database for the evaluation of the extreme performance of cementitious composites.

7. Conclusions

7.1. Summary and major findings of this study

This study conducted a series of experimental and numerical works to establish a test method for the concrete compressive SHPB test.

First of all, the contents that the test method has to mandatorily contain were drawn through the review of previous studies. Then, three major contents that need to be included were derived: specimen dimension, lubrication method, and loading condition.

In order to suggest a guideline to determine the specimen dimension, the effect of maximum coarse aggregate size was investigated. The SHPB experiments for the normal-strength mortar and concrete with various G_{max} were performed for 240 specimens. The effect of the G_{max} was investigated in two aspects: dispersion of the test results due to the heterogeneity induced by the G_{max} and the pure rate DIF according to the G_{max}. It was observed that the relatively large G_{max} resulted in the dispersive test results. Moreover, the pure rate DIFs varied according to G_{max} without a specific tendency. The identical findings were derived in the previous study on high-strength concrete. From these observations, two guidelines to determine the appropriate specimen dimension were suggested: (1) specimen dimension should be at least three times G_{max} to reduce the dispersion of test results, and (2) the same G_{max} used in the real construction site should be considered in the concrete SHPB test to accurately evaluate the strain-rate effect.

Secondly, a proper lubrication method to remove the frictional effect in the concrete SHPB test was proposed from the concrete SHPB test for 52 specimens and verified through follow-up concrete SHPB tests for 75 specimens. The lubrication method was suggested through the concrete SHPB test conducted for various lubrication conditions including the type and the amounts of lubricants. Then the proposed lubrication method was verified through a follow-up concrete SHPB test with specimens of various dimensions. In addition, the pure rate DIF was obtained and verified through numerical analysis. As a result, an effective lubrication method was derived; both ends of the specimen should be lubricated with one of the lubricants among high-vacuum grease, petroleum jelly, and Teflon with the amount of 12 mg/cm^2 or more.

The method to determine the loading condition using the available incident stress wave rate range was suggested. Since the loading condition is decided with a combination of the impact velocity, pulse shaper, and striker length, the incident stress wave rate is a representative parameter. Therefore, the available incident stress wave rate range which makes the specimen satisfy a specific level of the dynamic stress equilibrium was proposed using the previous SHPB test results. The derived available incident stress wave rate range was verified through the concrete SHPB tests for 184 specimens with various properties including the specimen dimension and the static compressive strength. Then, the suggested range was modified using the additional test results from the verification test as presented in Equations (7.1)–(7.4).

$$\dot{\sigma}_{incident} \le \frac{A_s}{A_b}\frac{1}{k}\frac{1}{(1+\alpha)}\frac{c_{1,s}}{l_s}\gamma_{app} f_c \tag{7.1}$$

$$\alpha = 0.5981 \tag{7.2}$$

$$k \le K_{cal} \tag{7.3}$$

$$\mathrm{R}_{reg} = -\frac{4}{\pi}\tan^{-1}(4.4011 K_{cal}) + 2 \tag{7.4}$$

Finally, the test method for the concrete compressive SHPB test to improve the consistency and the accuracy of the test result was established by organizing the suggestions of each category. The applicability and the effectivity of the developed test method were validated through the comparison of the test results according to the application of the test method. The pure rate DIF model was also provided using valid test results.

7.2. Recommendations for further studies

This study established the test method for the concrete SHPB test. Since the test method was developed through experimental and numerical studies and the applicability was verified through numerous test results, this can be used as a basis for developing standard test methods for construction materials subjected to extreme loadings. Accordingly, several recommendations for further studies are described as follows.

- This study conducted experiments with representative variables such as G_{max}, lubrication method, L/D ratio, and static compressive strength. However, various variables can be additionally considered such as the characteristics of the specimen end, different specimen conditions induced by the fabrication, or the amounts of lubricants that are leaked when placing the specimen after the lubrication. Therefore, the experimental and numerical studies considering these variables can improve the developed concrete SHPB test method.

- The concrete SHPB test procedure was developed and verified for the same test apparatus in this study. Therefore, it is recommended to verify the applicability of the developed concrete SHPB test method for other SHPB systems and to modify the developed test method to cover the various characteristics of the apparatus.

- In this study, the lubrication method was suggested to eliminate the frictional effect during the SHPB test. Based on the findings of this study, it might be possible to suggest the frictional effect correction

method from the test results without lubrication through sufficient experimental research.

- The obtained dynamic material properties through the concrete SHPB test should be applied to numerical analysis to evaluate the extreme performance of the structures. Therefore, a comprehensive study to connect the dynamic material properties obtained from the SHPB test to the material model of finite element analysis is necessary. Since the high-quality database of the concrete can be established by applying the developed test method, a representative concrete material model can be suggested.

- It was difficult to measure or evaluate the fracture energy of the specimen through the conventional concrete SHPB test and data analysis method. However, fracture energy is an important parameter to establish the material model, especially for the determination of damage accumulation. Therefore, it is necessary to develop a novel method to evaluate the fracture energy through the conventional SHPB test or other dynamic material test techniques.

- This study developed the test method only for normal concrete. However, various cementitious composites such as fiber-reinforced concrete are also widely used in construction. Therefore, the establishment of test methods to evaluate the dynamic performance of various cementitious composites is necessary.

- The available strain rate range is limited in the concrete SHPB test to obtain the test results satisfying the dynamic stress equilibrium state. Therefore, it is necessary to develop a novel dynamic material test technique to cover a higher strain rate range to establish a reliable concrete material model for the numerical analysis of extreme events.

Reference

ACI Committee 318. Building Code Requirements for Structural Concrete (ACI 318-19). American Concrete Institute. Farmington Hills, MI, U.S. 2019.

ACI Committee 349. Code Requirements for Nuclear Safety-Related Concrete Structures (ACI 349-13) & Commentary. American Concrete Institute. Farmington Hills, MI, U.S. 2014.

ACI Committee 370. Report for the Design of Concrete Structures for Blast Effects. American Concrete Institute. Farmington Hills, MI, U.S. 2014.

Albert, A. and L. Zhang. A novel definition of the multivariate coefficient of variation. Biometrical Journal, 2010. 52(5): p. 667-675.

ASTM C192. Standard Practice for Making and Curing Concrete Test Specimens in the Laboratory. ASTM International. West Conshohocken, PA, U.S. 2019.

ASTM C39. Standard test method for compressive strength of cylindrical concrete specimens. ASTM International. West Conshohocken, PA, U.S. 2020.

Bhargava, J. and Å. Rehnström. Dynamic strength of polymer modified and fiber-reinforced concretes. Cement and Concrete Research, 1977. 7(2): p. 199-207.

CEB-FIP Model Code 1990: Design Code. Committee Euro-International du Beton. Thomas Telford, London, 1993.

Chen, W.W. and B. Song. Split Hopkinson (Kolsky) bar: design, testing and applications. Springer Science & Business Media, New York, NY, U.S. 2010.

Chen, X., S. Wu, and J. Zhou. Experimental and modeling study of dynamic mechanical properties of cement paste, mortar and concrete. Construction and Building Materials, 2013. 47: p. 419-430.

Daudeville, L. and Y. Malécot. Concrete structures under impact. European Journal of Environmental and Civil Engineering, 2011. 15(sup1): p. 101-140.

Fagerlund, G. and B. Larsson. Impact Strength of Concrete (Betongs Slaghallfasthet). CBI Forsk (Cement-och Betonginstitutet), 1979. 4.

fib Bulletin 65. Model Code 2010 Final draft Volume 1. fib Fédération internationale du béton, Lausanne, Switzerland. 2012.

fib Bulletin 66. Model Code 2010 Final draft Volume 2. fib Fédération internationale du béton, Lausanne, Switzerland. 2012.

Flores-Johnson, E.A. and Q.M. Li. Structural effects on compressive strength enhancement of concrete-like materials in a split Hopkinson pressure bar test. International Journal of Impact Engineering, 2017. 109: p. 408-418.

Grote, D.L., S.W. Park, and M. Zhou. Dynamic behavior of concrete at high strain rates and pressures: I. experimental characterization. International Journal of Impact Engineering, 2001. 25(9): p. 869-886.

Guo, Y.B., G.F. Gao, L. Jing, and V.P.W. Shim. Response of high-strength concrete to dynamic compressive loading. International Journal of Impact Engineering, 2017. 108: p. 114-135.

Hao, Y. and H. Hao. Numerical evaluation of the influence of aggregates on concrete compressive strength at high strain rate. International Journal of Protective Structures, 2011. 2(2): p. 177-206.

Hao, Y. and H. Hao. Dynamic compressive behaviour of spiral steel fibre reinforced concrete in split Hopkinson pressure bar tests. Construction and Building Materials, 2013. 48: p. 521-532.

Hao, Y., H. Hao, G.P. Jiang, and Y. Zhou. Experimental confirmation of some factors influencing dynamic concrete compressive strengths in high-speed impact tests. Cement and Concrete Research, 2013a. 52: p. 63-70.

Hao, Y., H. Hao, and Z.X. Li. Influence of end friction confinement on impact tests of concrete material at high strain rate. International Journal of Impact Engineering, 2013b. 60: p.82-106.

Hassan, M. and K. Wille. Experimental impact analysis on ultra-high performance concrete (UHPC) for achieving stress equilibrium (SE) and constant strain rate (CSR) in Split Hopkinson pressure bar (SHPB) using

pulse shaping technique. Construction and Building Materials, 2017. 144: p. 747-757.

Heard, W.F., B.E. Martin, X. Nie, and T. Slawson. Annular pulse shaping technique for large-diameter Kolsky bar experiments on concrete. Experimental Mechanics, 2014. 54(8): p. 1343-1354.

Hopkinson, B. A Method of Measuring the Pressure Produced in the Detonation of High Explosives or by the Impact of Bullets. Philosophical Transactions of the Royal Society London Series A, 1914. 213: p. 437-456.

Hu, S., H.T. Tang, and S. Han. Energy absorption characteristics of PVC coarse aggregate concrete under impact load. International Journal of Concrete Structures and Materials, 2021. 15(1): p. 1-16.

Kim, D.J., K. Sirijaroonchai, S. Ek-Tawil, and A.E. Naaman. Numerical simulation of the split Hopkinson pressure bar test technique for concrete under compression. International Journal of Impact Engineering, 2010. 37(2): p. 141-149.

Kim, K.-M., S. Lee, and J.-Y. Cho. Effect of maximum coarse aggregate size on dynamic compressive strength of high-strength concrete. International Journal of Impact Engineering, 2019. 125: p. 107-116.

Kim, K.-M., S. Lee, and J.-Y. Cho. Influence of friction on the dynamic increase factor of concrete compressive strength in a split Hopkinson pressure bar test. Cement and Concrete Composites, 2022. 129: 104517.

Kolsky, H. An investigation of the mechanical properties of materials at very high rates of loading. Proceedings of the Physical Society, 1949. 62(11): p. 676-700.

Kong, X.Q. Fang, Q.M. Li, H. Wu, and J.E. Crawford. Modified K&C model for cratering and scabbing of concrete slabs under projectile impact. International Journal of Impact Engineering, 2017. 108: p.217-228.

KS F 1004. Concrete Terminology. Korean Agency for Technology and Standard. Republic of Korea. 2019.

KS F 2403. Standard Test Method for Making and Curing Concrete Specimens. Korean Agency for Technology and Standard. Republic of Korea. 2019.

KS F 2425. Standard Practice for Preparing Concrete Sample in the Laboratory. Korean Agency for Technology and Standard. Republic of Korea. 2017.

Lee, S., K.-M. Kim, J. Park, and J.-Y. Cho. Pure rate effect on the concrete compressive strength in the split Hopkinson pressure bar test. International Journal of Impact Engineering, 2018. 113: p. 191-202.

Li, Q.M. and H. Meng. About the dynamic strength enhancement of concrete-like materials in a split Hopkinson pressure bar test. International Journal of Solid Structures, 2003. 40: p. 343-360.

Li, Q.M., Y. Lu, and H. Meng. Further investigation on the dynamic compressive strength enhancement of concrete-like materials based on split Hopkinson pressure bar tests. Part II: numerical simulations. International Journal of Impact Engineering, 2009. 36(12): p. 1335-1345.

Li, M., H. Hao, Y. Shi, and Y. Hao. Specimen shape and size effects on the concrete compressive strength under static and dynamic tests. Construction and Building Materials, 2018. 161: p. 84-93.

Liu, P., D. Hu, Q. Wu, and X. Liu. Sensitivity and uncertainty analysis of interfacial effect in SHPB tests for concrete-like materials. Construction and Building Materials, 2018. 163: p. 414-427.

Lok, T.S., X.B. Li, D. Liu, and P.J. Zhao. Testing and Response of Large Diameter Brittle Materials Subjected to High Strain Rate. Journal of Materials in Civil Engineering, 2002. 14(3): 262-269.

Lu, Y.B. and Q.M. Li. Appraisal of Pulse-Shaping Technique in Split Hopkinson Pressure Bar Tests for Brittle Materials. International Journal of Protective Structures, 2010. 1(3): p. 363-390.

Malvar, L.J., J.E. Crawford, J.W. Wesevich, and D. Simons. A plasticity concrete material model for DYNA3D. International Journal of Impact Engineering, 1997. 19(9-10): p. 847-873.

Malvern, L.E., D.A. Jenkins, T.-X. Tang, and C.A. Ross. Dynamic compressive testing of concrete. Proceedings of 2nd symposium on the interaction of non-nuclear munitions with structures. 1985. p. 194-199.

Markovich, N., E. Kochavi, and G. Ben-Dor. An improved calibration of the concrete damage model. Finite Elements in Analysis and Design, 2011. 47(11): p. 1280-1290.

Ross, C.A. and J. Tedesco. Split-Hopkinson pressure-bar tests on concrete and mortar in tension and compression. ACI Materials Journal, 1989. 86(5): p. 475-481.

Ross, C.A., J.W. Tedesco, and S.T. Kuennen. Effects of strain rate on concrete strength. ACI Materials Journal, 1995. 92(1): p. 37-47.

Shemirani, A.B., R. Naghdabadi, and M. Ashrafi. Experimental and numerical study on choosing proper pulse shapers for testing concrete specimens by split Hopkinson pressure bar apparatus. Construction and Building Materials, 2016. 125: p. 326-336.

Sun, X., H. Wang, X. Cheng, and Y. Sheng. Effect of pore liquid viscosity on the dynamic compressive properties of concrete. Construction and Building Materials, 2020. 231: p. 117143.

Tang, T.-X., L.E. Malvern, and D.A. Jenkins. Dynamic compressive testing of concrete and mortar. Engineering Mechanics in Civil Engineering. ASCE, 1984. P. 663-666.

Tang, T., L.E. Malvern, and D.A. Jenkins. Rate effects in uniaxial dynamic compression of concrete. Journal of Engineering Mechanics, 1992. 118(1): p. 108-124.

Tedesco, J.W., J.C. Powell, C.A. Ross, and M.L. Hughes. A strain-rate-dependent concrete material model for ADINA. Computers and Structures, 1997. 64(5-6): p. 1053-1067.

Tedesco, J.W. and C.A. Ross. Strain-rate-dependent constitutive equations for concrete. Journal of Press Vessel Technology, 1998. 120(4): p. 398-405.

Trautmann, A., C.R. Siviour, S.M. Walley, and J.E. Field. Lubrication of polycarbonate at cryogenic temperatures in the split Hopkinson pressure bar. International Journal of Impact Engineering, 2005. 31: p. 523-544.

Unified Facilities Criteria (UFC) 3-340-02. Structures to Resist the Effects of Accidental Explosions. Department of Defense. Washington D.C., U.S. 2008.

Wang, S, M.-H. Zhang, and S.T. Quek. Effect of specimen size on static strength and dynamic increase factor of high-strength concrete from SHPB test. Journal of Testing and Evaluation, 2011. 39(5): p.1-10.

Wu, Y. and J.E. Crawford. Numerical modeling of concrete using a partially associative plasticity model. Journal of Engineering Mechanics, 2015. 141(12): 04015051.

Xiao, J., L. Li, L. She, and C.S. Poon. Compressive behaviour of recycled aggregate concrete under impact loading. Cement and Concrete Research, 2015. 71: p. 46-55.

Xu, M. and K. Wille. Numerical investigation of the effects of pulse shaper, lateral inertia, and friction on the calculated strain-rate sensitivity of UHP-FRC using a split Hopkinson pressure bar. Journal of Materials in Civil Engineering, 2016. 28(11): p. 04016114.

Zhou, X.Q. and H. Hao. Modeling of compressive behavior of concrete-like materials at high strain rate. International Journal of Solids and Structures, 2008. 45(17): p. 4648-4661.

Zhang, M., H.J. Wu, Q.M. Li, and F.L. Huang. Further investigation on the dynamic compressive strength enhancement of concrete-like materials based on split Hopkinson pressure bar tests. Part I: experiments. International Journal of Impact Engineering, 2009. 36(12): p. 1327-1334.

Zhang, X., Y.-W. Chiu, H. Hao, and J. Cui. Free water effect on the dynamic compressive properties of mortar. Cement and Concrete Composites, 2021. 118: p. 103933.

Appendix A

Developed Test Method for Concrete SHPB Test

A.1. Method for Making Cylindrical Concrete Specimens for Split Hopkinson Pressure Bar Test

A.1.1. Scope

This method covers the procedure for making cylindrical specimens for split Hopkinson pressure bar (SHPB) test for normal concrete.

A.1.2. Referenced documents

This method referred to other standards described below.

KS F 1004, Concrete Terminology

KS F 2403, Standard Test Method for Making and Curing Concrete Specimens

KS F 2425, Standard Practice for Preparing Concrete Sample in the Laboratory

ASTM C192/C192M, Standard Practice for Making and Curing Concrete Test Specimens in the Laboratory

ASTM C39/C39M, Standard Test Method for Compressive Strength of Cylindrical Concrete Specimens

A.1.3. Terminology

A.1.3.1. Maximum size of coarse aggregate

The size of the coarse aggregate representing the minimum sieve sizes that the coarse aggregate of 90% or more by mass has passed.

A.1.3.2. Heterogeneity over cross-section

The characteristic and state of the cross-section with irregularly distributed coarse aggregates of different properties from the mortar matrix in the cross-section of the specimen.

A.1.3.3. Error of perpendicularity

The degree to which the axis in the longitudinal direction of the specimen deviates from 90º with respect to the specimen cross-section.

A.1.4. Apparatus

A.1.4.1. Molds

The inner diameter of molds for specimens shall be identical with the diameter of the specimen to fabricate. Molds shall conform to the requirements specified in KS F 2403, 4.2.1 as follows.

a) Molds shall be non-absorbent and be made of materials that are not eroded by cement.

b) Molds shall be made precisely and leak shall be prevented.

c) Mineral oil or non-reactive peeling agent shall be applied to the inner surface of molds before casting the concrete.

For molds that are consisted of a few components, the components shall be assembled after applying the thin layer of grease on seam.

A.1.4.2. Tamping rod

Tamping rod shall be used to cast the concrete into molds after mixing. The diameter of tamping rod shall be determined following Table A.1. One end of tamping rod shall be hemispherical, the length shall be 500 to 600 mm, and the rod shall be made of steel following KS F 2403, 4.2.2.

Table A.1 Diameter of tamping rod according to the diameter of the specimen

Specimen diameter, mm	Tamping rod diameter, mm
smaller than 100	10±2
up to 150	16±2

A.1.5. Making specimen

Concrete shall be mixed following KS F 2425, 5. The mixed concrete shall be placed in molds and cut to target dimension for the test after curing.

A.1.5.1. Determination of the specimen dimension

A.1.5.1.1. Specimen diameter

Specimen diameter shall be at least three times the maximum coarse aggregate size and equal to or smaller than the diameter of SHPB bar components.

A.1.5.1.2. Specimen length

Specimen length shall be at least three times the maximum coarse aggregate size to reduce the heterogeneity of the specimen in a longitudinal direction.

A.1.5.2. Procedure

A.1.5.2.1. Mixing and molding

Mixed concrete shall be placed in prepared molds.

A.1.5.2.2. Consolidation

The mixed concrete shall be placed with a few layers according to the specimen diameter and lengths as described in Table A.2. Then the molded concrete shall be consolidated with a tamping rod and the number of rodding for each layer is specified in Table A.2. During rodding, the tamping rod shall be only reached until the lower layer. If the material is concerned to be separated, the number of rodding shall be reduced.

Table A.2 Number of layer and rodding

Specimen diameter, mm	Number of layer	Number of rodding/layer
smaller than 100	Round up of length/diameter	25
up to 150	Round up of length/100	25

A.1.5.3. Removal from molds and curing

The specimens shall be removed from the molds and cured following KS F 2403, 7.

a) Molds shall be removed between 16 hours and 3 days after casting. The moisture loss and vibration shall be prevented until the removal of the molds.

b) The specimens shall be cured at a temperature of (20±2)ºC. The specimen shall be moist cured after demolding until the test.

In the case of curing using a water storage tank, 3 g/L of calcium hydroxide shall be added to the water to prevent the loss of the calcium hydroxide components from the specimen.

A.1.5.4. Cutting

The specimens shall be cut with a concrete cutter after curing. Both ends of the cured specimens shall be cut out to a target specimen length for the test. The perpendicularity to the axis shall be secured during the cutting.

A.1.6. Measurement

A.1.6.1. Specimen length

Specimen lengths shall be measured at least three locations spaced evenly around the circumference. The average specimen length shall be obtained by averaging the measured length at each location.

A.1.6.2. Error of specimen lengths

The error of specimen length shall be evaluated as a difference between the maximum and minimum lengths measured at each location.

A.1.7. Estimation of the error of perpendicularity

The error of perpendicularity to the axis (EP) shall not be larger than 0.5º as specified in ASTM C39 and KS F 2403, 4.5 c). The error of perpendicularity to the axis can be estimated following Equation (A.1), where e and d denote the error of specimen length and the specimen diameter, respectively.

$$EP = \left|\frac{e}{d}\right| \times \frac{180°}{\pi} \tag{A.1}$$

A.1.8. Reports

The report shall include the information of the specimen as follows.

a) Designation of the specimen

b) Mix proportion of concrete

c) Date of placement

d) Curing method and curing period

e) Date of cutting

f) Diameter of the specimen

g) Length of the specimen (at least three locations, average, and error)

h) Error of the perpendicularity to the axis

A.2. Method for Concrete Compressive Split Hopkinson Pressure Bar Test

A.2.1. Scope

This method covers the concrete compressive split Hopkinson pressure bar (SHPB) test for normal concrete.

A.2.2. Referenced documents

This method referred to other research described below.

Chen, W.W. and B. Song. Split Hopkinson (Kolsky) bar: design, testing and applications. Springer Science & Business Media, New York, NY, U.S. 2010.

Kim, K.-M., S. Lee, and J.-Y. Cho. Influence of friction on the dynamic increase factor of concrete compressive strength in a split Hopkinson pressure bar test. Cement and Concrete Composites, 2022. 129: 104517.

Kolsky, H. An investigation of the mechanical properties of materials at very high rates of loading. Proceedings of the Physical Society, 1949. 62(11): p. 676-700.

Lee, S., K.-M. Kim, J. Park, and J.-Y. Cho. Pure rate effect on the concrete compressive strength in the split Hopkinson pressure bar test. International Journal of Impact Engineering, 2018. 113: p. 191-202.

Trautmann, A., C.R. Siviour, S.M. Walley, and J.E. Field. Lubrication of polycarbonate at cryogenic temperatures in the split Hopkinson pressure bar. International Journal of Impact Engineering, 2005. 31: p. 523-544.

A.2.3. Terminology

A.2.3.1. Split Hopkinson pressure bar (SHPB)

Testing apparatus to obtain the dynamic mechanical properties of materials such as dynamic compressive strength at a high strain rate range (Kolsky, 1949).

A.2.3.2. Striker bar

One of the bar components of the SHPB, which imposes the compressive stress wave on the incident bar.

A.2.3.3. Incident bar

One of the bar components of the SHPB system, which transmits the stress wave imposed by the striker to the specimen.

A.2.3.4. Transmitted bar

One of the bar components of the SHPB system, which take over the part of the stress wave transmitted from the specimen.

A.2.3.5. Pulse shaper

Expendable to mitigate the rate of compressive stress wave to make the specimen achieve the dynamic stress equilibrium state.

A.2.3.6. Apparent dynamic increase factor (apparent DIF)

The ratio of the dynamic compressive strength obtained through the SHPB test to the static compressive strength of the material (Lee et al., 2018).

A.2.4. Apparatus

A.2.4.1. SHPB system

The SHPB system shall satisfy the conditions specified below (Chen and Song, 2010).

a) The diameter of the SHPB bar components (D) shall be large enough to conduct the dynamic compressive test for non-homogeneous material such as concrete.

b) All of the bar components, striker, incident bar, and transmitted bar shall be made of the same material with the same diameter.

c) The length of the incident and transmitted bar (L) shall be straight and long enough (at least L/D = 20) to apply the one-dimensional stress wave theory since the SHPB test obtains the dynamic stress-strain relationship of the material based on the one-dimensional stress wave theory.

d) Bar components of the SHPB system shall be free to move without the effect of friction.

It is recommended to use a shield to prevent the debris which may damage the data acquisition system after the fracture of the concrete specimen.

A.2.4.2. Impact velocity measuring laser system (optional)

The impact velocity of the striker shall be measured with the laser measuring system shown in Figure A.1. When the striker is launched, the striker covers each laser. The impact velocity of the striker shall be obtained by measuring the time difference of each laser when those are covered. Divide the distance between each laser into the time difference to calculate the impact velocity of the striker.

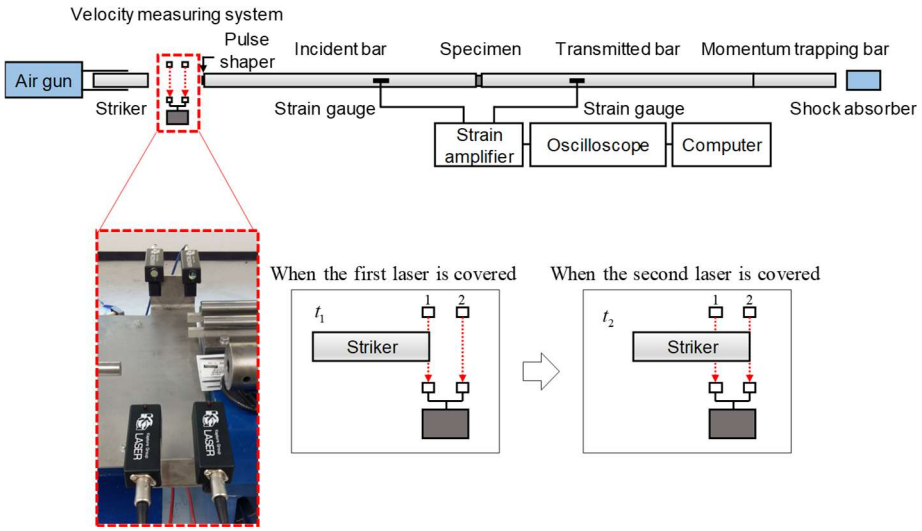

Figure A.1 Impact velocity measuring laser system

A.2.4.3. Strain gauges

A.2.4.3.1. Strain gauges for SHPB bar components

The stress waves of the test shall be measured by strain gauges attached to the incident and transmitted bars. The incident and reflected stress waves shall be measured through the strain gauge attached to the incident bar and the transmitted stress wave shall be measured through the strain gauge attached to the transmitted bar. The strain gauges on the incident and transmitted bars shall be attached to the location where the reflected waves shall not be superposed (at least the wavelength shall be ensured). It is recommended to attach at least two strain gauges to each bar component at a location of 180º and use the average strains to check and minimize the effect of the eccentricity.

A.2.4.3.2. Strain gauges for concrete specimen

The strain gauges shall be attached to the specimen to measure the circumferential strains. It is recommended to attach at least two strain gauges and use the average strains for the circumferential strain of the specimen. The strain gauges can be attached to the specimen in the axial direction if necessary. The gauge length of the strain gauge shall be decided considering the coarse aggregate sizes included in the concrete specimen.

A.2.4.4. Dynamic data logger

A dynamic data logger shall be prepared to measure the strain of the gauges on the SHPB bar components and the specimen. It is recommended to

use a high sampling rate (at least 100 kHz) to prevent the distortion of the strain waves.

A.2.4.5. High-speed camera (optional)

A high-speed camera is optional to check the normality of the test. In addition, the crack pattern or the fracture can be observed using the high-speed camera. In the case of using a high-speed camera, a sufficient frame rate shall be ensured to clearly observe the crack pattern or fracture of the specimen since the test is ended in a very short time (under 2 msec).

A.2.5. Specimens and test condition

A.2.5.1. Specimens

Concrete specimens shall be made following the standard method, A.1.

A.2.5.2. Determination of incident stress wave

In the SHPB test, the compressive stress wave is imposed by the collision of the striker to the incident bar. Then the compressive stress wave is transmitted to the specimen and the stress wave is called the incident stress wave. The incident stress wave is determined by the combination of the striker, pulse shaper, and impact velocity which can be controlled by the air pressure. In the concrete SHPB test, the incident stress wave is closely related to the dynamic equilibrium state of the specimen. Therefore, it is important to determine the appropriate incident stress wave to obtain the test results satisfying the dynamic stress equilibrium.

The incident stress wave rate ($\dot{\sigma}_{incident}$) that makes the specimen achieve a dynamic stress equilibrium at a specific level shall be decided following Equation (A.2), where A_b and A_s denote the cross-section area of bar components and specimen, respectively; $c_{1,s}$, l_s, γ_{app}, and f_c denote the elastic wave velocity, initial length, apparent DIF, and static compressive strength of the specimen, respectively; k and α are constants related to the dynamic stress equilibrium state and the relationship between the incident and reflected stress waves, respectively. Here, $\alpha = 0.5981$.

$$\dot{\sigma}_{incident} \le \frac{A_s}{A_b}\frac{1}{k}\frac{1}{(1+\alpha)}\frac{c_{1,s}}{l_s}\gamma_{app} f_c \tag{A.2}$$

The constant k shall be determined using Equations (A.3)–(A.5), where K_{cal} and R_{reg} are the threshold value of the constant related to the dynamic stress equilibrium and the regression curve related to the dynamic stress equilibrium, respectively. Figure A.2 shows the relationship between K_{cal} and R_{reg}, and the previous concrete SHPB test results used to acquire the relationship, where R-value indicates the dynamic stress equilibrium state.

$$K_{cal} = \frac{A_s}{A_b}\frac{1}{(1+\alpha)\dot{\sigma}_{incident}}\frac{c_{1,s}}{l_s}\gamma_{app} f_c \tag{A.3}$$

$$k \le K_{cal} \tag{A.4}$$

$$\mathrm{R}_{reg} = -\frac{4}{\pi}\tan^{-1}(4.4011 K_{cal}) + 2 \tag{A.5}$$

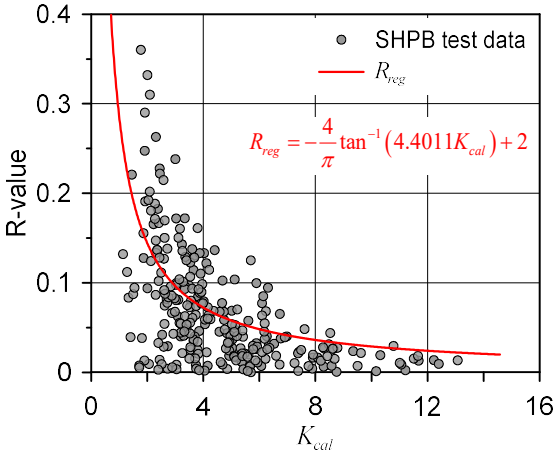

Figure A.2 Previous SHPB test results and the regression curve

The loading condition such as the striker, pulse shaper, and impact velocity to satisfy the determined incident stress wave rate following the above procedure shall be decided by the experimenter because it is difficult to quantitatively suggest a single parameter.

A.2.5.3. Determination of lubrication method

High vacuum grease, petroleum jelly, and Teflon are available as lubricants for the concrete SHPB test to remove the frictional effect (Trautmann et al., 2005, Kim et al., 2022). The amount of lubricant shall be at least 12 mg/cm^2 for the concrete specimen regardless of the lubricant type (Kim et al., 2022). The lubricants shall be applied to both ends of the specimen evenly.

A.2.6. Test procedure

A.2.6.1. Before the test

a) Attach the strain gauges to the incident and transmitted bar following *A.2.4.3.1* and check the status to normally measure the strains.

b) Attach the strain gauges to the concrete specimen in circumferential and axial directions following *A.2.4.3.2*.

c) Apply lubricant to both ends of the concrete specimen following A.2.5.3 and place the specimen between the incident and transmitted bar. Put the specimen shield to prevent the debris.

d) Apply lubricant to both ends of the pulse shaper and attach the lubricated pulse shaper to the impact end of the incident bar.

e) Check the status of the impact velocity measure laser system, dynamic data logger, high-speed camera, and other measurement apparatus.

A.2.6.2. Performing the test

a) Determine the air pressure for target impact velocity and fill the air cylinder.

b) Launch the striker to conduct the test.

c) Discharge the air pressure left in the cylinder safely after conducting the test and finish the test.

A.2.7. Data measurement and processing

A.2.7.1. Data measurement

A.2.7.1.1. Impact velocity of striker

The impact velocity of the striker shall be calculated following A.2.4.2.

A.2.7.1.2. Stress waves from strain gauges of SHPB bar components

The strain waves shall be measured following *A.2.4.3.1*. The strain waves shall be averaged to remove the effect of eccentricity if two strain gauges were attached to each bar at a 180º location. The stress waves shall be obtained by multiplying the elastic modulus of the SHPB bar components (E_b) by the strain. If the unnecessary noises are measured, the stress waves shall be filtered and the filtering method shall be described in the report.

A.2.7.1.3. Strains of concrete specimen

The strains of the concrete specimen shall be measured following *A.2.4.3.2*. The strains shall be checked and filtered in the unnecessary noises are included. The filtering method shall be described in the report.

A.2.7.2. Data processing

A.2.7.2.1. Time histories of dynamic behavior of concrete specimen

The time histories of the dynamic behavior of the concrete specimen shall be obtained through one-dimensional stress wave theory as follows, where $\varepsilon_{incident}$, $\varepsilon_{reflected}$, and $\varepsilon_{transmitted}$ denote the incident, reflected, and transmitted strain waves, respectively; $c_{1,s}$ and t denote the elastic wave velocity of bar components and the time, respectively.

a) Dynamic axial stress at a front surface of specimen ($\sigma_{x,front}$)

$$\sigma_{x,front} = \frac{A_b}{A_s} E_b \left(\varepsilon_{incident} + \varepsilon_{reflected} \right) \tag{A.6}$$

b) Dynamic axial stress at a back surface of specimen ($\sigma_{x,back}$)

$$\sigma_{x,back} = \frac{A_b}{A_s} E_b \varepsilon_{transmitted} \tag{A.7}$$

c) Dynamic axial stress of specimen (σ_x)

$$\sigma_x = \frac{\sigma_{x,front} + \sigma_{x,back}}{2} \tag{A.8}$$

d) Engineering axial strain rate of specimen ($\dot{\varepsilon}_x^{eng}$)

$$\dot{\varepsilon}_x^{eng} = c_{1,b} \left(\frac{\varepsilon_{incident} - \varepsilon_{reflected} - \varepsilon_{transmitted}}{l_s} \right) \tag{A.9}$$

e) Engineering axial strain of specimen (ε_x^{eng})

$$\varepsilon_x^{eng} = \int_0^t \dot{\varepsilon}_x^{eng}(\tau)\, d\tau \tag{A.10}$$

f) Engineering axial strain acceleration of specimen ($\ddot{\varepsilon}_x^{eng}$)

$$\ddot{\varepsilon}_x^{eng} = \frac{d\,\dot{\varepsilon}_x^{eng}}{dt} \tag{A.11}$$

The radial strain (ε_r^{eng}) of the specimen can be assumed to be identical to the circumferential strain of the specimen under the uniform deformation state. Therefore, the effective deviatoric strain rate of specimen ($\dot{e}_{eff}$) shall be calculated as follows, where $\dot{\varepsilon}_x^t$ and $\dot{\varepsilon}_r^t$ denote the true axial and radial strain rate of specimen, respectively.

g) Effective deviatoric strain rate of specimen ($\dot{e}_{eff}$)

$$\dot{e}_{eff} = \frac{2}{3}\left(\dot{\varepsilon}_x^t - \dot{\varepsilon}_r^t\right) \tag{A.12}$$

$$\dot{\varepsilon}_x^t = -\frac{d}{dt}\left\{\ln\left(1-\varepsilon_x^{eng}\right)\right\} \tag{A.13}$$

$$\dot{\varepsilon}_r^t = -\frac{d}{dt}\left\{\ln\left(1-\varepsilon_r^{eng}\right)\right\} \tag{A.14}$$

A.2.7.2.2. Evaluation of dynamic stress equilibrium state of concrete specimen

The dynamic stress equilibrium state of the concrete specimen shall be evaluated as a difference between the front stress ($\sigma_{x,front}$) and back stress ($\sigma_{x,back}$) of the specimen at the maximum stress as shown in Equation (A.15). The test results with a high R-value shall be excluded for the reliability of the test results. It is recommended to use 10% as a criterion.

$$R = \left| \frac{\sigma_{x,front} - \sigma_{x,back}}{\sigma_x} \right|_{\text{at maximum average stress}} \quad \text{(A.15)}$$

A.2.8. Acquisition of test results

A.2.8.1. Dynamic compressive strength of concrete specimen

The dynamic compressive strength of the concrete specimen shall be obtained as the maximum average stress.

A.2.8.2. Dynamic axial strain rate

The dynamic axial strain rate can be obtained as an instantaneous axial strain rate at the maximum average stress. If the other method is used to obtain dynamic axial strain rate, the details shall be included in the report.

A.2.8.3. Dynamic axial strain acceleration

The dynamic axial strain acceleration can be obtained as an instantaneous axial strain acceleration at the maximum average stress. If the

other method is used to obtain dynamic axial strain acceleration, the details shall be included in the report.

A.2.8.4. Dynamic radial strain rate

The dynamic radial strain rate can be obtained as an instantaneous radial strain rate at the maximum average stress. If the other method is used to obtain dynamic radial strain rate, the details shall be included in the report.

A.2.8.5. Apparent DIF

The apparent DIF shall be calculated by dividing the dynamic compressive strength (A.2.8.1) into the static compressive strength of the concrete specimen. The static compressive strength of the concrete specimen shall be obtained through the static compressive strength test with the cylindrical specimen of the same diameter as the SHPB test specimen. Describe the relationship between the apparent DIF and the axial strain rate, effective deviatoric strain rate, or other parameters.

A.2.8.6. Dynamic stress-strain curve

Describe the relationship between the dynamic axial stress and dynamic axial strain. Describe the strain rate if necessary.

A.2.9. Reports

The report shall include the information of the test as follows.

a) Designation of the specimen

b) Dimension of the specimen

c) Details of lubrication method

d) Incident stress wave condition

e) Incident and reflected stress wave rate

f) Static compressive strength (including the specimen dimension)

g) Dynamic compressive strength

h) Strain rate

i) Strain acceleration (optional)

j) Dynamic stress equilibrium state of the specimen (R-value)

k) Apparent DIF

l) Dynamic stress-strain curve

Appendix B

Experimental Results of SHPB Test for Investigation on the Effect of Maximum Coarse Aggregate Size

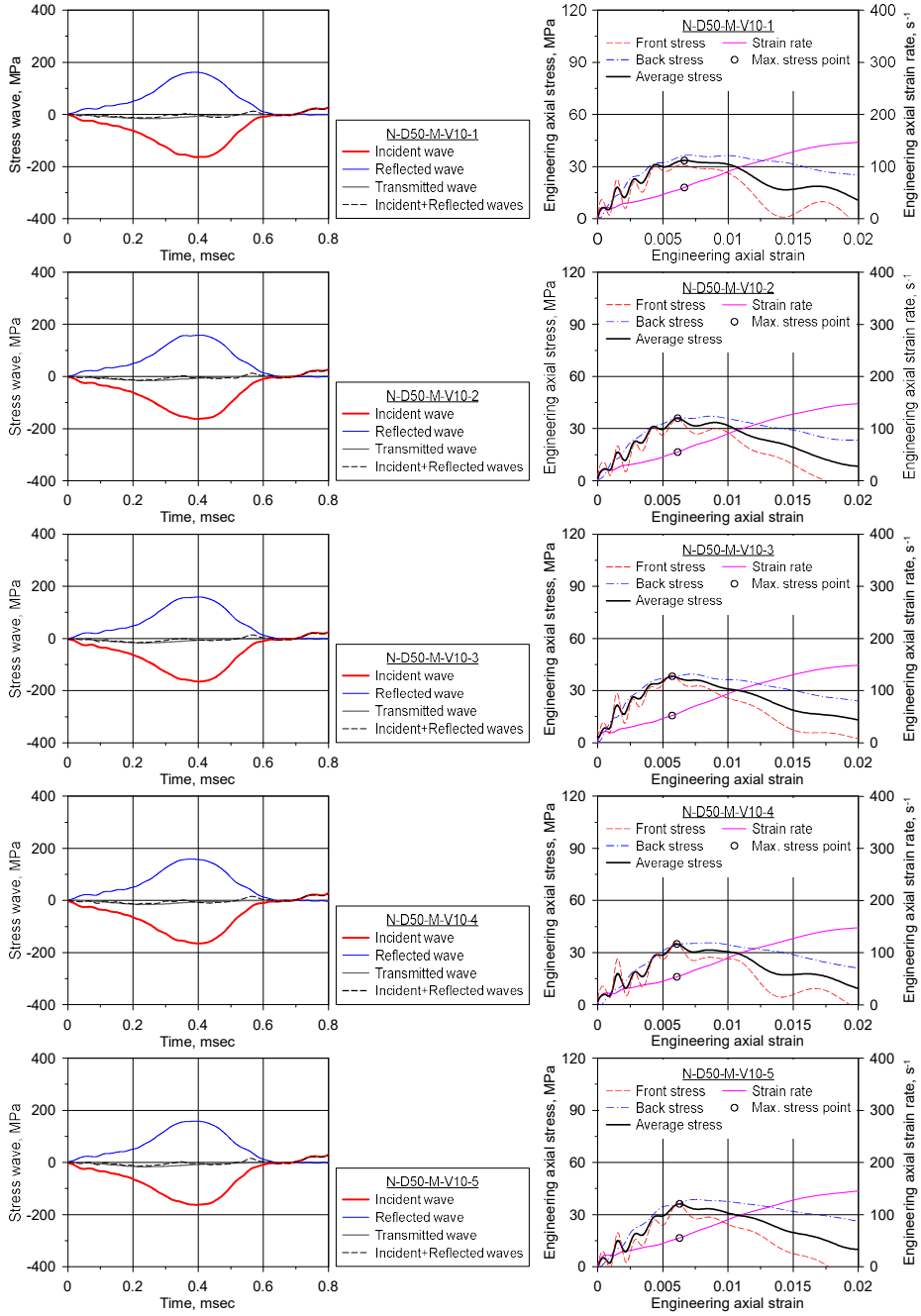
Stress wave, MPa
Time, msec
N-D50-M-V10-1
Incident wave
Reflected wave
Transmitted wave
Incident+Reflected waves
Engineering axial stress, MPa
Engineering axial strain rate, s-1
Engineering axial strain
Front stress
Back stress
Average stress
Strain rate
Max. stress point
N-D50-M-V10-2
N-D50-M-V10-3
N-D50-M-V10-4
N-D50-M-V10-5

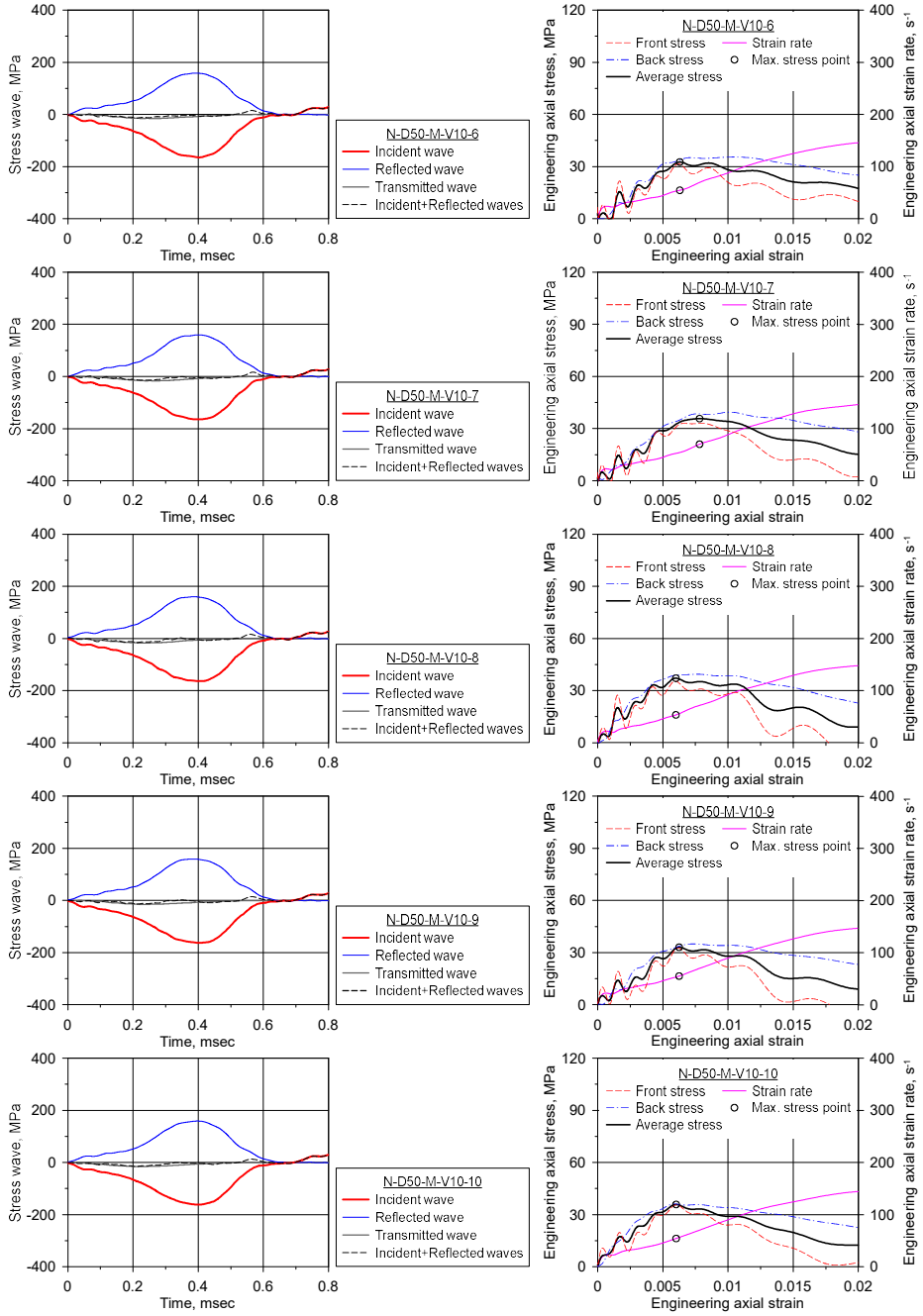

Figure B.1 Stress waves and the axial stress–strain curve of N-D50-M-V10

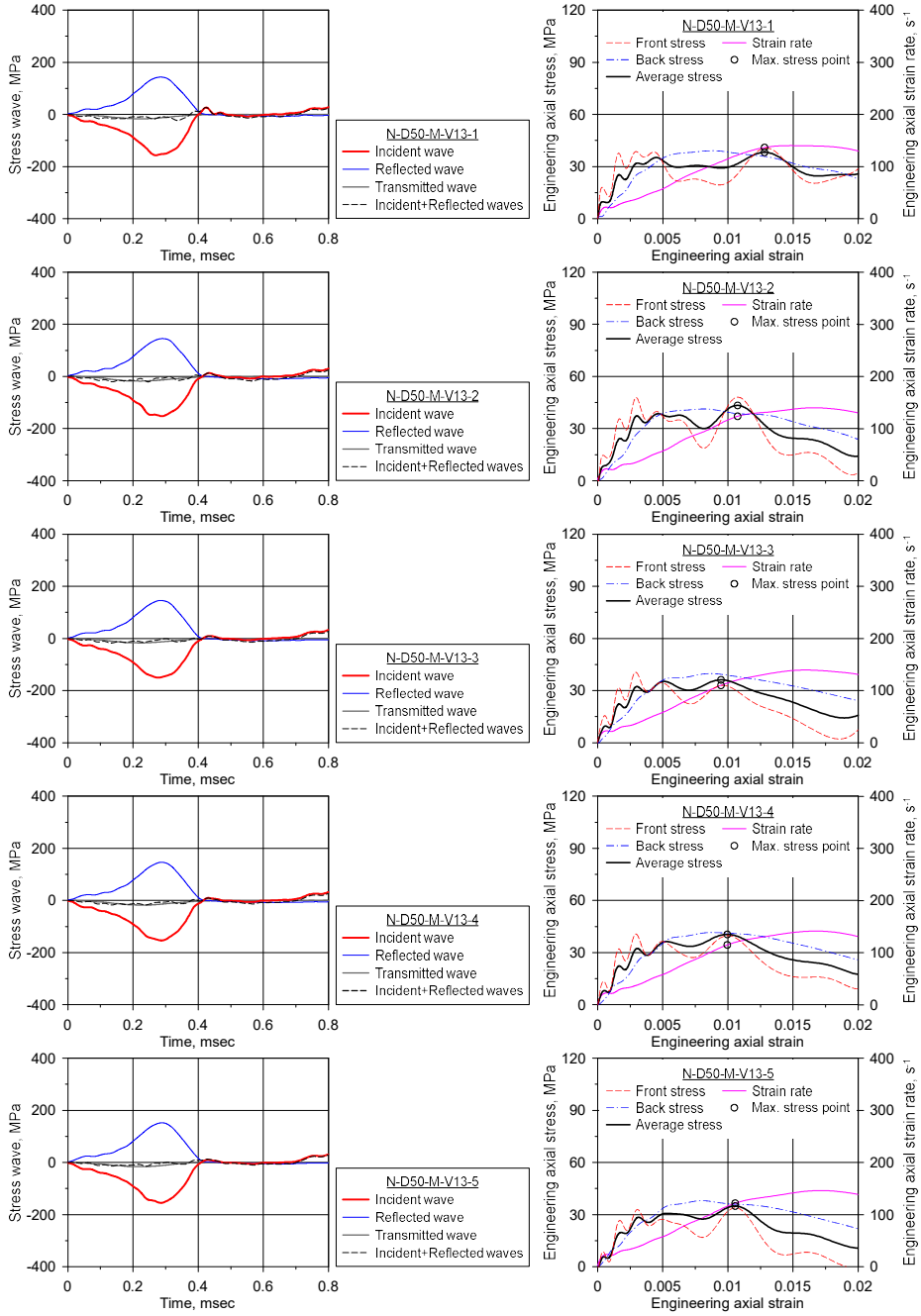
Stress wave, MPa
Time, msec
N-D50-M-V13-1
Incident wave
Reflected wave
Transmitted wave
Incident+Reflected waves
Engineering axial stress, MPa
Engineering axial strain rate, s⁻¹
Engineering axial strain
Front stress
Back stress
Average stress
Strain rate
Max. stress point
N-D50-M-V13-2
N-D50-M-V13-3
N-D50-M-V13-4
N-D50-M-V13-5

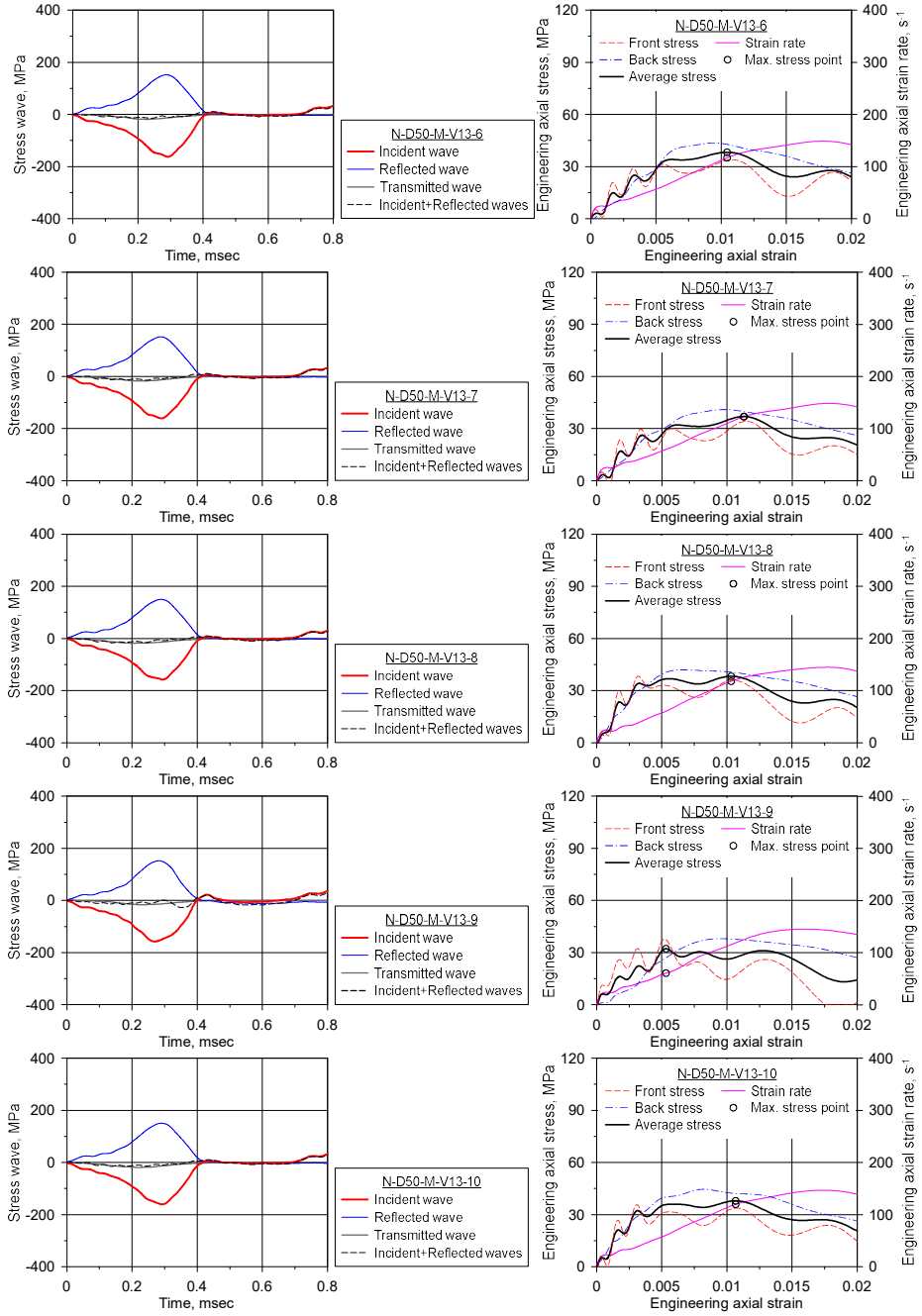

Figure B.2 Stress waves and the axial stress–strain curve of N-D50-M-V13

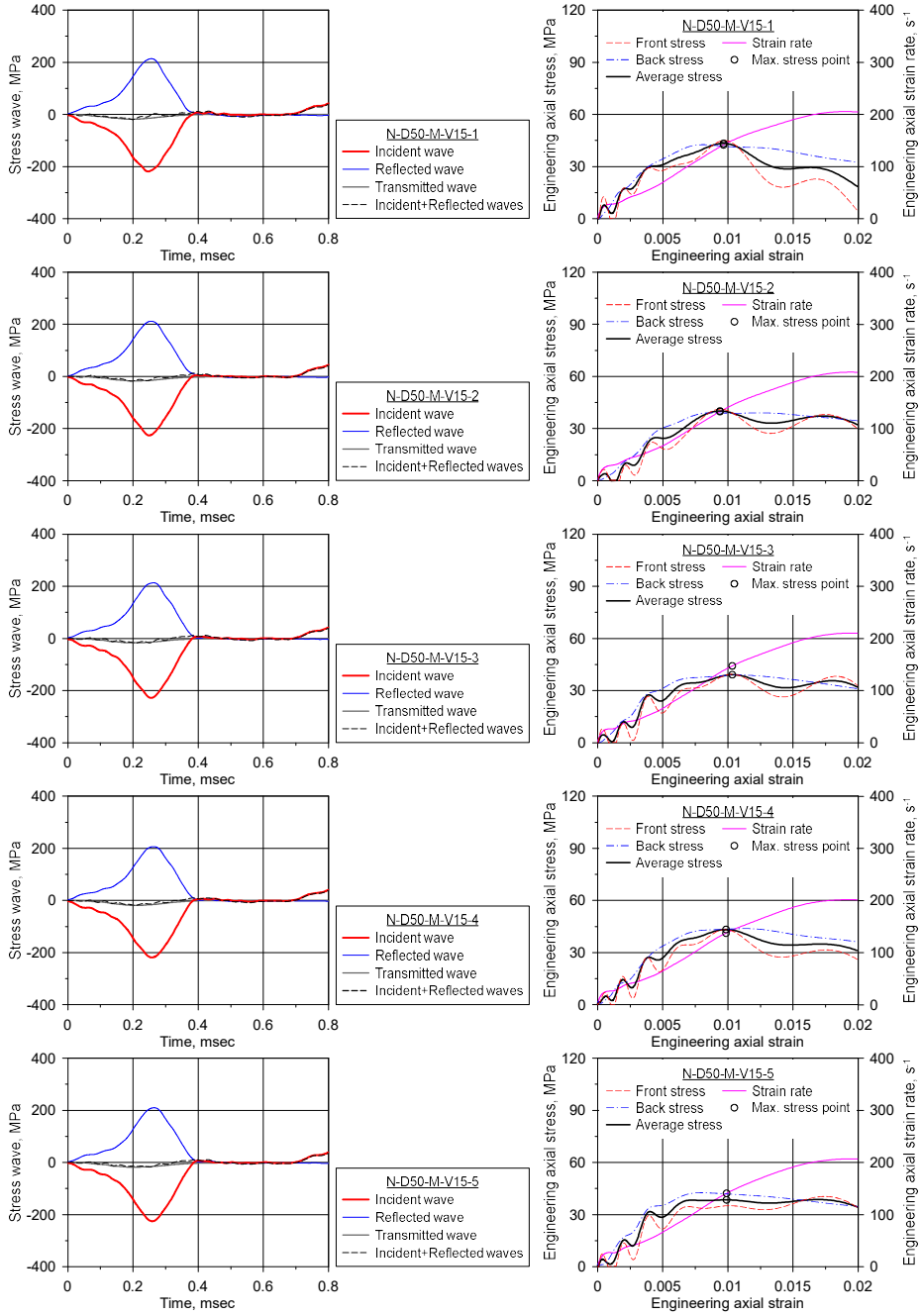
Stress wave, MPa
Time, msec
N-D50-M-V15-1
Incident wave
Reflected wave
Transmitted wave
Incident+Reflected waves
Engineering axial stress, MPa
Engineering axial strain rate, s⁻¹
Engineering axial strain
Front stress
Back stress
Average stress
Strain rate
Max. stress point
N-D50-M-V15-2
N-D50-M-V15-3
N-D50-M-V15-4
N-D50-M-V15-5

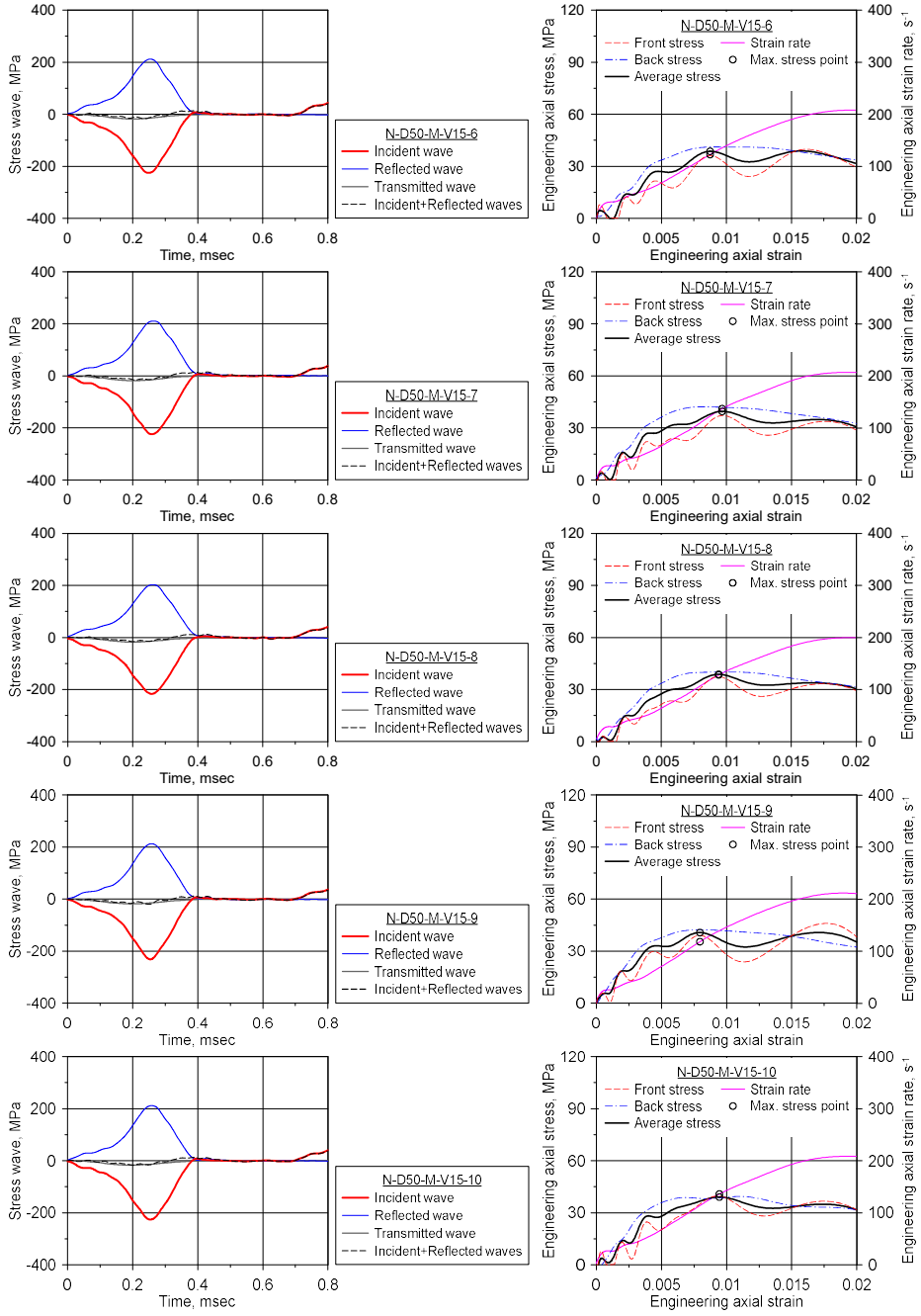

Figure B.3 Stress waves and the axial stress–strain curve of N-D50-M-V15

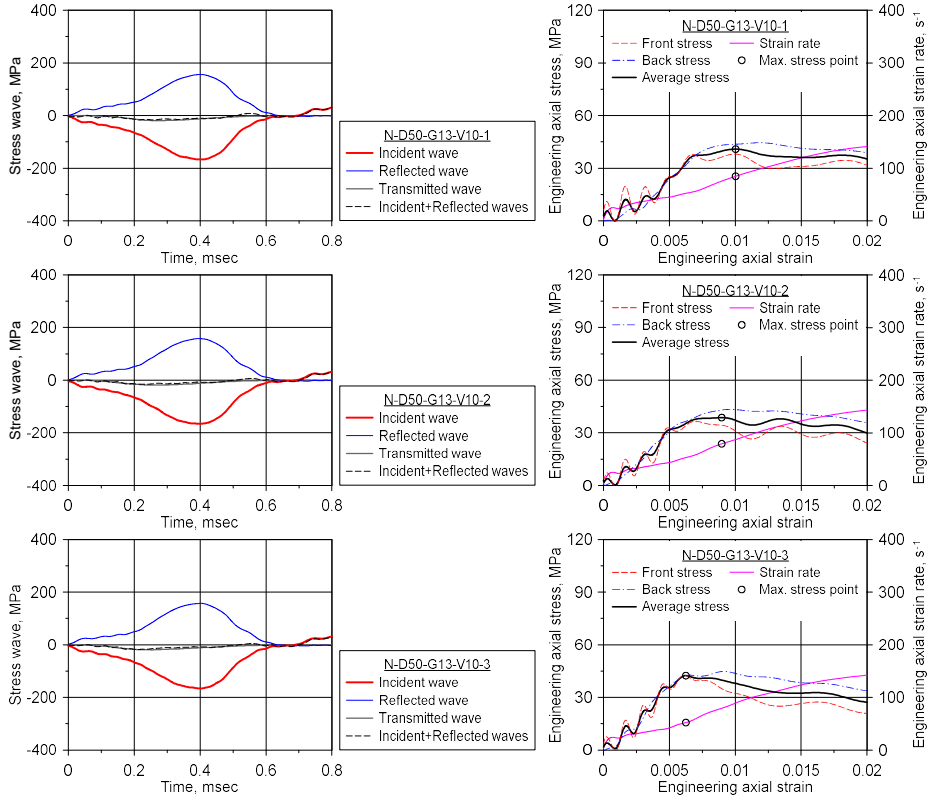
Stress wave, MPa
Time, msec
N-D50-G13-V10-1
Incident wave
Reflected wave
Transmitted wave
Incident+Reflected waves
Engineering axial stress, MPa
Engineering axial strain rate, s-1
Engineering axial strain
Front stress
Back stress
Average stress
Strain rate
Max. stress point
N-D50-G13-V10-2
N-D50-G13-V10-3

(c)

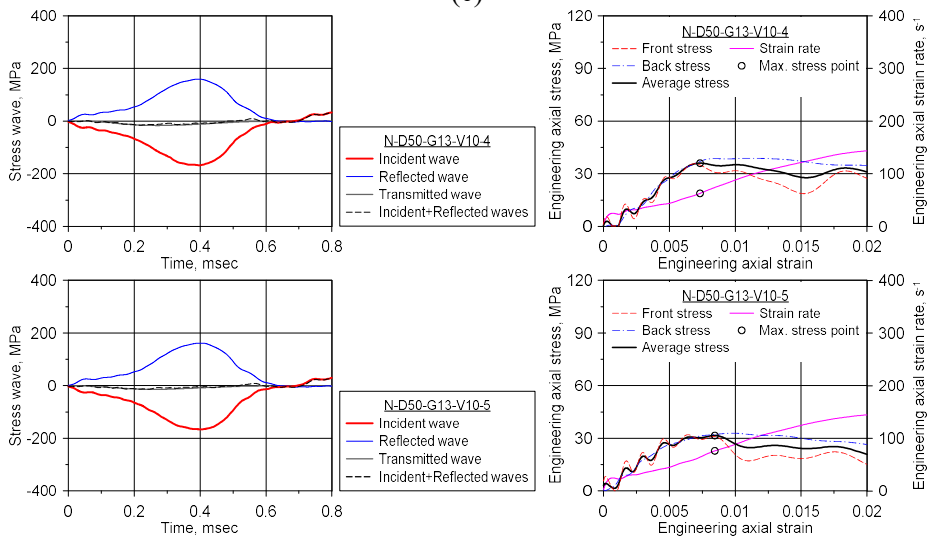
Stress wave, MPa
Time, msec
N-D50-G13-V10-4
Incident wave
Reflected wave
Transmitted wave
Incident+Reflected waves
Engineering axial stress, MPa
Engineering axial strain rate, s-1
Engineering axial strain
Front stress
Back stress
Average stress
Strain rate
Max. stress point
N-D50-G13-V10-5

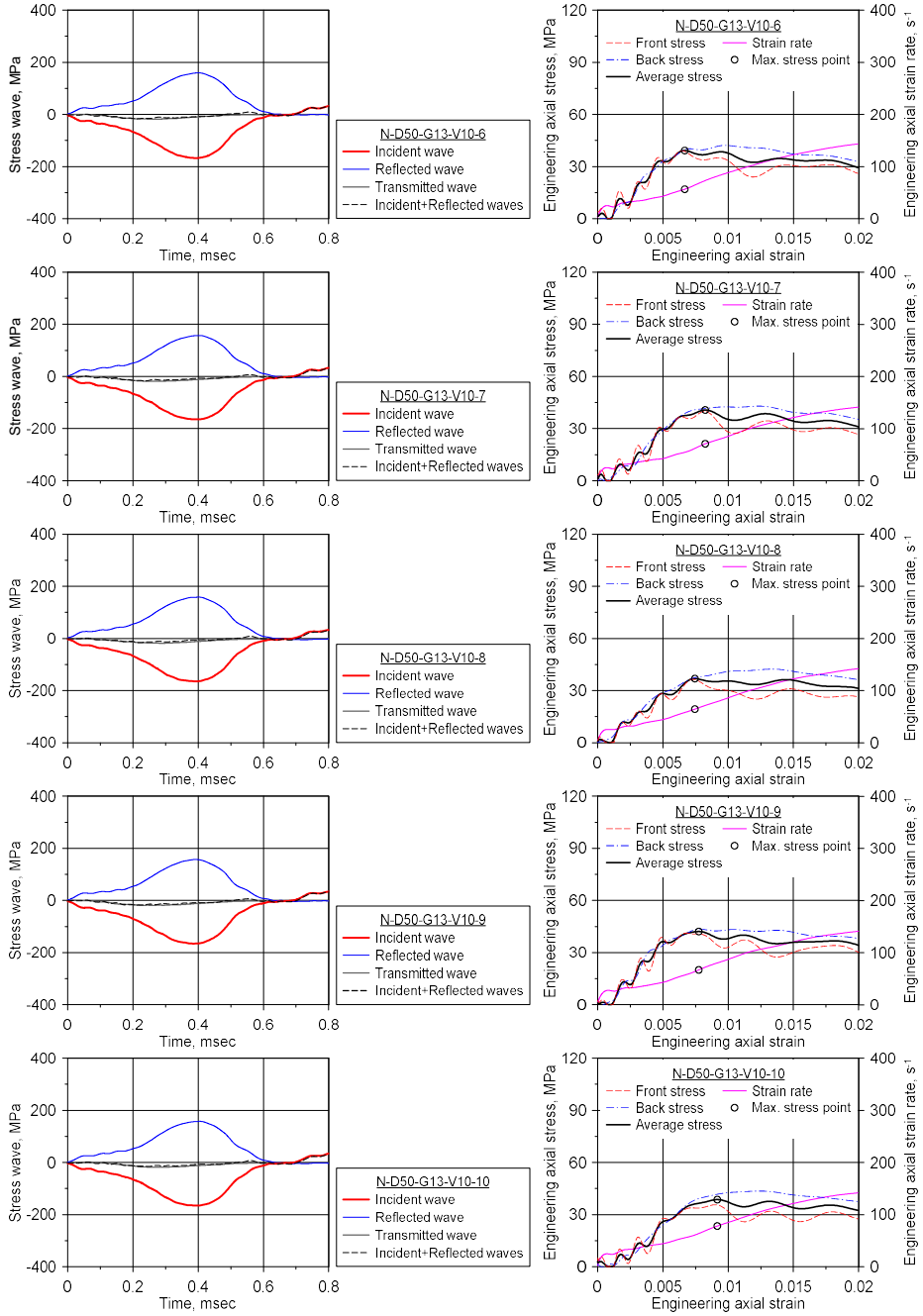

Figure B.4 Stress waves and the axial stress–strain curve of N-D50-G13-V10

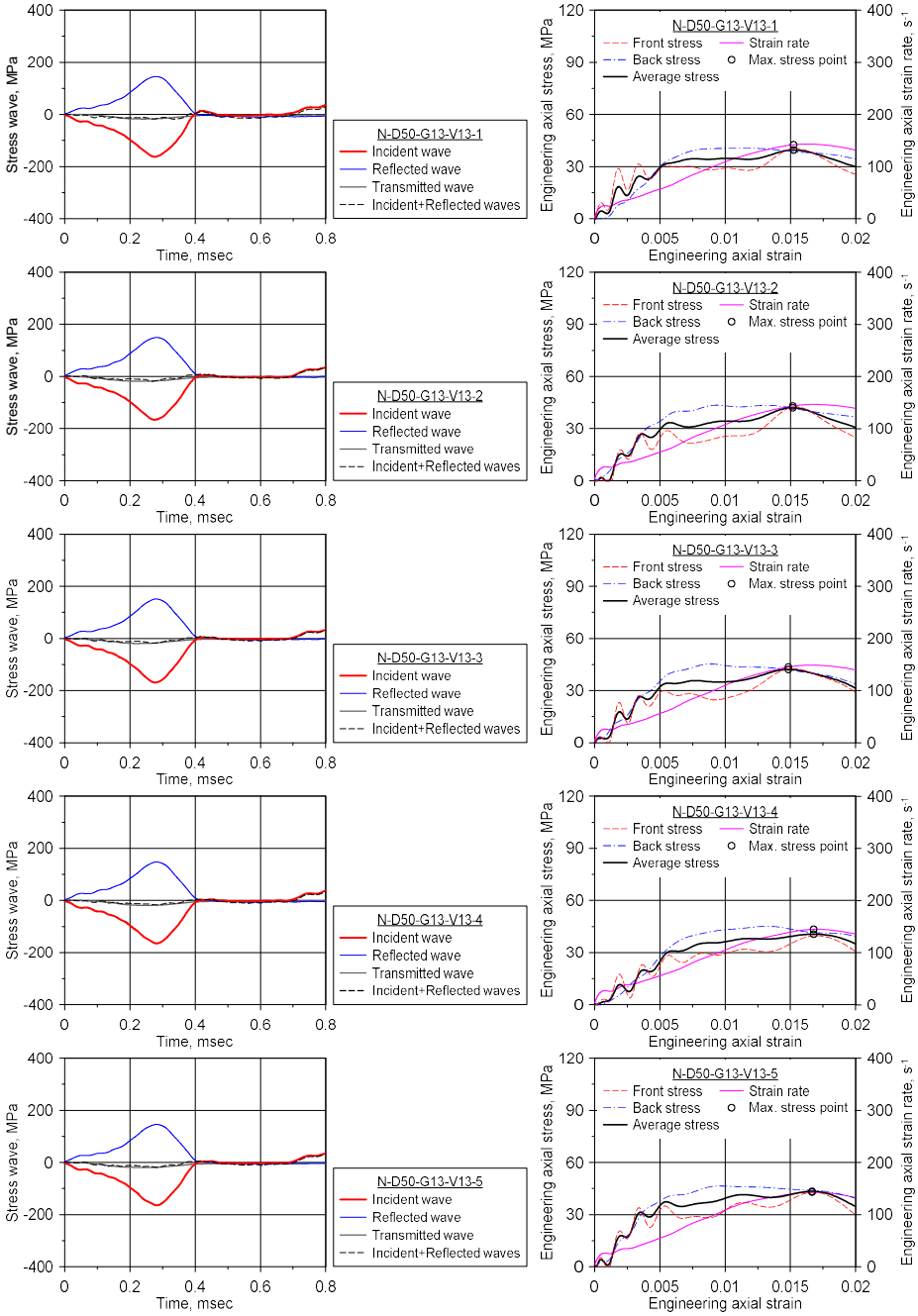
Stress wave, MPa
Time, msec
N-D50-G13-V13-1
Incident wave
Reflected wave
Transmitted wave
Incident+Reflected waves
Engineering axial stress, MPa
Engineering axial strain rate, s-1
Engineering axial strain
Front stress
Back stress
Average stress
Strain rate
Max. stress point
N-D50-G13-V13-2
N-D50-G13-V13-3
N-D50-G13-V13-4
N-D50-G13-V13-5

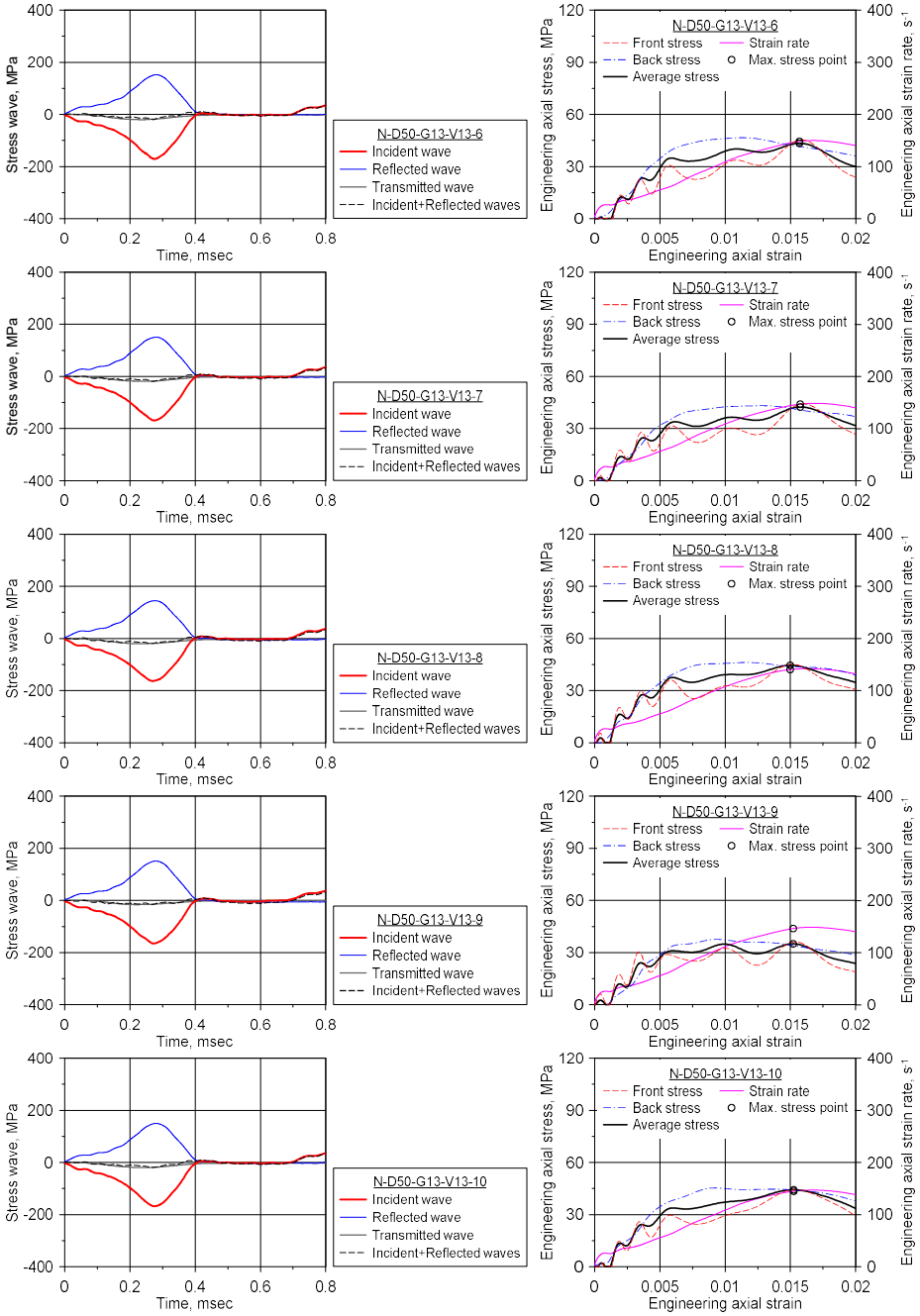

Figure B.5 Stress waves and the axial stress–strain curve of N-D50-G13-V13

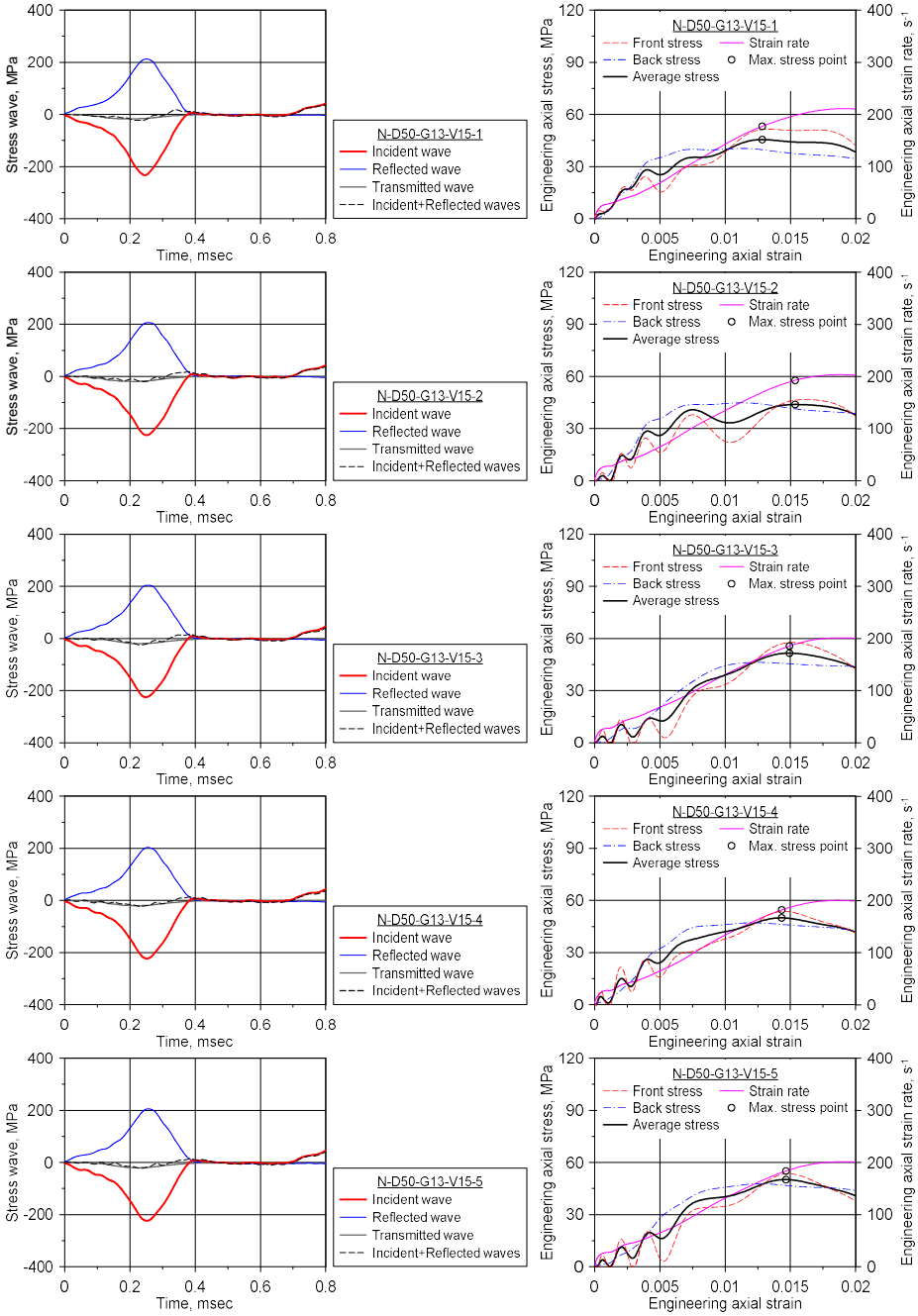
Stress wave, MPa
Time, msec
N-D50-G13-V15-1
Incident wave
Reflected wave
Transmitted wave
Incident+Reflected waves
Engineering axial stress, MPa
Engineering axial strain
Engineering axial strain rate, s-1
Front stress
Back stress
Average stress
Strain rate
Max. stress point
N-D50-G13-V15-2
N-D50-G13-V15-3
N-D50-G13-V15-4
N-D50-G13-V15-5

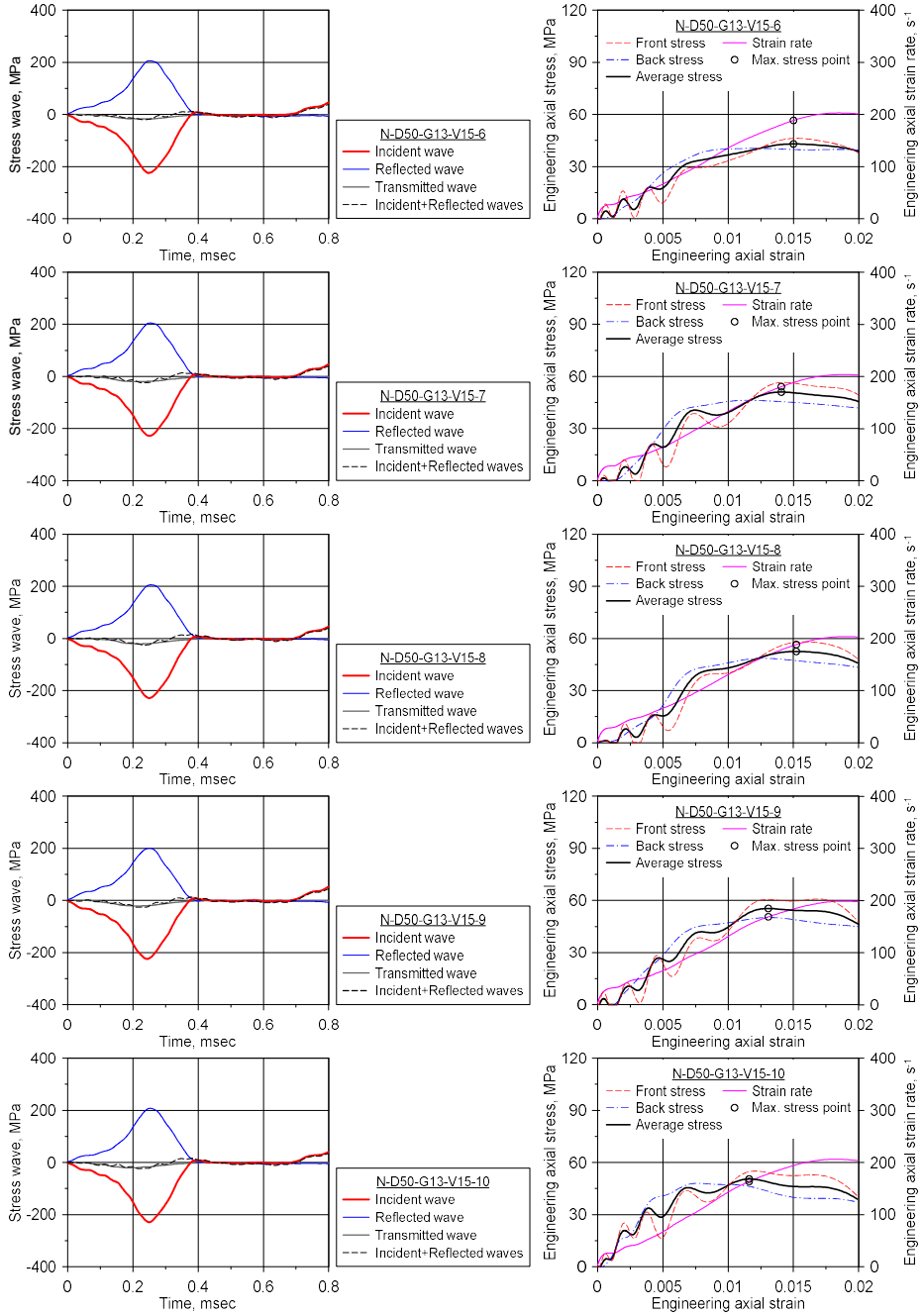

Figure B.6 Stress waves and the axial stress–strain curve of N-D50-G13-V15

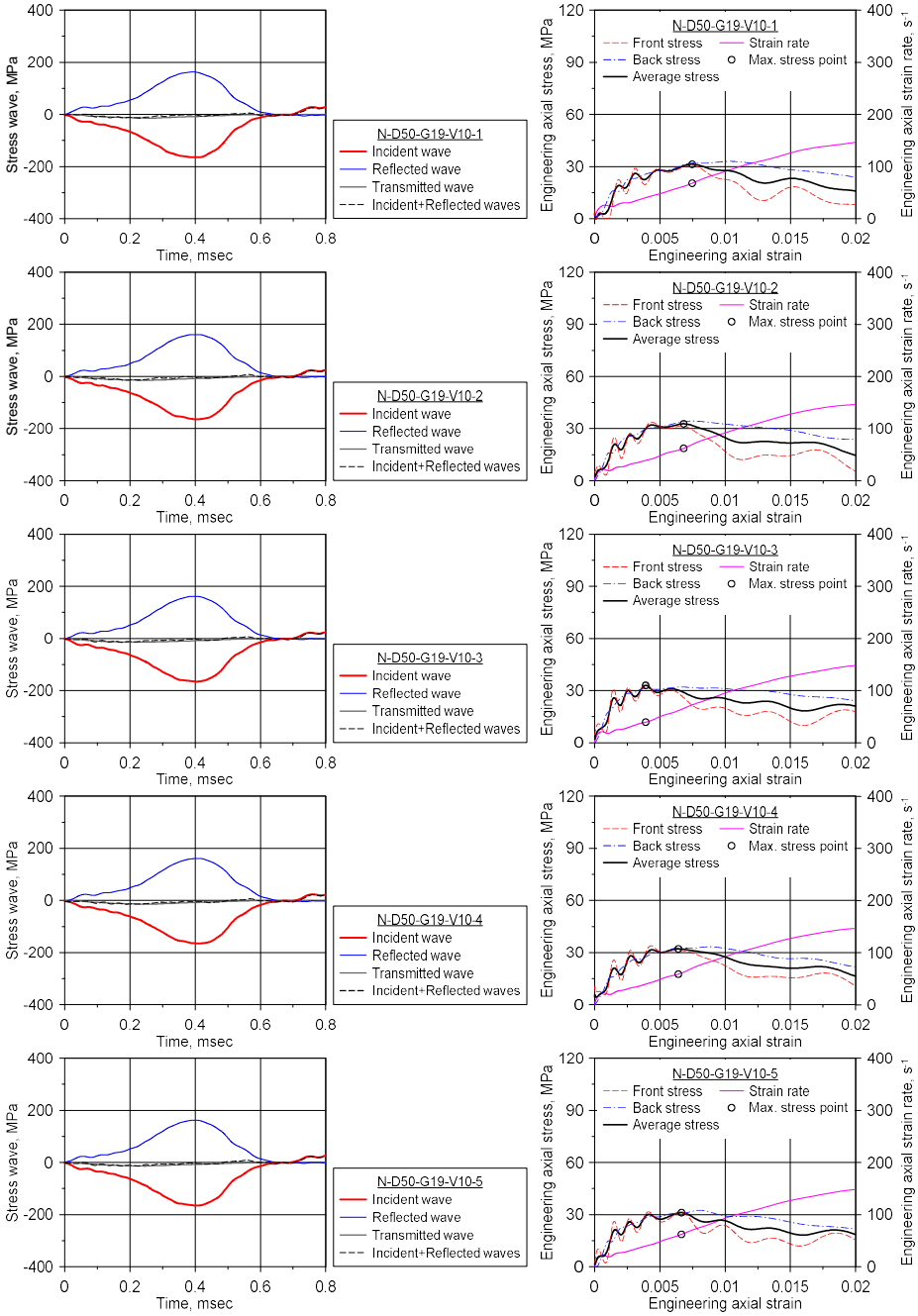
Stress wave, MPa
Time, msec
N-D50-G19-V10-1
Incident wave
Reflected wave
Transmitted wave
Incident+Reflected waves
Engineering axial stress, MPa
Engineering axial strain
Engineering axial strain rate, s-1
Front stress
Back stress
Average stress
Strain rate
Max. stress point
N-D50-G19-V10-2
N-D50-G19-V10-3
N-D50-G19-V10-4
N-D50-G19-V10-5

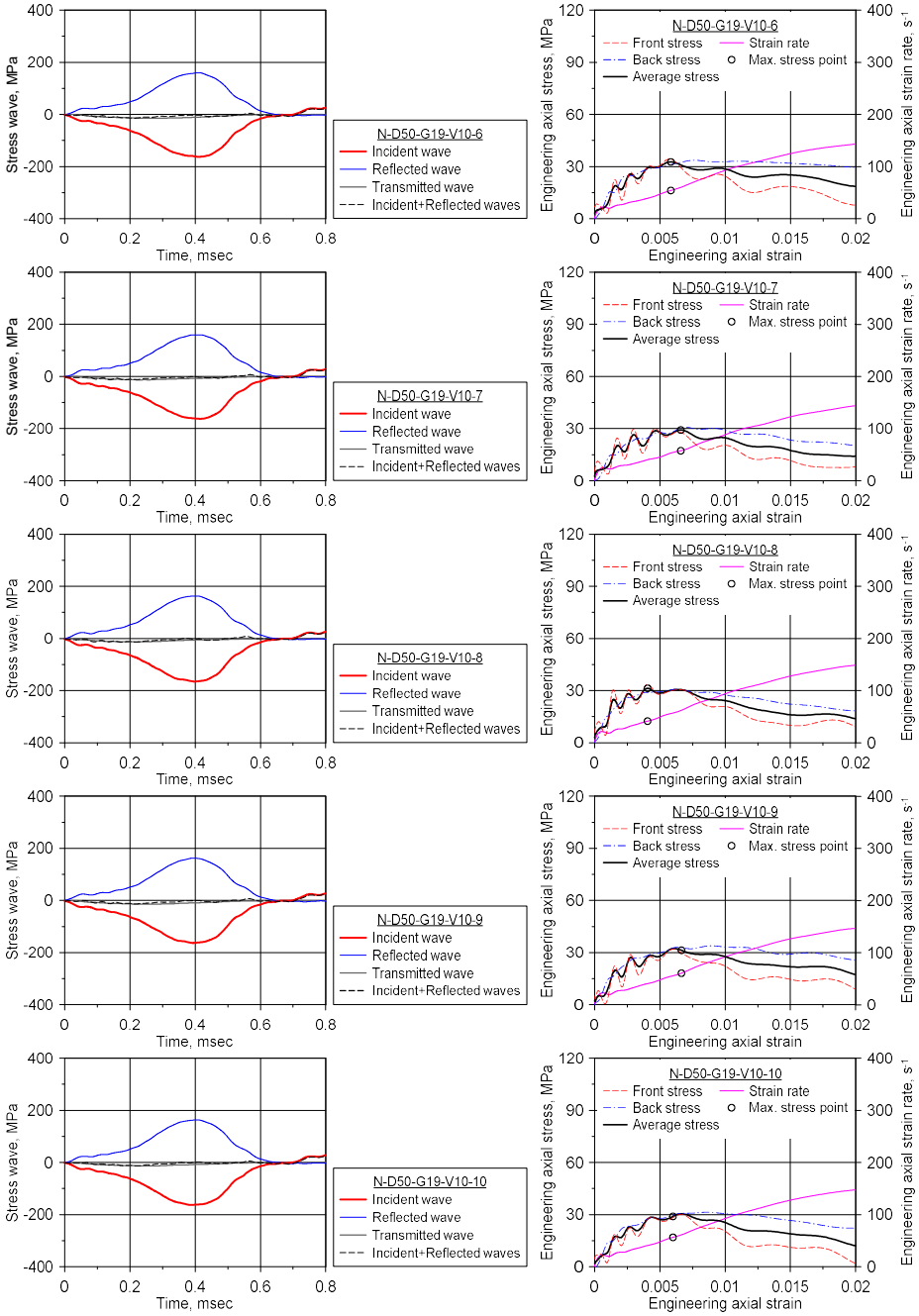

Figure B.7 Stress waves and the axial stress–strain curve of N-D50-G19-V10

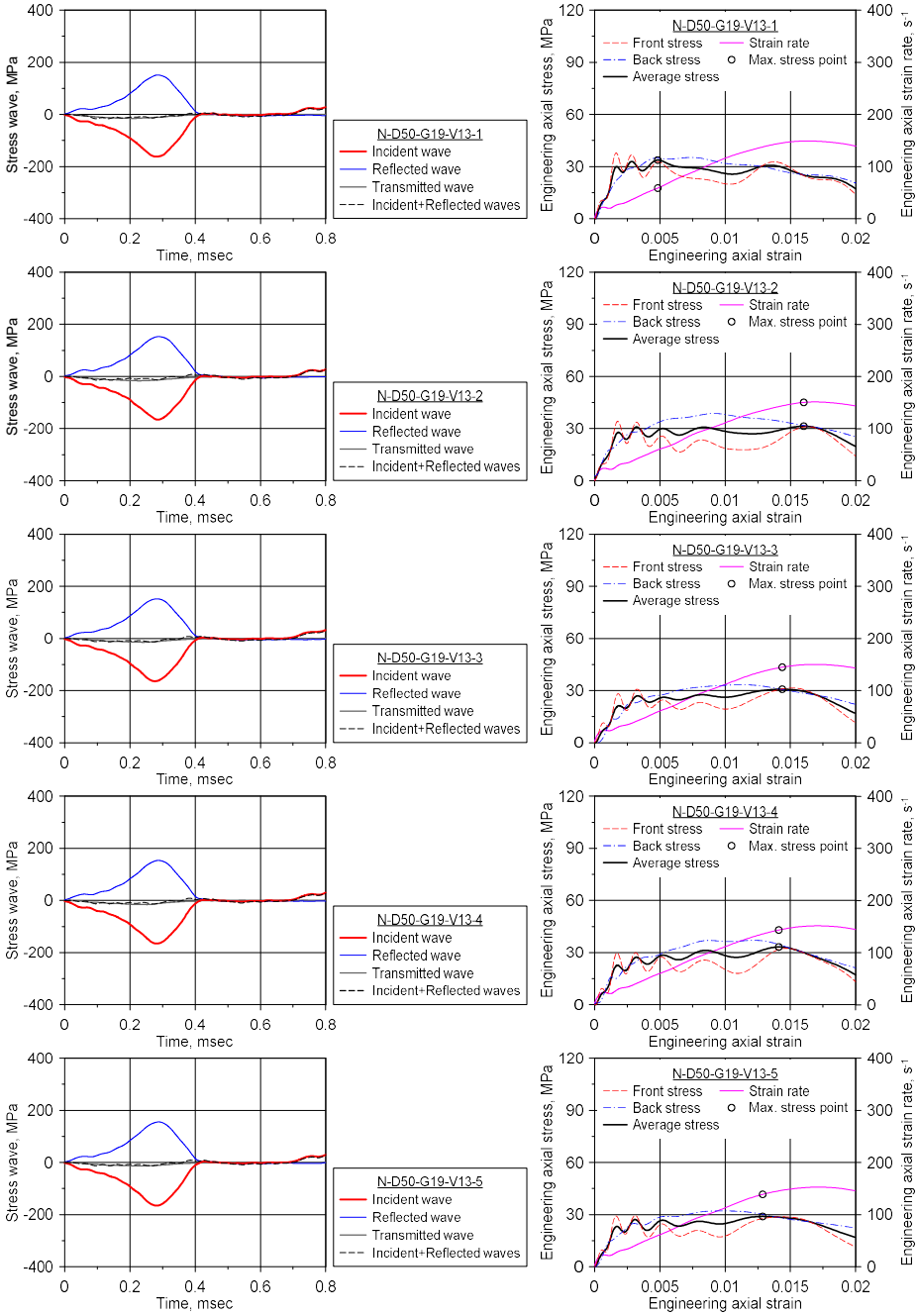
Stress wave, MPa
Time, msec
N-D50-G19-V13-1
Incident wave
Reflected wave
Transmitted wave
Incident+Reflected waves
Engineering axial stress, MPa
Engineering axial strain
Engineering axial strain rate, s-1
Front stress
Back stress
Average stress
Strain rate
Max. stress point
N-D50-G19-V13-2
N-D50-G19-V13-3
N-D50-G19-V13-4
N-D50-G19-V13-5

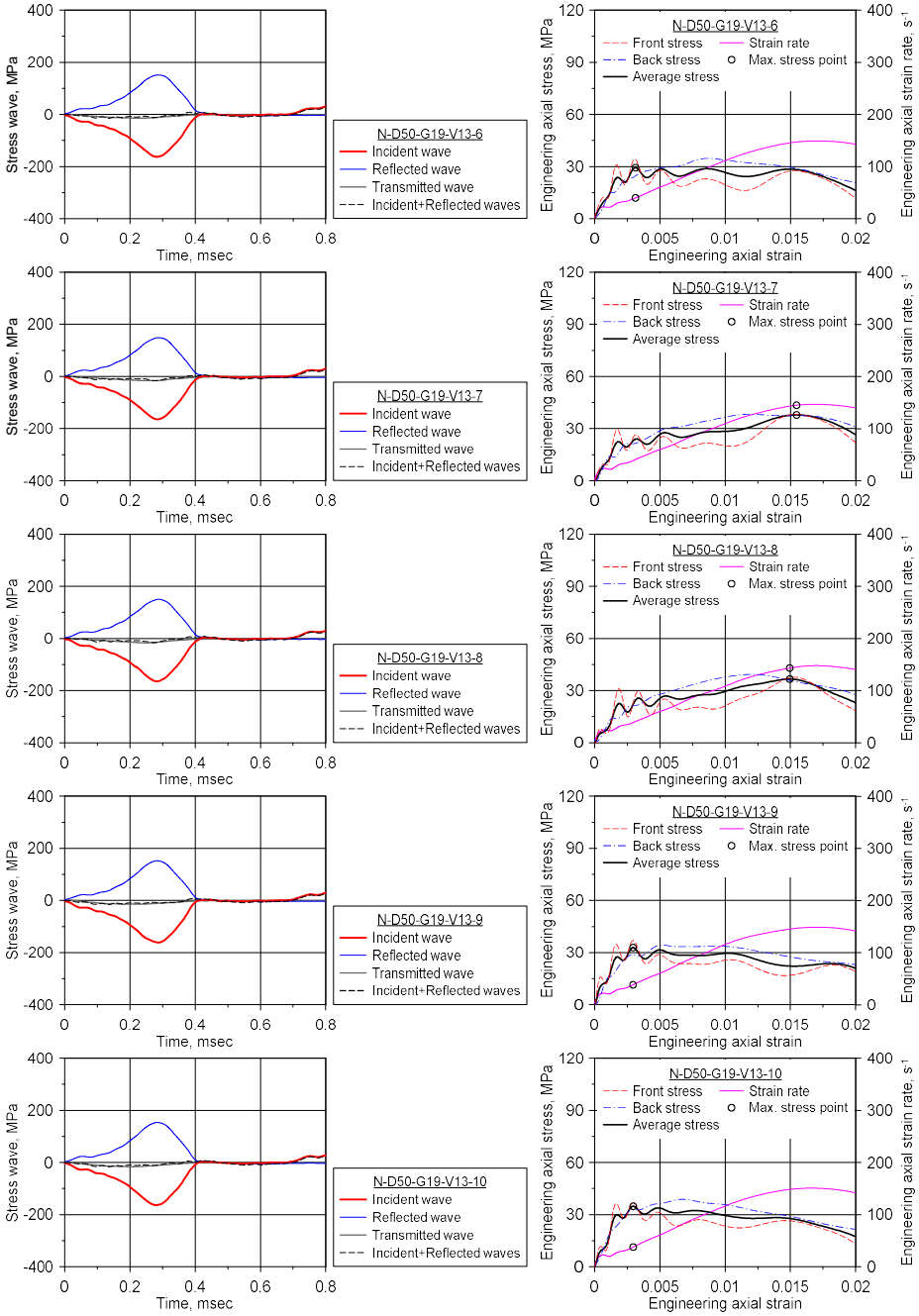

Figure B.8 Stress waves and the axial stress–strain curve of N-D50-G19-V13

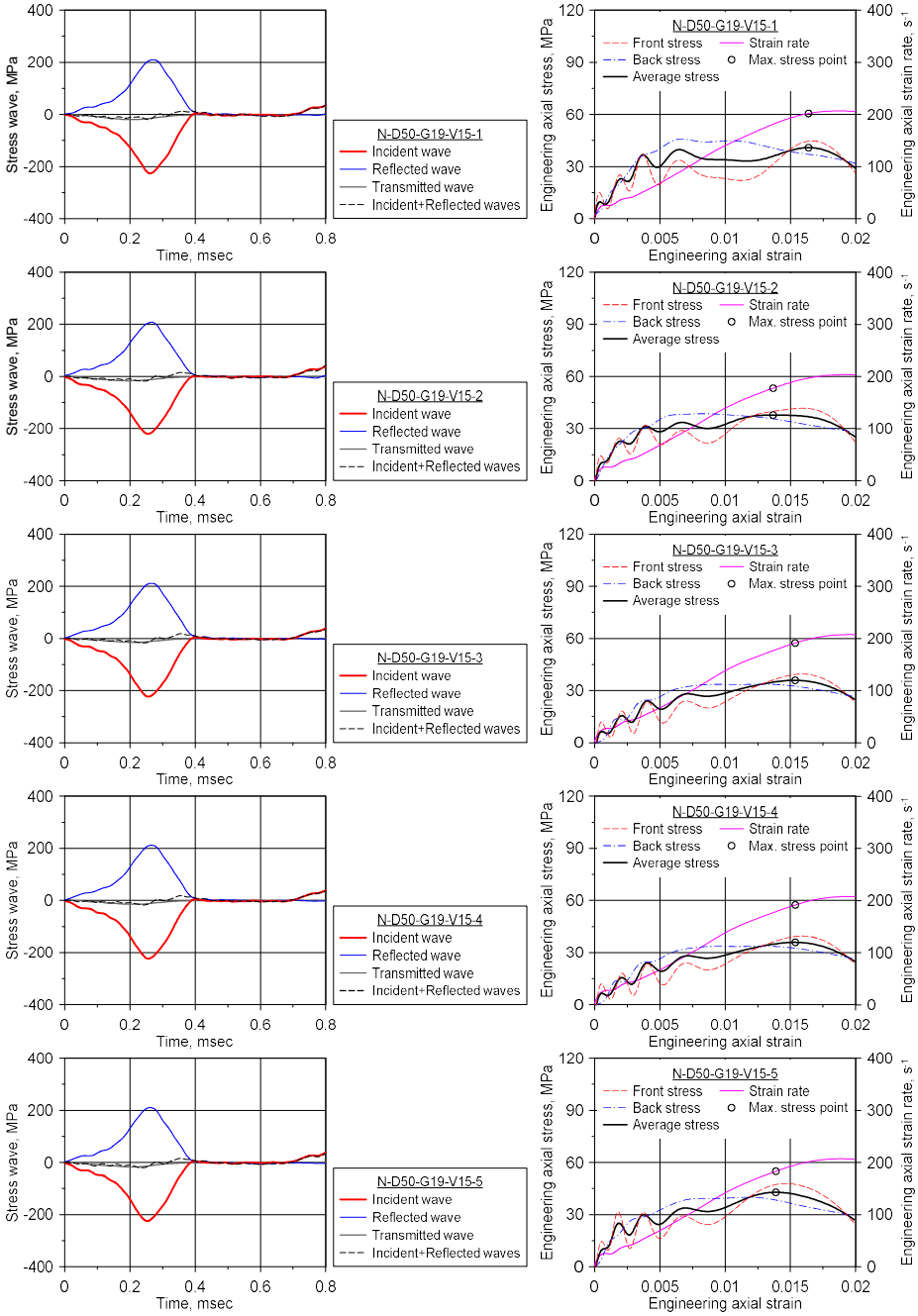
Stress wave, MPa
Time, msec
N-D50-G19-V15-1
Incident wave
Reflected wave
Transmitted wave
Incident+Reflected waves
Engineering axial stress, MPa
Engineering axial strain rate, s-1
Engineering axial strain
Front stress
Back stress
Average stress
Strain rate
Max. stress point
N-D50-G19-V15-2
N-D50-G19-V15-3
N-D50-G19-V15-4
N-D50-G19-V15-5

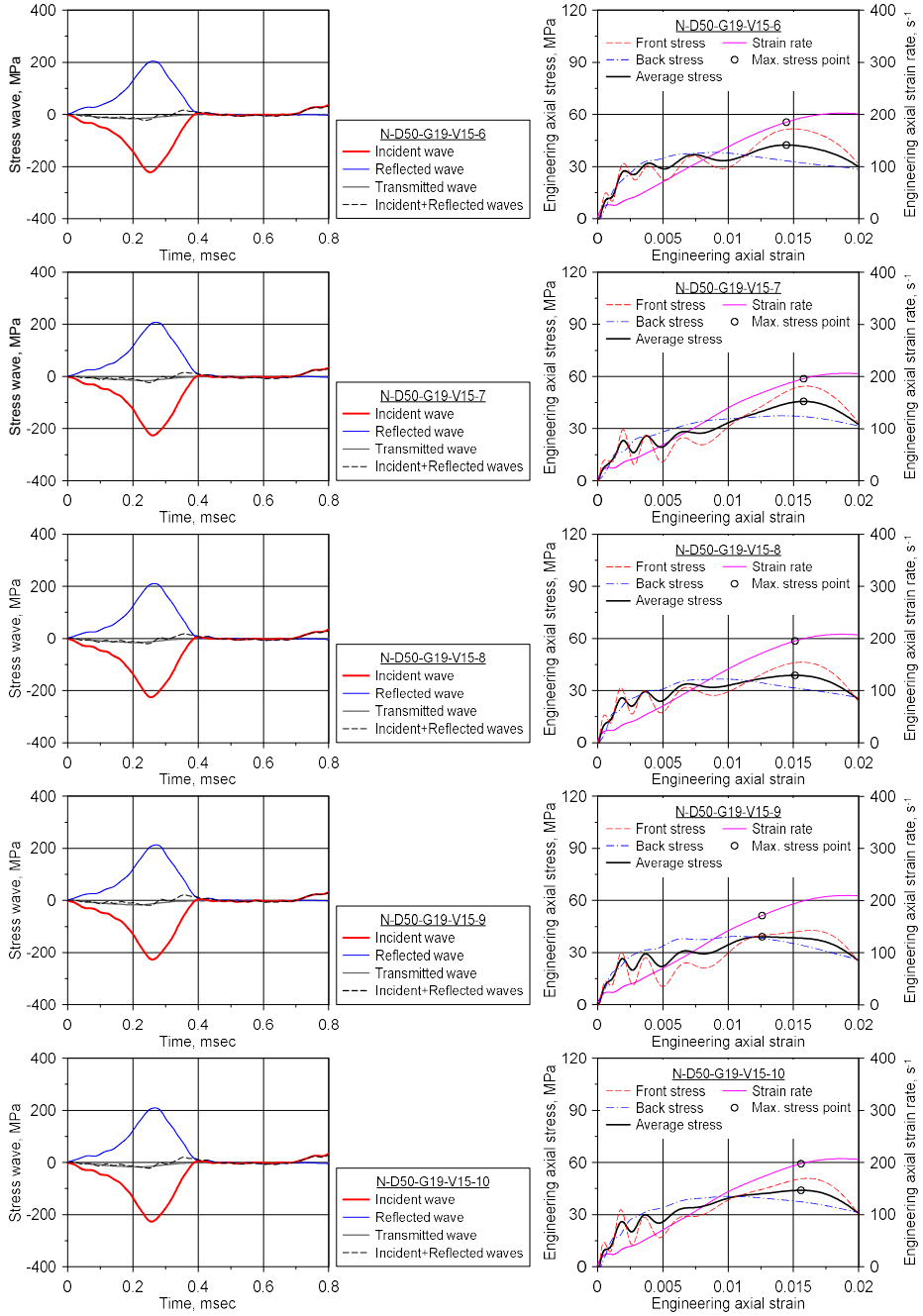

Figure B.9 Stress waves and the axial stress–strain curve of N-D50-G19-V15

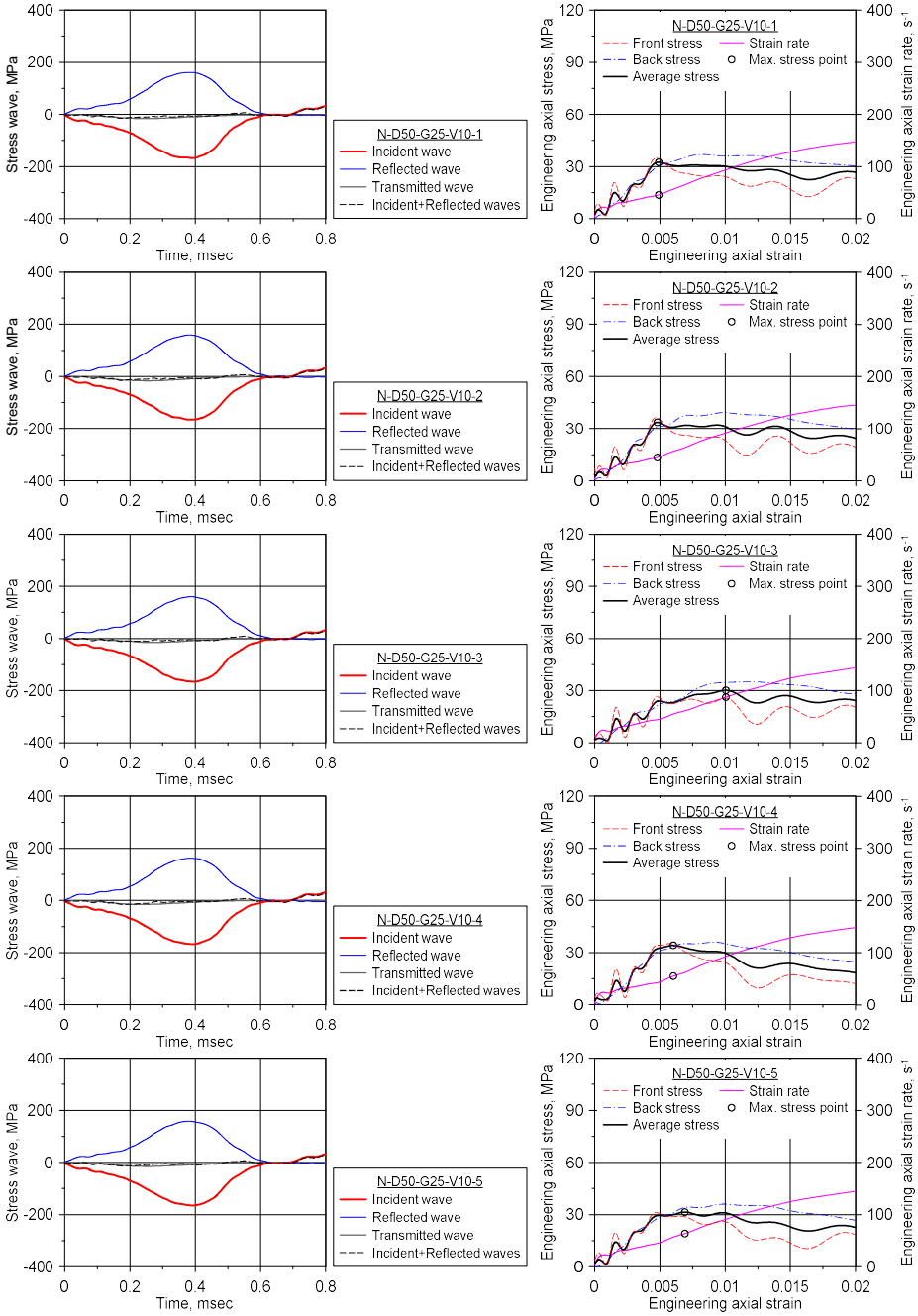
Stress wave, MPa
Time, msec
N-D50-G25-V10-1
Incident wave
Reflected wave
Transmitted wave
Incident+Reflected waves
Engineering axial stress, MPa
Engineering axial strain
Engineering axial strain rate, s-1
Front stress
Back stress
Average stress
Strain rate
Max. stress point
N-D50-G25-V10-2
N-D50-G25-V10-3
N-D50-G25-V10-4
N-D50-G25-V10-5

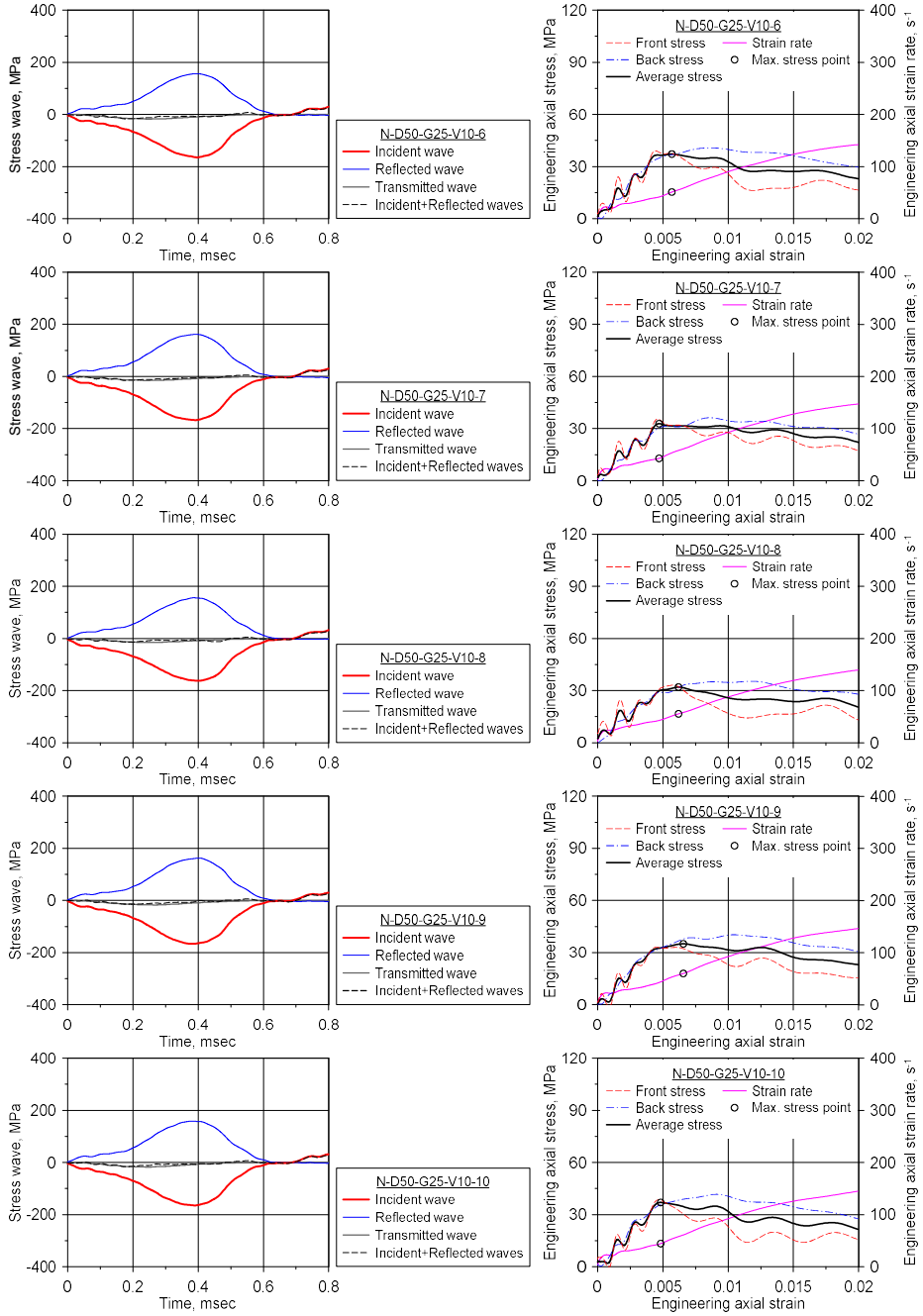

Figure B.10 Stress waves and the axial stress–strain curve of N-D50-G25-V10

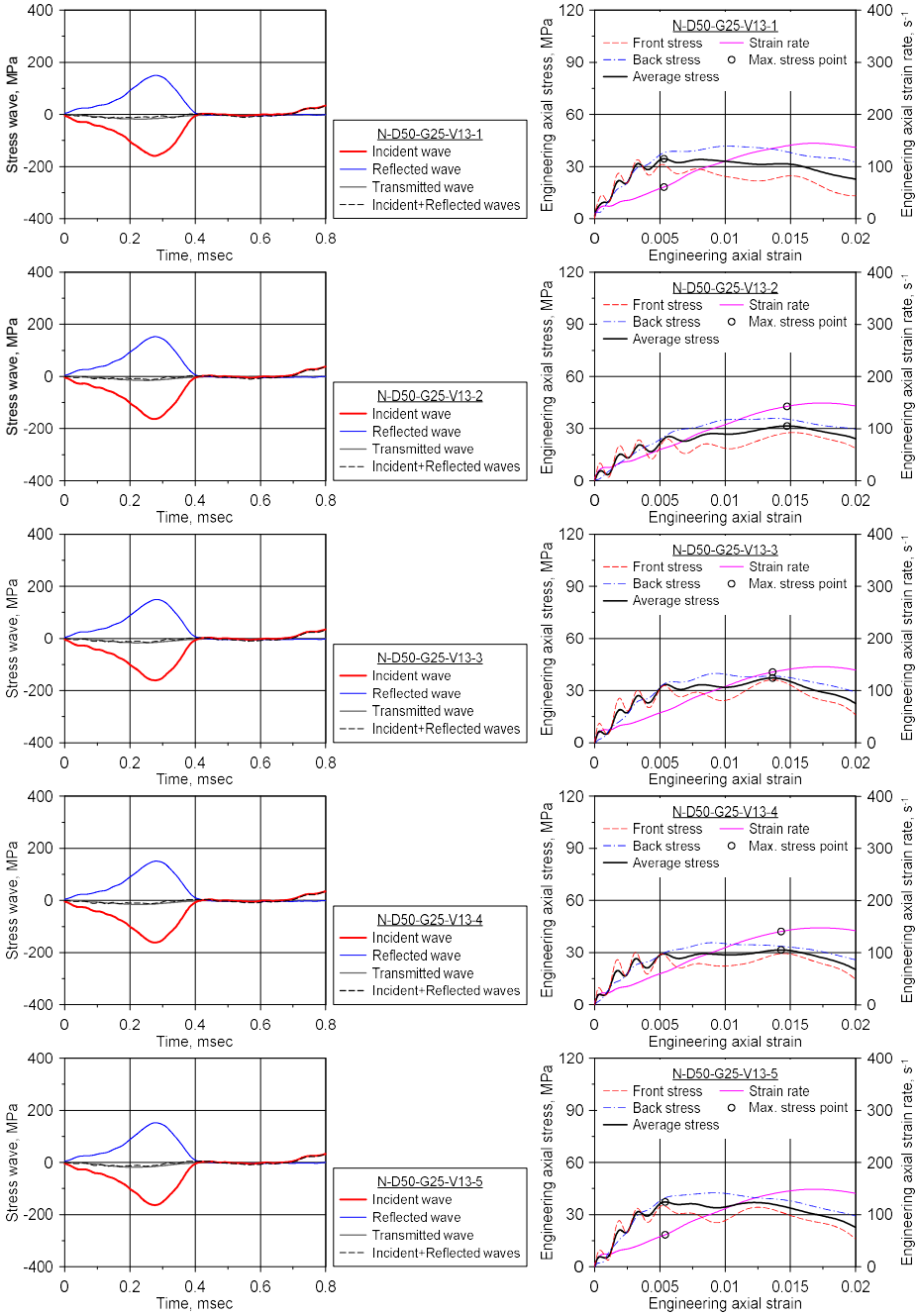
Stress wave, MPa
Time, msec
N-D50-G25-V13-1
Incident wave
Reflected wave
Transmitted wave
Incident+Reflected waves
Engineering axial stress, MPa
Engineering axial strain
Engineering axial strain rate, s-1
Front stress
Back stress
Average stress
Strain rate
Max. stress point
N-D50-G25-V13-2
N-D50-G25-V13-3
N-D50-G25-V13-4
N-D50-G25-V13-5

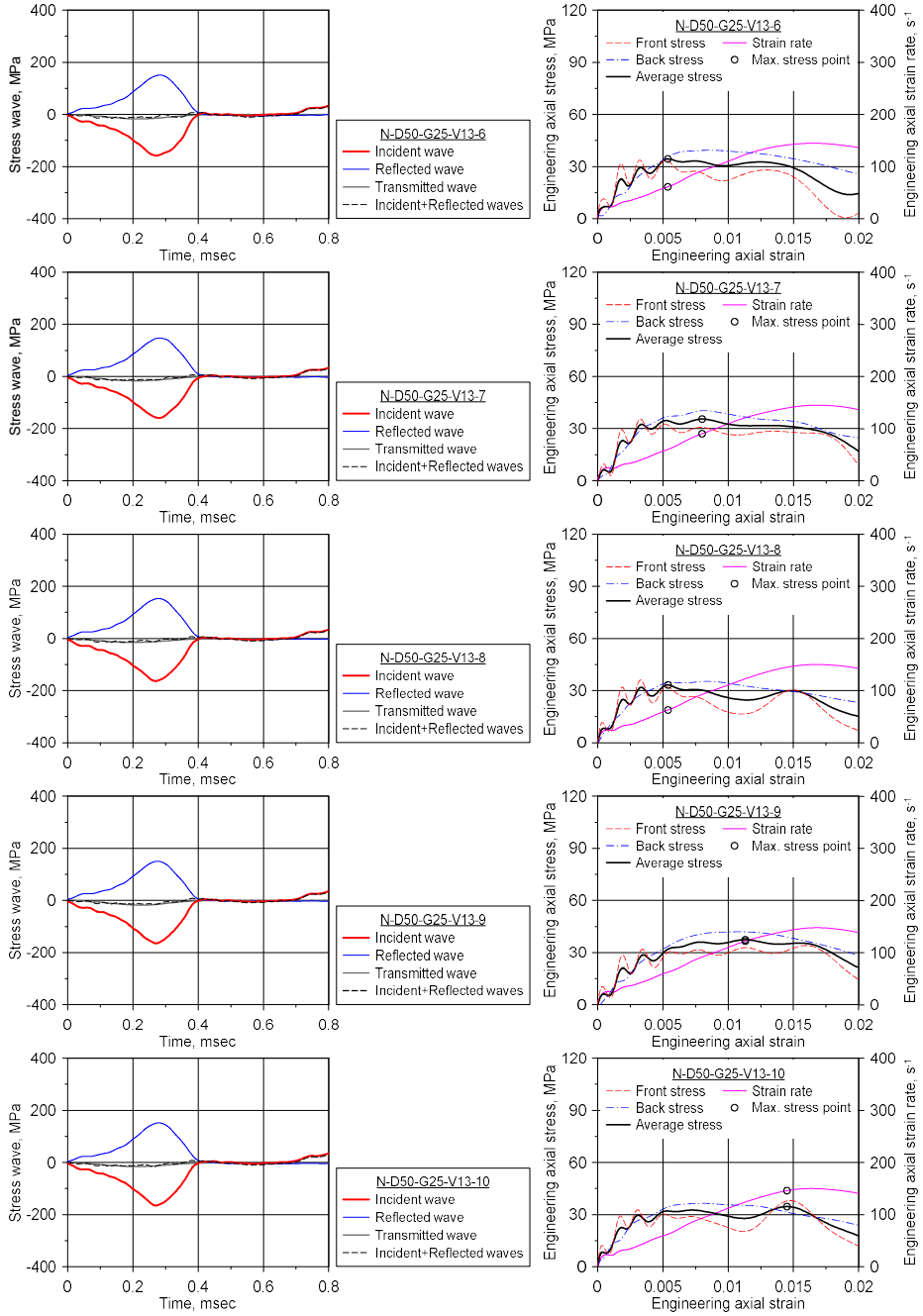

Figure B.11 Stress waves and the axial stress–strain curve of N-D50-G25-V13

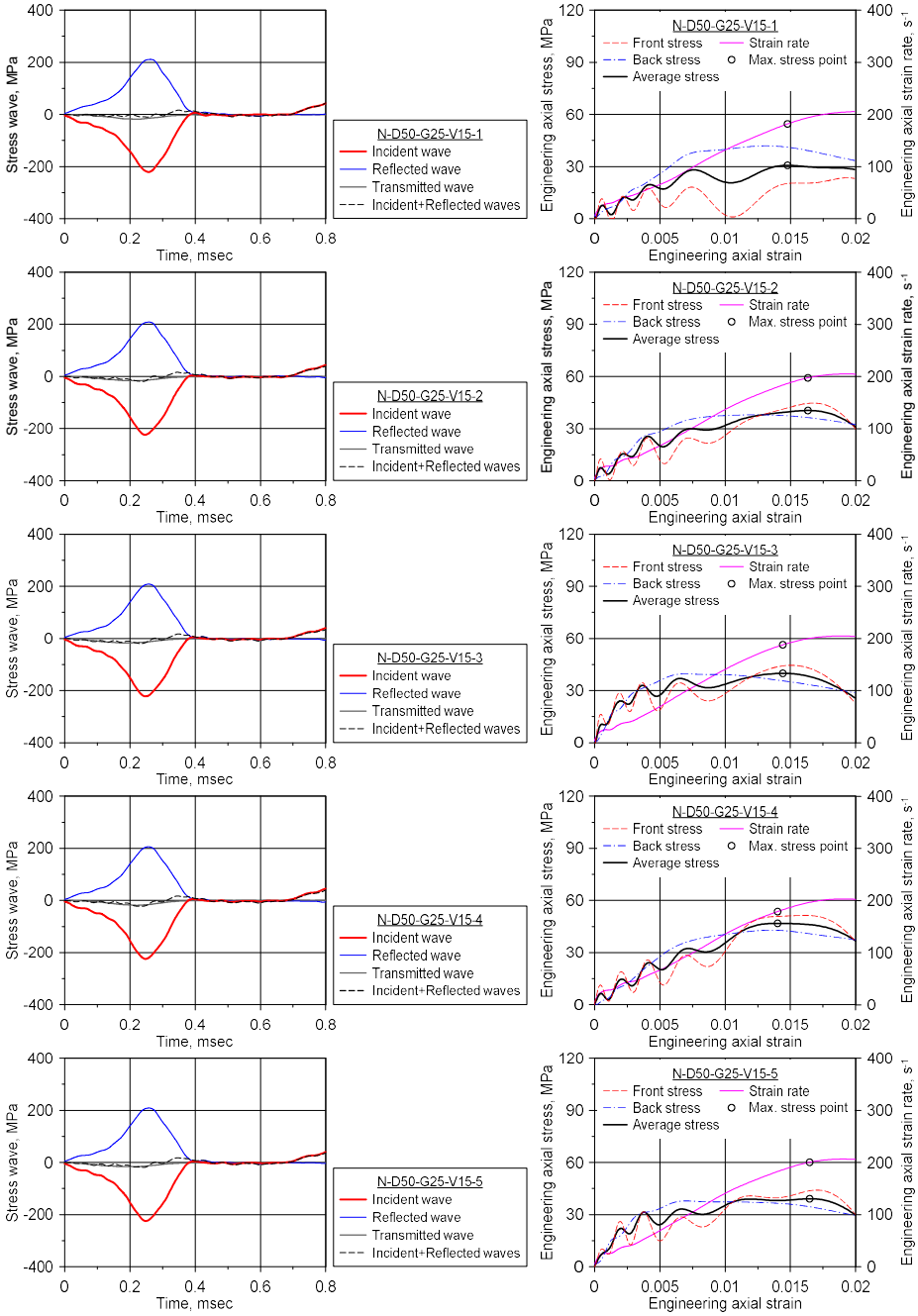
Stress wave, MPa
Time, msec
N-D50-G25-V15-1
Incident wave
Reflected wave
Transmitted wave
Incident+Reflected waves
Engineering axial stress, MPa
Engineering axial strain rate, s-1
Engineering axial strain
Front stress
Back stress
Average stress
Strain rate
Max. stress point
N-D50-G25-V15-2
N-D50-G25-V15-3
N-D50-G25-V15-4
N-D50-G25-V15-5

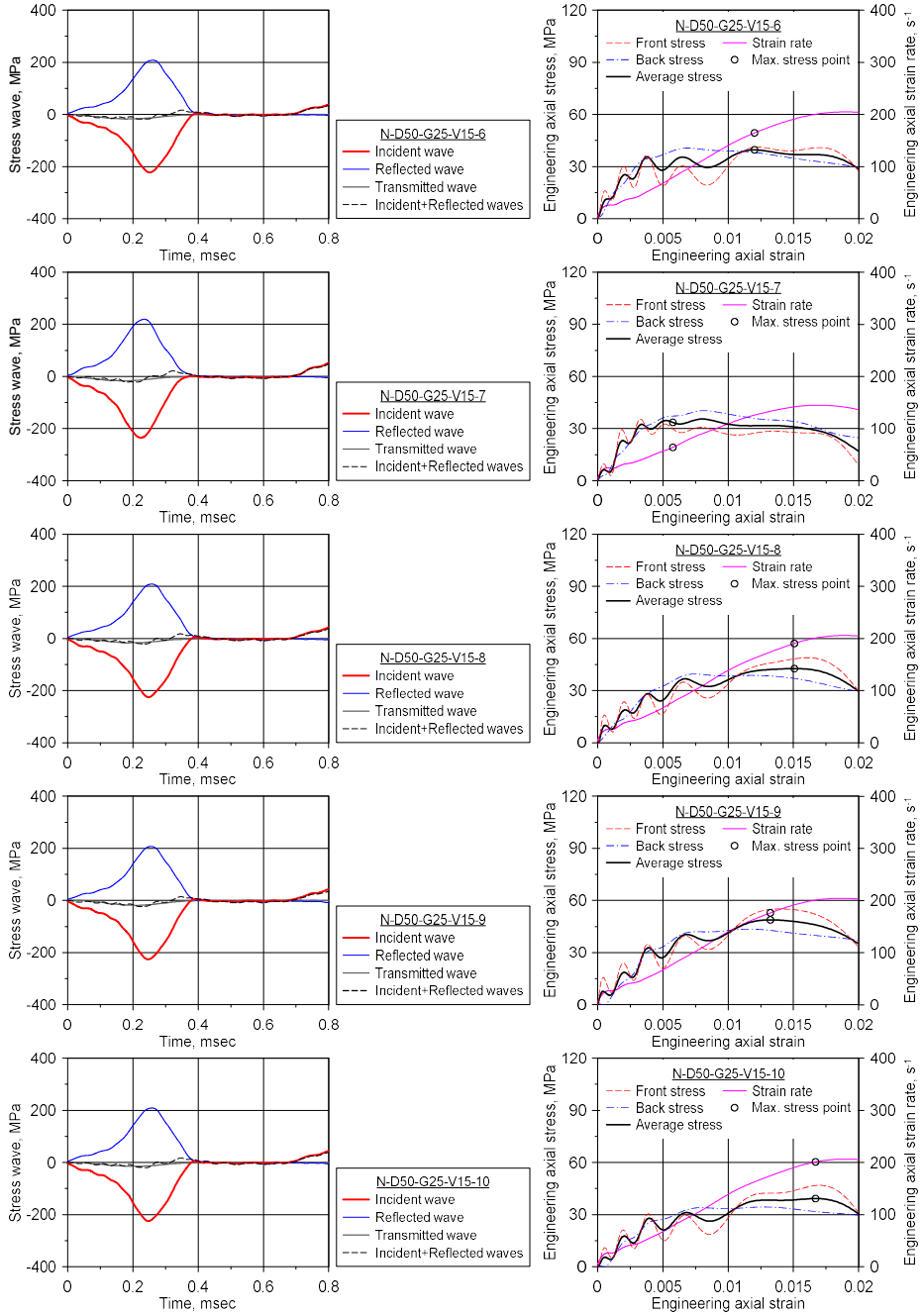

Figure B.12 Stress waves and the axial stress–strain curve of N-D50-G25-V15

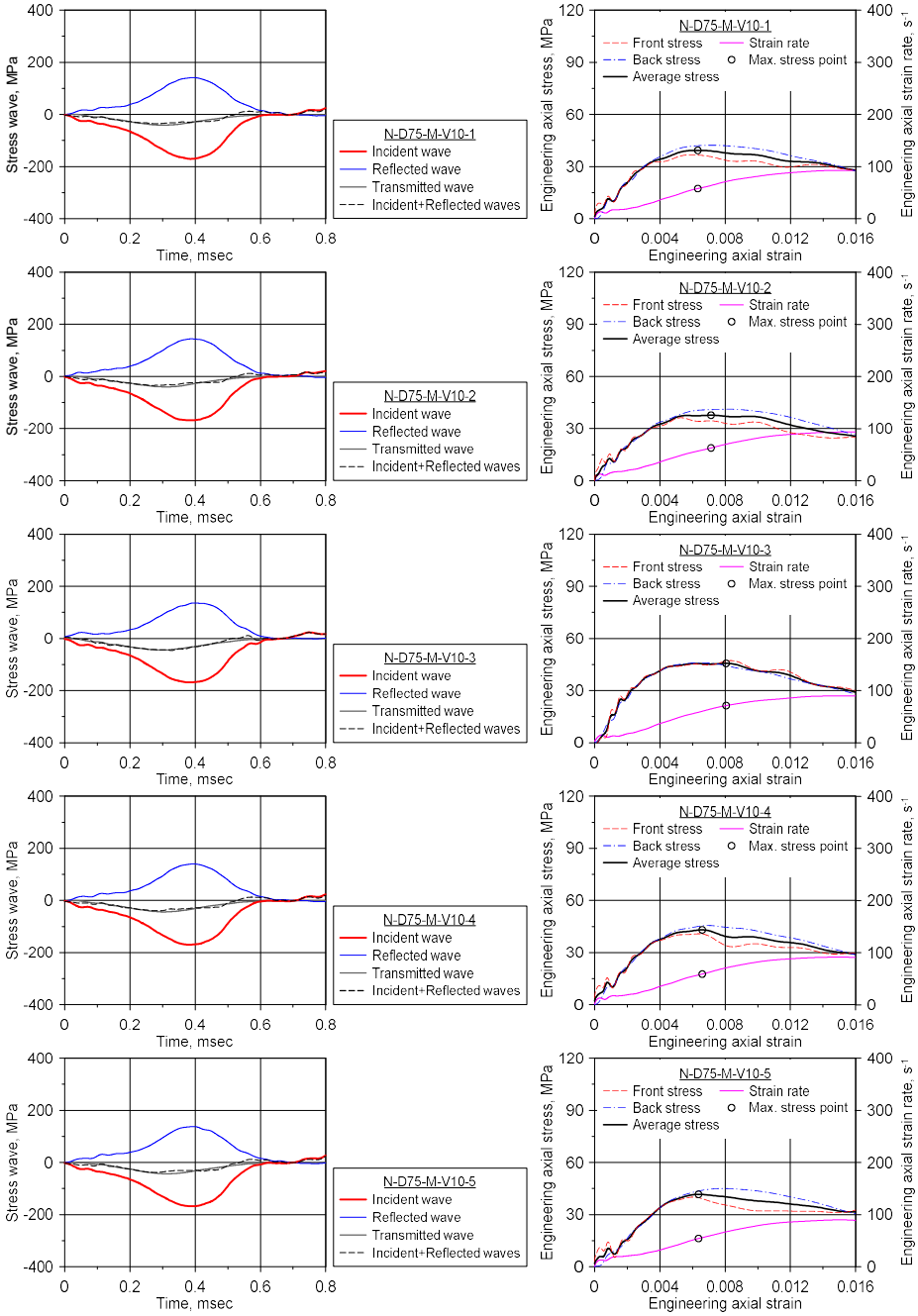
Stress wave, MPa
Time, msec
N-D75-M-V10-1
Incident wave
Reflected wave
Transmitted wave
Incident+Reflected waves
Engineering axial stress, MPa
Engineering axial strain rate, s-1
Engineering axial strain
Front stress
Back stress
Average stress
Strain rate
Max. stress point
N-D75-M-V10-2
N-D75-M-V10-3
N-D75-M-V10-4
N-D75-M-V10-5

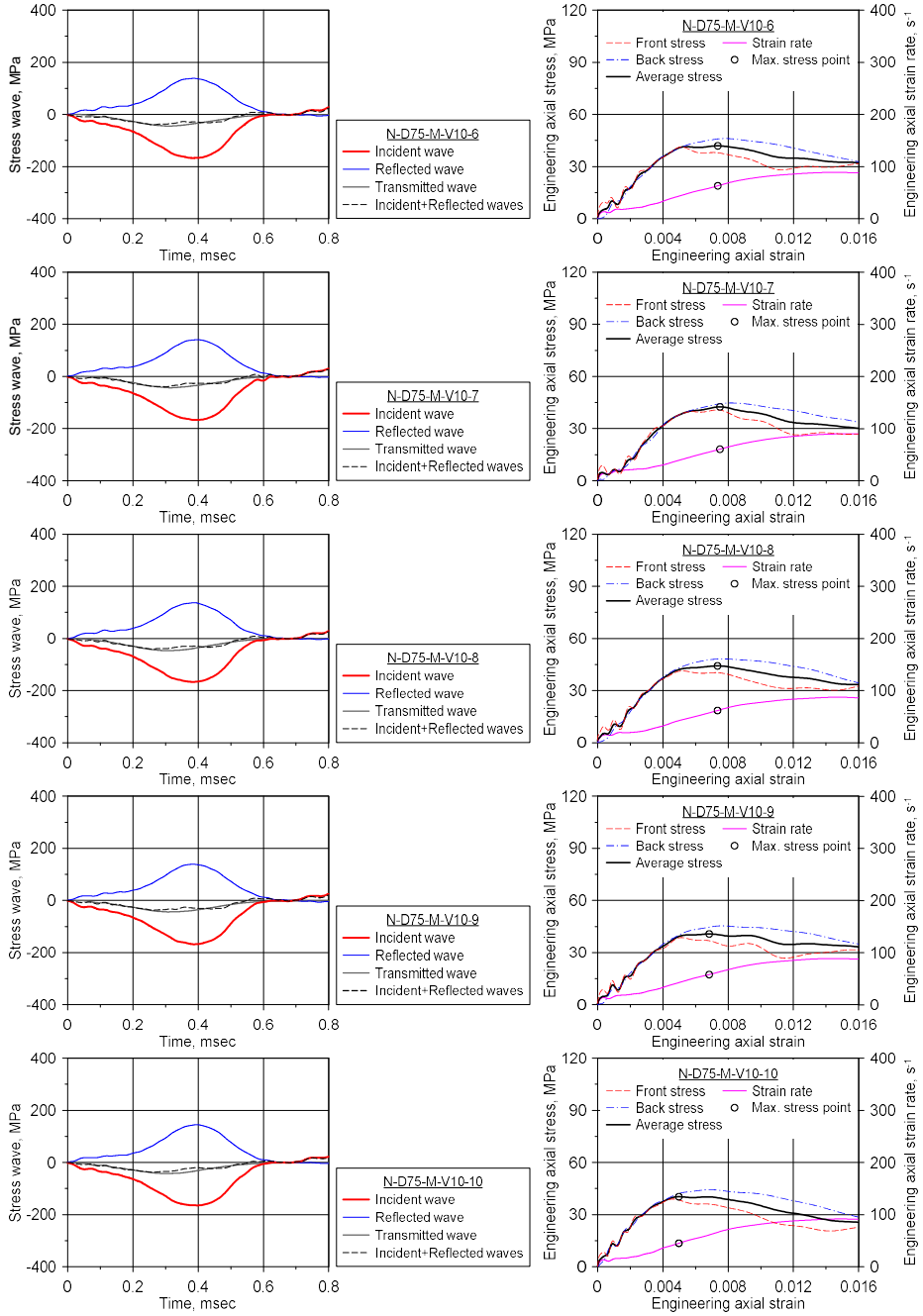

Figure B.13 Stress waves and the axial stress–strain curve of N-D75-M-V10

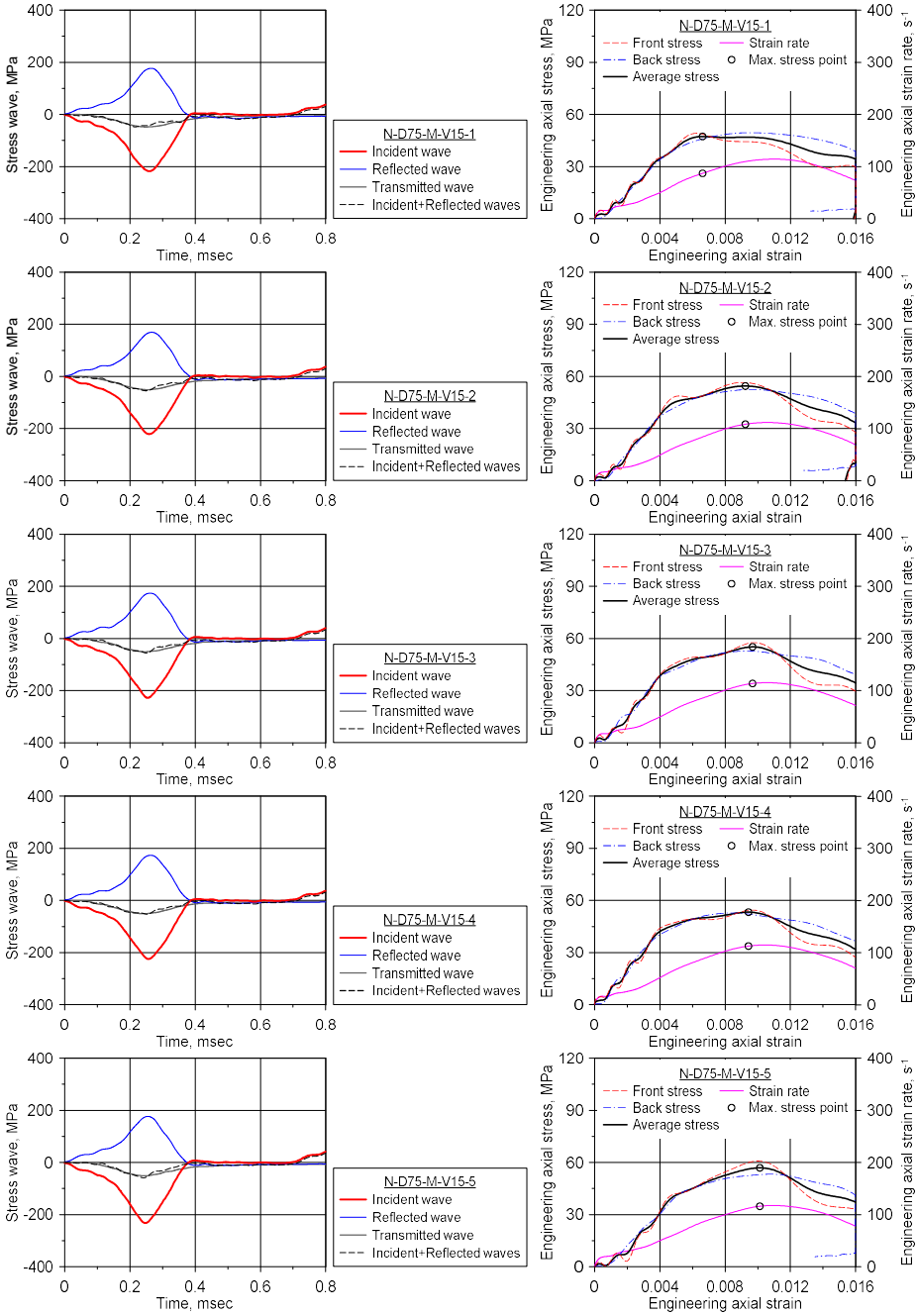
Stress wave, MPa
Time, msec
N-D75-M-V15-1
Incident wave
Reflected wave
Transmitted wave
Incident+Reflected waves
Engineering axial stress, MPa
Engineering axial strain
Engineering axial strain rate, s-1
Front stress
Back stress
Average stress
Strain rate
Max. stress point
N-D75-M-V15-2
N-D75-M-V15-3
N-D75-M-V15-4
N-D75-M-V15-5

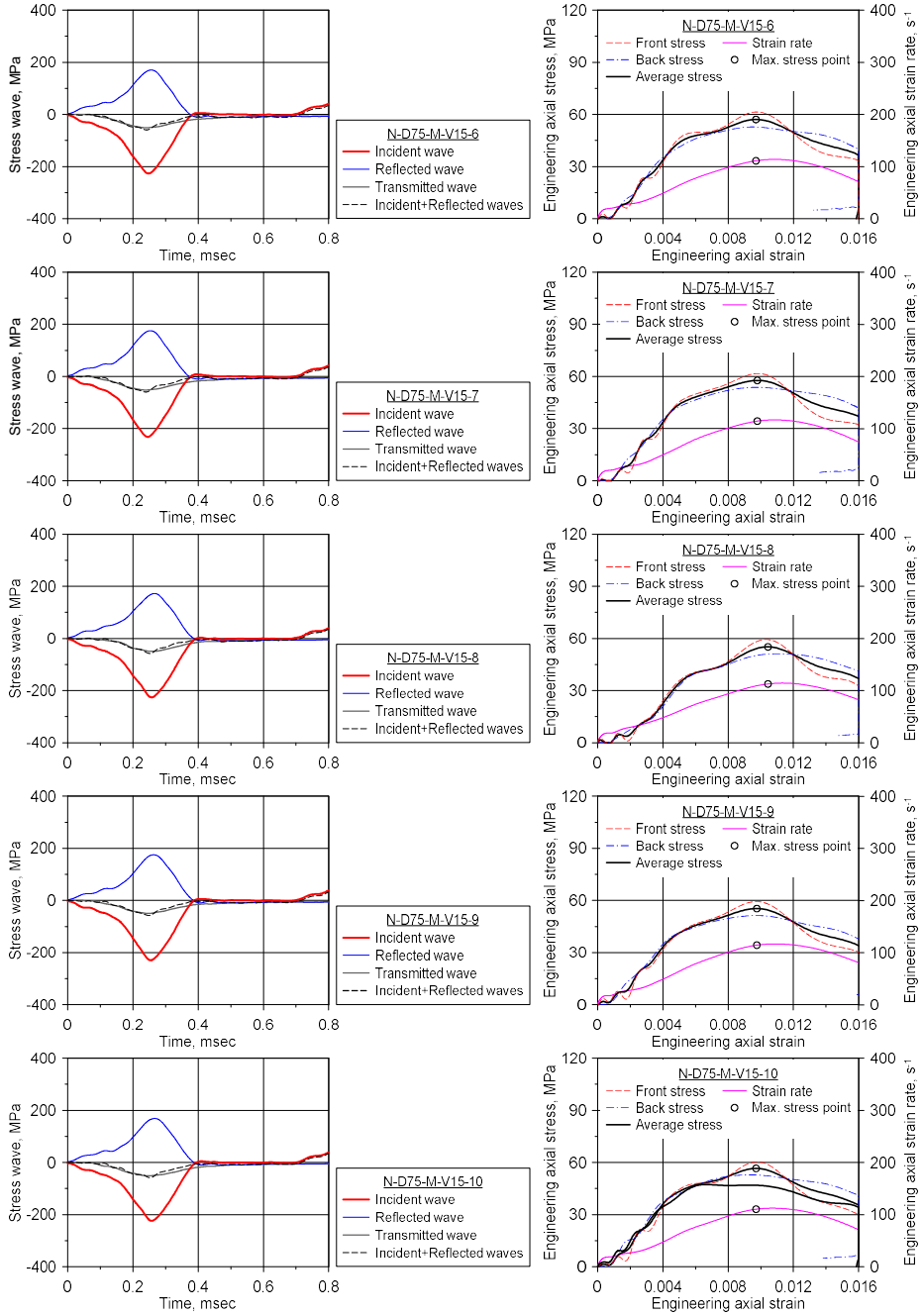

Figure B.14 Stress waves and the axial stress–strain curve of N-D75-M-V15

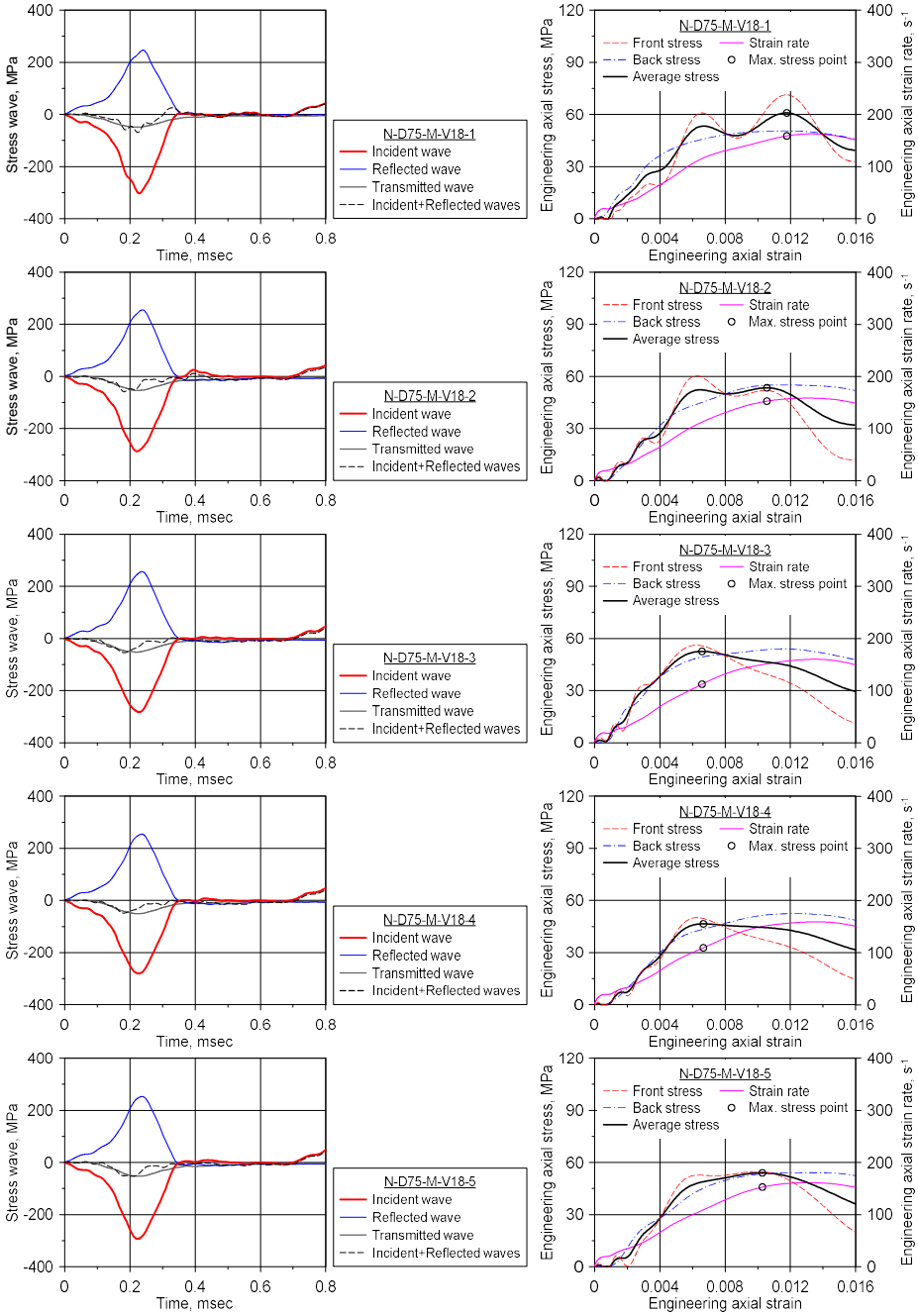
Stress wave, MPa
Time, msec
N-D75-M-V18-1
Incident wave
Reflected wave
Transmitted wave
Incident+Reflected waves
Engineering axial stress, MPa
Engineering axial strain
Engineering axial strain rate, s-1
Front stress
Back stress
Average stress
Strain rate
Max. stress point
N-D75-M-V18-2
N-D75-M-V18-3
N-D75-M-V18-4
N-D75-M-V18-5

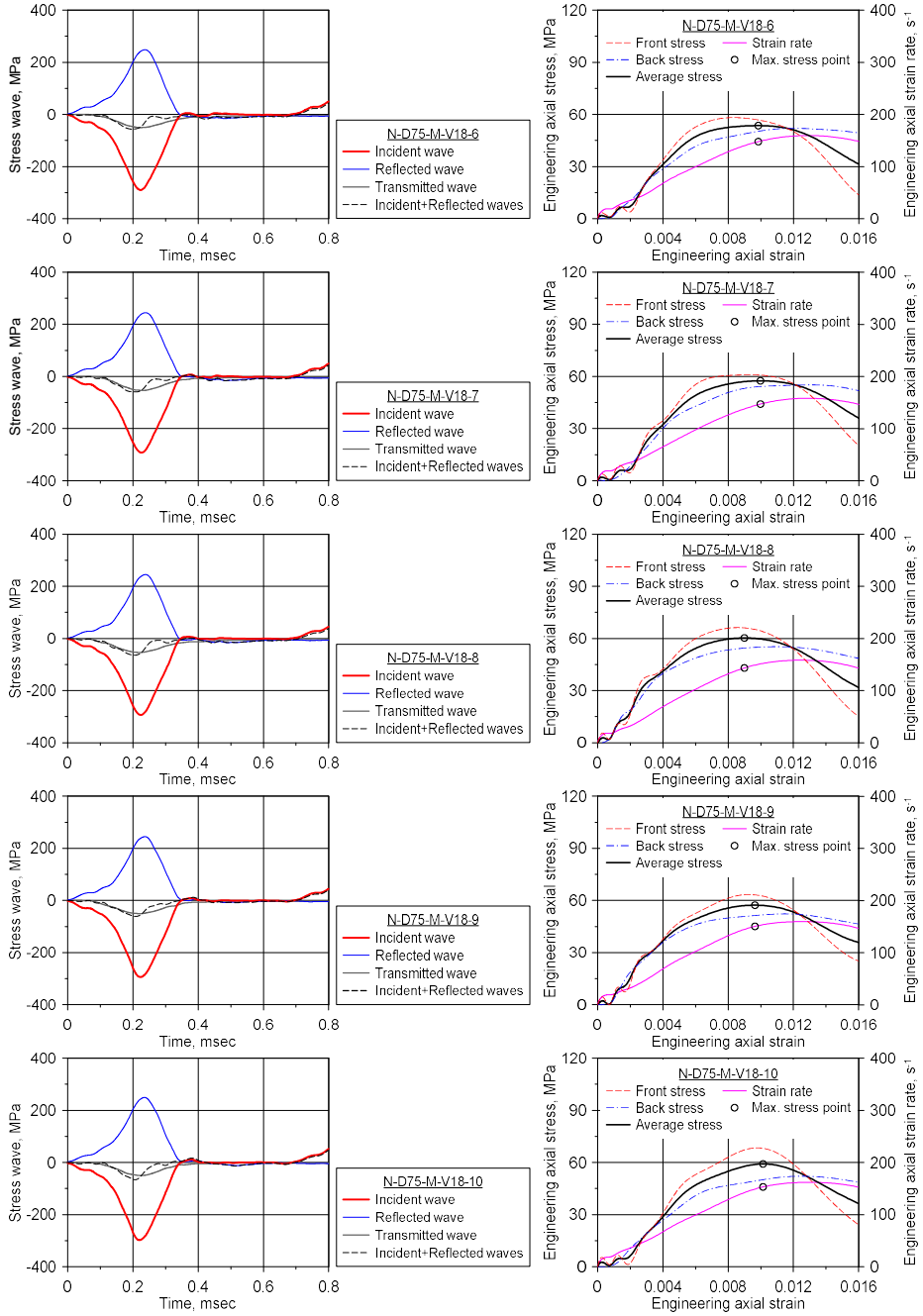

Figure B.15 Stress waves and the axial stress–strain curve of N-D75-M-V18

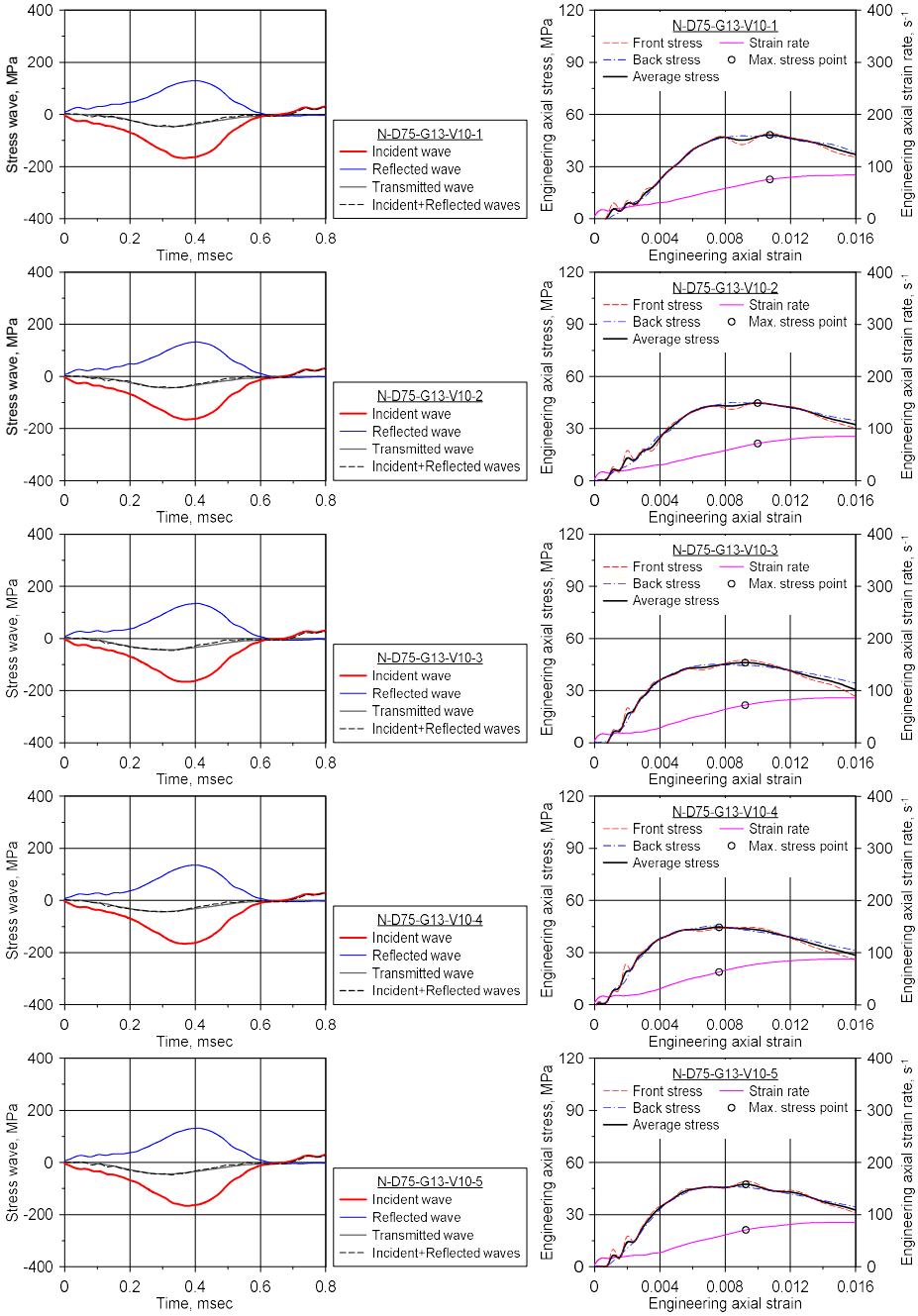
Stress wave, MPa
Time, msec
N-D75-G13-V10-1
Incident wave
Reflected wave
Transmitted wave
Incident+Reflected waves
Engineering axial stress, MPa
Engineering axial strain rate, s-1
Engineering axial strain
Front stress
Back stress
Average stress
Strain rate
Max. stress point
N-D75-G13-V10-2
N-D75-G13-V10-3
N-D75-G13-V10-4
N-D75-G13-V10-5

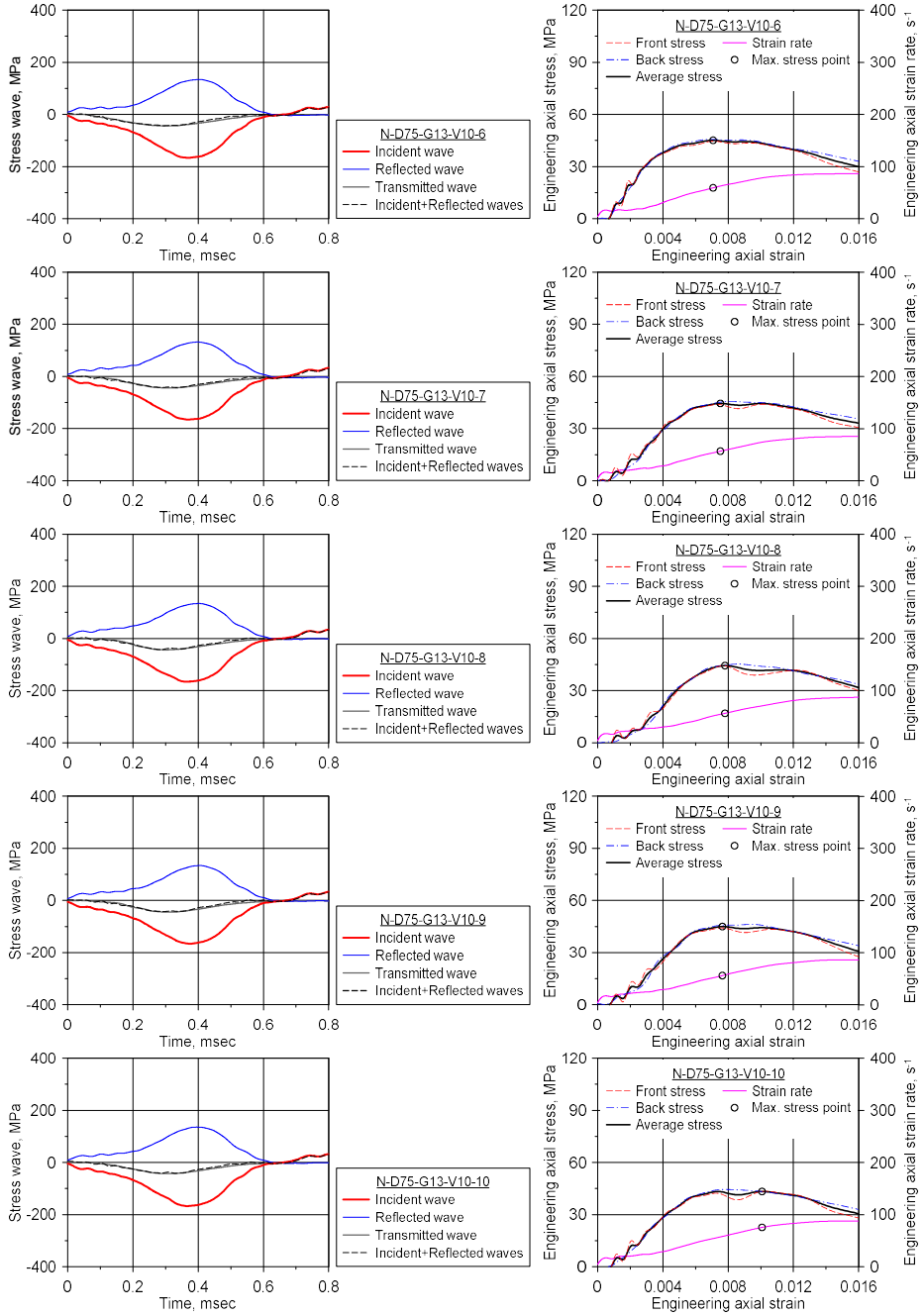

Figure B.16 Stress waves and the axial stress–strain curve of N-D75-G13-V10

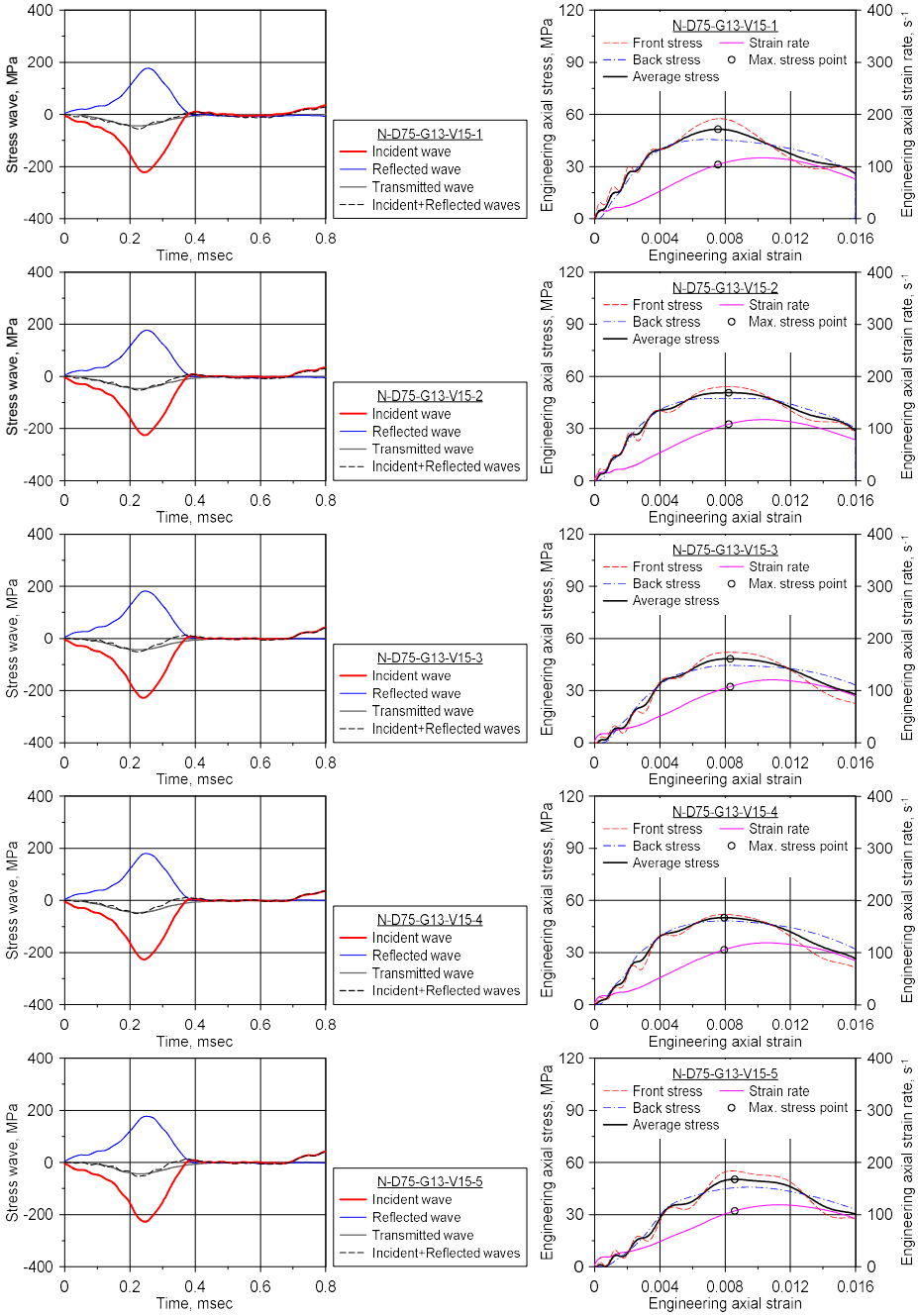
Stress wave, MPa
Time, msec
N-D75-G13-V15-1
Incident wave
Reflected wave
Transmitted wave
Incident+Reflected waves
Engineering axial stress, MPa
Engineering axial strain
Engineering axial strain rate, s-1
Front stress
Back stress
Average stress
Strain rate
Max. stress point
N-D75-G13-V15-2
N-D75-G13-V15-3
N-D75-G13-V15-4
N-D75-G13-V15-5

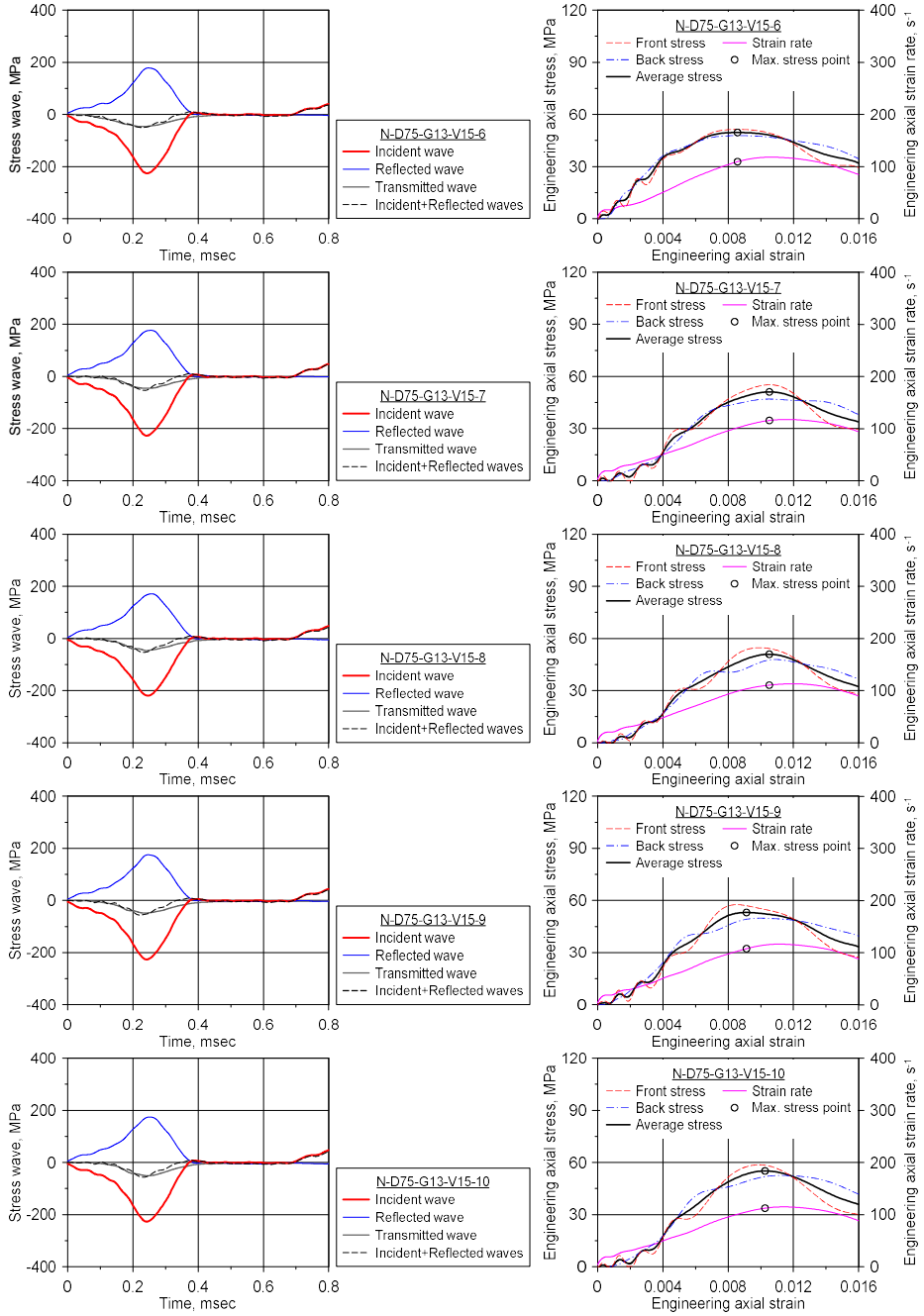

Figure B.17 Stress waves and the axial stress–strain curve of N-D75-G13-V15

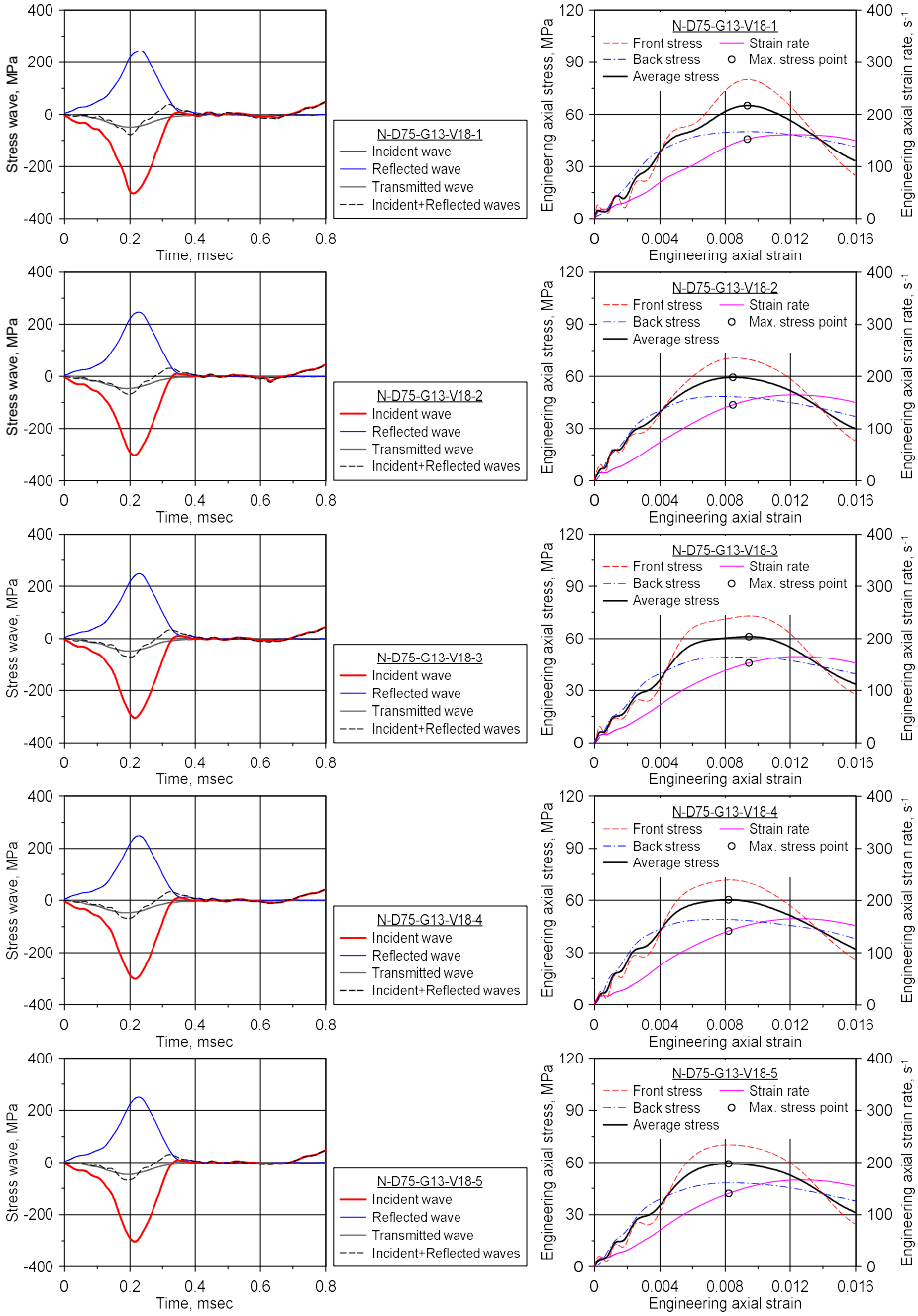
Stress wave, MPa
Time, msec
N-D75-G13-V18-1
Incident wave
Reflected wave
Transmitted wave
Incident+Reflected waves
Engineering axial stress, MPa
Engineering axial strain rate, s-1
Engineering axial strain
Front stress
Back stress
Average stress
Strain rate
Max. stress point
N-D75-G13-V18-2
N-D75-G13-V18-3
N-D75-G13-V18-4
N-D75-G13-V18-5

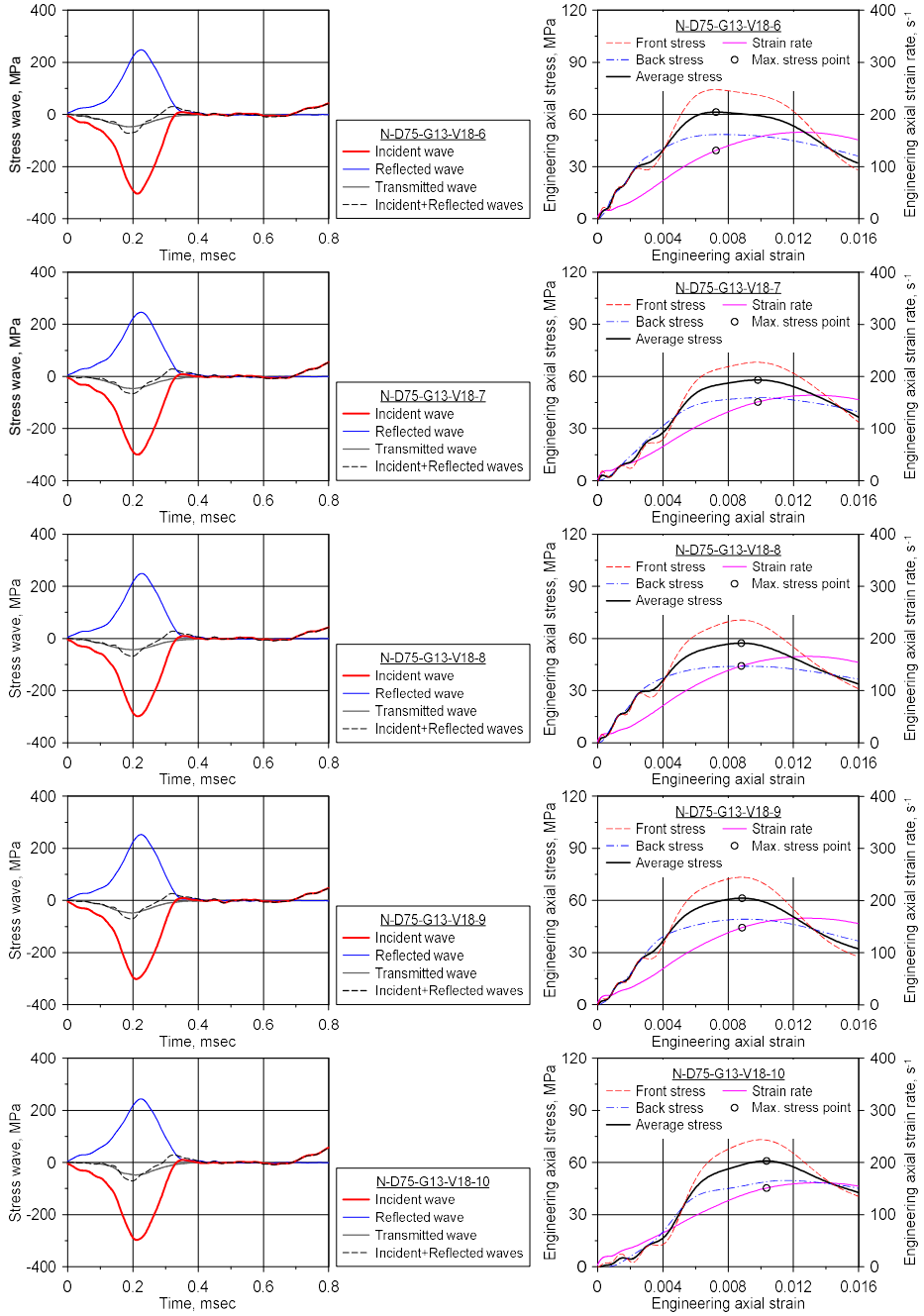

Figure B.18 Stress waves and the axial stress–strain curve of N-D75-G13-V18

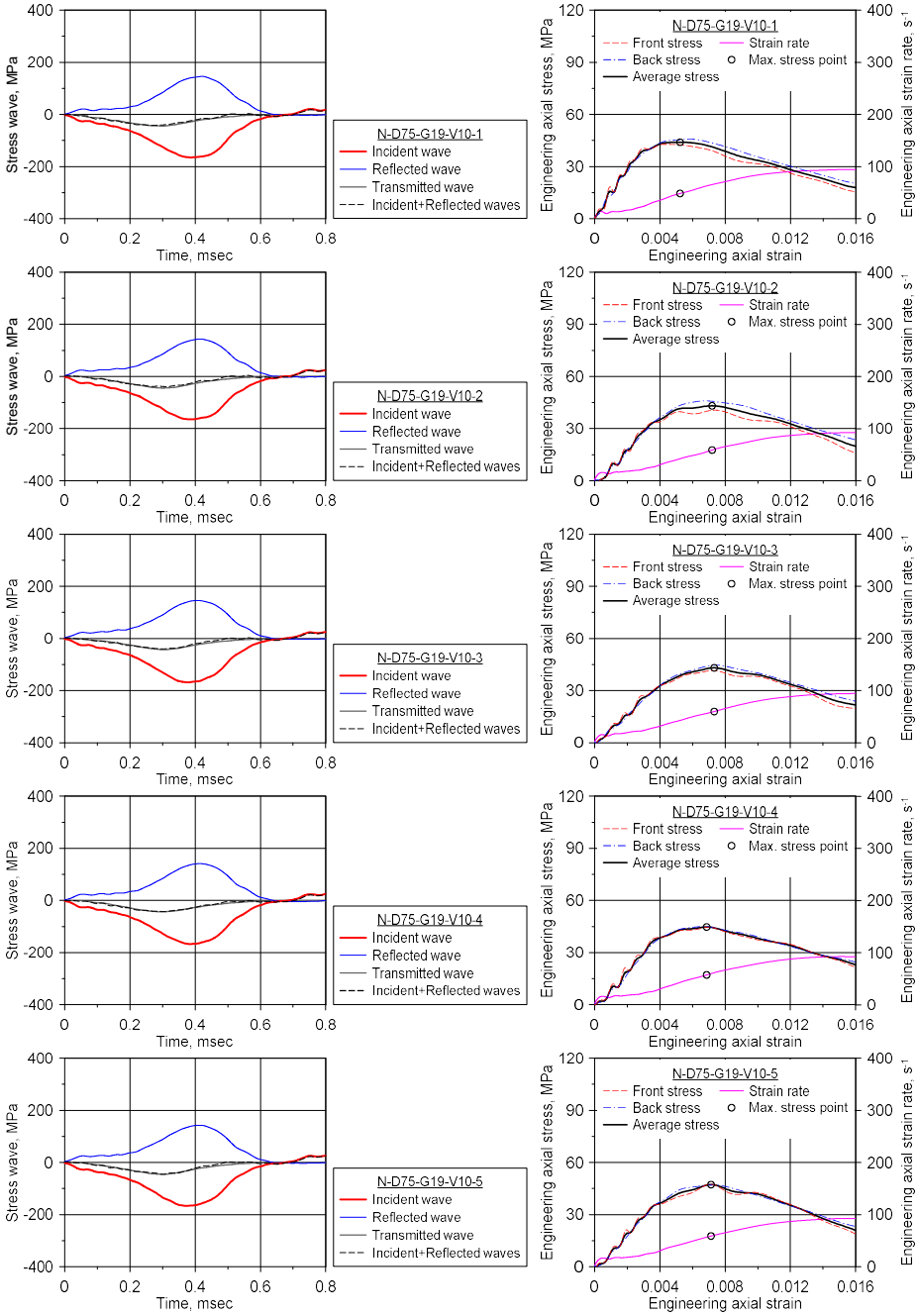
Stress wave, MPa
Time, msec
N-D75-G19-V10-1
Incident wave
Reflected wave
Transmitted wave
Incident+Reflected waves
Engineering axial stress, MPa
Engineering axial strain
Engineering axial strain rate, s-1
Front stress
Back stress
Average stress
Strain rate
Max. stress point
N-D75-G19-V10-2
N-D75-G19-V10-3
N-D75-G19-V10-4
N-D75-G19-V10-5

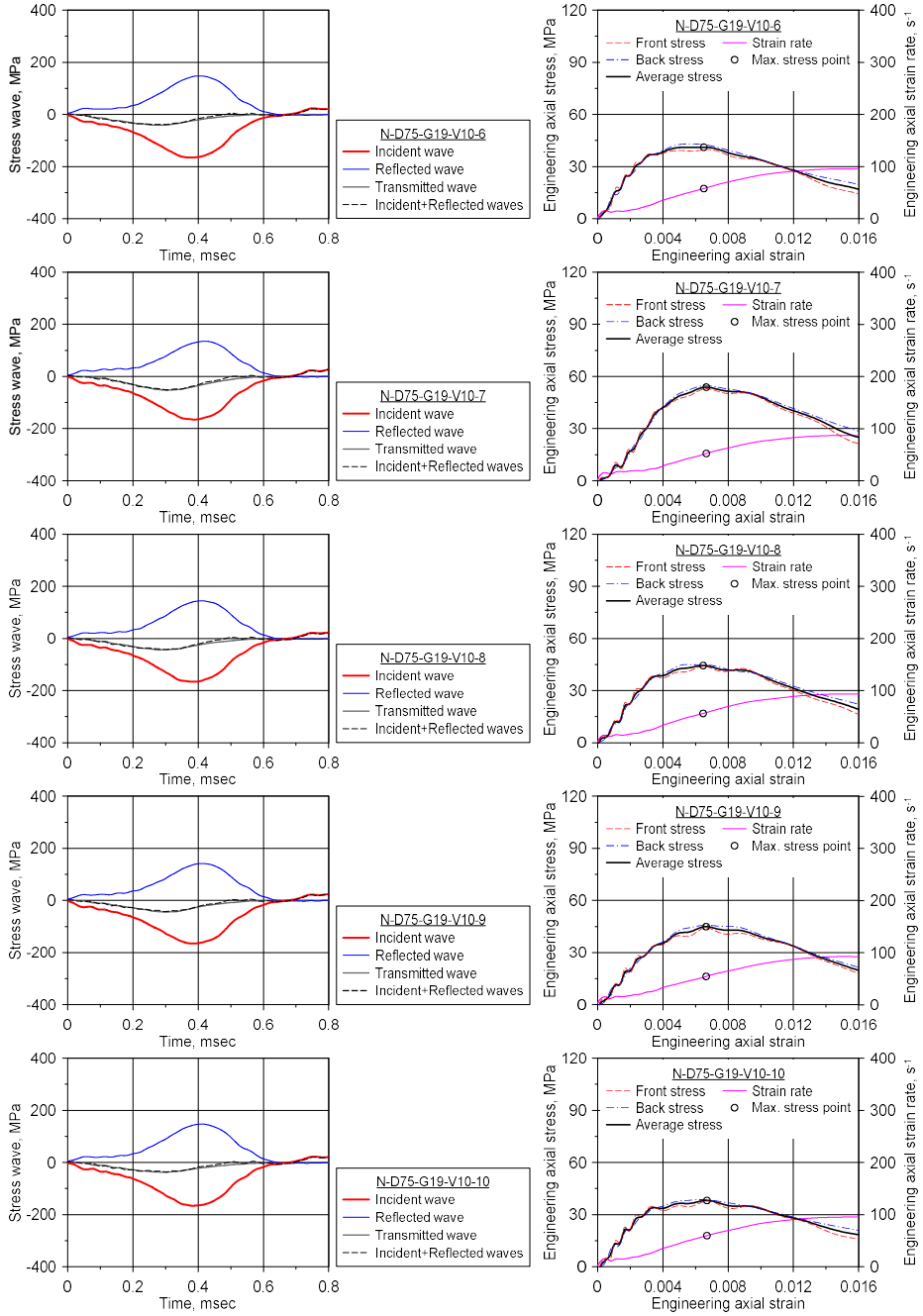

Figure B.19 Stress waves and the axial stress–strain curve of N-D75-G19-V10

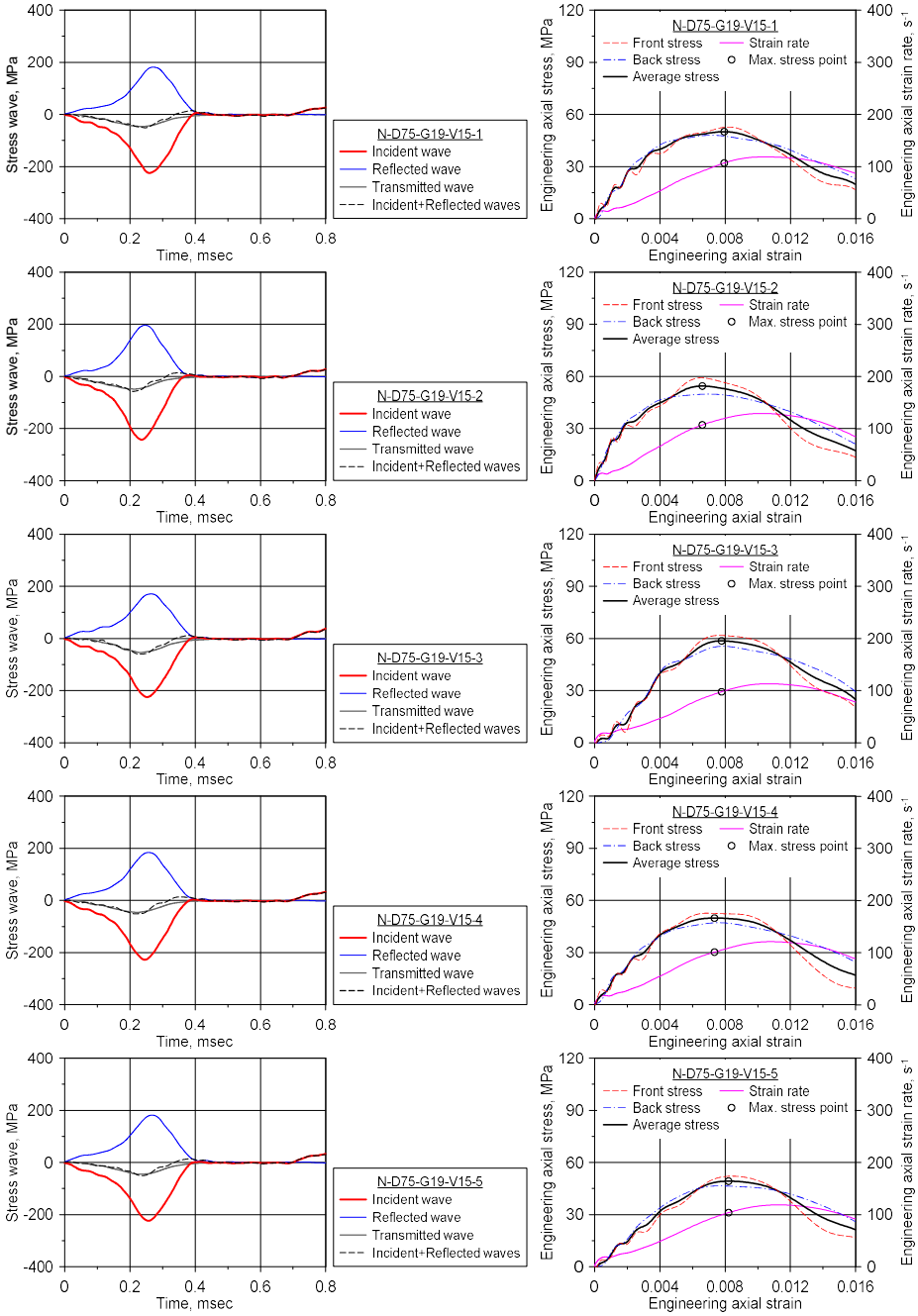
Stress wave, MPa
Time, msec
N-D75-G19-V15-1
Incident wave
Reflected wave
Transmitted wave
Incident+Reflected waves
Engineering axial stress, MPa
Engineering axial strain
Engineering axial strain rate, s-1
Front stress
Back stress
Average stress
Strain rate
Max. stress point
N-D75-G19-V15-2
N-D75-G19-V15-3
N-D75-G19-V15-4
N-D75-G19-V15-5

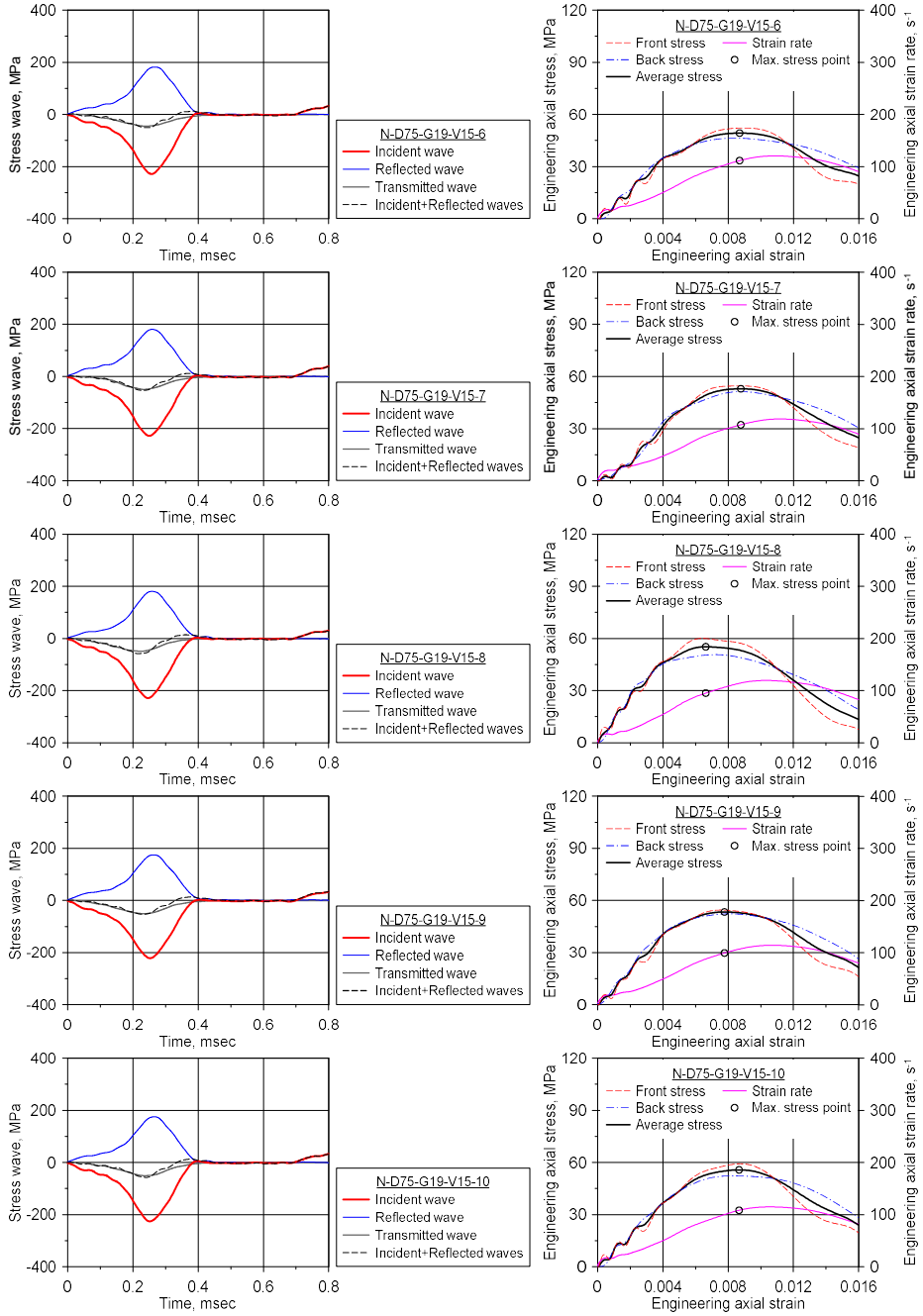

Figure B.20 Stress waves and the axial stress–strain curve of N-D75-G19-V15

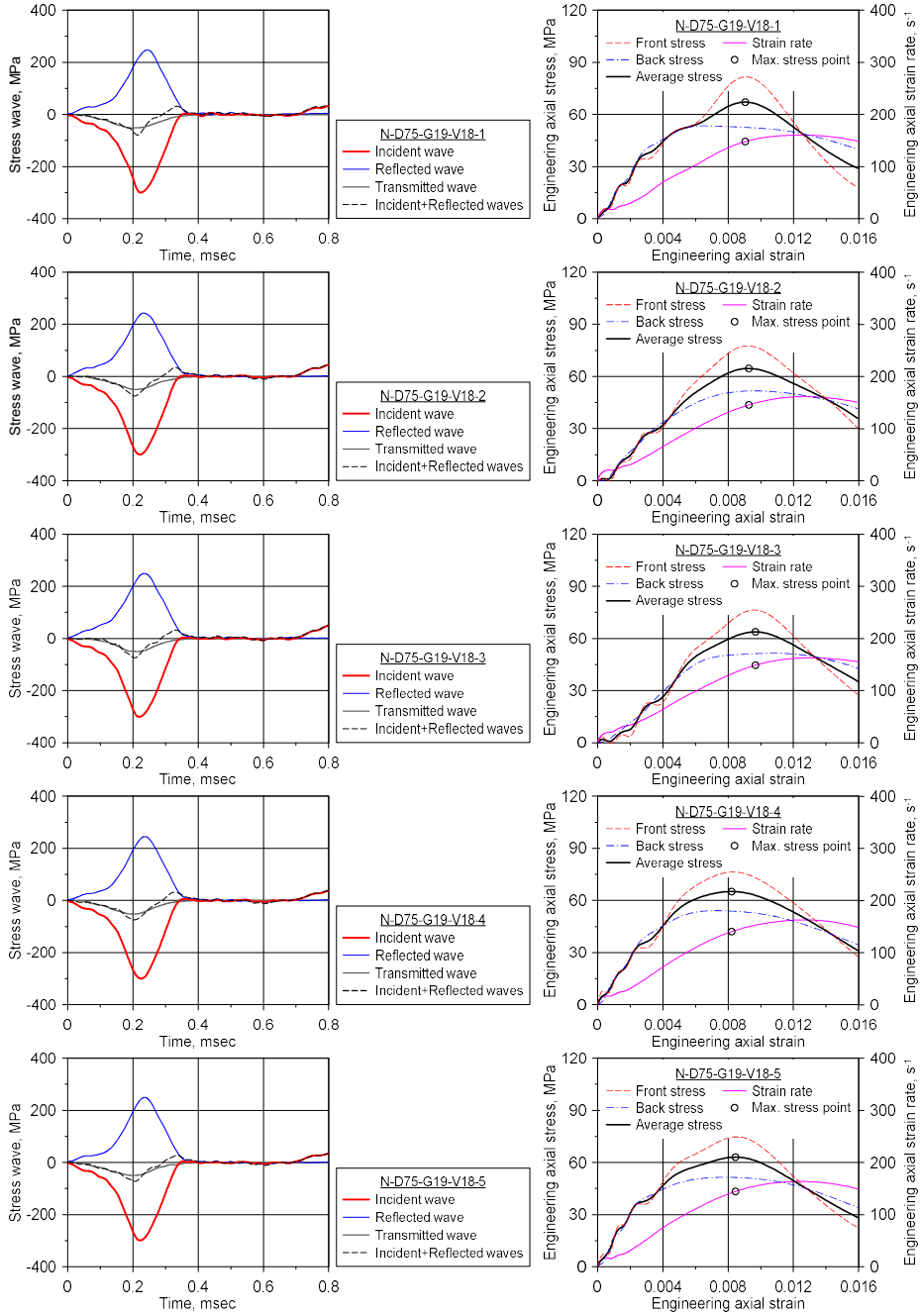
Stress wave, MPa
Time, msec
N-D75-G19-V18-1
Incident wave
Reflected wave
Transmitted wave
Incident+Reflected waves
Engineering axial stress, MPa
Engineering axial strain
Engineering axial strain rate, s-1
Front stress
Back stress
Average stress
Strain rate
Max. stress point
N-D75-G19-V18-2
N-D75-G19-V18-3
N-D75-G19-V18-4
N-D75-G19-V18-5

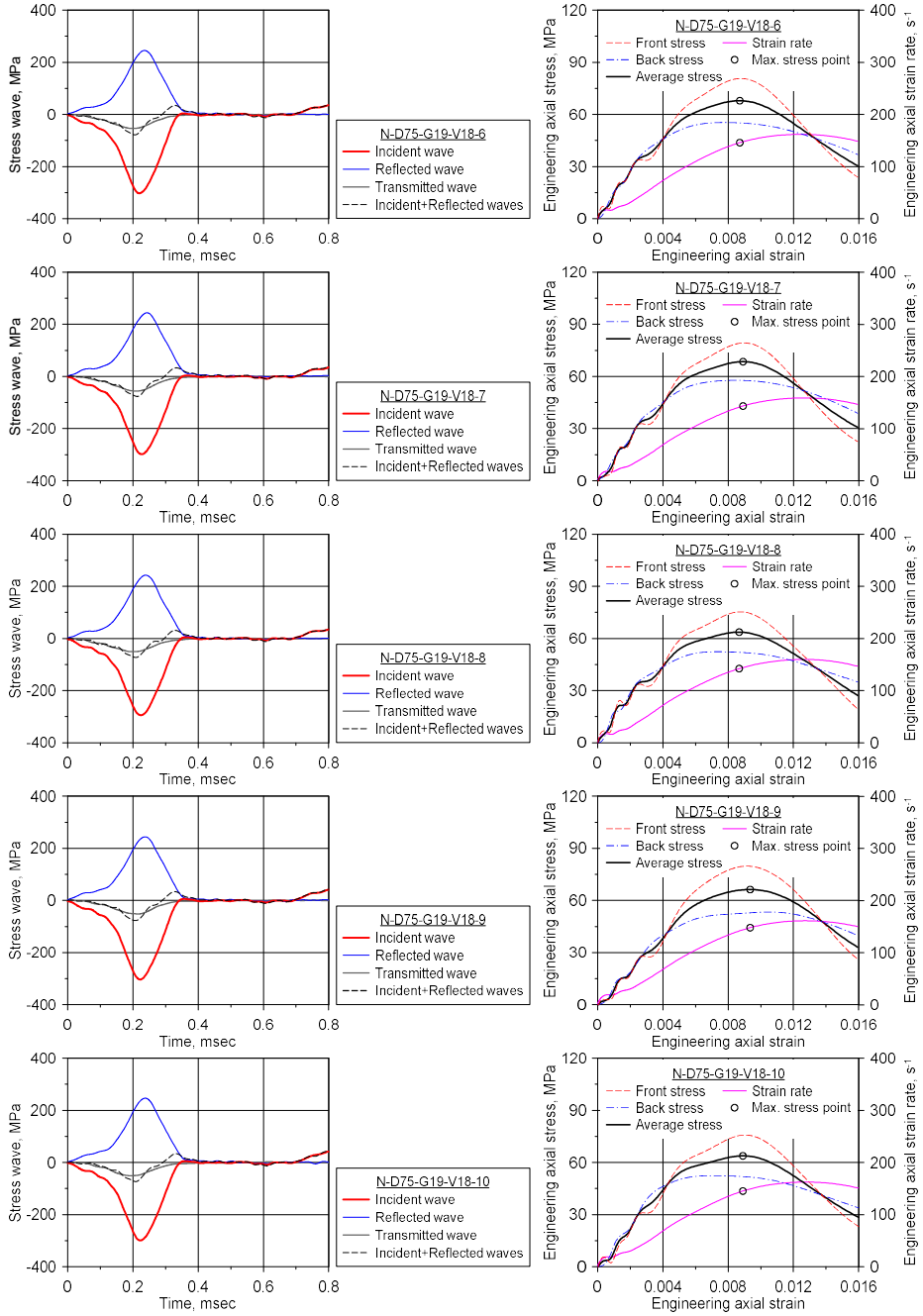

Figure B.21 Stress waves and the axial stress–strain curve of N-D75-G19-V18

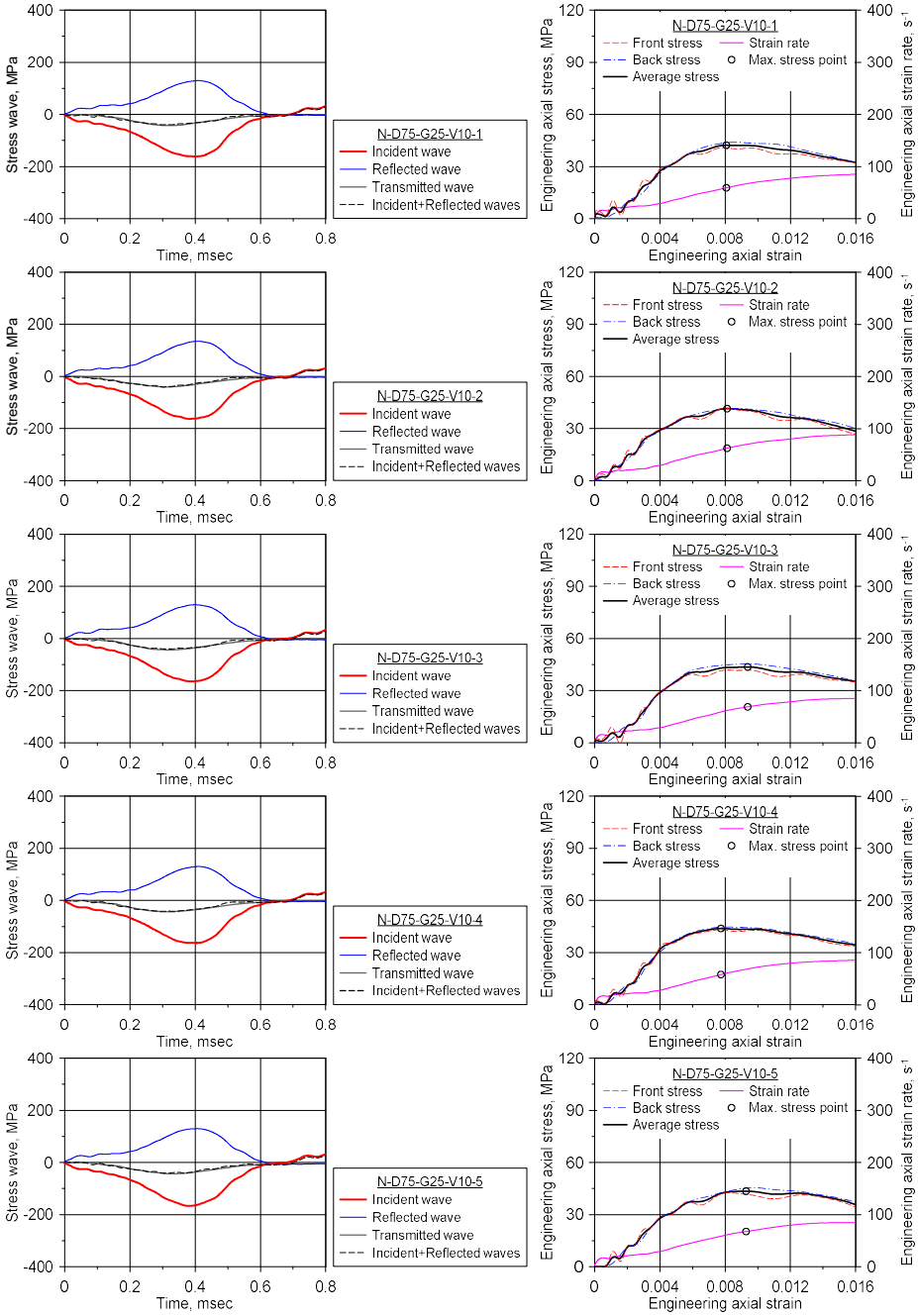
Stress wave, MPa
Time, msec
N-D75-G25-V10-1
Incident wave
Reflected wave
Transmitted wave
Incident+Reflected waves
Engineering axial stress, MPa
Engineering axial strain rate, s-1
Engineering axial strain
Front stress
Back stress
Average stress
Strain rate
Max. stress point
N-D75-G25-V10-2
N-D75-G25-V10-3
N-D75-G25-V10-4
N-D75-G25-V10-5

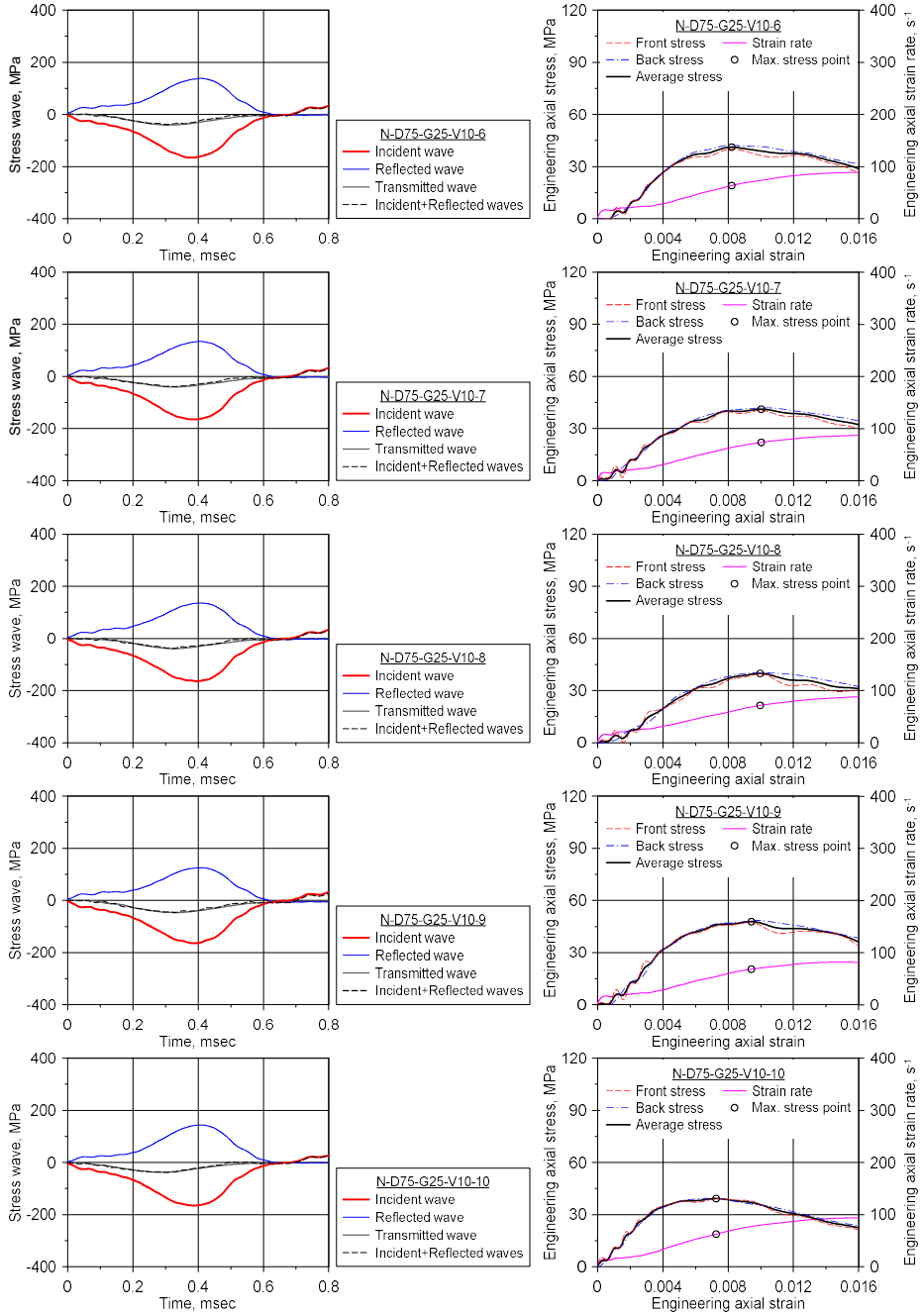

Figure B.22 Stress waves and the axial stress–strain curve of N-D75-G25-V10

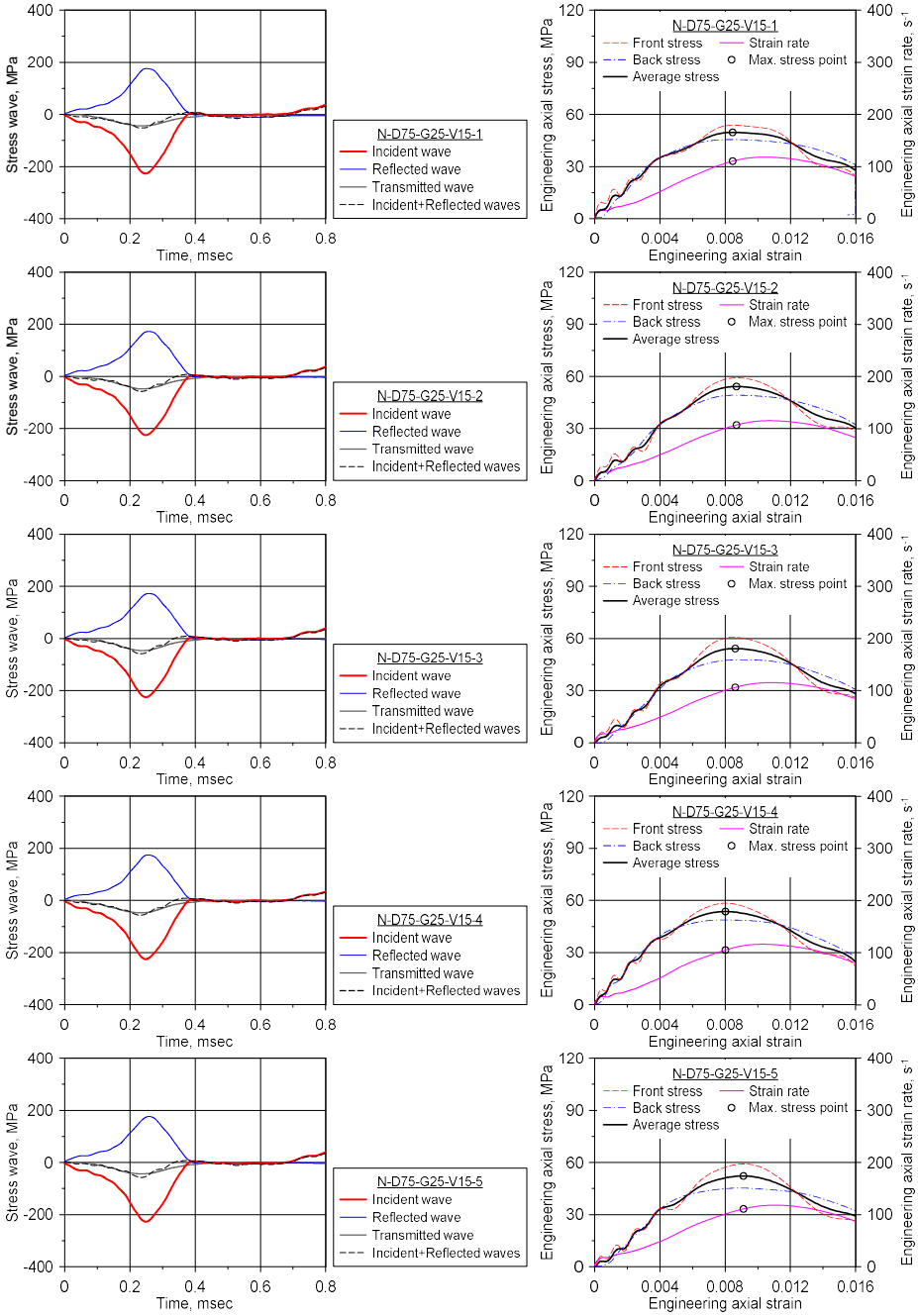
Stress wave, MPa
Time, msec
N-D75-G25-V15-1
Incident wave
Reflected wave
Transmitted wave
Incident+Reflected waves
Engineering axial stress, MPa
Engineering axial strain rate, s-1
Engineering axial strain
Front stress
Back stress
Average stress
Strain rate
Max. stress point
N-D75-G25-V15-2
N-D75-G25-V15-3
N-D75-G25-V15-4
N-D75-G25-V15-5

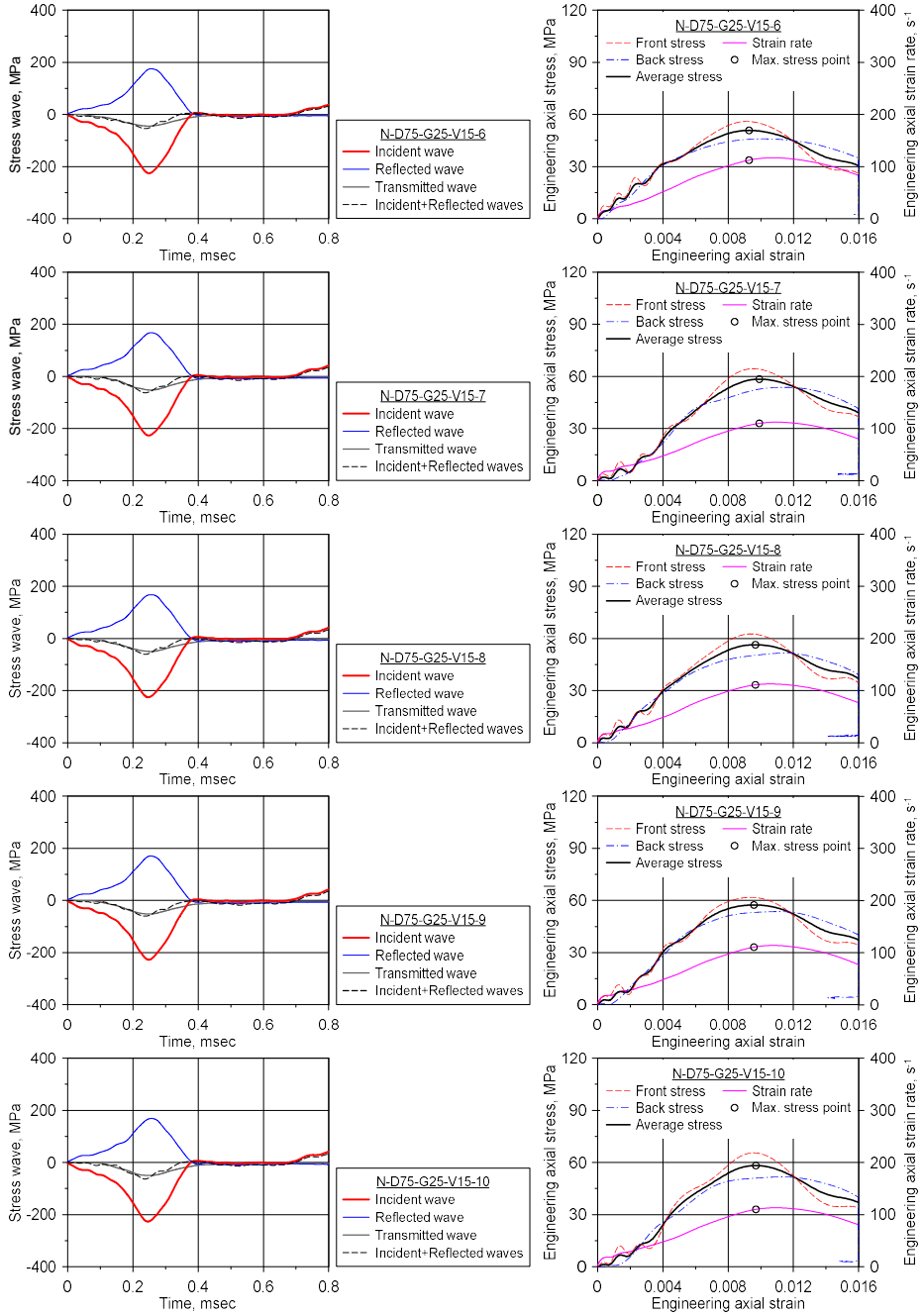

Figure B.23 Stress waves and the axial stress–strain curve of N-D75-G25-V15

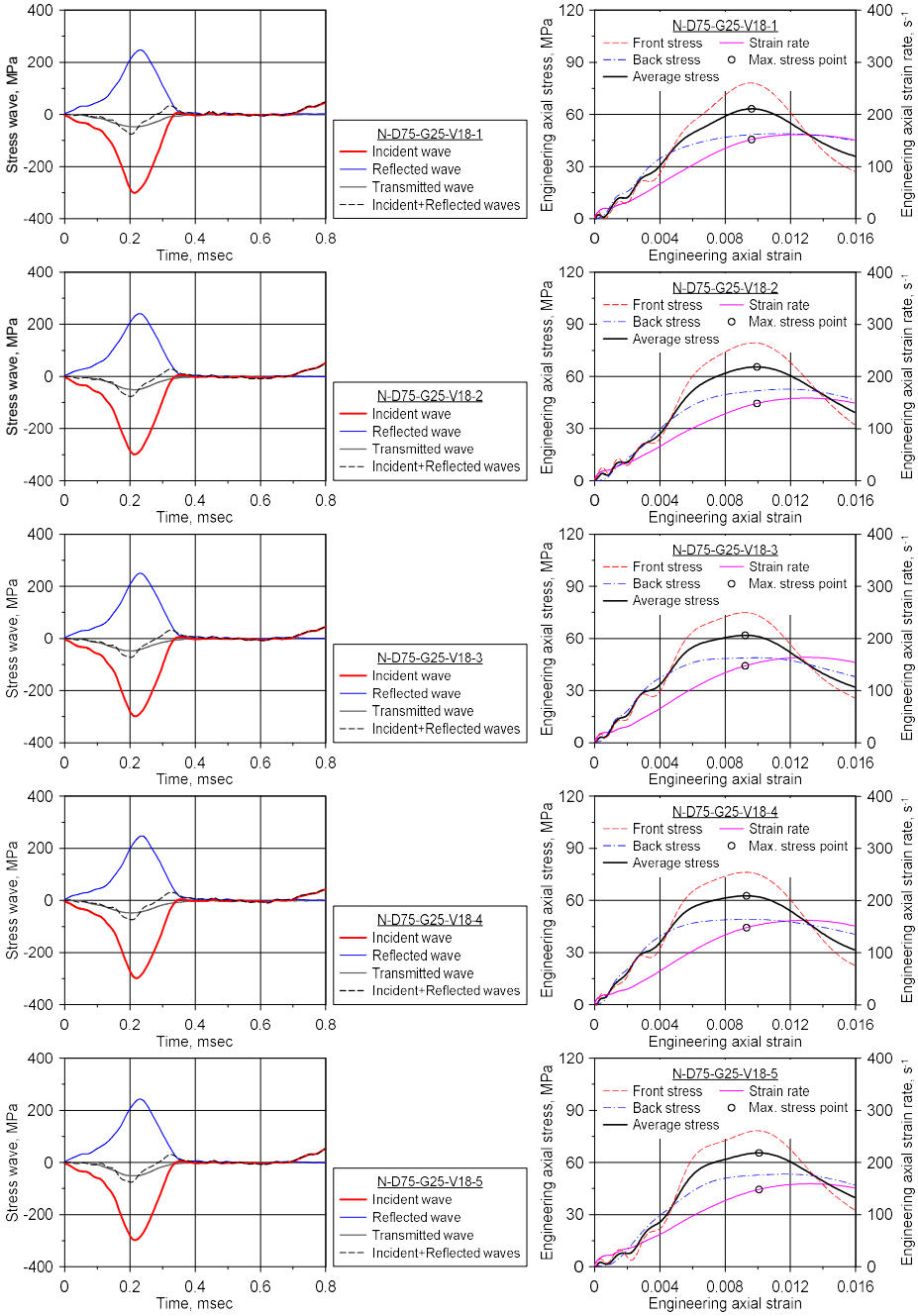
Stress wave, MPa
Time, msec
N-D75-G25-V18-1
Incident wave
Reflected wave
Transmitted wave
Incident+Reflected waves
Engineering axial stress, MPa
Engineering axial strain rate, s-1
Engineering axial strain
Front stress
Back stress
Average stress
Strain rate
Max. stress point
N-D75-G25-V18-2
N-D75-G25-V18-3
N-D75-G25-V18-4
N-D75-G25-V18-5

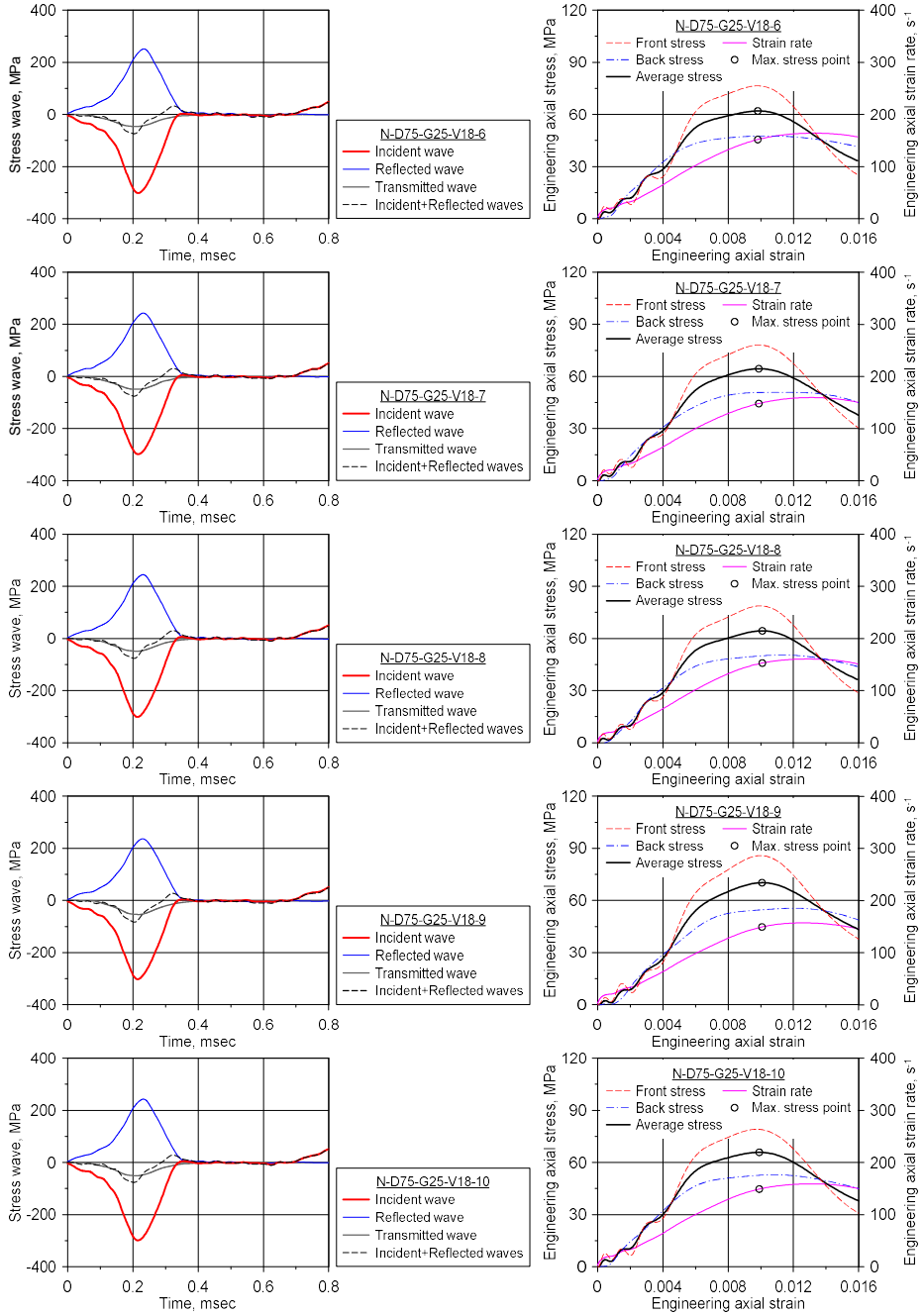

Figure B.24 Stress waves and the axial stress–strain curve of N-D75-G25-V18

Appendix C

Experimental Results of SHPB Test for Investigation on the Effect of Friction

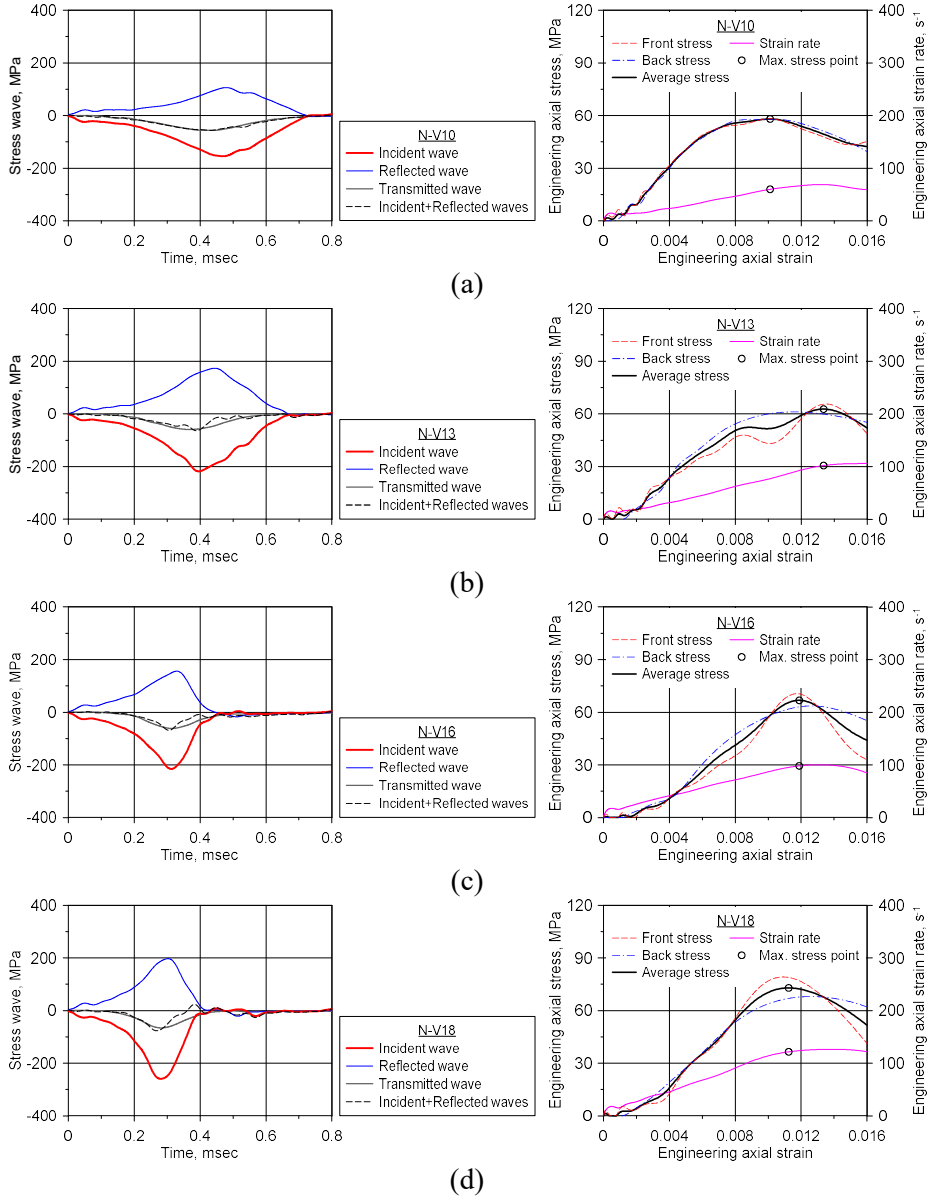

Figure C.1 Stress waves and the axial stress–strain curve of N;

(a) N-V10; (b) N-V13; (c) N-V16; (d) N-V18

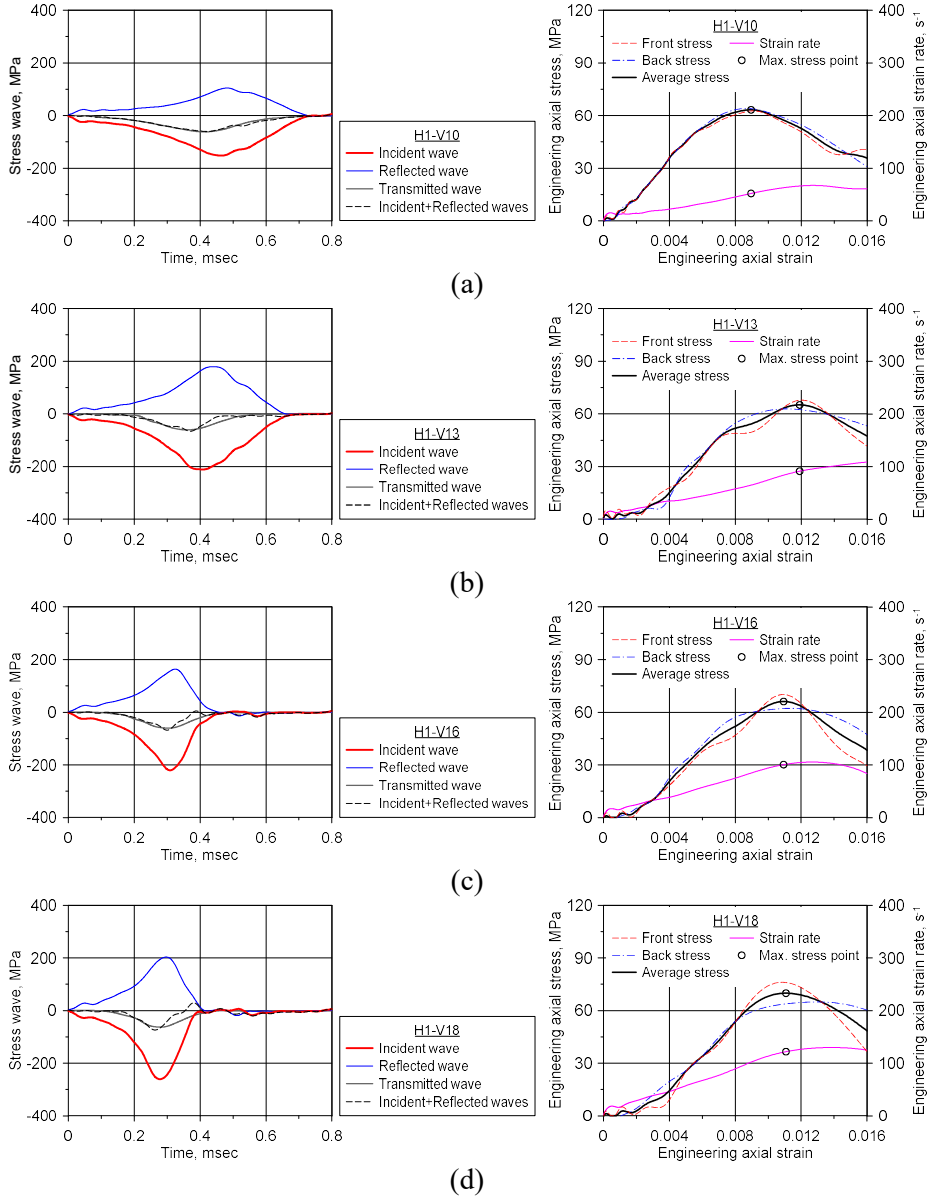

Figure C.2 Stress waves and the axial stress–strain curve of H1;

(a) H1-V10; (b) H1-V13; (c) H1-V16; (d) H1-V18

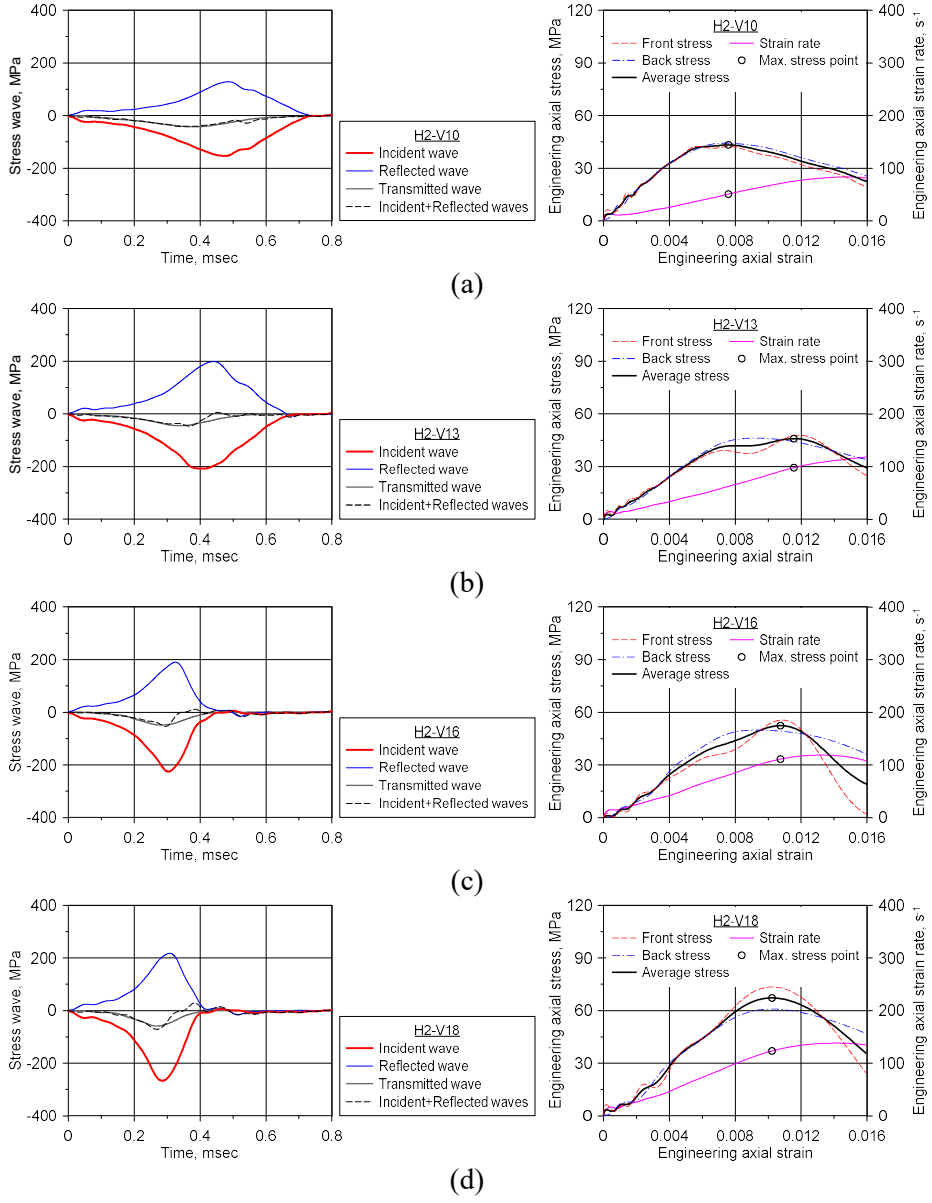

Figure C.3 Stress waves and the axial stress–strain curve of H2;

(a) H2-V10; (b) H2-V13; (c) H2-V16; (d) H2-V18

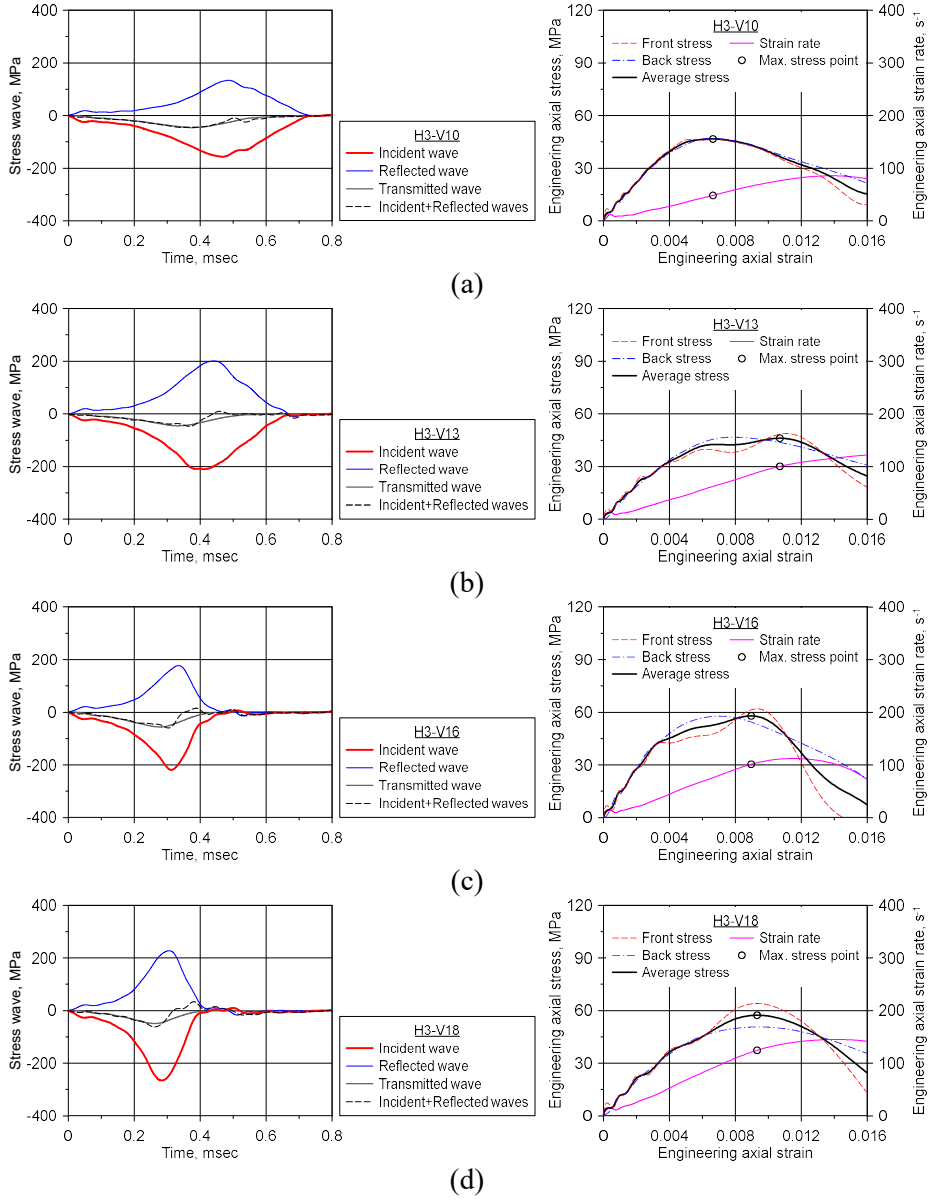

Figure C.4 Stress waves and the axial stress–strain curve of H3;

(a) H3-V10; (b) H3-V13; (c) H3-V16; (d) H3-V18

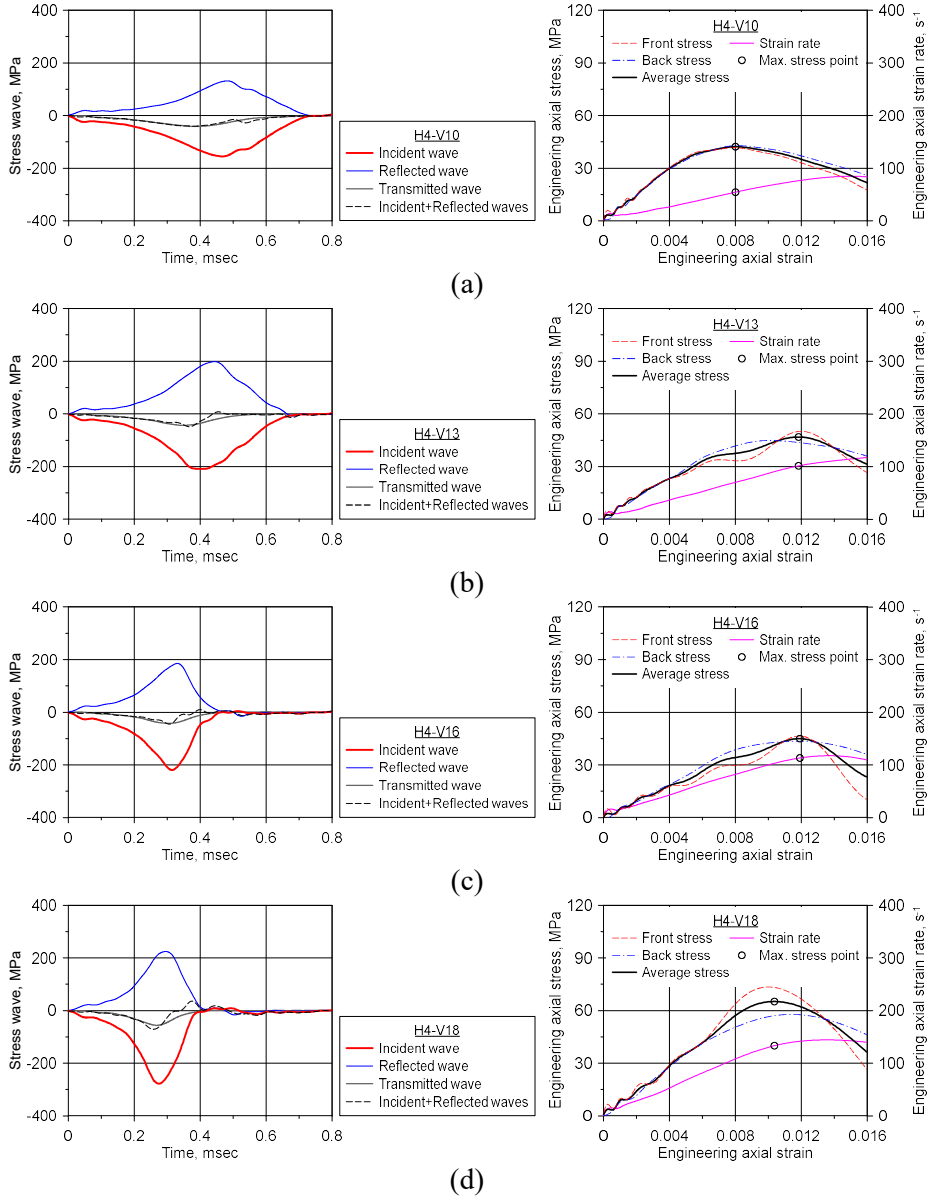

Figure C.5 Stress waves and the axial stress–strain curve of H4;

(a) H4-V10; (b) H4-V13; (c) H4-V16; (d) H4-V18

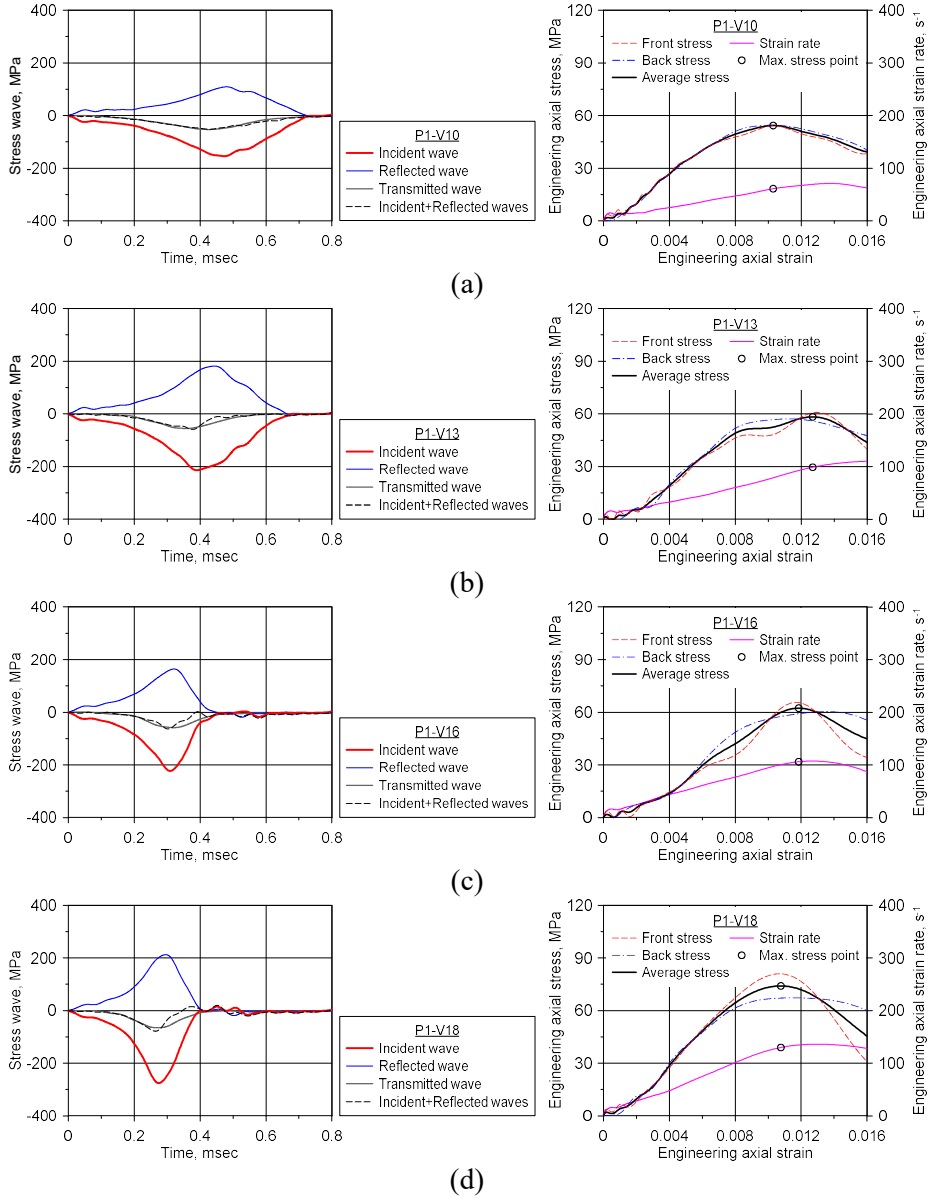

Figure C.6 Stress waves and the axial stress–strain curve of P1;

(a) P1-V10; (b) P1-V13; (c) P1-V16; (d) P1-V18

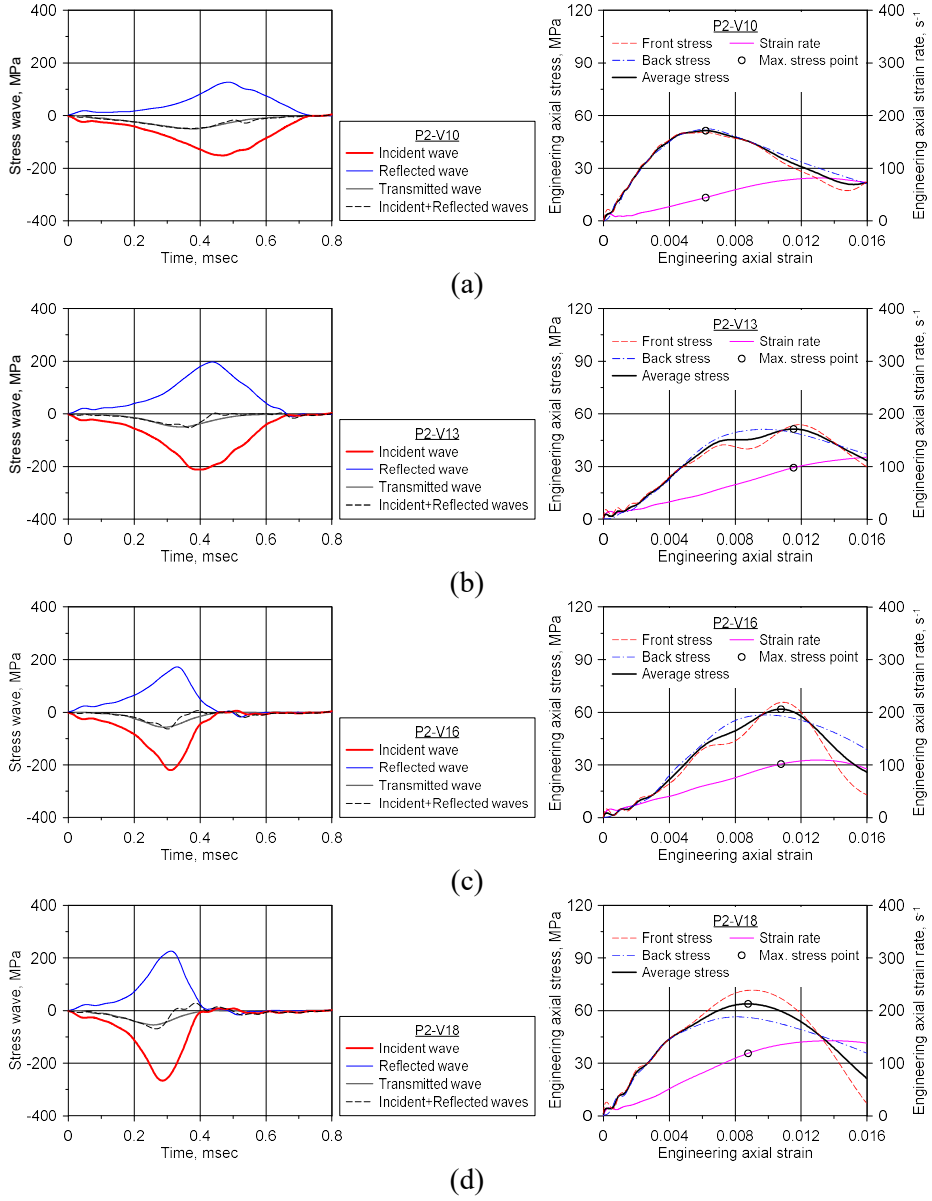

Figure C.7 Stress waves and the axial stress–strain curve of P2;

(a) P2-V10; (b) P2-V13; (c) P2-V16; (d) P2-V18

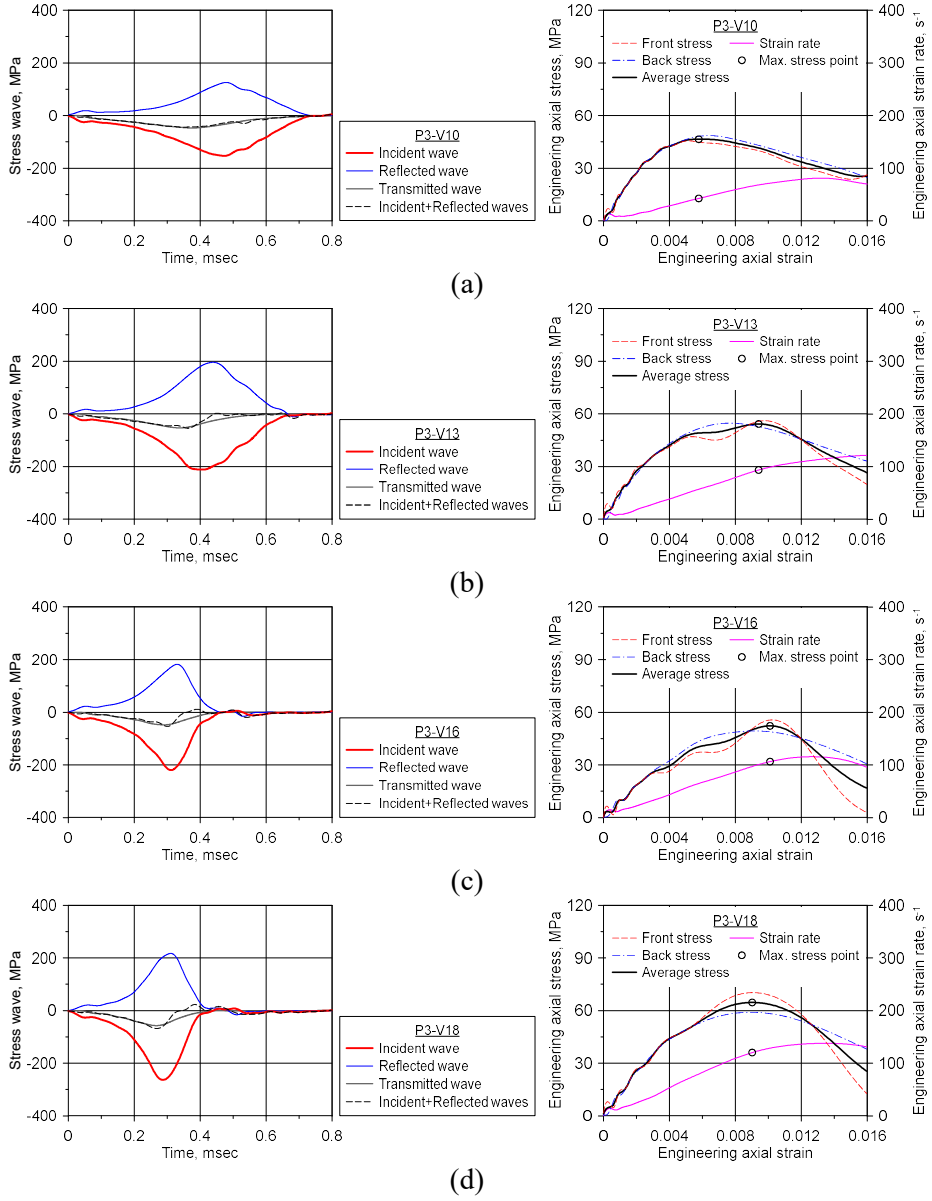

Figure C.8 Stress waves and the axial stress–strain curve of P3;

(a) P3-V10; (b) P3-V13; (c) P3-V16; (d) P3-V18

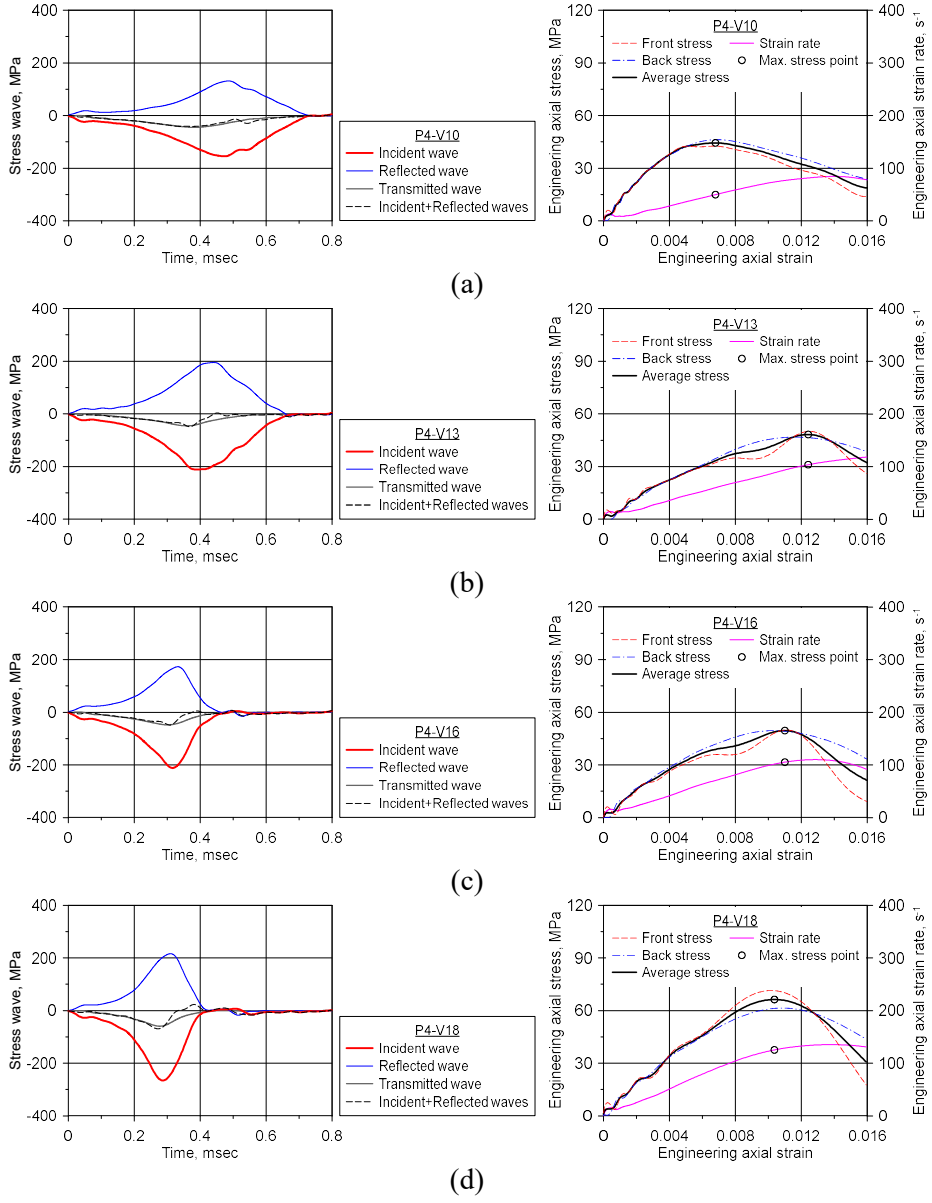

Figure C.9 Stress waves and the axial stress–strain curve of P4;

(a) P4-V10; (b) P4-V13; (c) P4-V16; (d) P4-V18

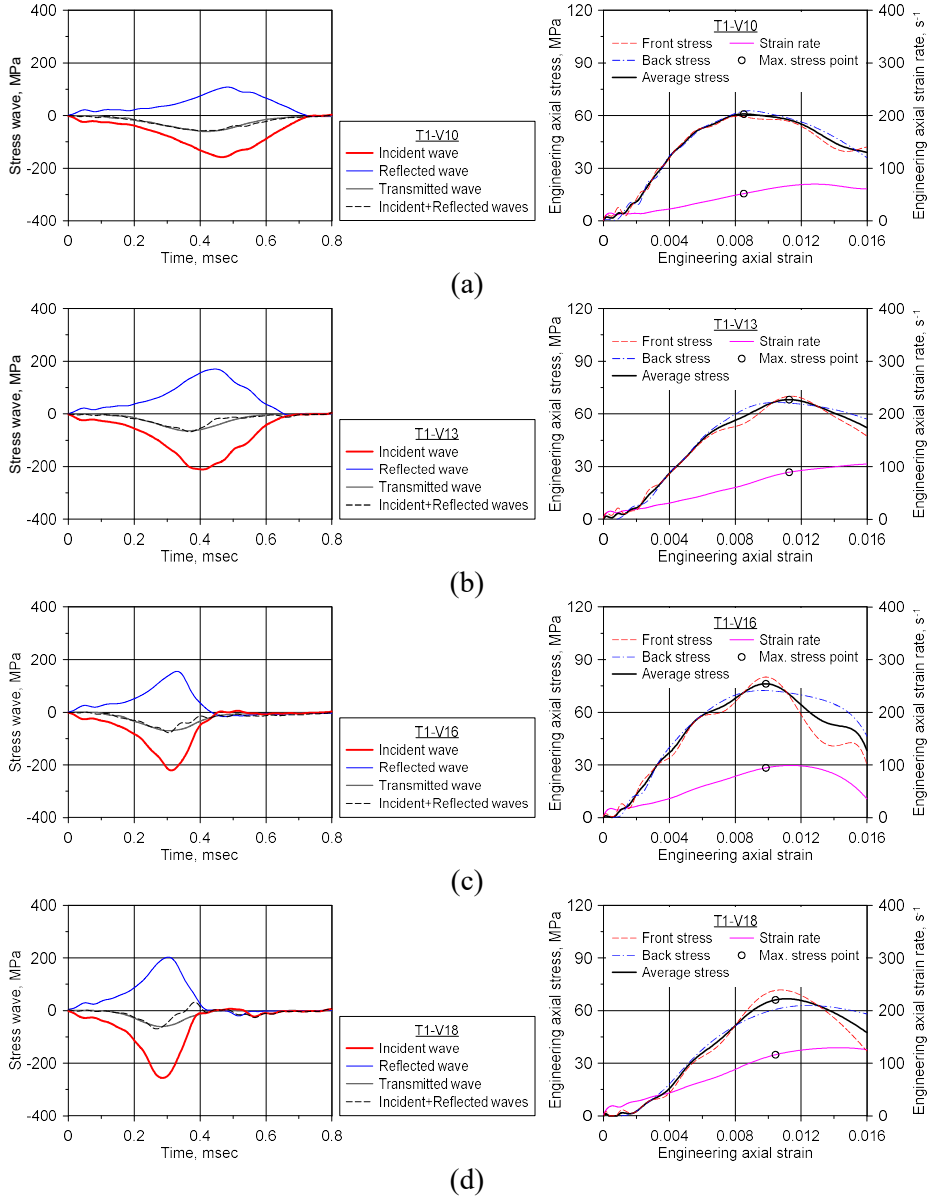

Figure C.10 Stress waves and the axial stress–strain curve of T1;

(a) T1-V10; (b) T1-V13; (c) T1-V16; (d) T1-V18

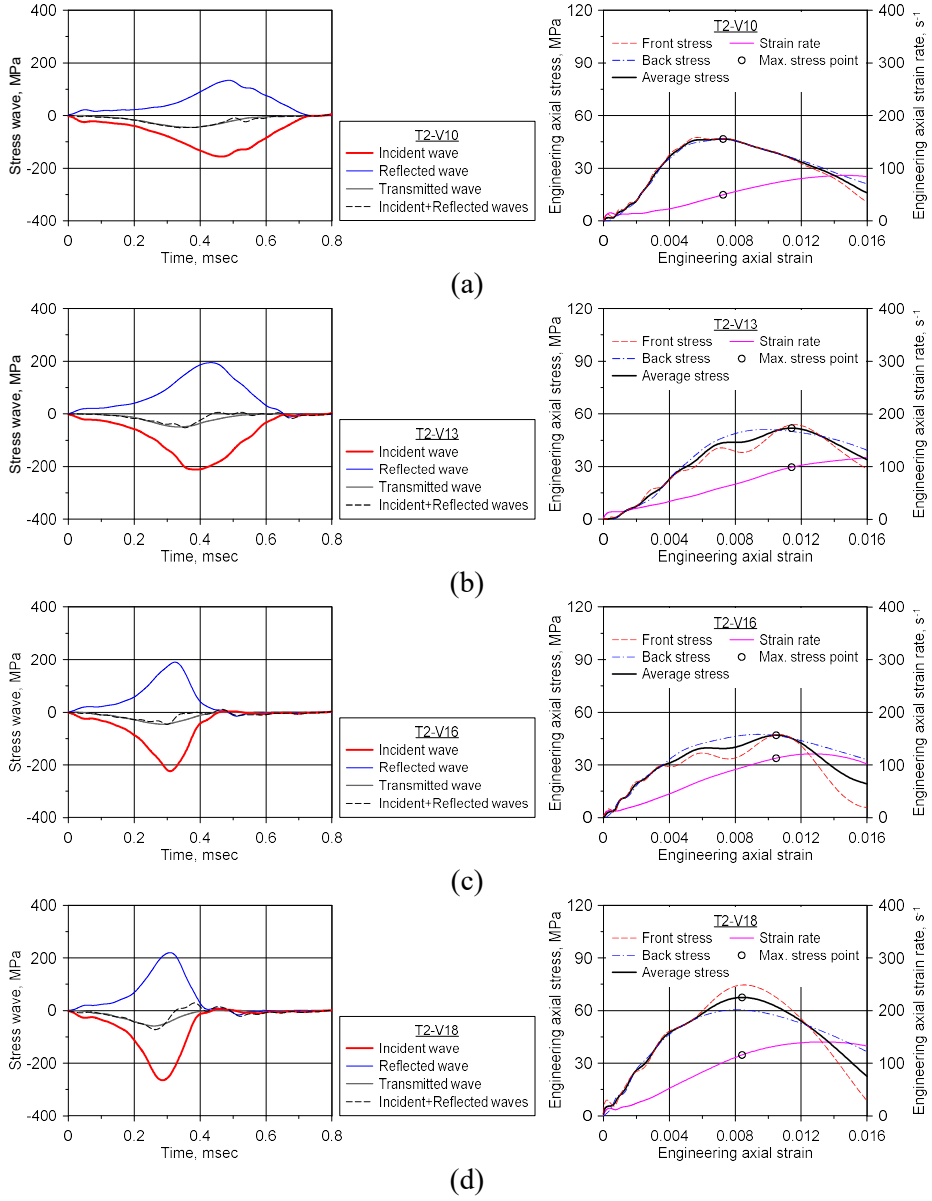

Figure C.11 Stress waves and the axial stress–strain curve of T2;

(a) T2-V10; (b) T2-V13; (c) T2-V16; (d) T2-V18

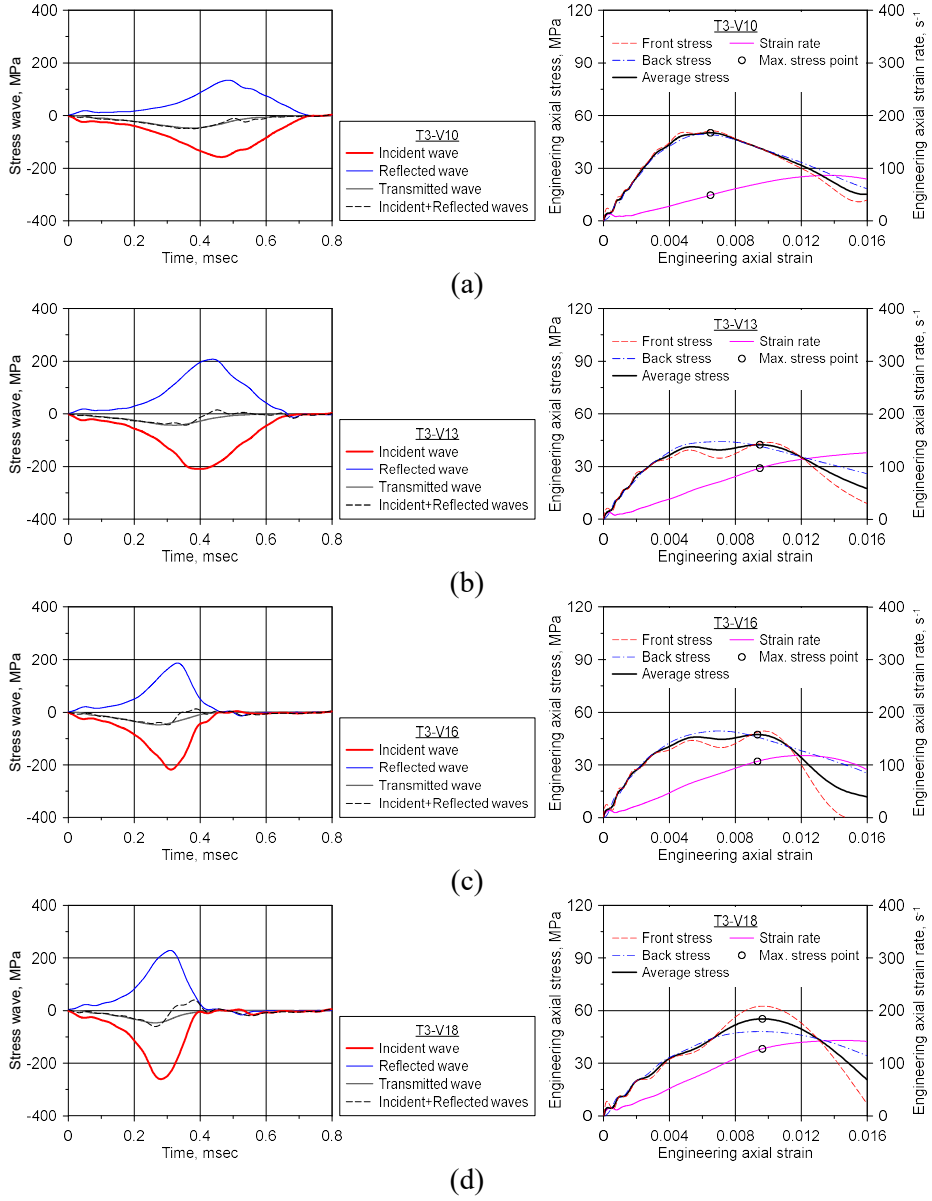

Figure C.12 Stress waves and the axial stress–strain curve of T3;

(a) T3-V10; (b) T3-V13; (c) T3-V16; (d) T3-V18

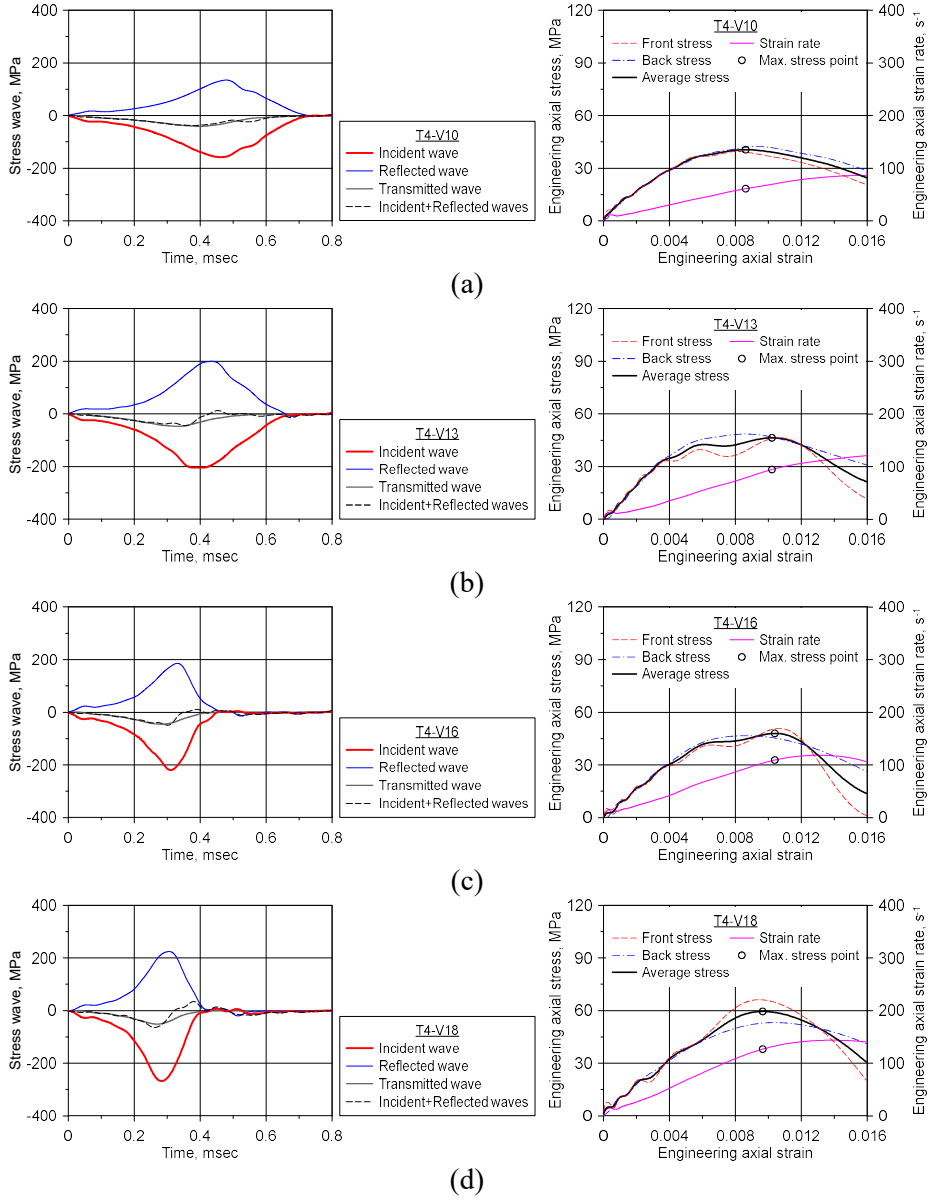

Figure C.13 Stress waves and the axial stress–strain curve of T4;

(a) T4-V10; (b) T4-V13; (c) T4-V16; (d) T4-V18

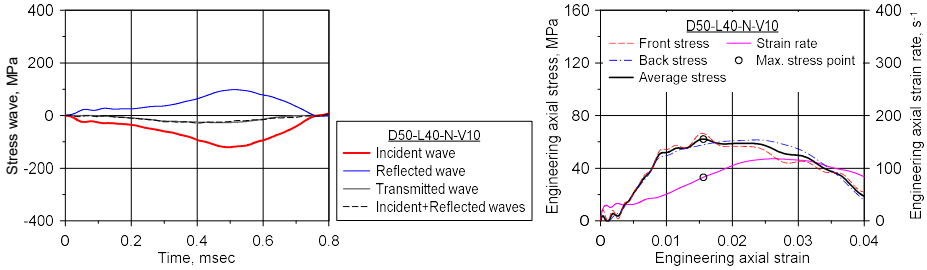
Stress wave, MPa
Time, msec
D50-L40-N-V10
Incident wave
Reflected wave
Transmitted wave
Incident+Reflected waves
Engineering axial stress, MPa
Engineering axial strain rate, s-1
Engineering axial strain
Front stress
Back stress
Average stress
Strain rate
Max. stress point

(a)

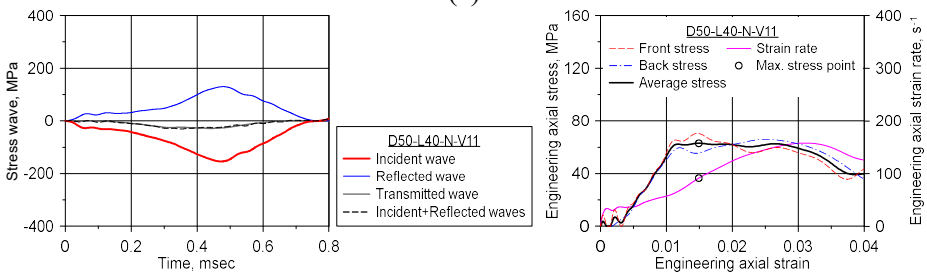
Stress wave, MPa
Time, msec
D50-L40-N-V11
Incident wave
Reflected wave
Transmitted wave
Incident+Reflected waves
Engineering axial stress, MPa
Engineering axial strain rate, s-1
Engineering axial strain
Front stress
Back stress
Average stress
Strain rate
Max. stress point

(b)

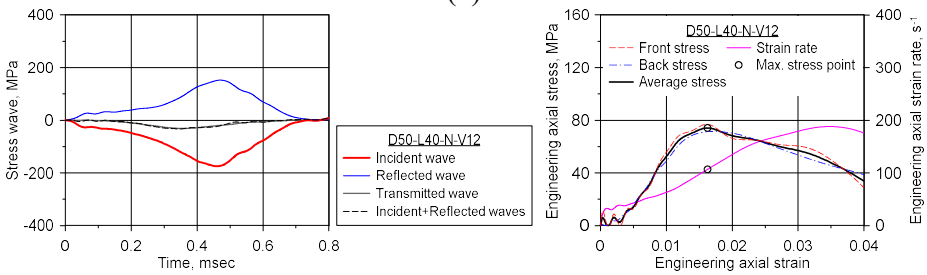
Stress wave, MPa
Time, msec
D50-L40-N-V12
Incident wave
Reflected wave
Transmitted wave
Incident+Reflected waves
Engineering axial stress, MPa
Engineering axial strain rate, s-1
Engineering axial strain
Front stress
Back stress
Average stress
Strain rate
Max. stress point

(c)

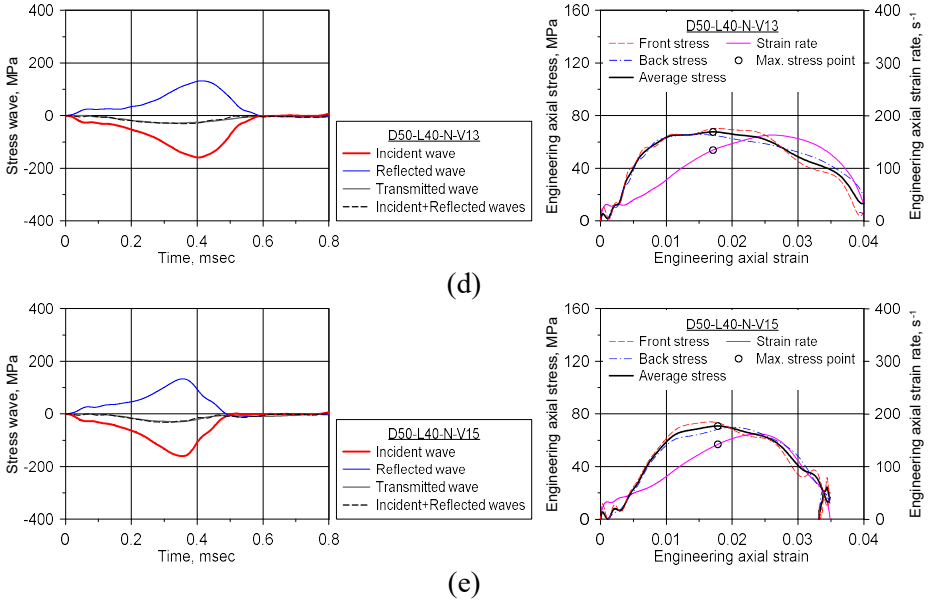

Figure C.14 Stress waves and the axial stress–strain curve of D50-L40-N; (a) D50-L40-N-V10; (b) D50-L40-N-V11; (c) D50-L40-N-V12; (d) D50-L40-N-V13; (e) D50-L40-N-V15

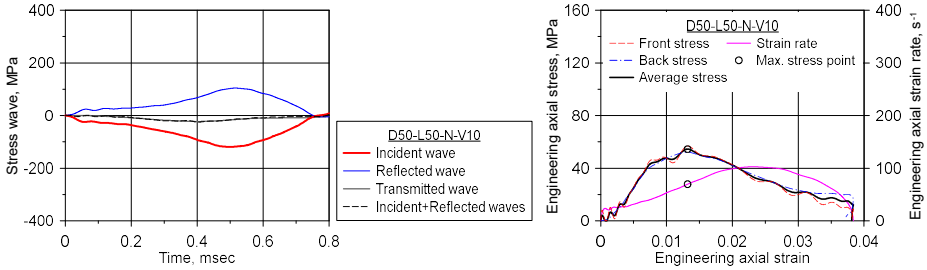
Stress wave, MPa
Time, msec
D50-L50-N-V10
Incident wave
Reflected wave
Transmitted wave
Incident+Reflected waves
Engineering axial stress, MPa
Engineering axial strain
Engineering axial strain rate, s-1
Front stress
Back stress
Average stress
Strain rate
Max. stress point

(a)

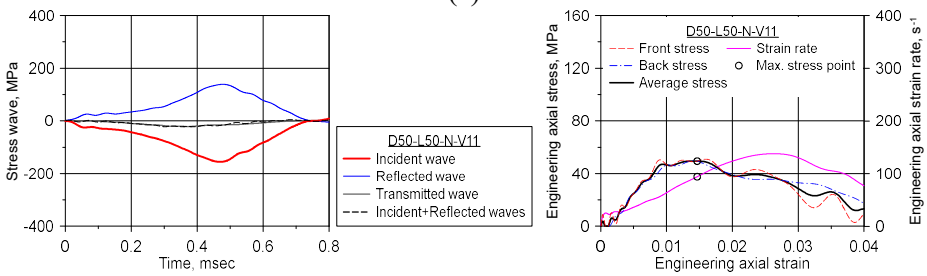
Stress wave, MPa
Time, msec
D50-L50-N-V11
Incident wave
Reflected wave
Transmitted wave
Incident+Reflected waves
Engineering axial stress, MPa
Engineering axial strain
Engineering axial strain rate, s-1
Front stress
Back stress
Average stress
Strain rate
Max. stress point

(b)

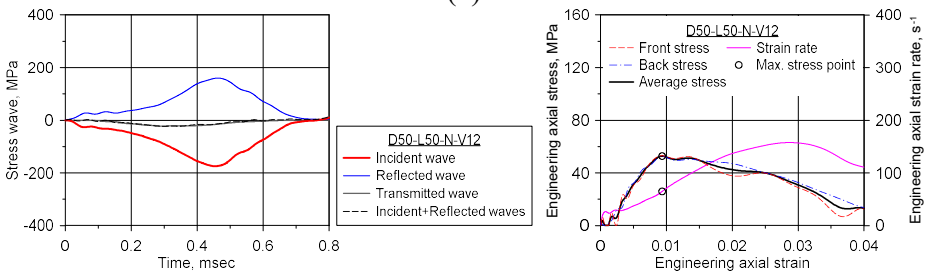
Stress wave, MPa
Time, msec
D50-L50-N-V12
Incident wave
Reflected wave
Transmitted wave
Incident+Reflected waves
Engineering axial stress, MPa
Engineering axial strain
Engineering axial strain rate, s-1
Front stress
Back stress
Average stress
Strain rate
Max. stress point

(c)

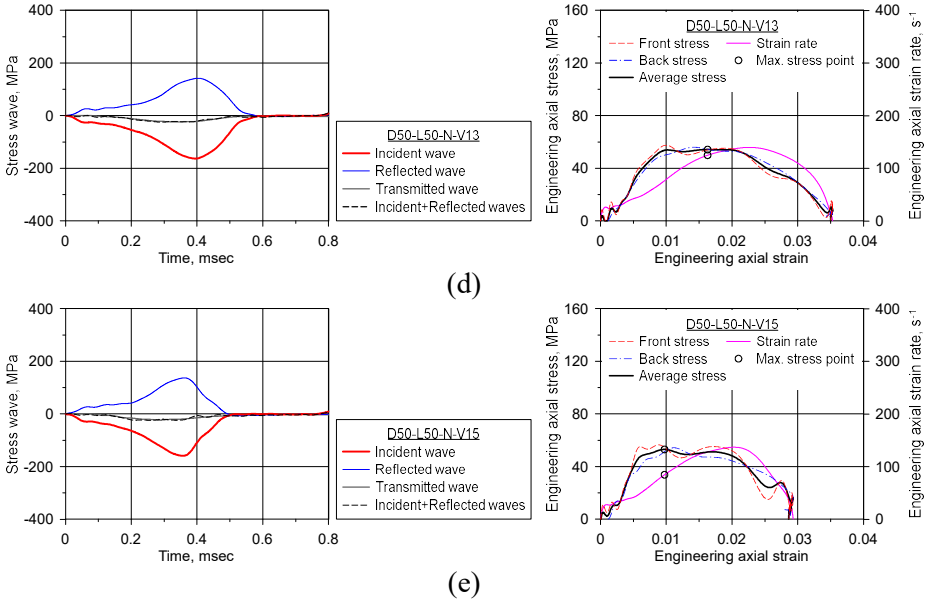

Figure C.15 Stress waves and the axial stress–strain curve of D50-L50-N;

(a) D50-L50-N-V10; (b) D50-L50-N-V11; (c) D50-L50-N-V12;

(d) D50-L50-N-V13; (e) D50-L50-N-V15

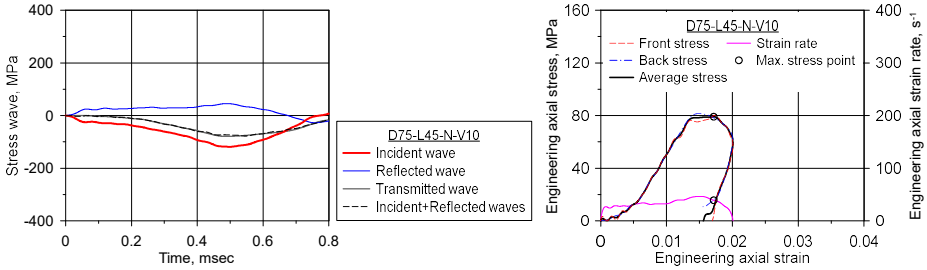
Stress wave, MPa
Time, msec
D75-L45-N-V10
Incident wave
Reflected wave
Transmitted wave
Incident+Reflected waves
Engineering axial stress, MPa
Engineering axial strain rate, s-1
Engineering axial strain
Front stress
Back stress
Average stress
Strain rate
Max. stress point

(a)

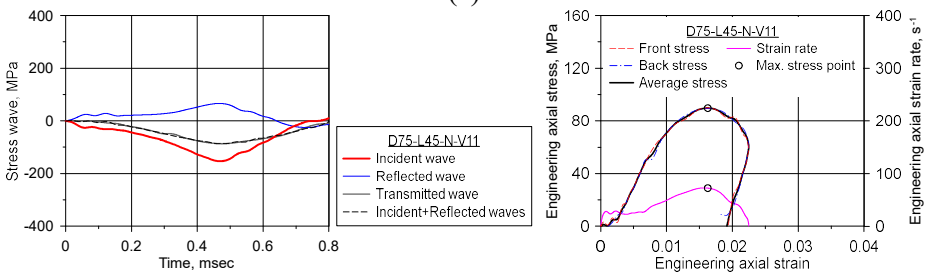
Stress wave, MPa
Time, msec
D75-L45-N-V11
Incident wave
Reflected wave
Transmitted wave
Incident+Reflected waves
Engineering axial stress, MPa
Engineering axial strain rate, s-1
Engineering axial strain
Front stress
Back stress
Average stress
Strain rate
Max. stress point

(b)

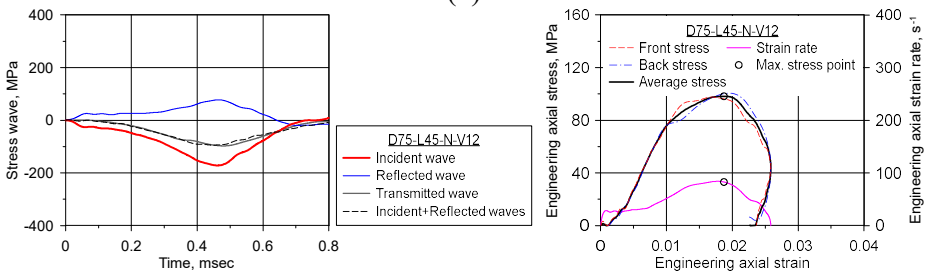
Stress wave, MPa
Time, msec
D75-L45-N-V12
Incident wave
Reflected wave
Transmitted wave
Incident+Reflected waves
Engineering axial stress, MPa
Engineering axial strain rate, s-1
Engineering axial strain
Front stress
Back stress
Average stress
Strain rate
Max. stress point

(c)

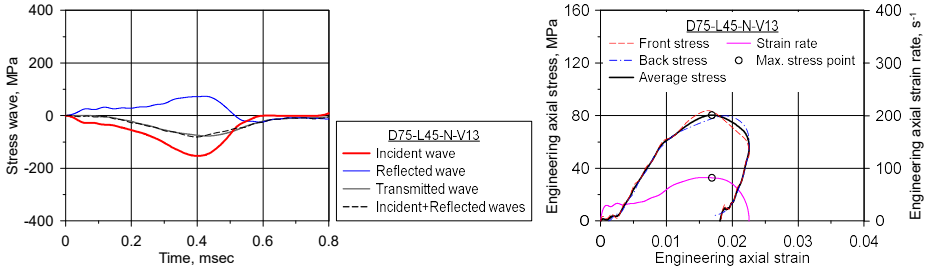

(d)

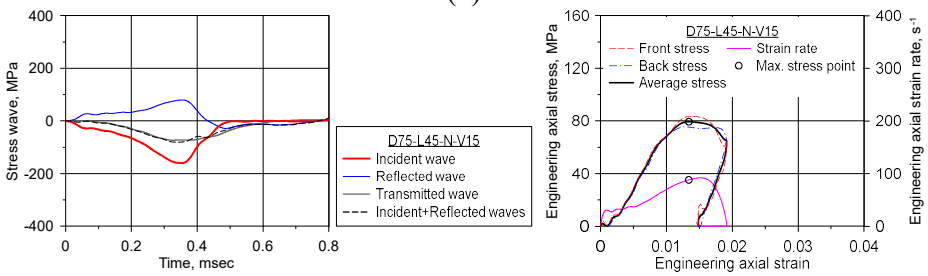

(e)

Figure C.16 Stress waves and the axial stress–strain curve of D75-L45-N;

(a) D75-L45-N-V10; (b) D75-L45-N-V11; (c) D75-L45-N-V12;

(d) D75-L45-N-V13; (e) D75-L45-N-V15

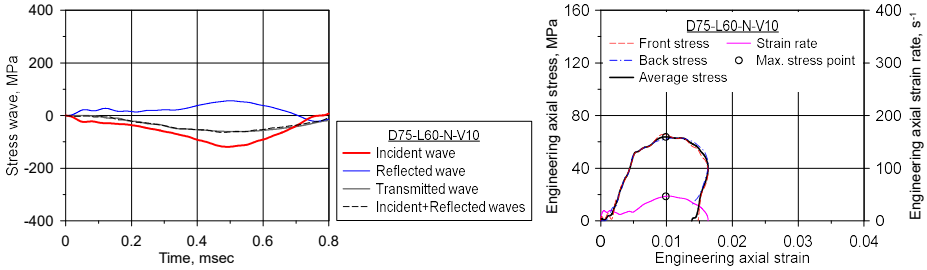
Stress wave, MPa
Time, msec
D75-L60-N-V10
Incident wave
Reflected wave
Transmitted wave
Incident+Reflected waves
Engineering axial stress, MPa
Engineering axial strain rate, s-1
Engineering axial strain
Front stress
Back stress
Average stress
Strain rate
Max. stress point

(a)

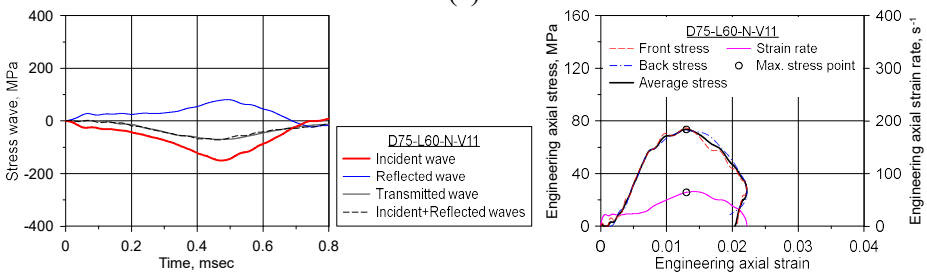
Stress wave, MPa
Time, msec
D75-L60-N-V11
Incident wave
Reflected wave
Transmitted wave
Incident+Reflected waves
Engineering axial stress, MPa
Engineering axial strain rate, s-1
Engineering axial strain
Front stress
Back stress
Average stress
Strain rate
Max. stress point

(b)

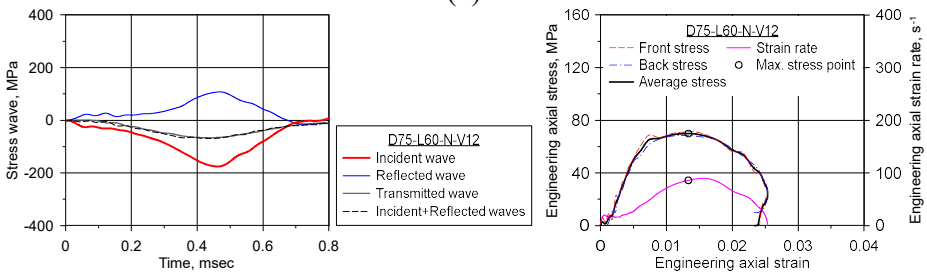
Stress wave, MPa
Time, msec
D75-L60-N-V12
Incident wave
Reflected wave
Transmitted wave
Incident+Reflected waves
Engineering axial stress, MPa
Engineering axial strain rate, s-1
Engineering axial strain
Front stress
Back stress
Average stress
Strain rate
Max. stress point

(c)

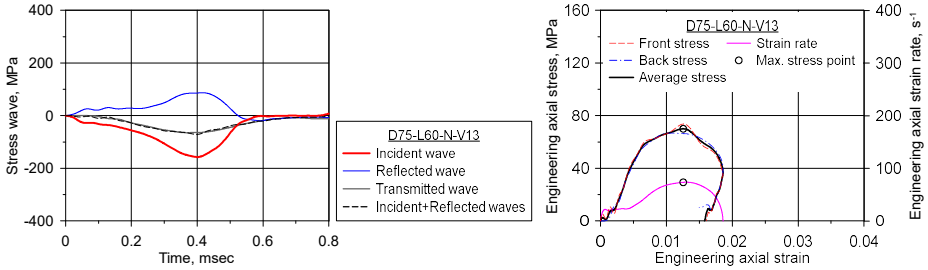

(d)

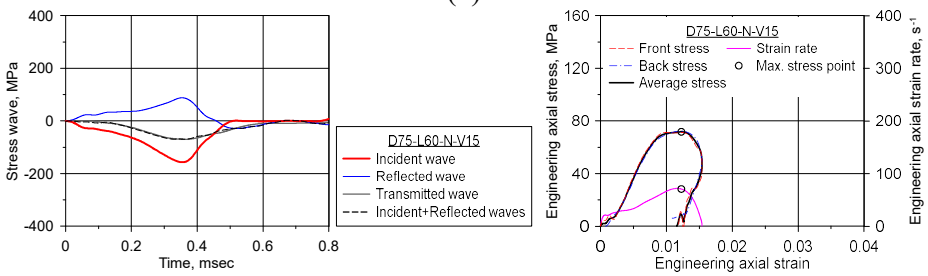

(e)

Figure C.17 Stress waves and the axial stress–strain curve of D75-L60-N;

(a) D75-L60-N-V10; (b) D75-L60-N-V11; (c) D75-L60-N-V12;

(d) D75-L60-N-V13; (e) D75-L60-N-V15

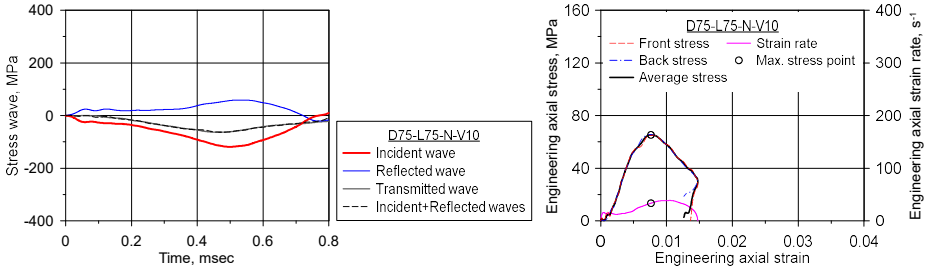
Stress wave, MPa
Time, msec
D75-L75-N-V10
Incident wave
Reflected wave
Transmitted wave
Incident+Reflected waves
Engineering axial stress, MPa
Engineering axial strain rate, s-1
Engineering axial strain
Front stress
Back stress
Average stress
Strain rate
Max. stress point

(a)

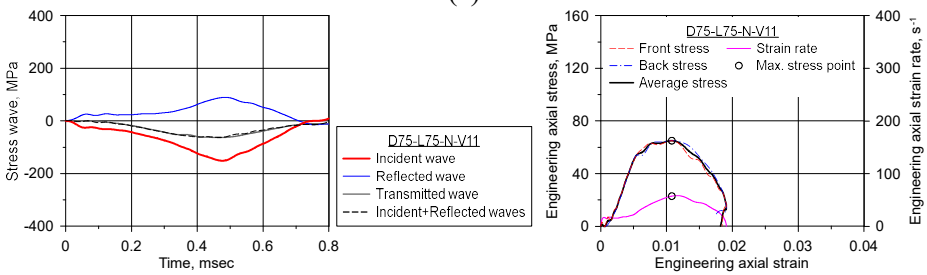
Stress wave, MPa
Time, msec
D75-L75-N-V11
Incident wave
Reflected wave
Transmitted wave
Incident+Reflected waves
Engineering axial stress, MPa
Engineering axial strain rate, s-1
Engineering axial strain
Front stress
Back stress
Average stress
Strain rate
Max. stress point

(b)

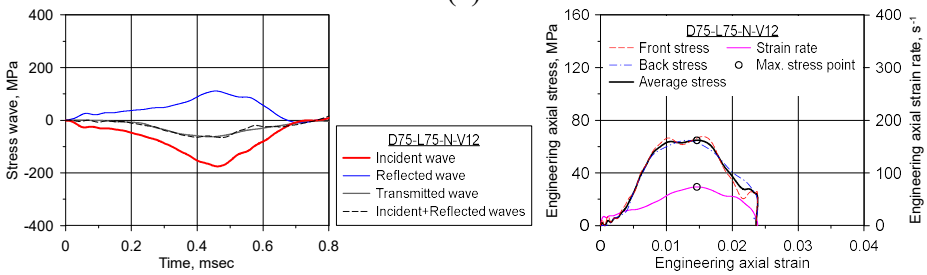
Stress wave, MPa
Time, msec
D75-L75-N-V12
Incident wave
Reflected wave
Transmitted wave
Incident+Reflected waves
Engineering axial stress, MPa
Engineering axial strain rate, s-1
Engineering axial strain
Front stress
Back stress
Average stress
Strain rate
Max. stress point

(c)

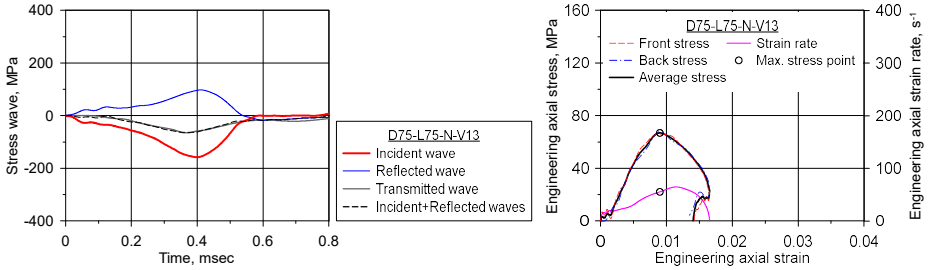

(d)

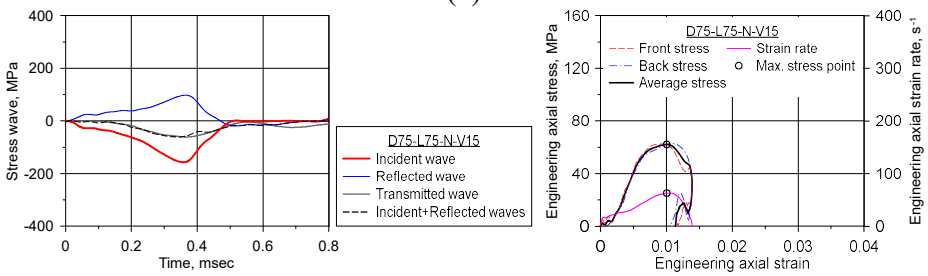

(e)

Figure C.18 Stress waves and the axial stress–strain curve of D75-L75-N;

(a) D75-L75-N-V10; (b) D75-L75-N-V11; (c) D75-L75-N-V12;

(d) D75-L75-N-V13; (e) D75-L75-N-V15

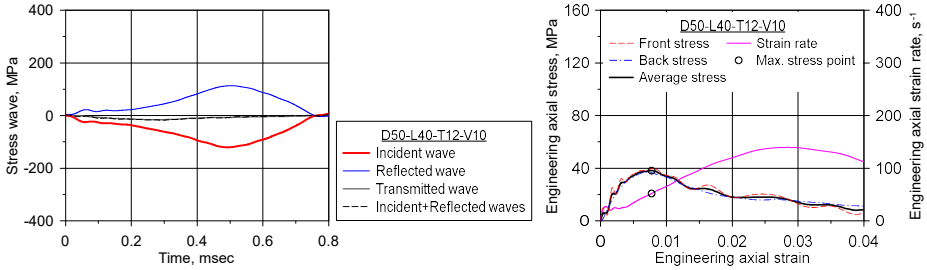
Stress wave, MPa
Time, msec
D50-L40-T12-V10
Incident wave
Reflected wave
Transmitted wave
Incident+Reflected waves
Engineering axial stress, MPa
Engineering axial strain rate, s-1
Engineering axial strain
Front stress
Back stress
Average stress
Strain rate
Max. stress point

(a)

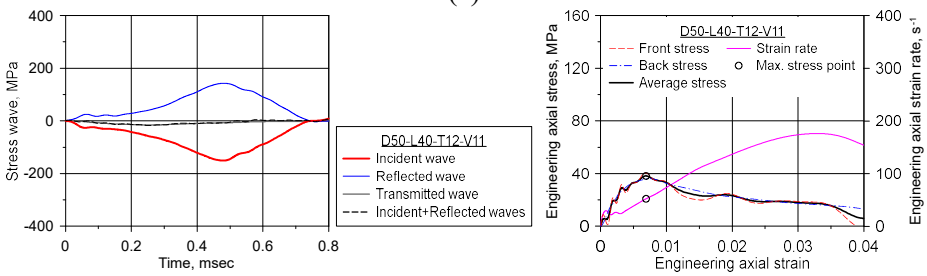
Stress wave, MPa
Time, msec
D50-L40-T12-V11
Incident wave
Reflected wave
Transmitted wave
Incident+Reflected waves
Engineering axial stress, MPa
Engineering axial strain rate, s-1
Engineering axial strain
Front stress
Back stress
Average stress
Strain rate
Max. stress point

(b)

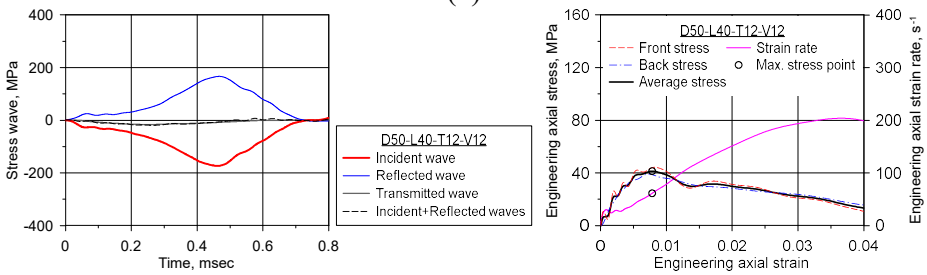
Stress wave, MPa
Time, msec
D50-L40-T12-V12
Incident wave
Reflected wave
Transmitted wave
Incident+Reflected waves
Engineering axial stress, MPa
Engineering axial strain rate, s-1
Engineering axial strain
Front stress
Back stress
Average stress
Strain rate
Max. stress point

(c)

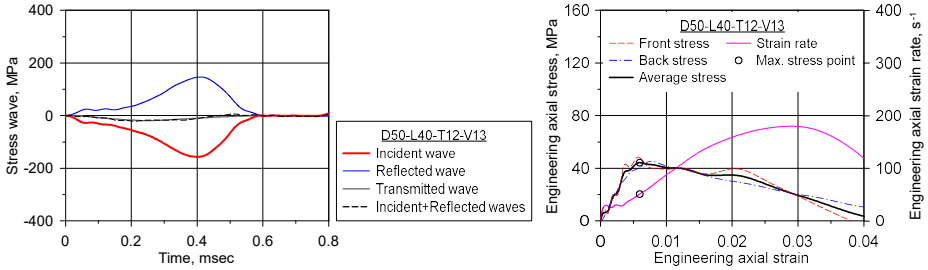

(d)

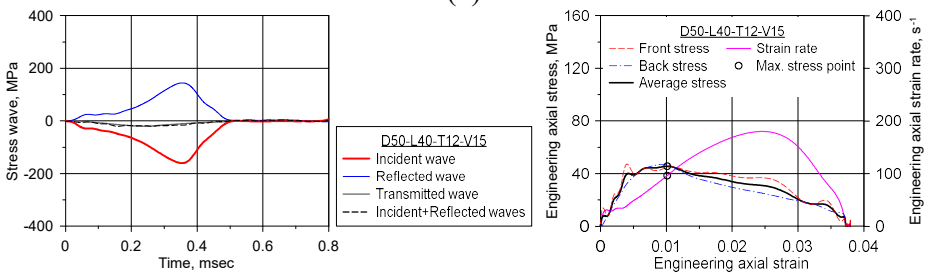

(e)

Figure C.19 Stress waves and the axial stress–strain curve of D50-L40-T12; (a) D50-L40-T12-V10; (b) D50-L40-T12-V11; (c) D50-L40-T12-V12; (d) D50-L40-T12-V13; (e) D50-L40-T12-V15

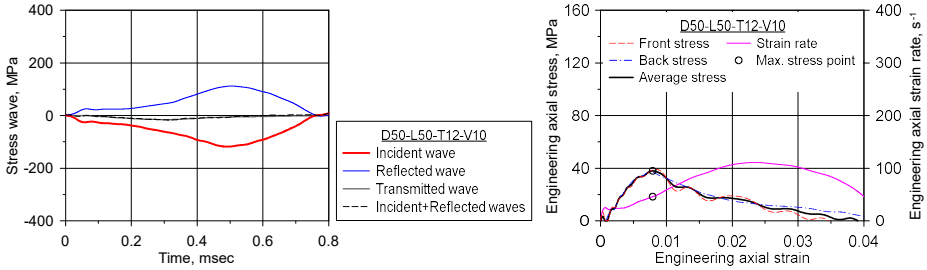
Stress wave, MPa
Time, msec
D50-L50-T12-V10
Incident wave
Reflected wave
Transmitted wave
Incident+Reflected waves
Engineering axial stress, MPa
Engineering axial strain rate, s-1
Engineering axial strain
Front stress
Back stress
Average stress
Strain rate
Max. stress point

(a)

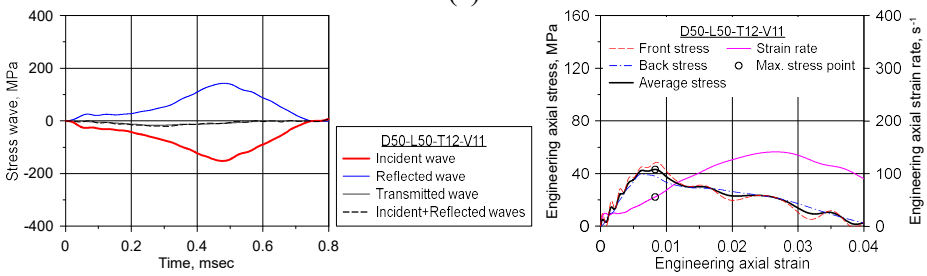
Stress wave, MPa
Time, msec
D50-L50-T12-V11
Incident wave
Reflected wave
Transmitted wave
Incident+Reflected waves
Engineering axial stress, MPa
Engineering axial strain rate, s-1
Engineering axial strain
Front stress
Back stress
Average stress
Strain rate
Max. stress point

(b)

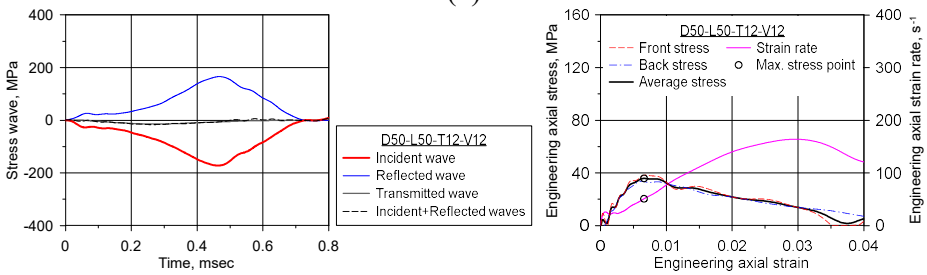
Stress wave, MPa
Time, msec
D50-L50-T12-V12
Incident wave
Reflected wave
Transmitted wave
Incident+Reflected waves
Engineering axial stress, MPa
Engineering axial strain rate, s-1
Engineering axial strain
Front stress
Back stress
Average stress
Strain rate
Max. stress point

(c)

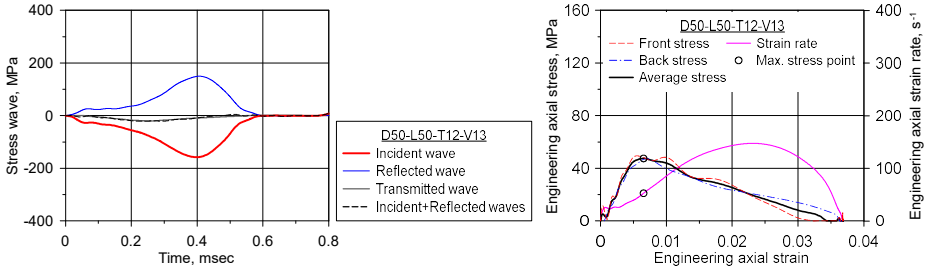

(d)

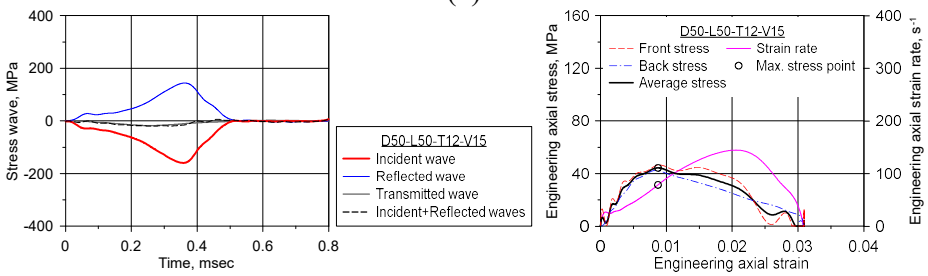

(e)

Figure C.20 Stress waves and the axial stress–strain curve of D50-L50-T12; (a) D50-L50-T12-V10; (b) D50-L50-T12-V11; (c) D50-L50-T12-V12; (d) D50-L50-T12-V13; (e) D50-L50-T12-V15

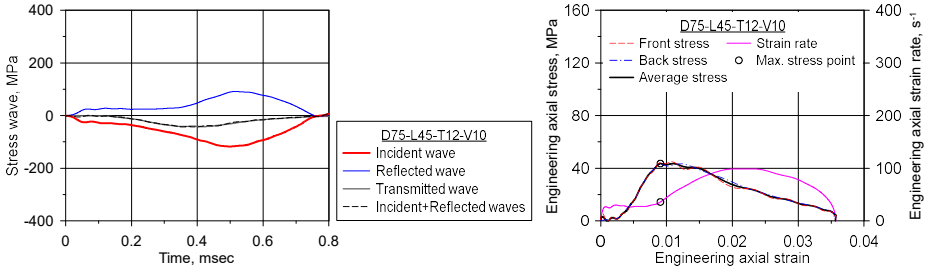
Stress wave, MPa
Time, msec
D75-L45-T12-V10
Incident wave
Reflected wave
Transmitted wave
Incident+Reflected waves
Engineering axial stress, MPa
Engineering axial strain rate, s-1
Engineering axial strain
Front stress
Back stress
Average stress
Strain rate
Max. stress point

(a)

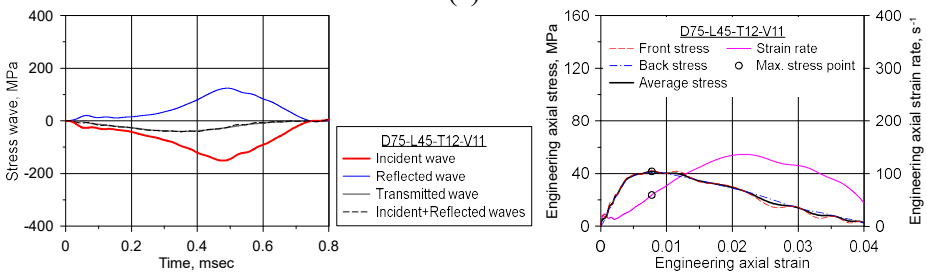
Stress wave, MPa
Time, msec
D75-L45-T12-V11
Incident wave
Reflected wave
Transmitted wave
Incident+Reflected waves
Engineering axial stress, MPa
Engineering axial strain rate, s-1
Engineering axial strain
Front stress
Back stress
Average stress
Strain rate
Max. stress point

(b)

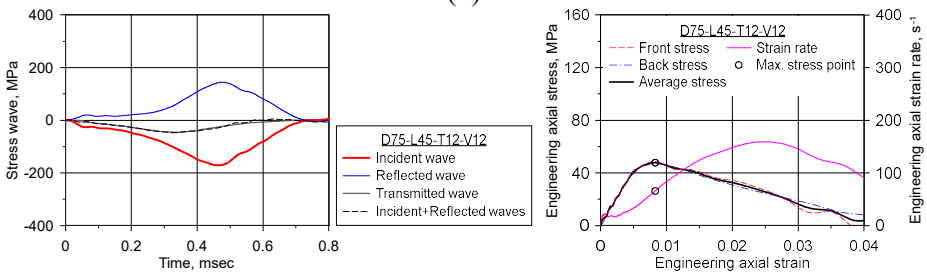
Stress wave, MPa
Time, msec
D75-L45-T12-V12
Incident wave
Reflected wave
Transmitted wave
Incident+Reflected waves
Engineering axial stress, MPa
Engineering axial strain rate, s-1
Engineering axial strain
Front stress
Back stress
Average stress
Strain rate
Max. stress point

(c)

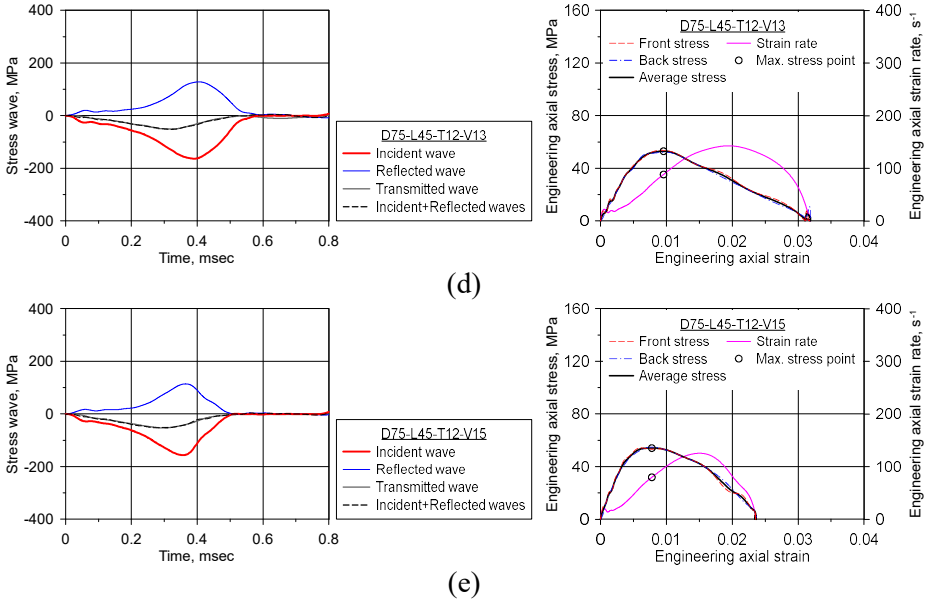

Figure C.21 Stress waves and the axial stress–strain curve of D75-L45-T12; (a) D75-L45-T12-V10; (b) D75-L45-T12-V11; (c) D75-L45-T12-V12; (d) D75-L45-T12-V13; (e) D75-L45-T12-V15

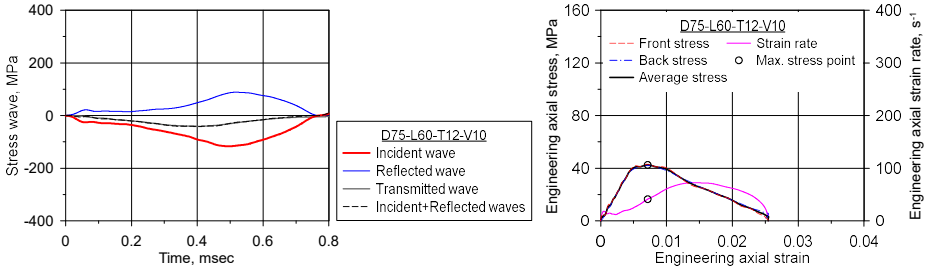
Stress wave, MPa
Time, msec
D75-L60-T12-V10
Incident wave
Reflected wave
Transmitted wave
Incident+Reflected waves
Engineering axial stress, MPa
Engineering axial strain rate, s-1
Engineering axial strain
Front stress
Back stress
Average stress
Strain rate
Max. stress point

(a)

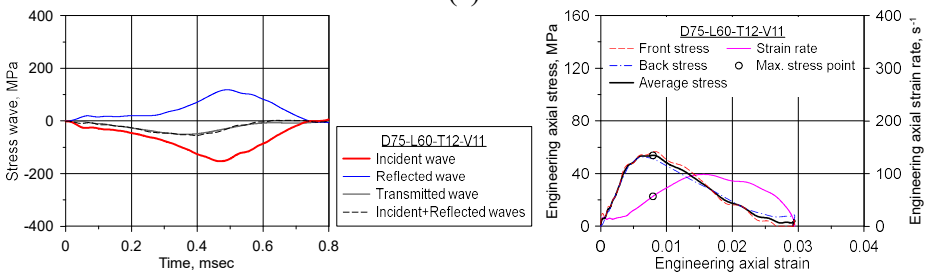
Stress wave, MPa
Time, msec
D75-L60-T12-V11
Incident wave
Reflected wave
Transmitted wave
Incident+Reflected waves
Engineering axial stress, MPa
Engineering axial strain rate, s-1
Engineering axial strain
Front stress
Back stress
Average stress
Strain rate
Max. stress point

(b)

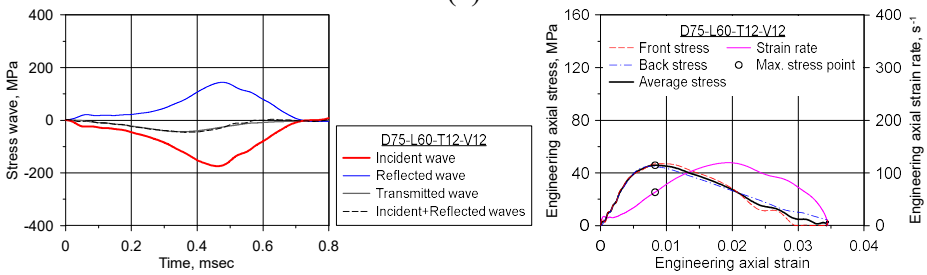
Stress wave, MPa
Time, msec
D75-L60-T12-V12
Incident wave
Reflected wave
Transmitted wave
Incident+Reflected waves
Engineering axial stress, MPa
Engineering axial strain rate, s-1
Engineering axial strain
Front stress
Back stress
Average stress
Strain rate
Max. stress point

(c)

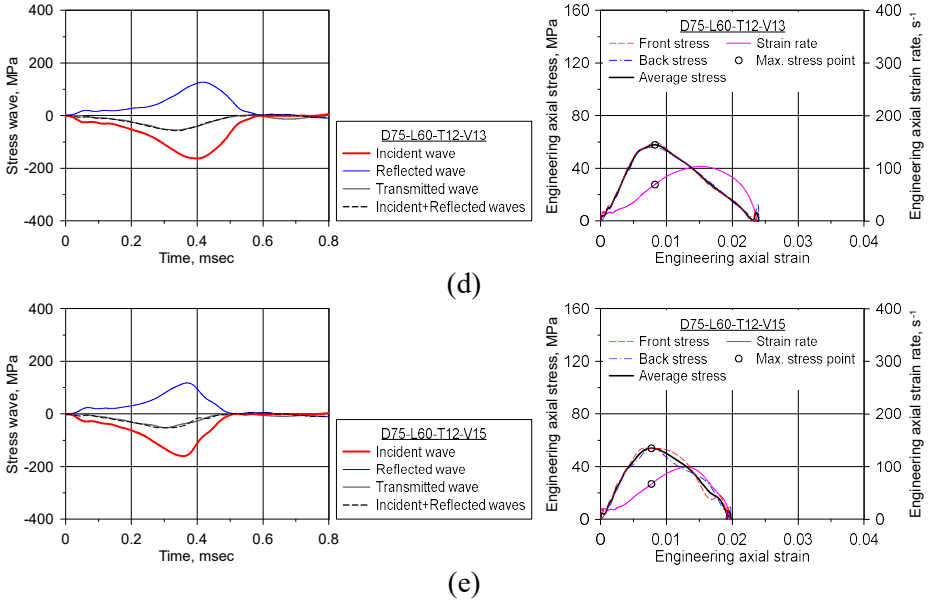

Figure C.22 Stress waves and the axial stress–strain curve of D75-L60-T12; (a) D75-L60-T12-V10; (b) D75-L60-T12-V11; (c) D75-L60-T12-V12; (d) D75-L60-T12-V13; (e) D75-L60-T12-V15

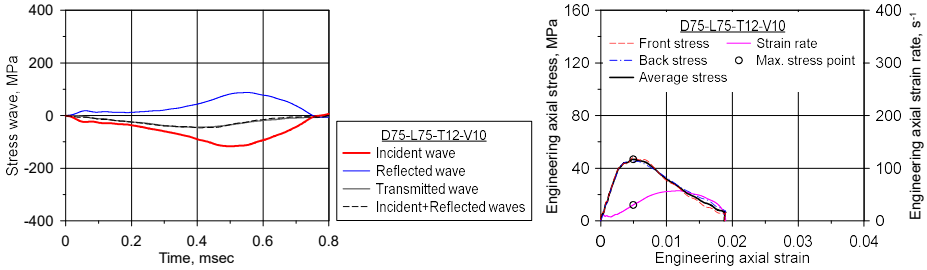
Stress wave, MPa
Time, msec
D75-L75-T12-V10
Incident wave
Reflected wave
Transmitted wave
Incident+Reflected waves
Engineering axial stress, MPa
Engineering axial strain rate, s-1
Engineering axial strain
Front stress
Back stress
Average stress
Strain rate
Max. stress point

(a)

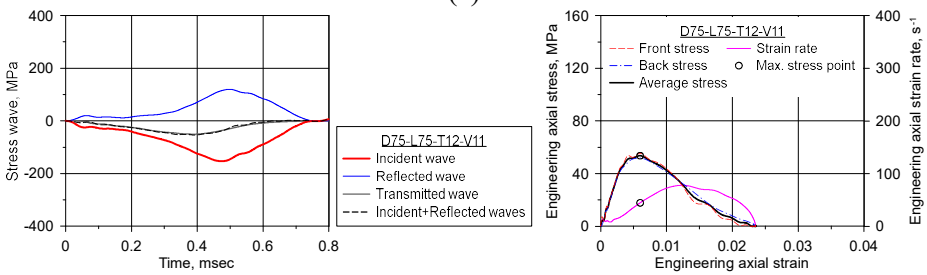
Stress wave, MPa
Time, msec
D75-L75-T12-V11
Incident wave
Reflected wave
Transmitted wave
Incident+Reflected waves
Engineering axial stress, MPa
Engineering axial strain rate, s-1
Engineering axial strain
Front stress
Back stress
Average stress
Strain rate
Max. stress point

(b)

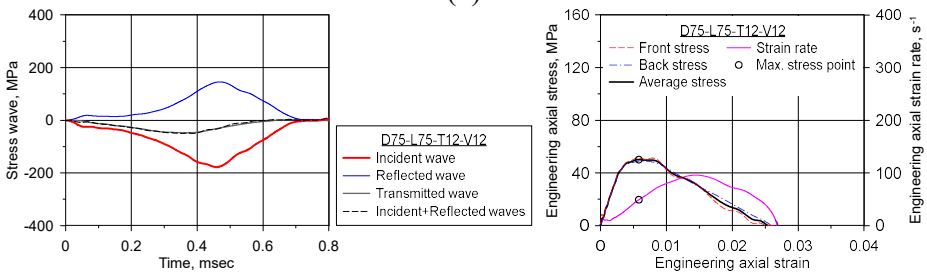
Stress wave, MPa
Time, msec
D75-L75-T12-V12
Incident wave
Reflected wave
Transmitted wave
Incident+Reflected waves
Engineering axial stress, MPa
Engineering axial strain rate, s-1
Engineering axial strain
Front stress
Back stress
Average stress
Strain rate
Max. stress point

(c)

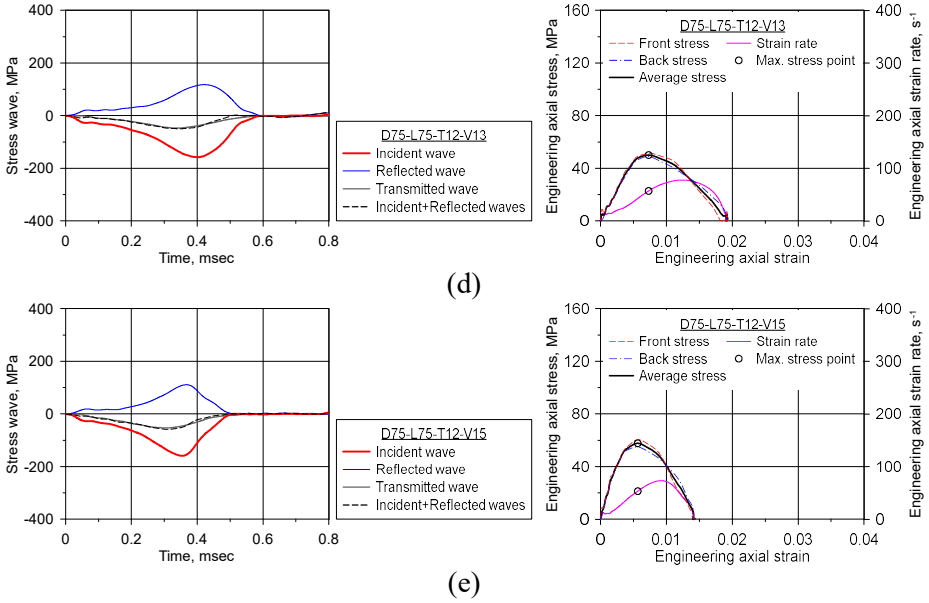

Figure C.23 Stress waves and the axial stress–strain curve of D75-L75-T12; (a) D75-L75-T12-V10; (b) D75-L75-T12-V11; (c) D75-L75-T12-V12; (d) D75-L75-T12-V13; (e) D75-L75-T12-V15

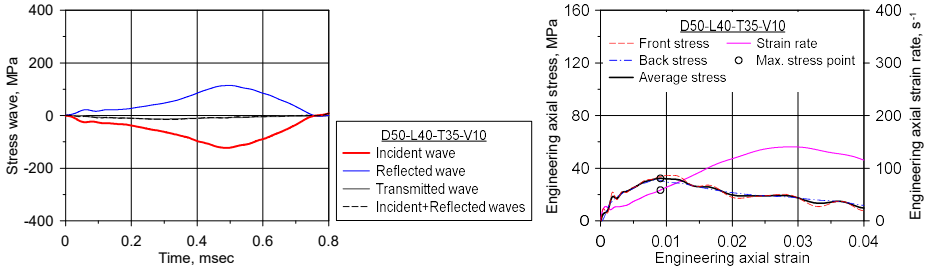
Stress wave, MPa
Time, msec
D50-L40-T35-V10
Incident wave
Reflected wave
Transmitted wave
Incident+Reflected waves
Engineering axial stress, MPa
Engineering axial strain rate, s-1
Engineering axial strain
Front stress
Back stress
Average stress
Strain rate
Max. stress point

(a)

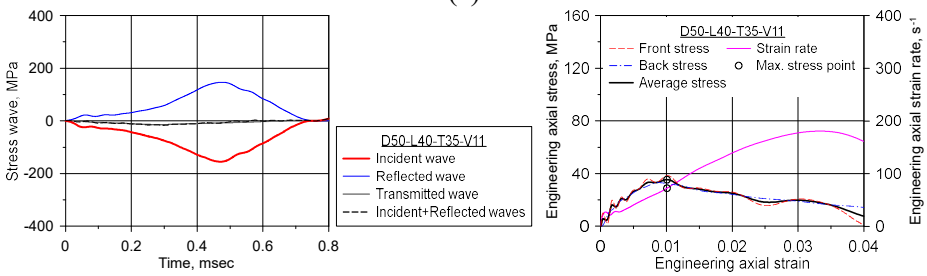
Stress wave, MPa
Time, msec
D50-L40-T35-V11
Incident wave
Reflected wave
Transmitted wave
Incident+Reflected waves
Engineering axial stress, MPa
Engineering axial strain rate, s-1
Engineering axial strain
Front stress
Back stress
Average stress
Strain rate
Max. stress point

(b)

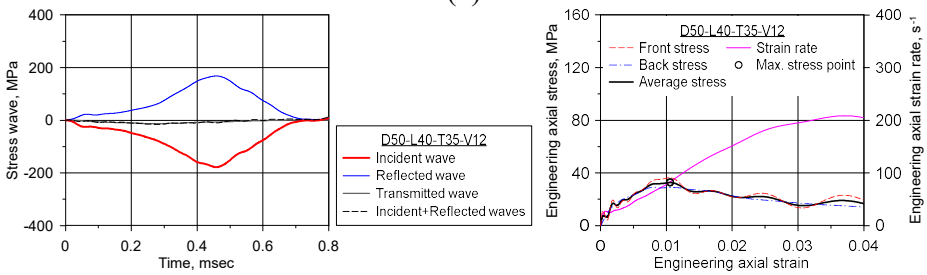
Stress wave, MPa
Time, msec
D50-L40-T35-V12
Incident wave
Reflected wave
Transmitted wave
Incident+Reflected waves
Engineering axial stress, MPa
Engineering axial strain rate, s-1
Engineering axial strain
Front stress
Back stress
Average stress
Strain rate
Max. stress point

(c)

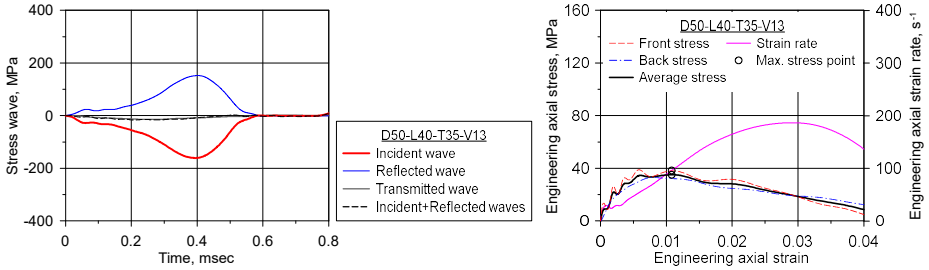

(d)

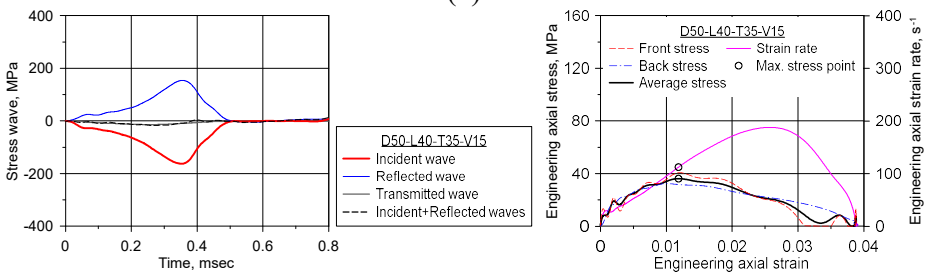

(e)

Figure C.24 Stress waves and the axial stress–strain curve of D50-L40-T35; (a) D50-L40-T35-V10; (b) D50-L40-T35-V11; (c) D50-L40-T35-V12; (d) D50-L40-T35-V13; (e) D50-L40-T35-V15

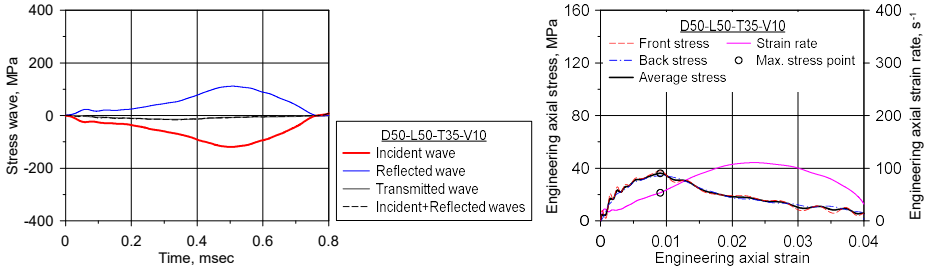
Stress wave, MPa
Time, msec
D50-L50-T35-V10
Incident wave
Reflected wave
Transmitted wave
Incident+Reflected waves
Engineering axial stress, MPa
Engineering axial strain rate, s-1
Engineering axial strain
Front stress
Back stress
Average stress
Strain rate
Max. stress point

(a)

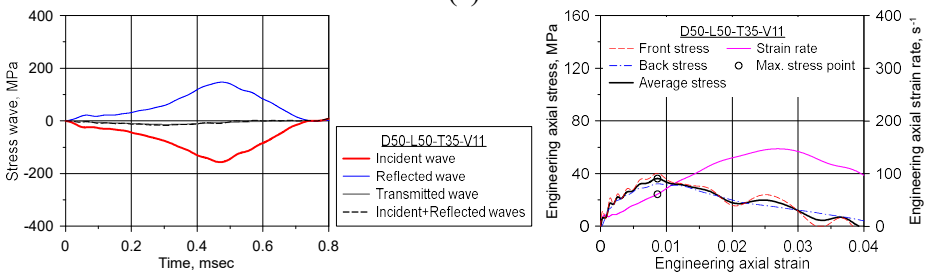
Stress wave, MPa
Time, msec
D50-L50-T35-V11
Incident wave
Reflected wave
Transmitted wave
Incident+Reflected waves
Engineering axial stress, MPa
Engineering axial strain rate, s-1
Engineering axial strain
Front stress
Back stress
Average stress
Strain rate
Max. stress point

(b)

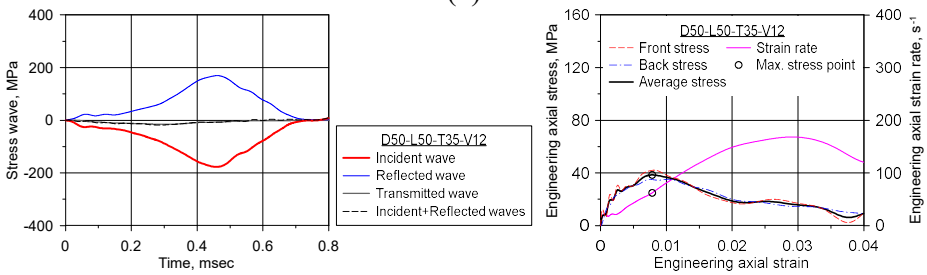
Stress wave, MPa
Time, msec
D50-L50-T35-V12
Incident wave
Reflected wave
Transmitted wave
Incident+Reflected waves
Engineering axial stress, MPa
Engineering axial strain rate, s-1
Engineering axial strain
Front stress
Back stress
Average stress
Strain rate
Max. stress point

(c)

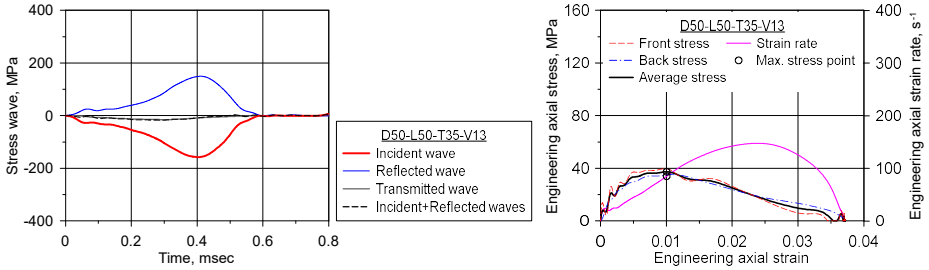

(d)

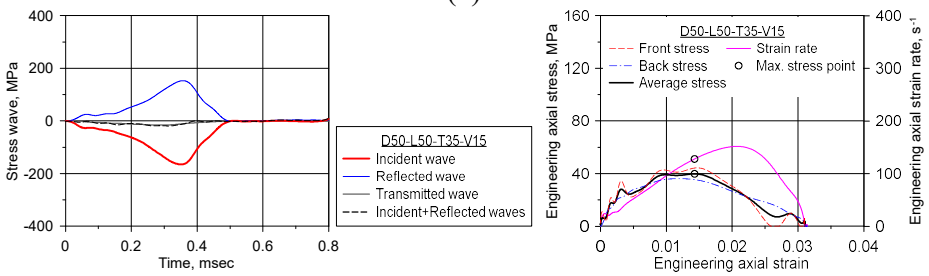

(e)

Figure C.25 Stress waves and the axial stress–strain curve of D50-L50-T35; (a) D50-L50-T35-V10; (b) D50-L50-T35-V11; (c) D50-L50-T35-V12; (d) D50-L50-T35-V13; (e) D50-L50-T35-V15

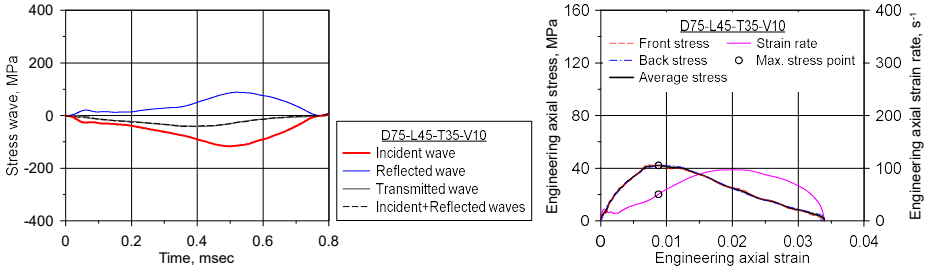
Stress wave, MPa
Time, msec
D75-L45-T35-V10
Incident wave
Reflected wave
Transmitted wave
Incident+Reflected waves
Engineering axial stress, MPa
Engineering axial strain rate, s-1
Engineering axial strain
Front stress
Back stress
Average stress
Strain rate
Max. stress point

(a)

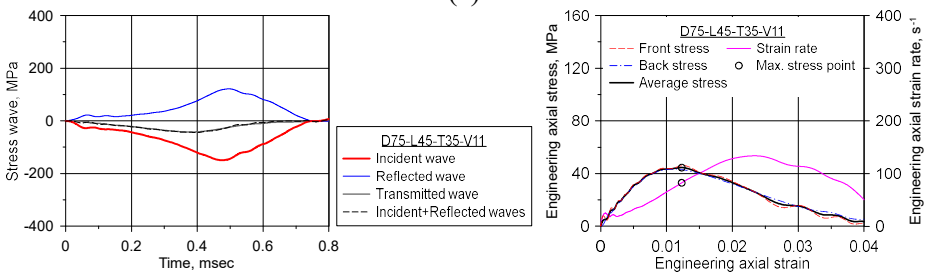
Stress wave, MPa
Time, msec
D75-L45-T35-V11
Incident wave
Reflected wave
Transmitted wave
Incident+Reflected waves
Engineering axial stress, MPa
Engineering axial strain rate, s-1
Engineering axial strain
Front stress
Back stress
Average stress
Strain rate
Max. stress point

(b)

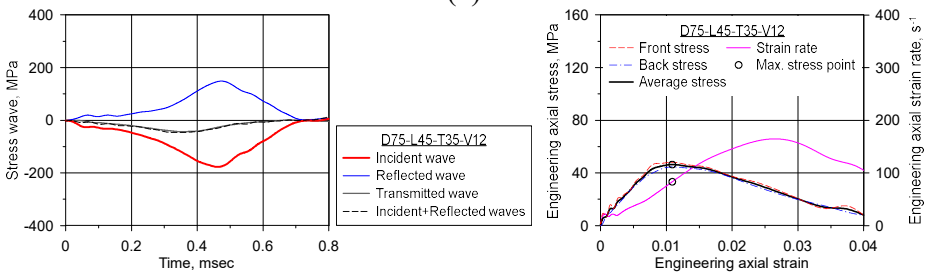
Stress wave, MPa
Time, msec
D75-L45-T35-V12
Incident wave
Reflected wave
Transmitted wave
Incident+Reflected waves
Engineering axial stress, MPa
Engineering axial strain rate, s-1
Engineering axial strain
Front stress
Back stress
Average stress
Strain rate
Max. stress point

(c)

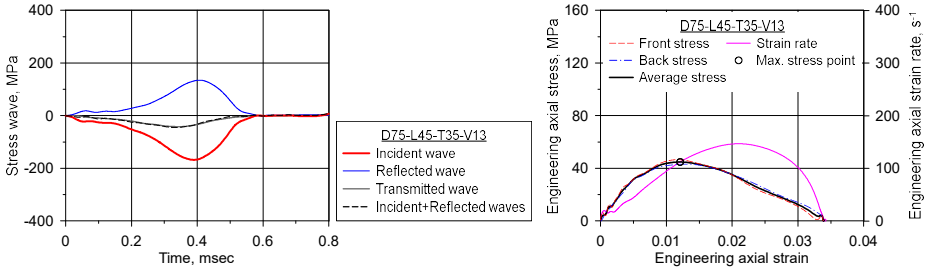

(d)

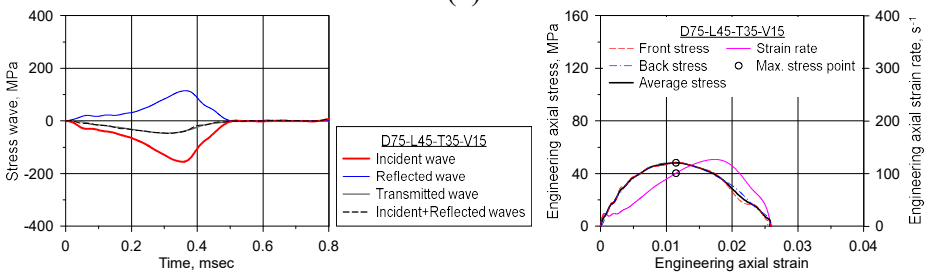

(e)

Figure C.26 Stress waves and the axial stress–strain curve of D75-L45-T35; (a) D75-L45-T35-V10; (b) D75-L45-T35-V11; (c) D75-L45-T35-V12; (d) D75-L45-T35-V13; (e) D75-L45-T35-V15

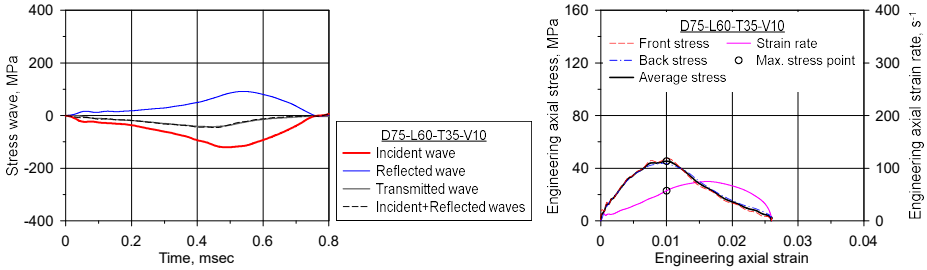
Stress wave, MPa
Time, msec
D75-L60-T35-V10
Incident wave
Reflected wave
Transmitted wave
Incident+Reflected waves
Engineering axial stress, MPa
Engineering axial strain rate, s-1
Engineering axial strain
Front stress
Back stress
Average stress
Strain rate
Max. stress point

(a)

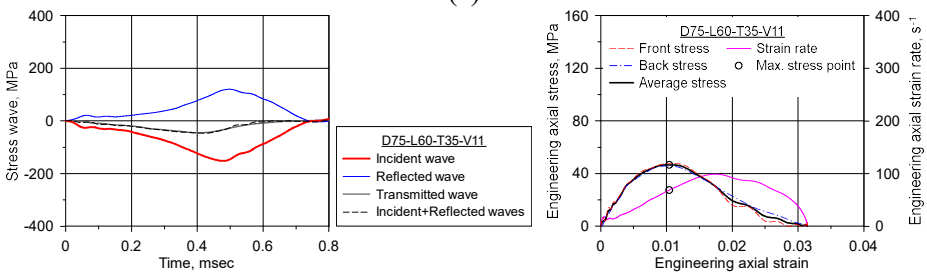
Stress wave, MPa
Time, msec
D75-L60-T35-V11
Incident wave
Reflected wave
Transmitted wave
Incident+Reflected waves
Engineering axial stress, MPa
Engineering axial strain rate, s-1
Engineering axial strain
Front stress
Back stress
Average stress
Strain rate
Max. stress point

(b)

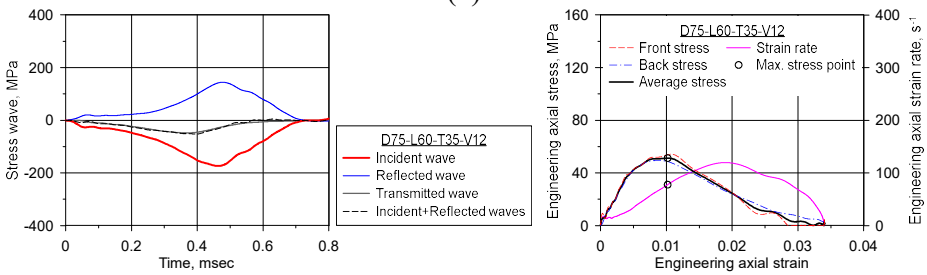
Stress wave, MPa
Time, msec
D75-L60-T35-V12
Incident wave
Reflected wave
Transmitted wave
Incident+Reflected waves
Engineering axial stress, MPa
Engineering axial strain rate, s-1
Engineering axial strain
Front stress
Back stress
Average stress
Strain rate
Max. stress point

(c)

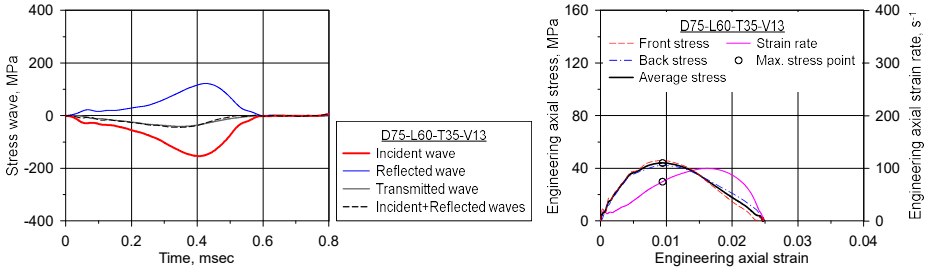

(d)

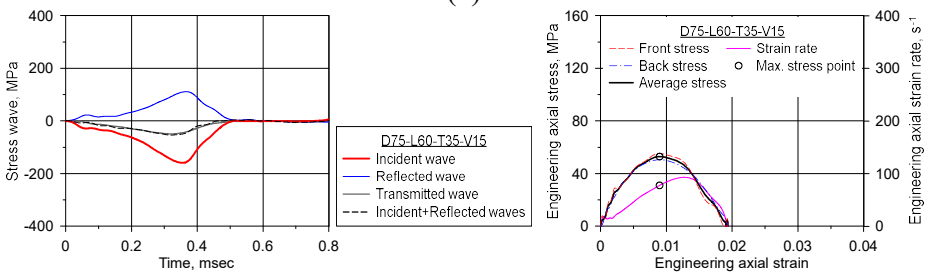

(e)

Figure C.27 Stress waves and the axial stress–strain curve of D75-L60-T35; (a) D75-L60-T35-V10; (b) D75-L60-T35-V11; (c) D75-L60-T35-V12; (d) D75-L60-T35-V13; (e) D75-L60-T35-V15

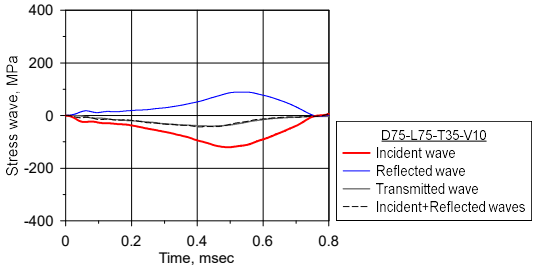
Stress wave, MPa
Time, msec
D75-L75-T35-V10
Incident wave
Reflected wave
Transmitted wave
Incident+Reflected waves

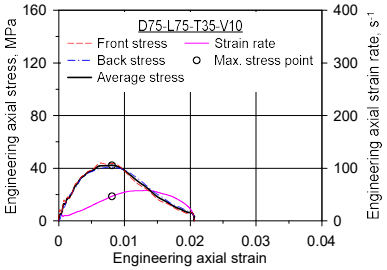
D75-L75-T35-V10
Front stress
Strain rate
Back stress
Max. stress point
Average stress
Engineering axial stress, MPa
Engineering axial strain rate, s-1
Engineering axial strain

(a)

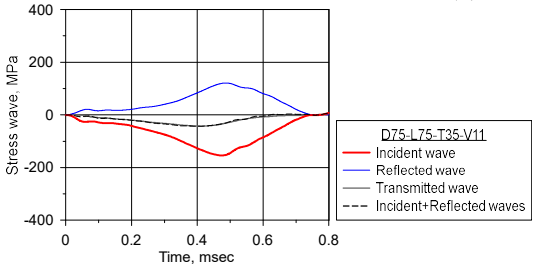
Stress wave, MPa
Time, msec
D75-L75-T35-V11
Incident wave
Reflected wave
Transmitted wave
Incident+Reflected waves

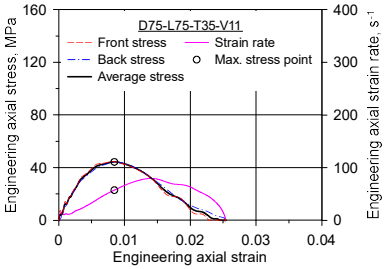
D75-L75-T35-V11
Front stress
Strain rate
Back stress
Max. stress point
Average stress
Engineering axial stress, MPa
Engineering axial strain rate, s-1
Engineering axial strain

(b)

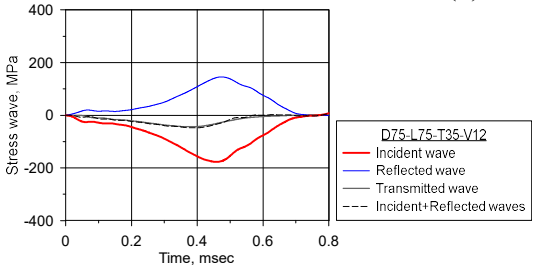
Stress wave, MPa
Time, msec
D75-L75-T35-V12
Incident wave
Reflected wave
Transmitted wave
Incident+Reflected waves

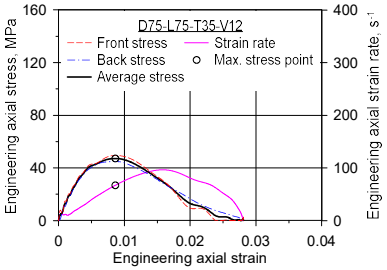
D75-L75-T35-V12
Front stress
Strain rate
Back stress
Max. stress point
Average stress
Engineering axial stress, MPa
Engineering axial strain rate, s-1
Engineering axial strain

(c)

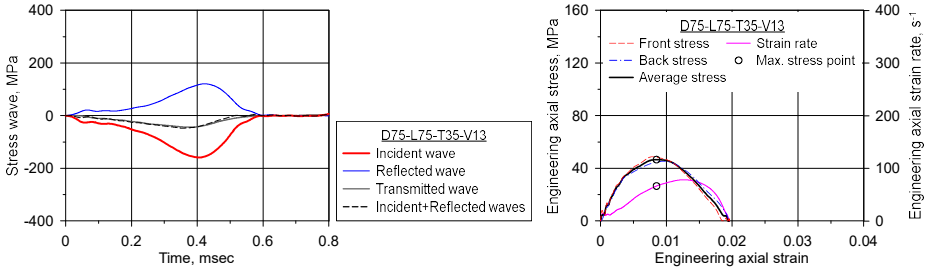

(d)

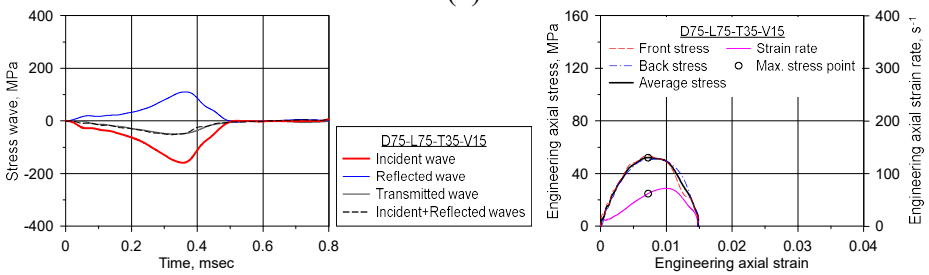

(e)

Figure C.28 Stress waves and the axial stress–strain curve of D75-L75-T35; (a) D75-L75-T35-V10; (b) D75-L75-T35-V11; (c) D75-L75-T35-V12; (d) D75-L75-T35-V13; (e) D75-L75-T35-V15

Appendix D

Experimental Results of SHPB Test for Investigation on the Effect of Incident Wave Rate

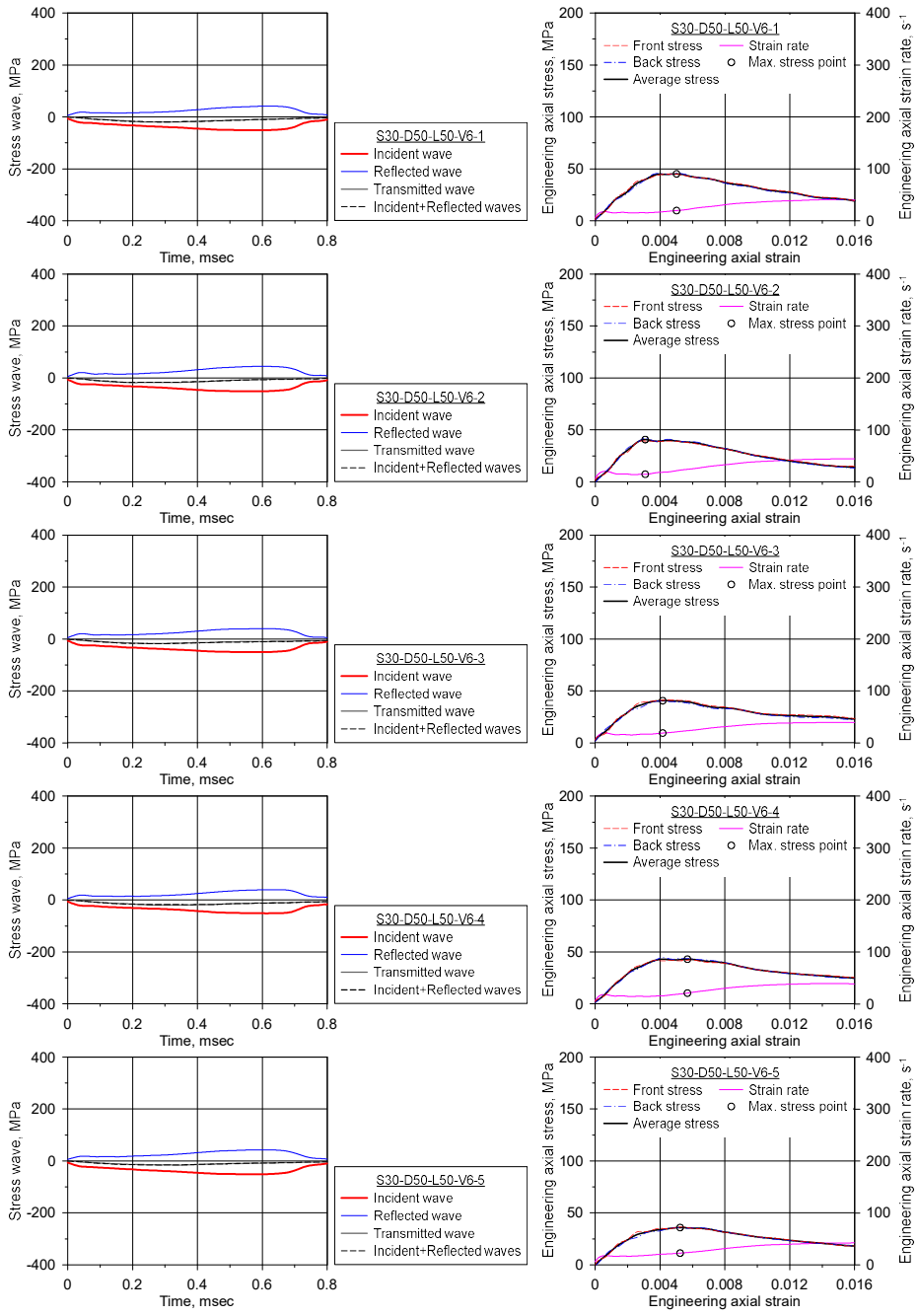

Figure D.1 Stress waves and the axial stress–strain curve of S30-D50-L50-V6

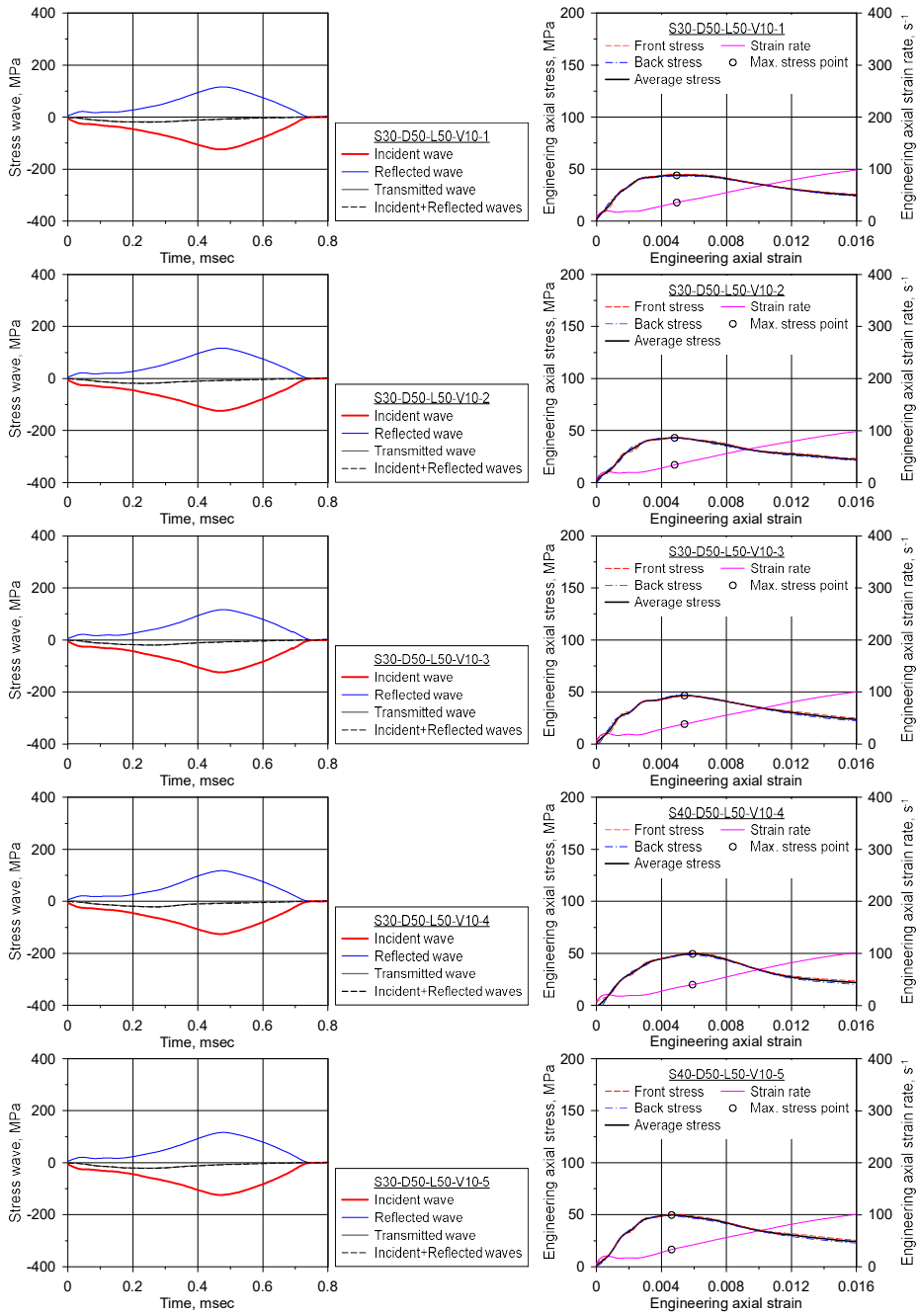

Figure D.2 Stress waves and the axial stress–strain curve of S30-D50-L50-V10

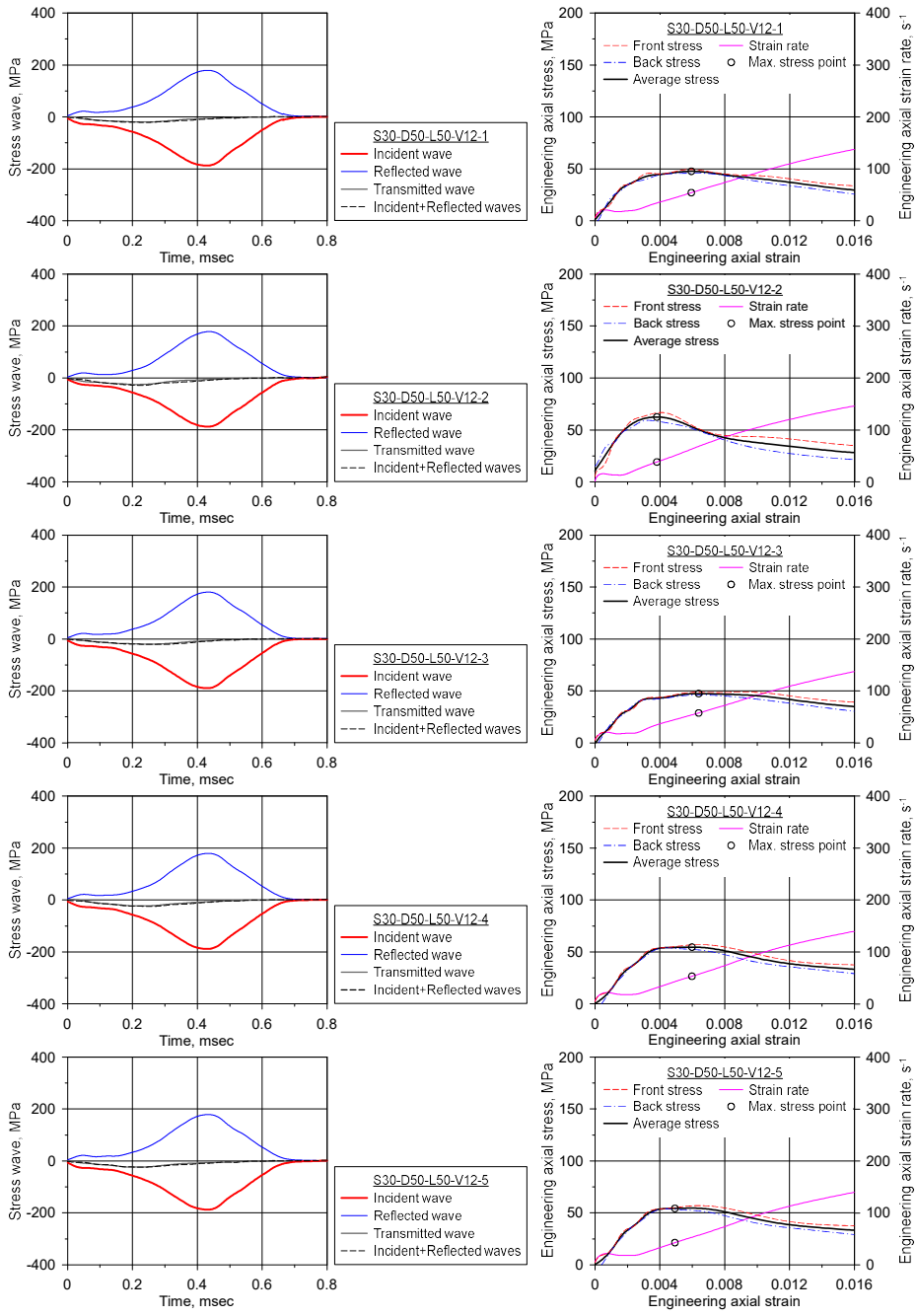

Figure D.3 Stress waves and the axial stress–strain curve of S30-D50-L50-V12

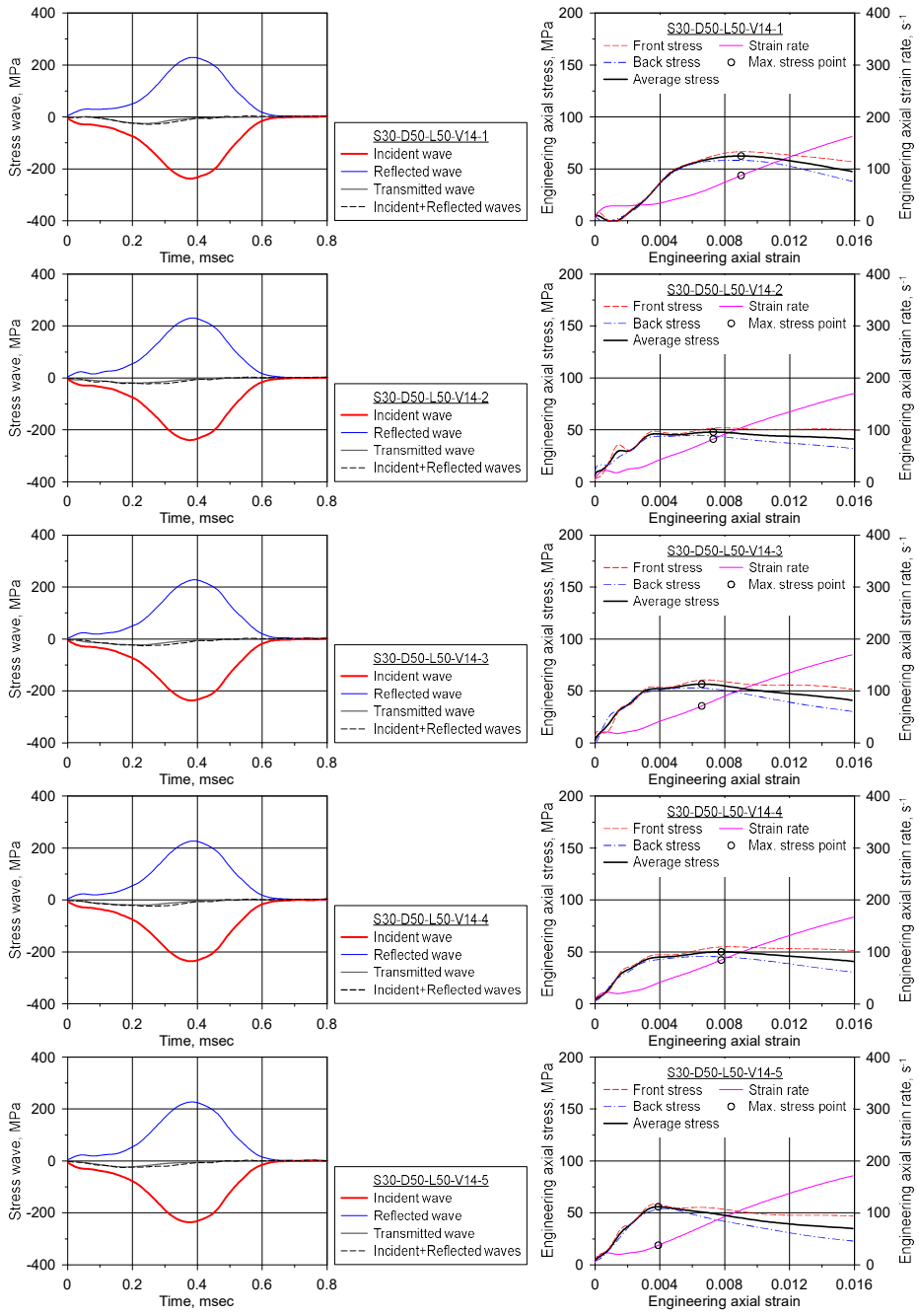

Figure D.4 Stress waves and the axial stress–strain curve of S30-D50-L50-V14

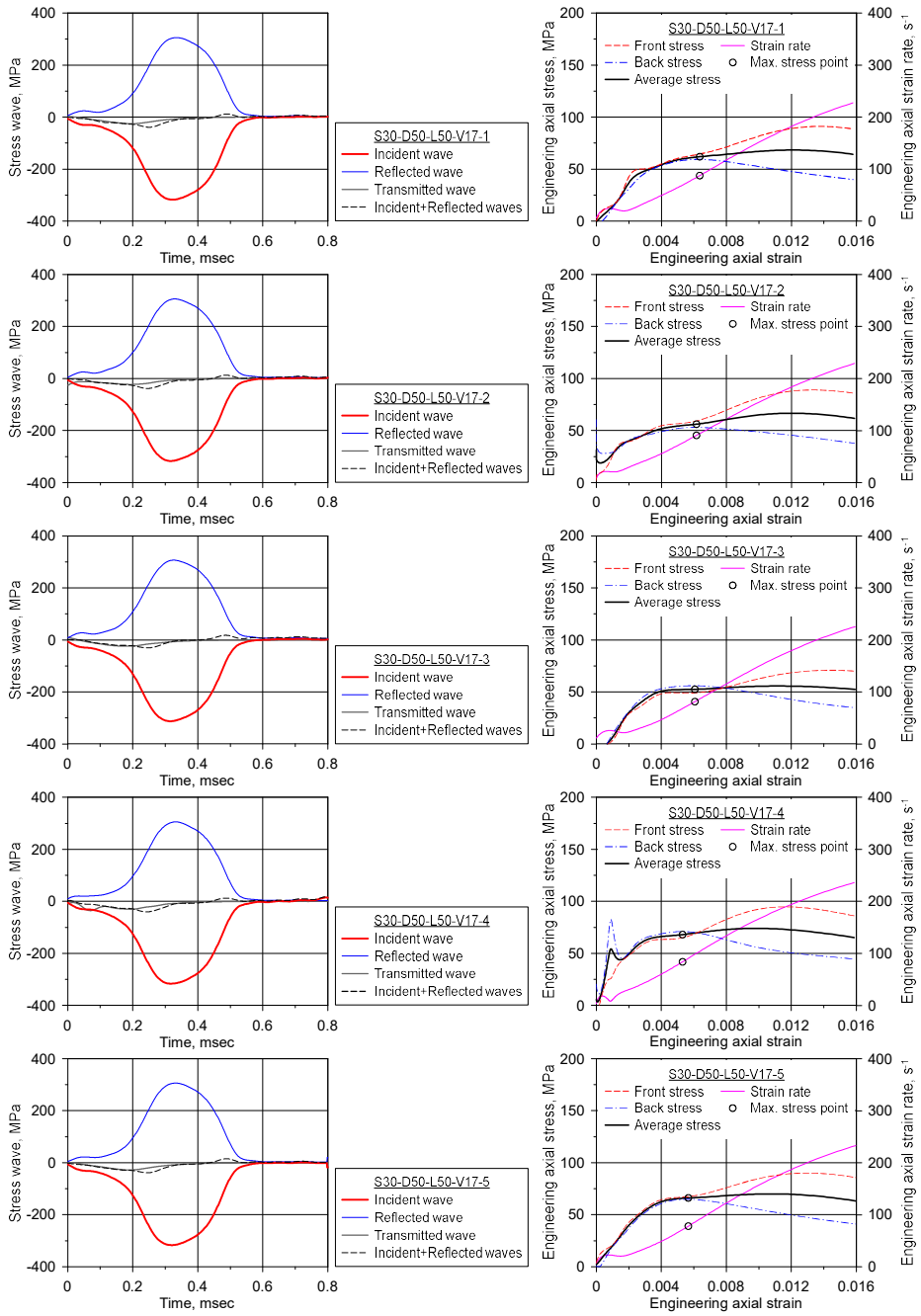

Figure D.5 Stress waves and the axial stress–strain curve of S30-D50-L50-V17

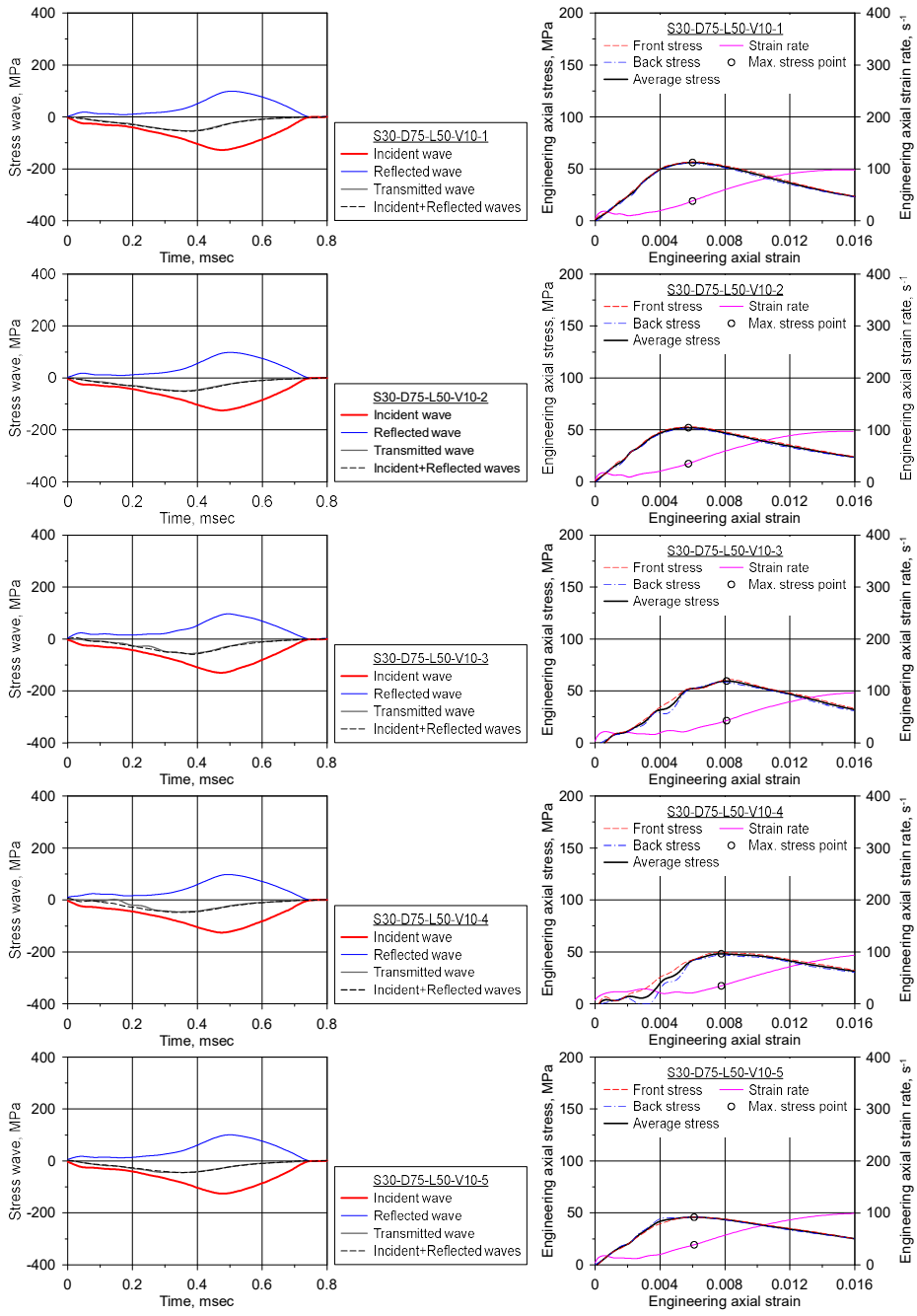

Figure D.6 Stress waves and the axial stress–strain curve of S30-D75-L50-V10

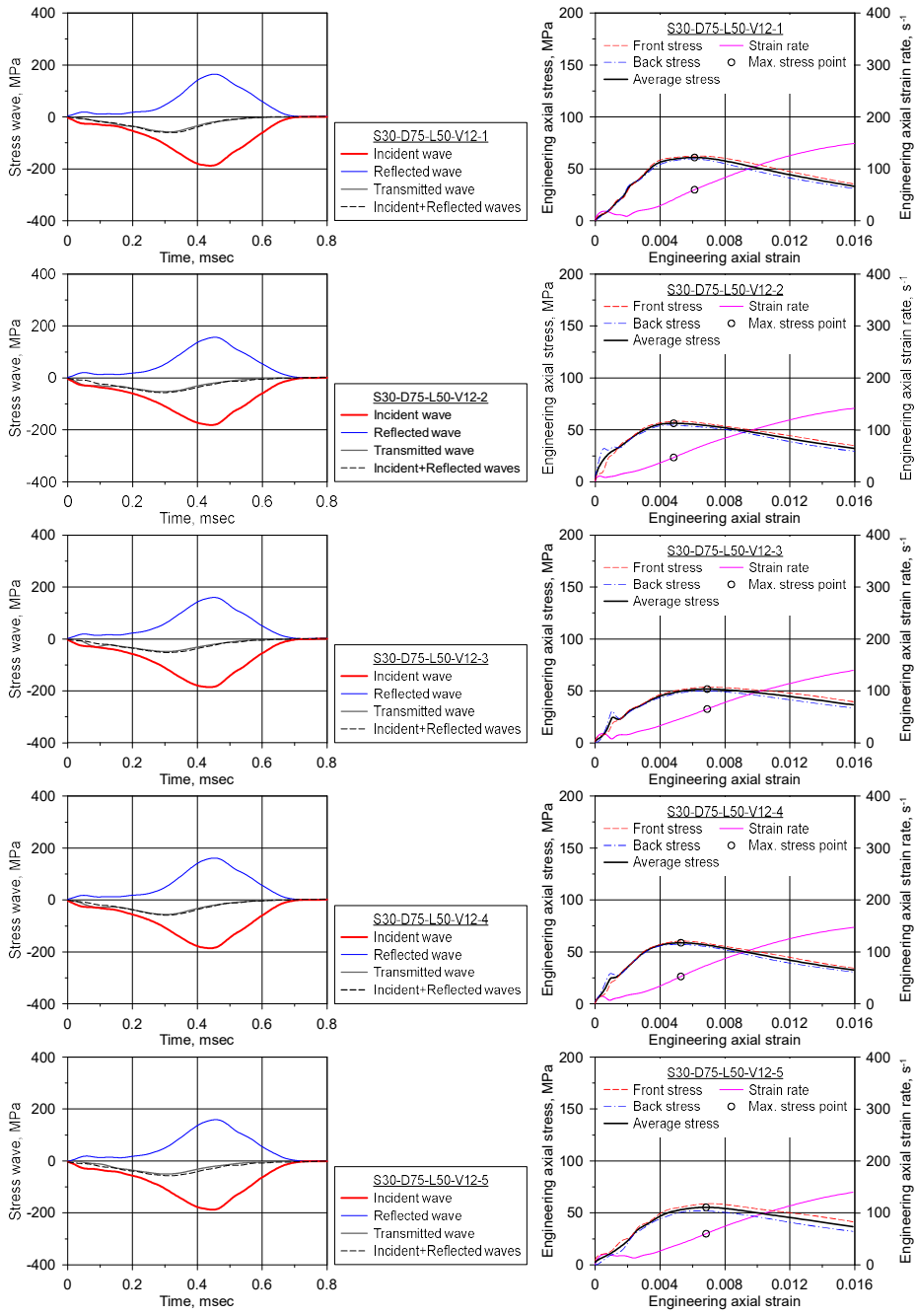

Figure D.7 Stress waves and the axial stress–strain curve of S30-D75-L50-V12

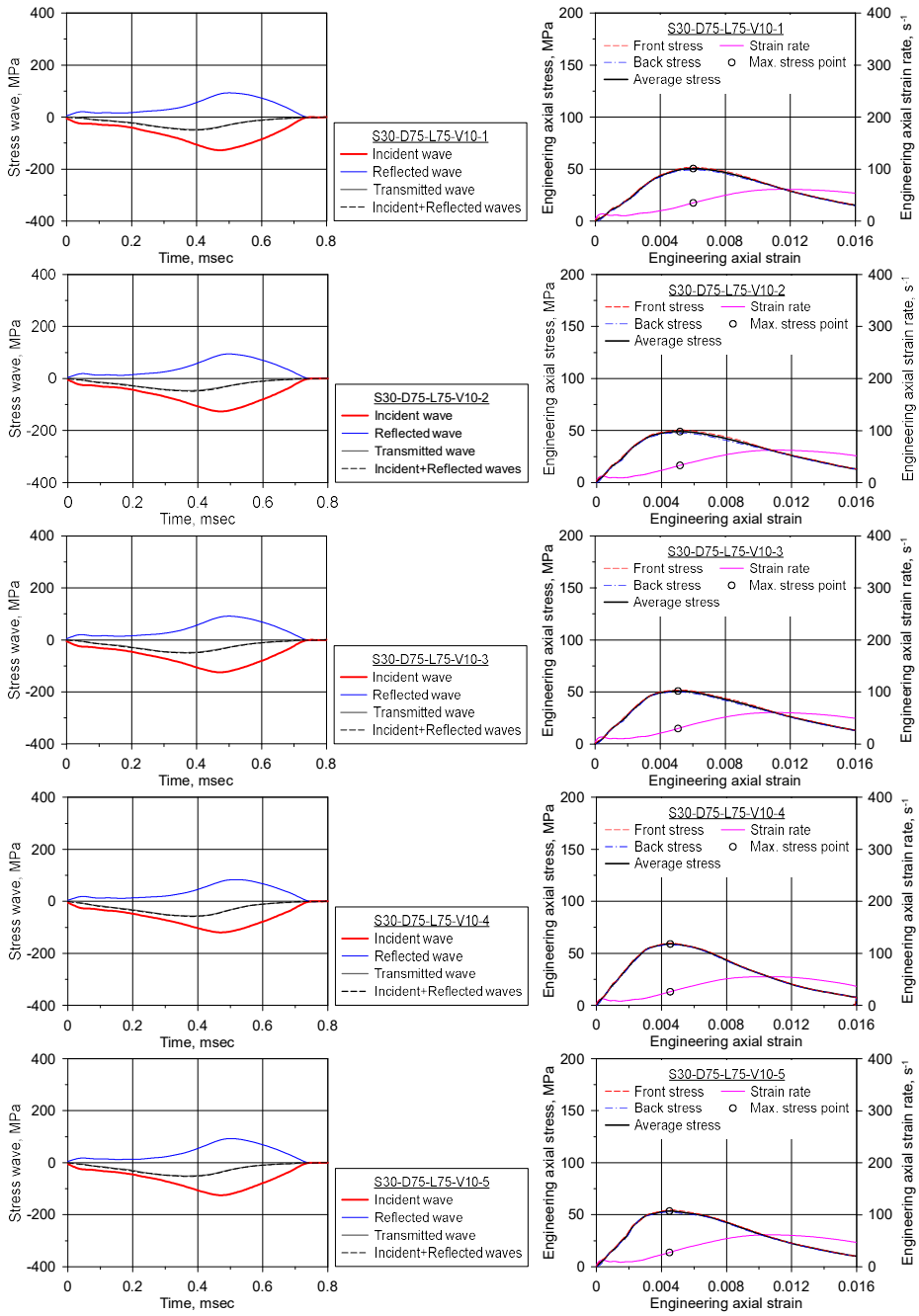

Figure D.8 Stress waves and the axial stress–strain curve of S30-D75-L75-V10

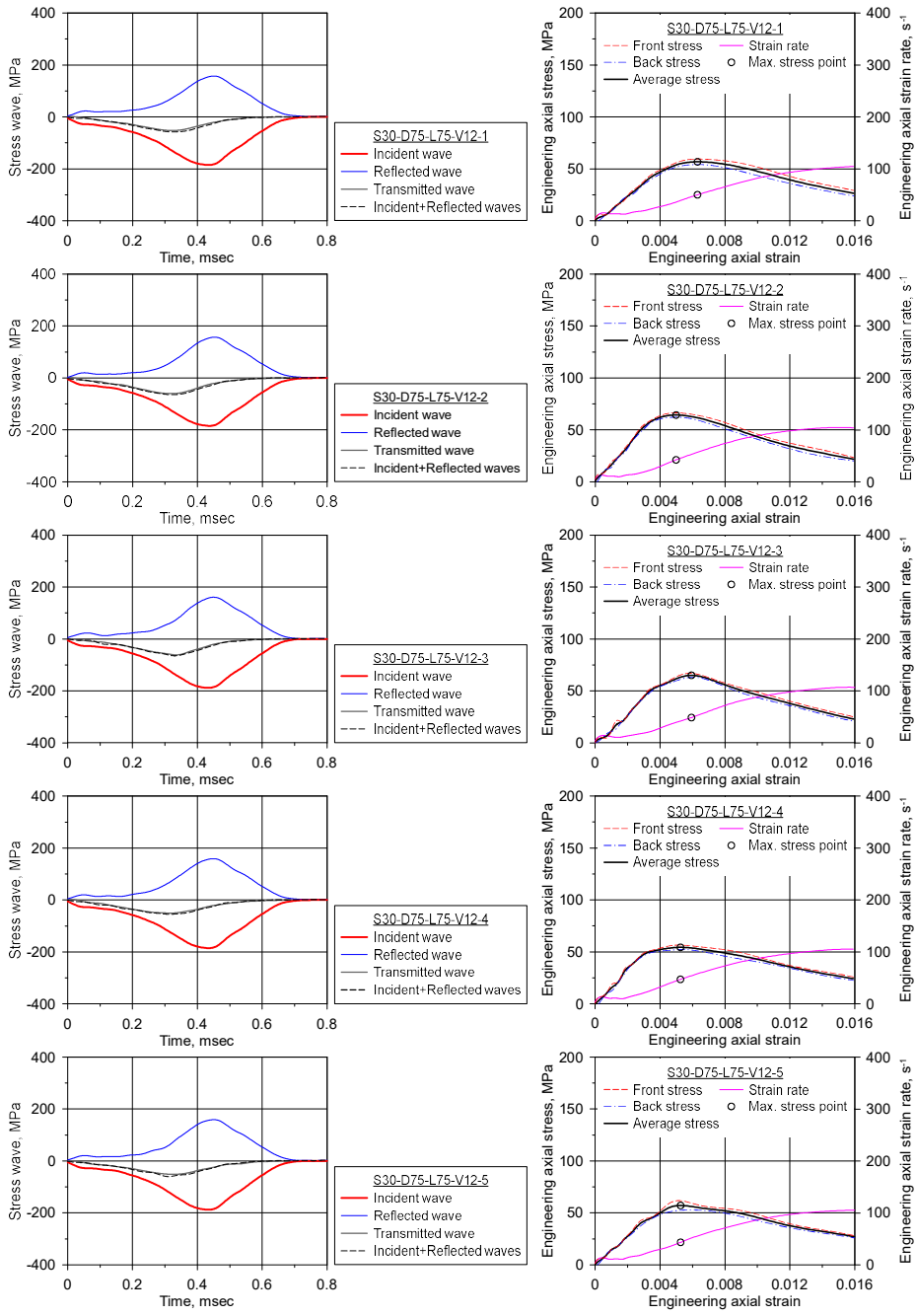

Figure D.9 Stress waves and the axial stress–strain curve of S30-D75-L75-V12

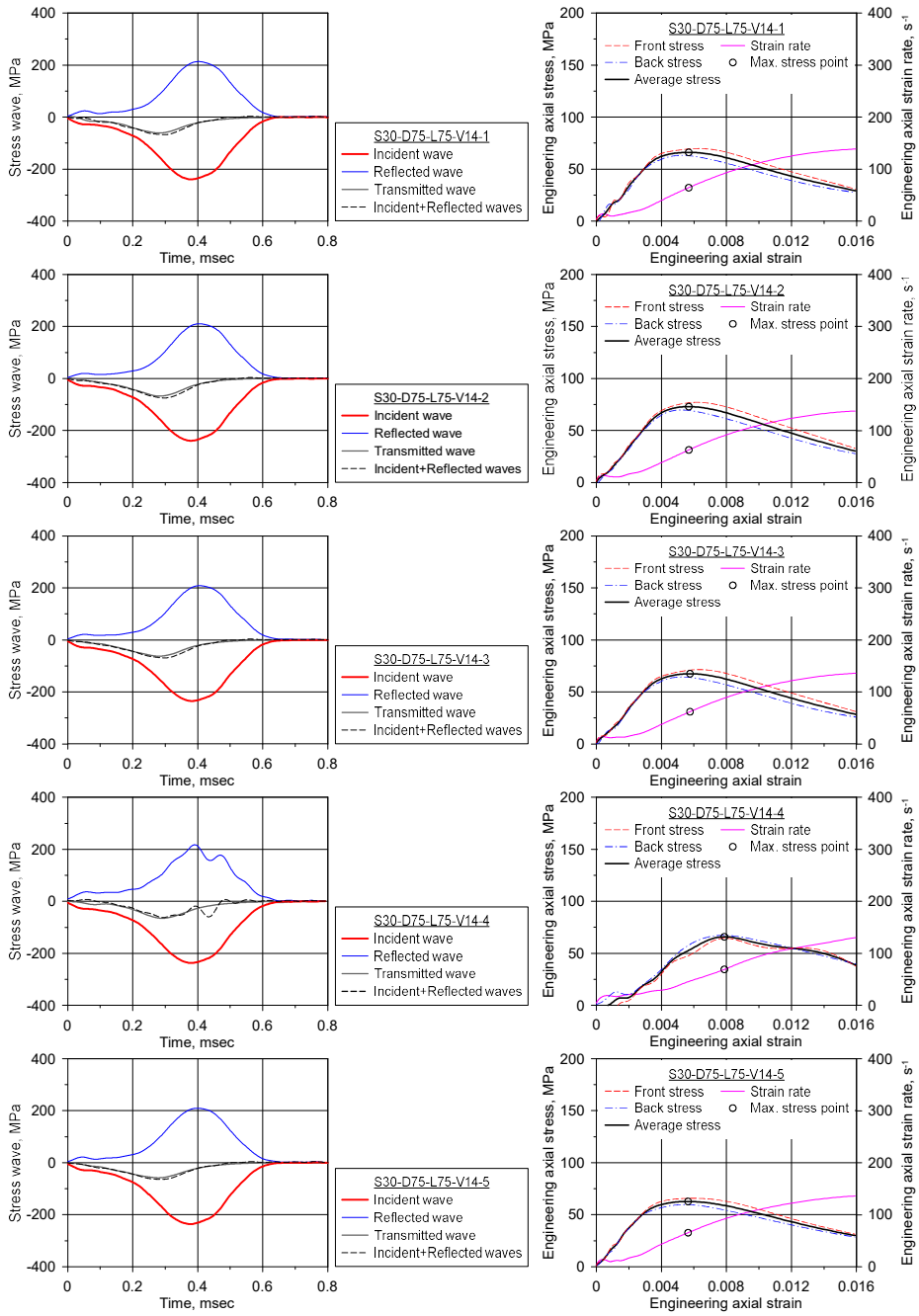

Figure D.10 Stress waves and the axial stress–strain curve of S30-D75-L75-V14

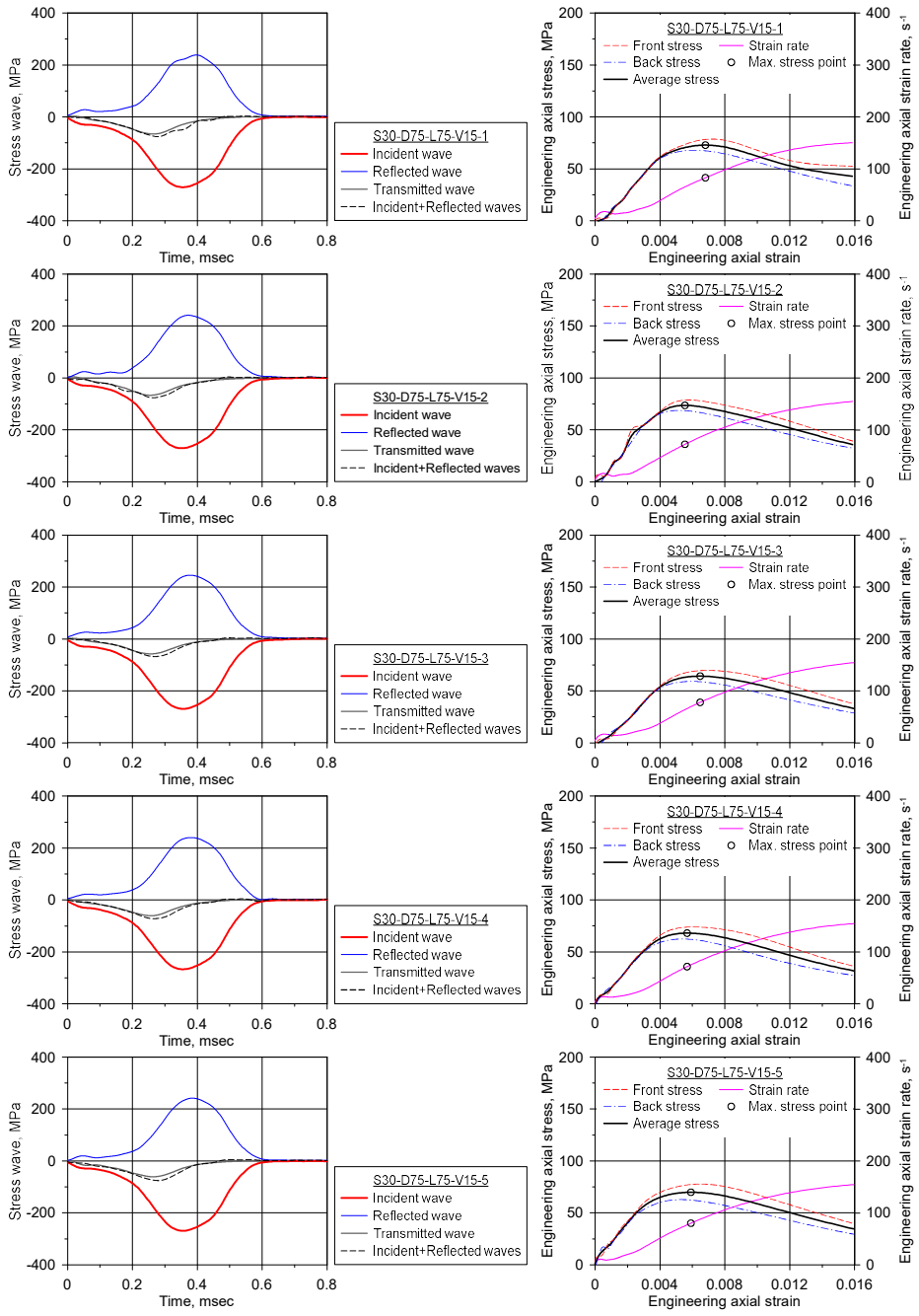

Figure D.11 Stress waves and the axial stress–strain curve of S30-D75-L75-V15

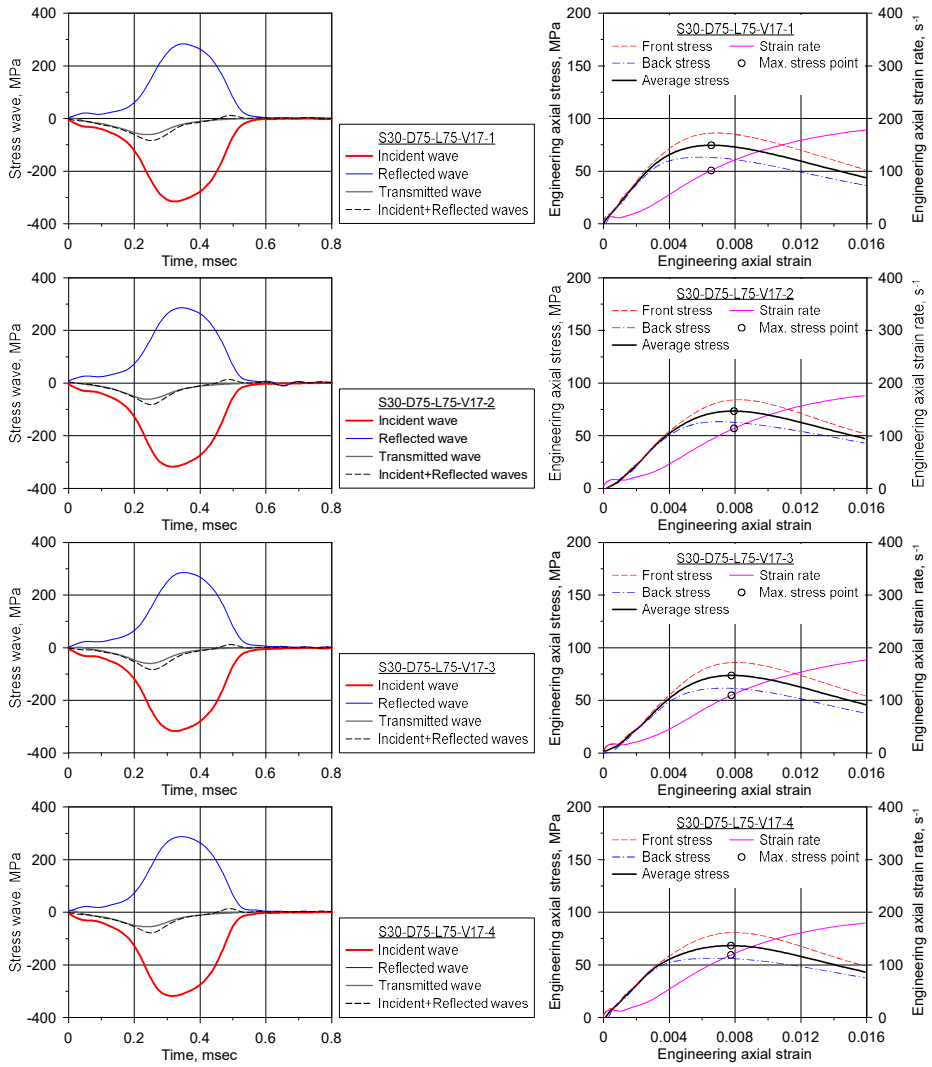

Figure D.12 Stress waves and the axial stress–strain curve of S30-D75-L75-V17

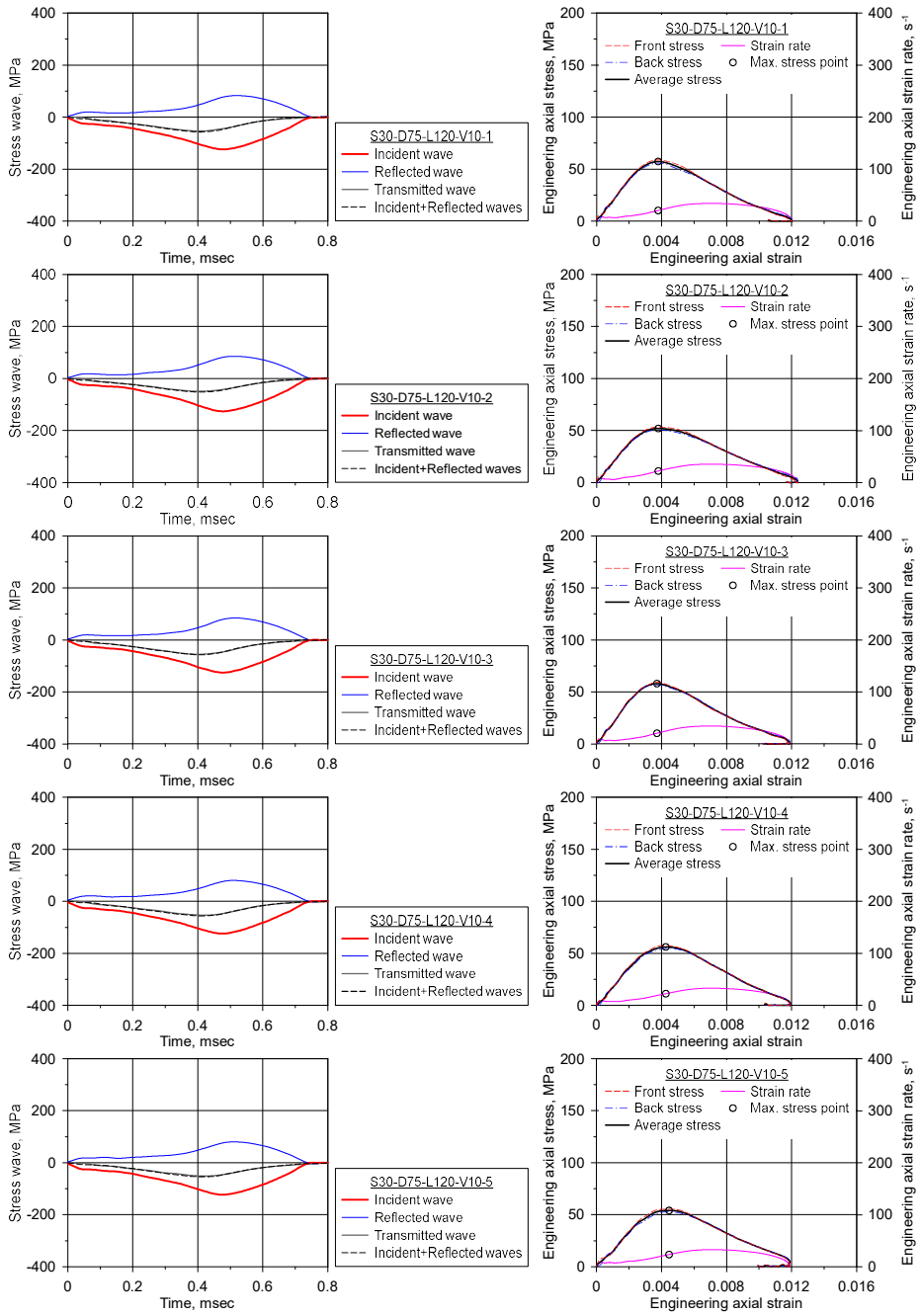

Figure D.13 Stress waves and the axial stress–strain curve of S30-D75-L120-V10

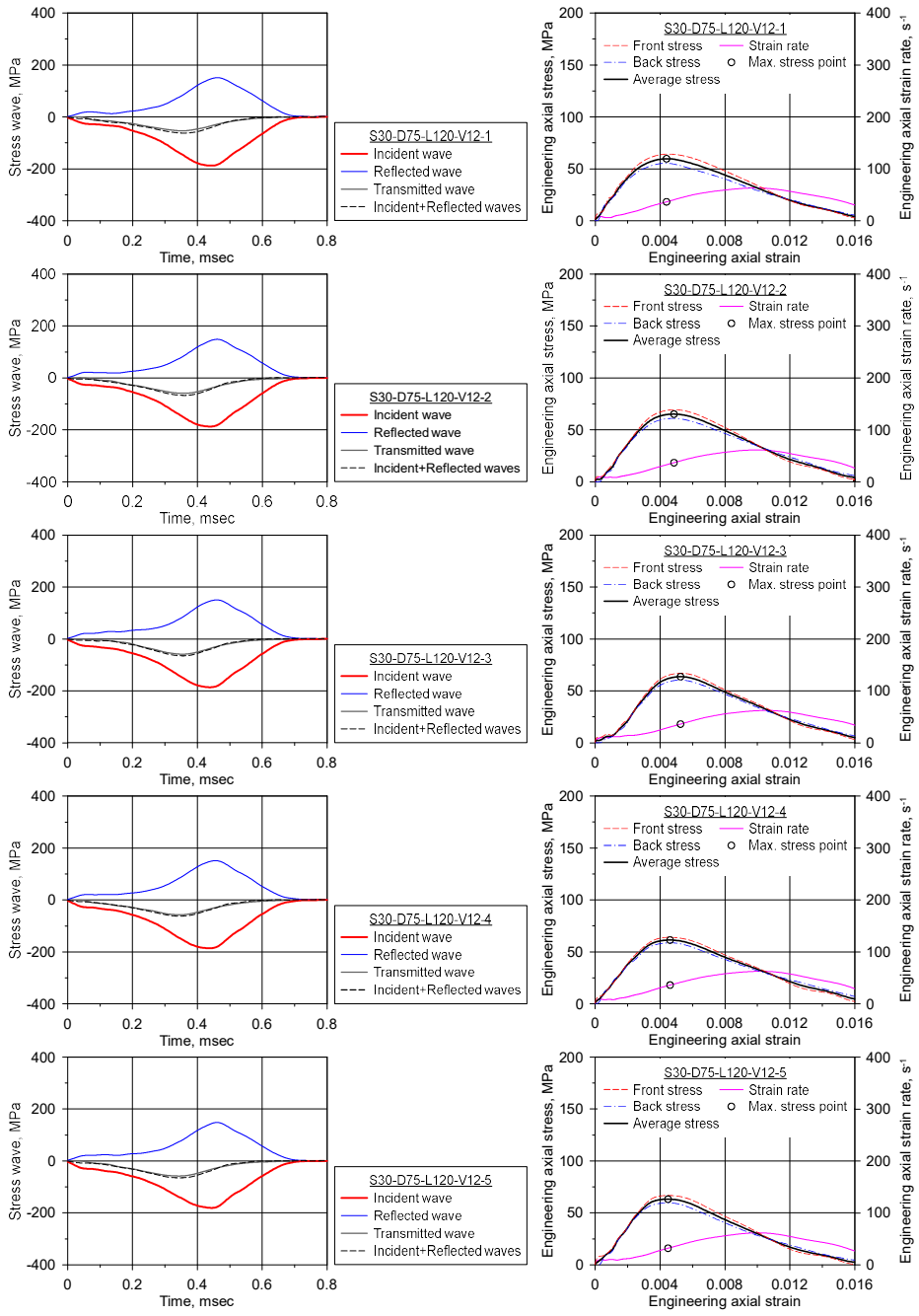

Figure D.14 Stress waves and the axial stress–strain curve of S30-D75-L120-V12

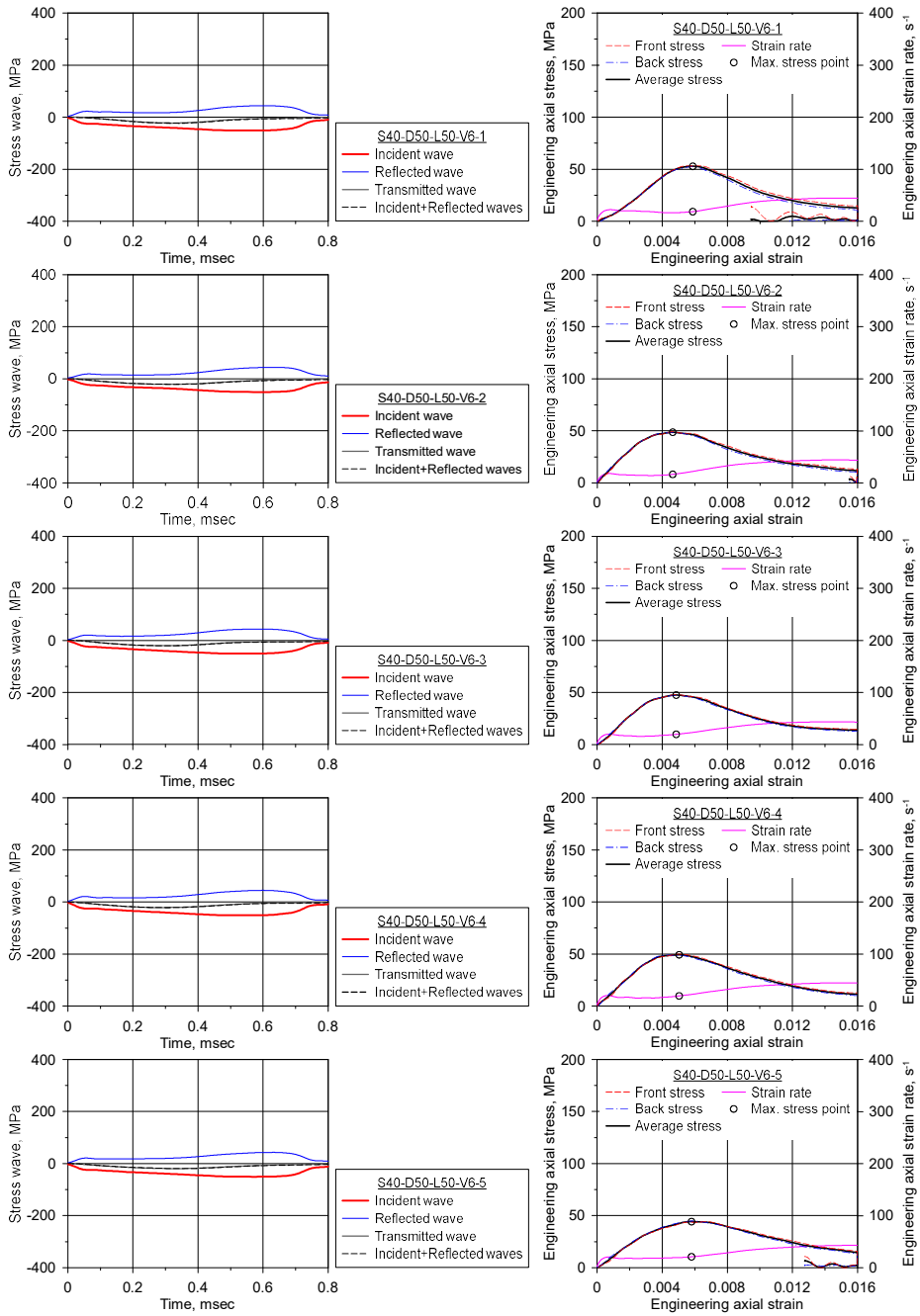

Figure D.15 Stress waves and the axial stress–strain curve of S40-D50-L50-V6

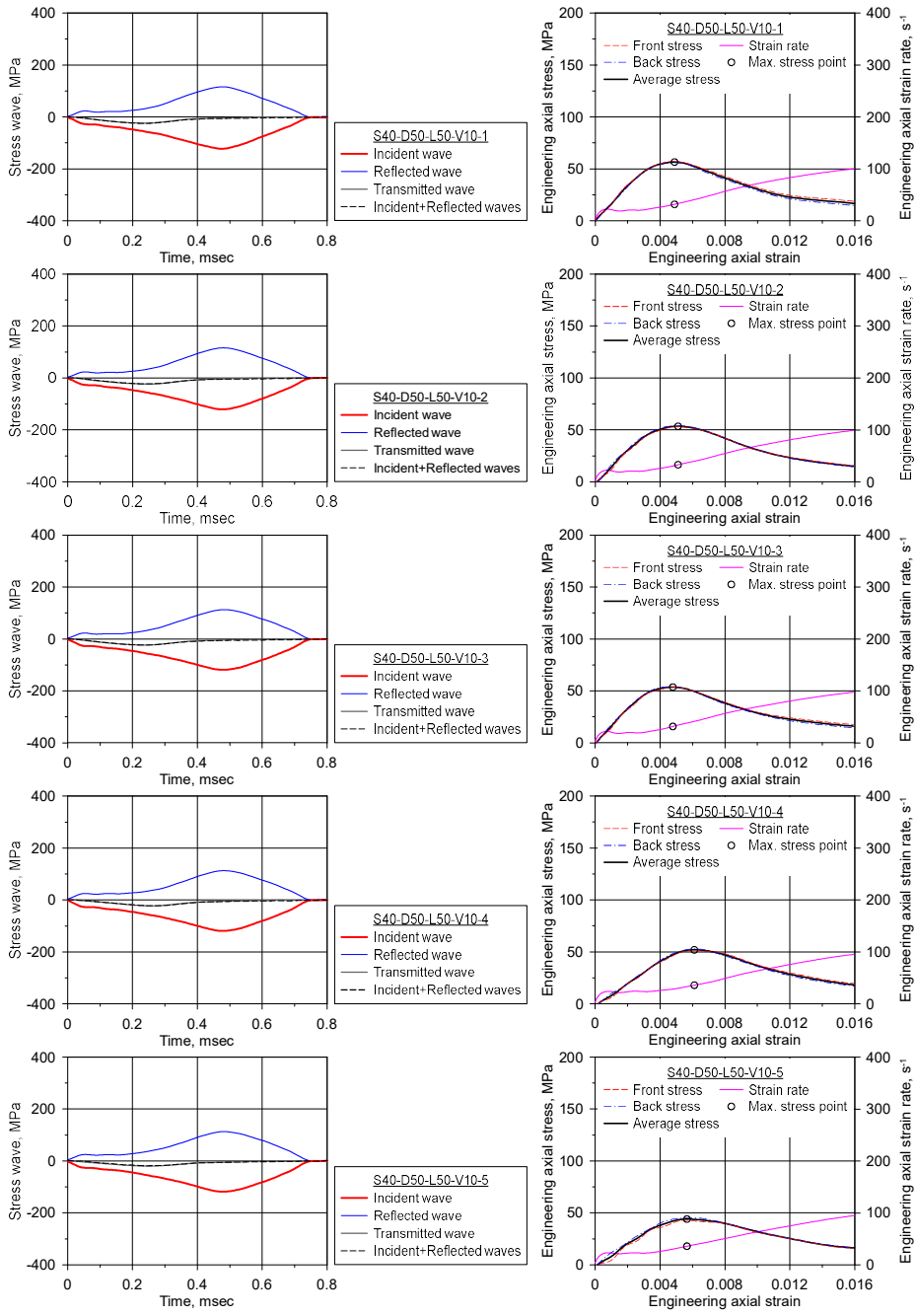

Figure D.16 Stress waves and the axial stress–strain curve of S40-D50-L50-V10

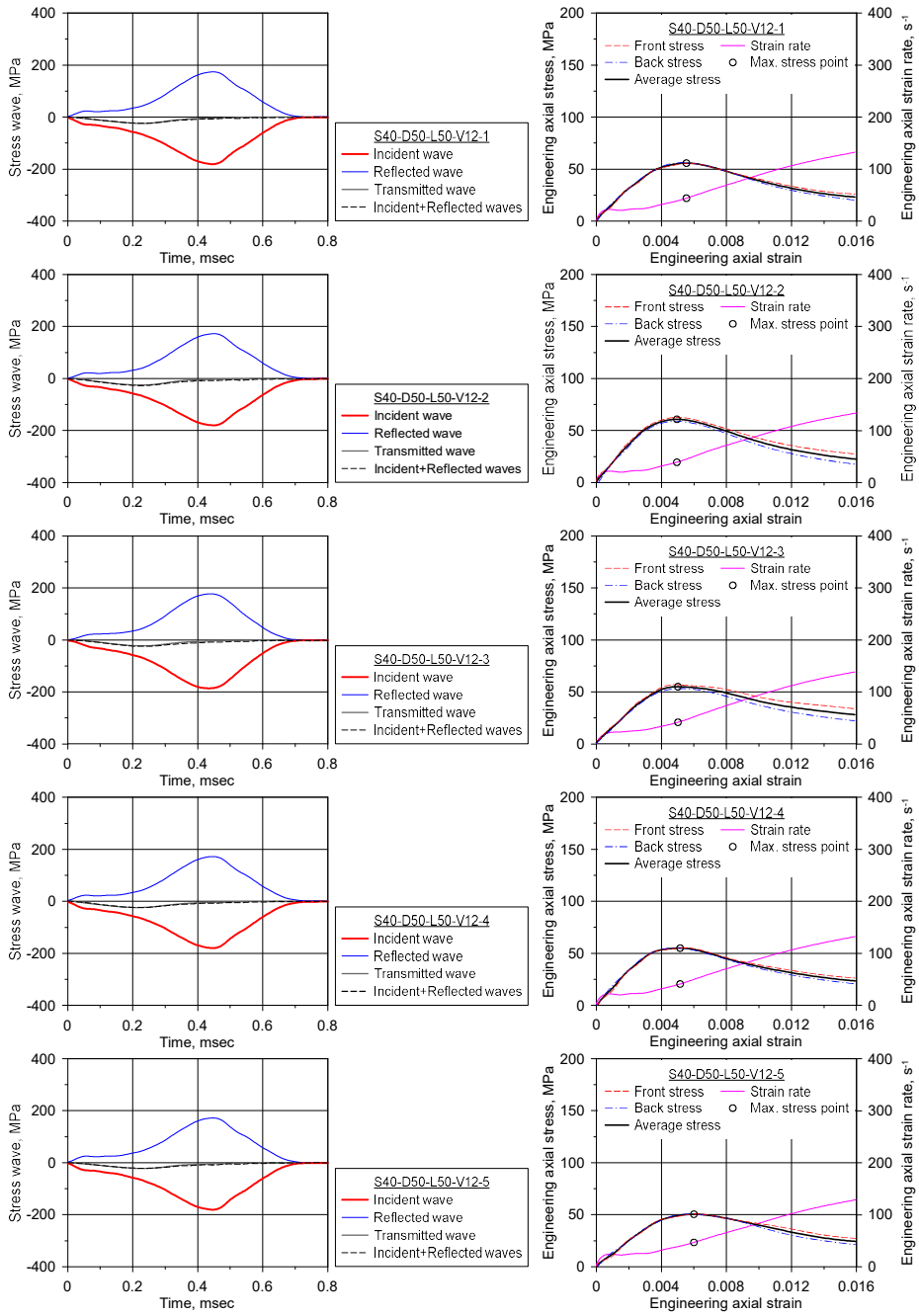

Figure D.17 Stress waves and the axial stress–strain curve of S40-D50-L50-V12

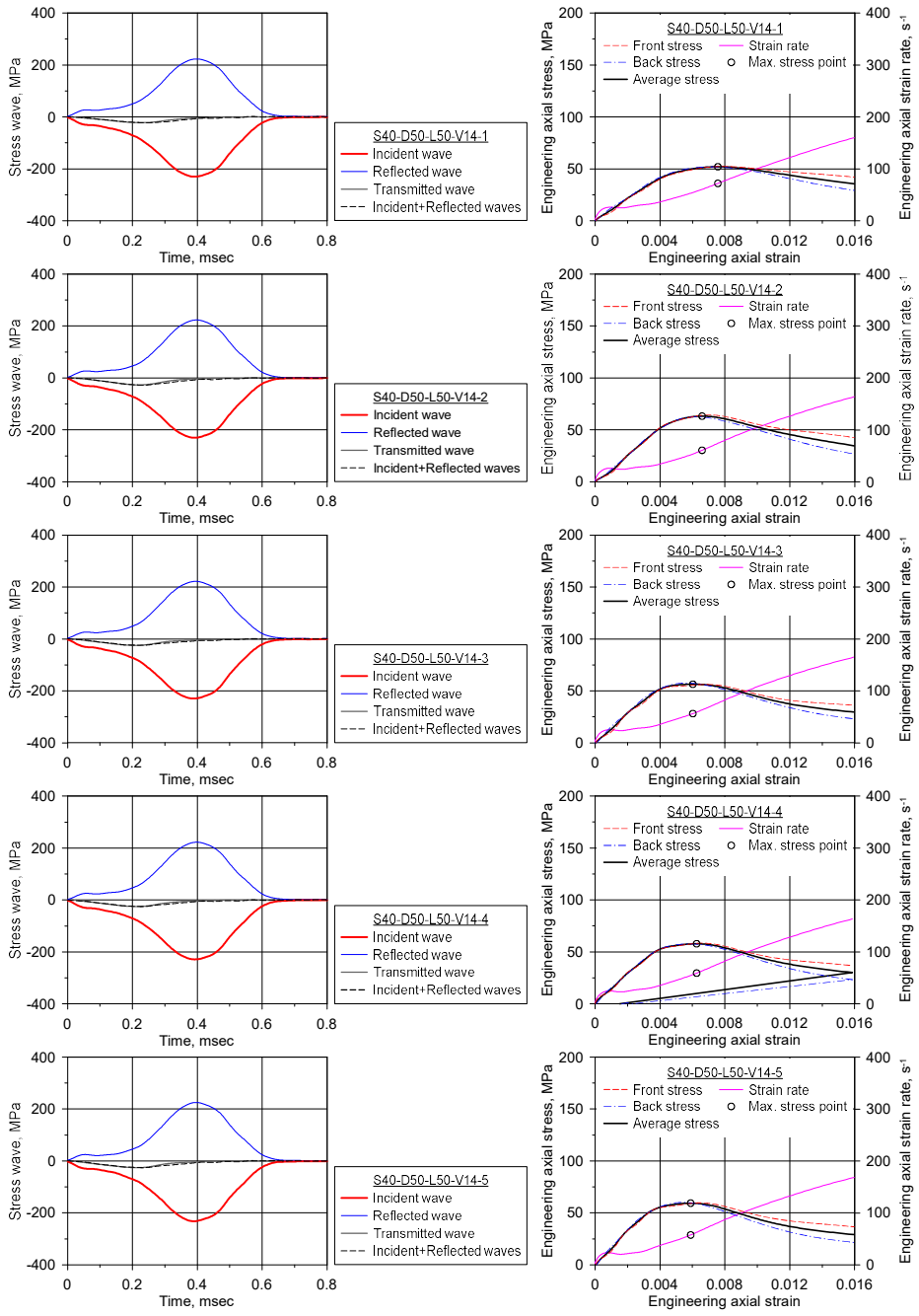

Figure D.18 Stress waves and the axial stress–strain curve of S40-D50-L50-V14

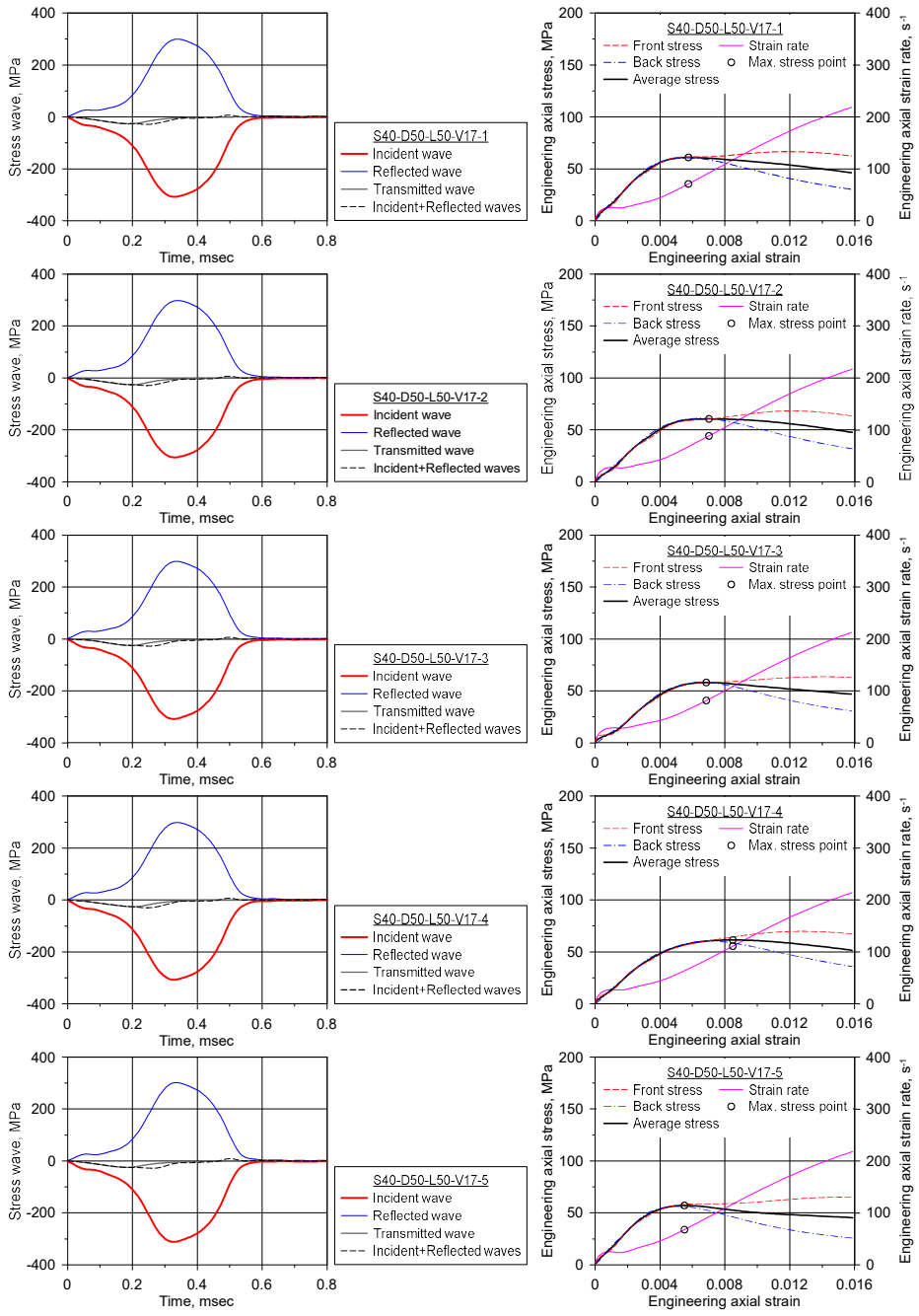

Figure D.19 Stress waves and the axial stress–strain curve of S40-D50-L50-V17

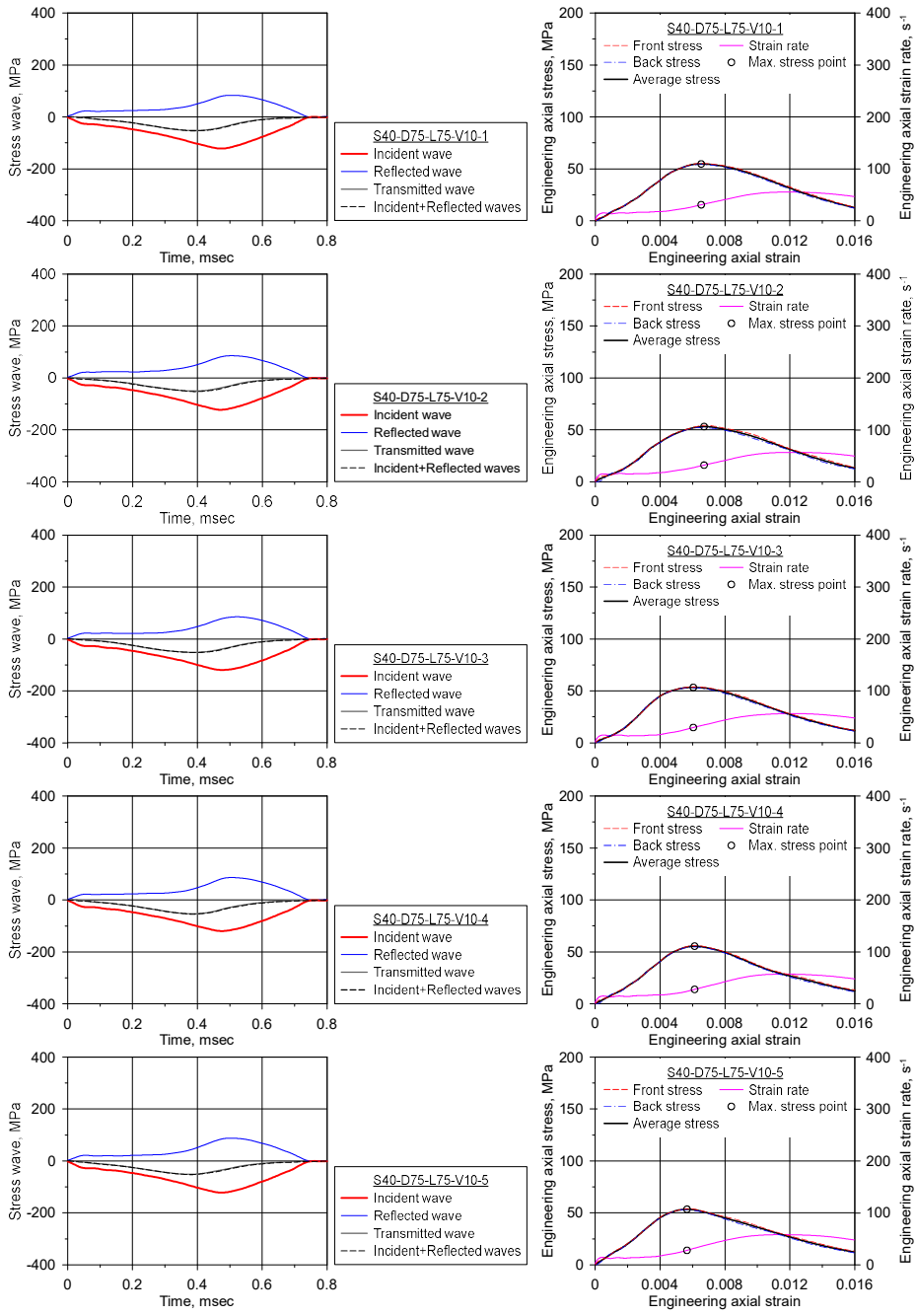

Figure D.20 Stress waves and the axial stress–strain curve of S40-D75-L75-V10

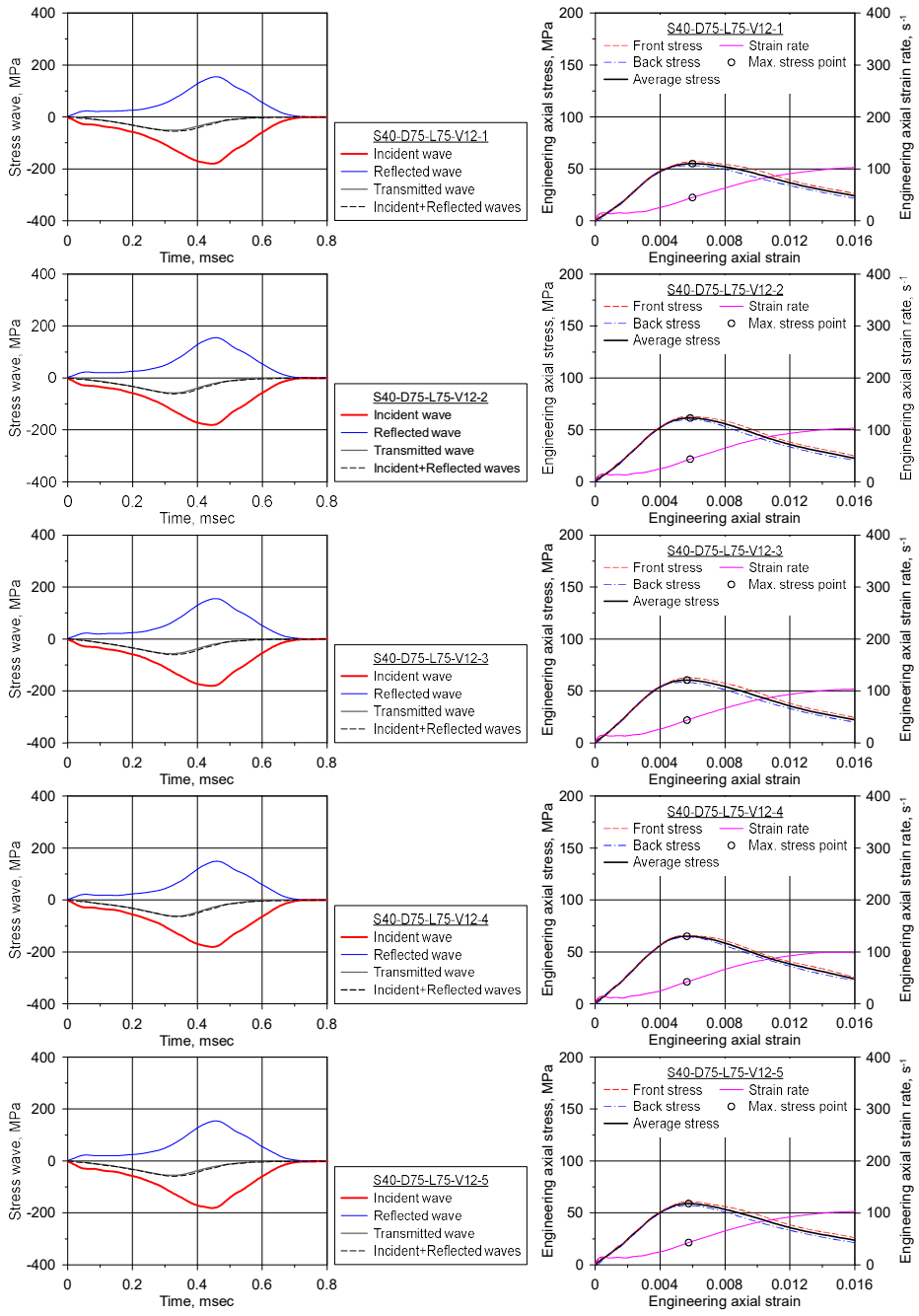

Figure D.21 Stress waves and the axial stress–strain curve of S40-D75-L75-V12

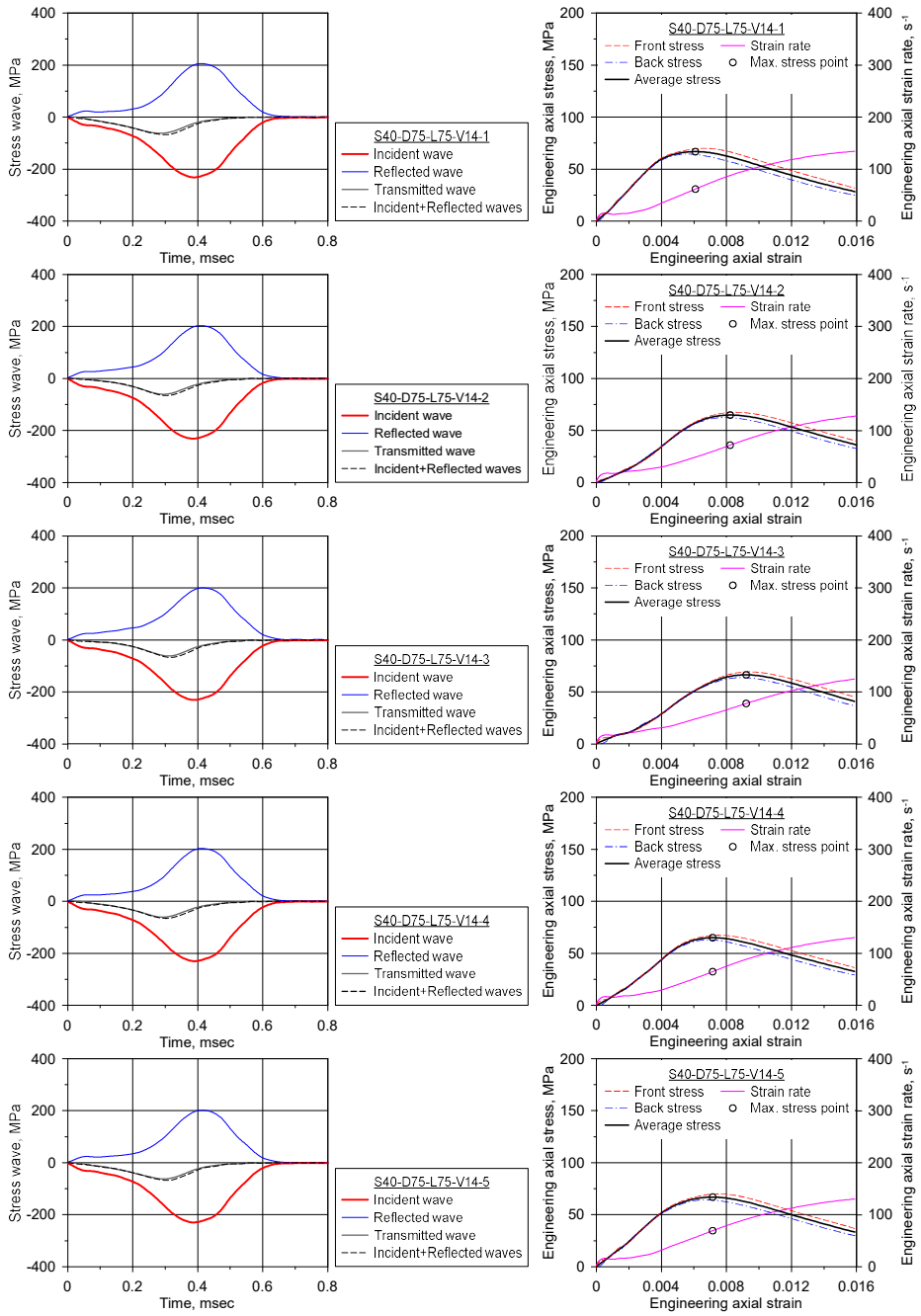

Figure D.22 Stress waves and the axial stress–strain curve of S40-D75-L75-V14

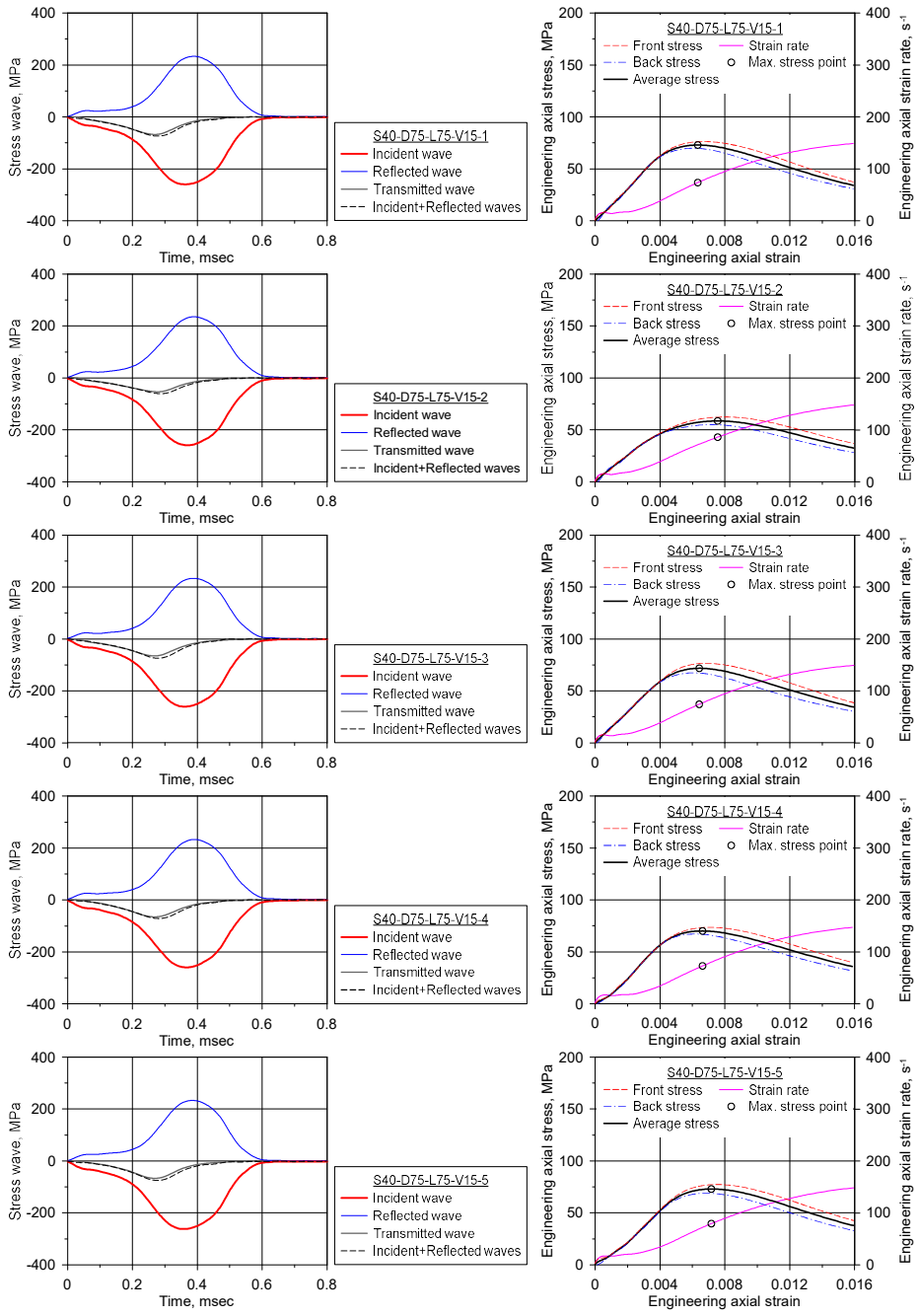

Figure D.23 Stress waves and the axial stress–strain curve of S40-D75-L75-V15

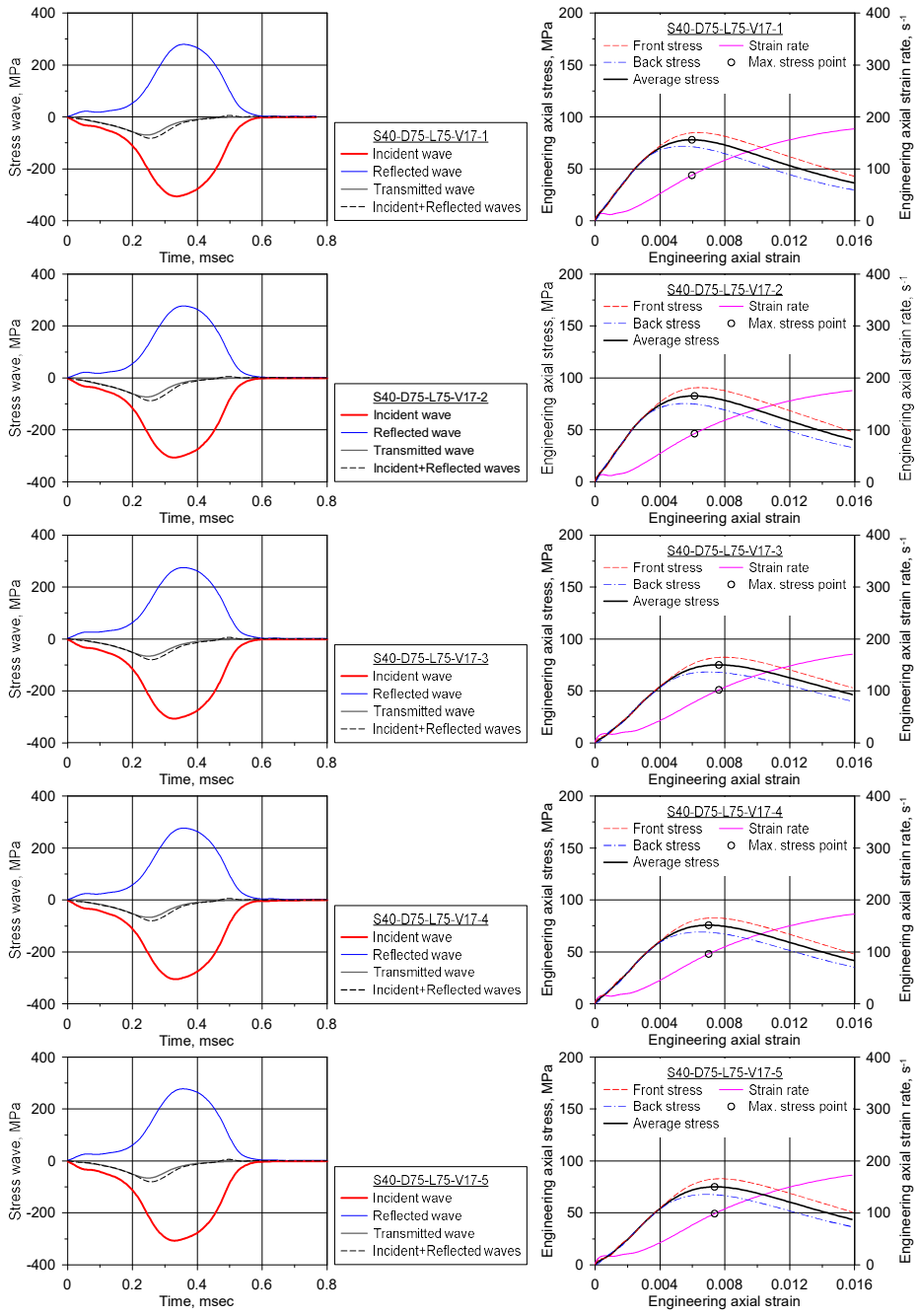

Figure D.24 Stress waves and the axial stress–strain curve of S40-D75-L75-V17

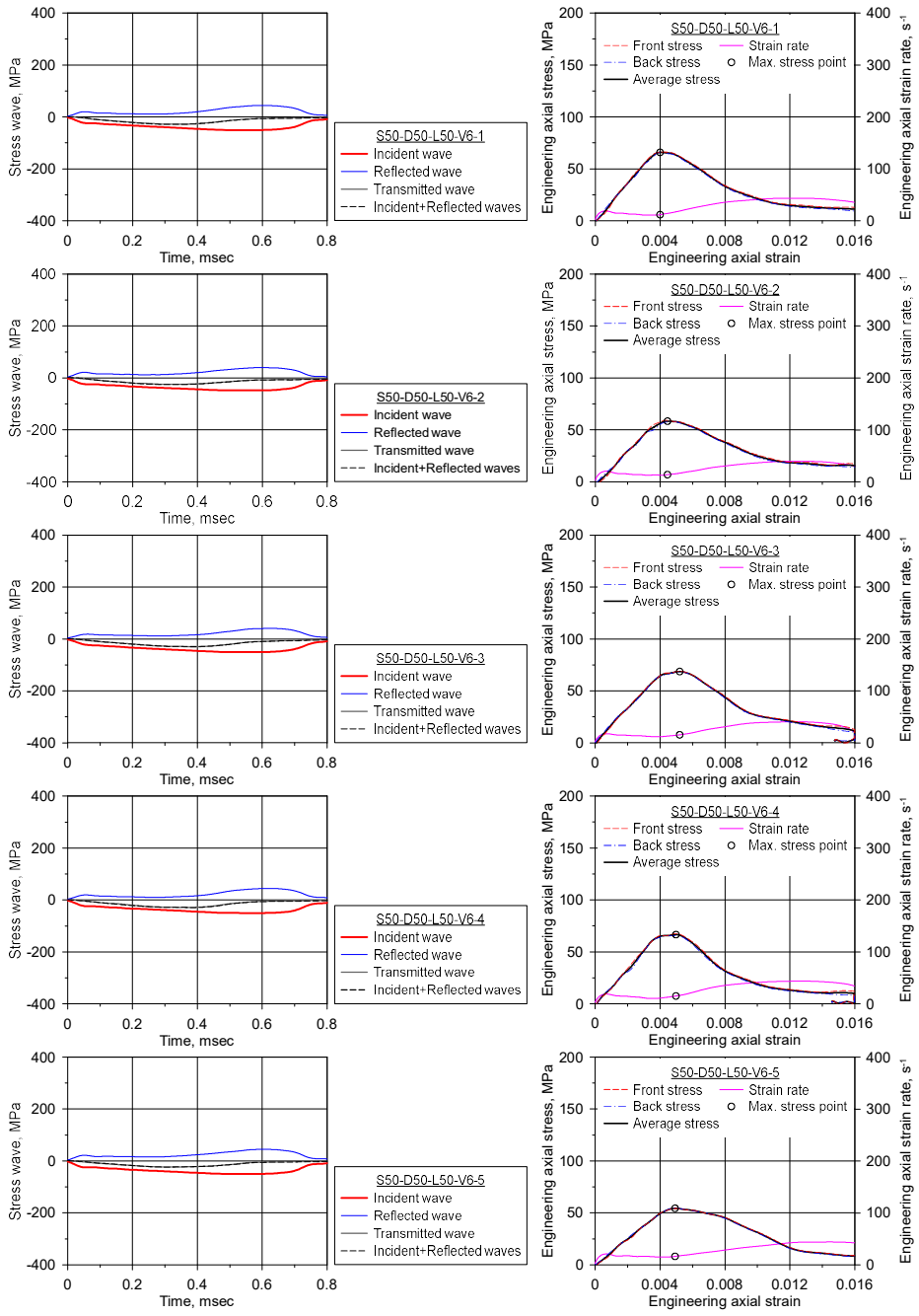

Figure D.25 Stress waves and the axial stress–strain curve of S50-D50-L50-V6

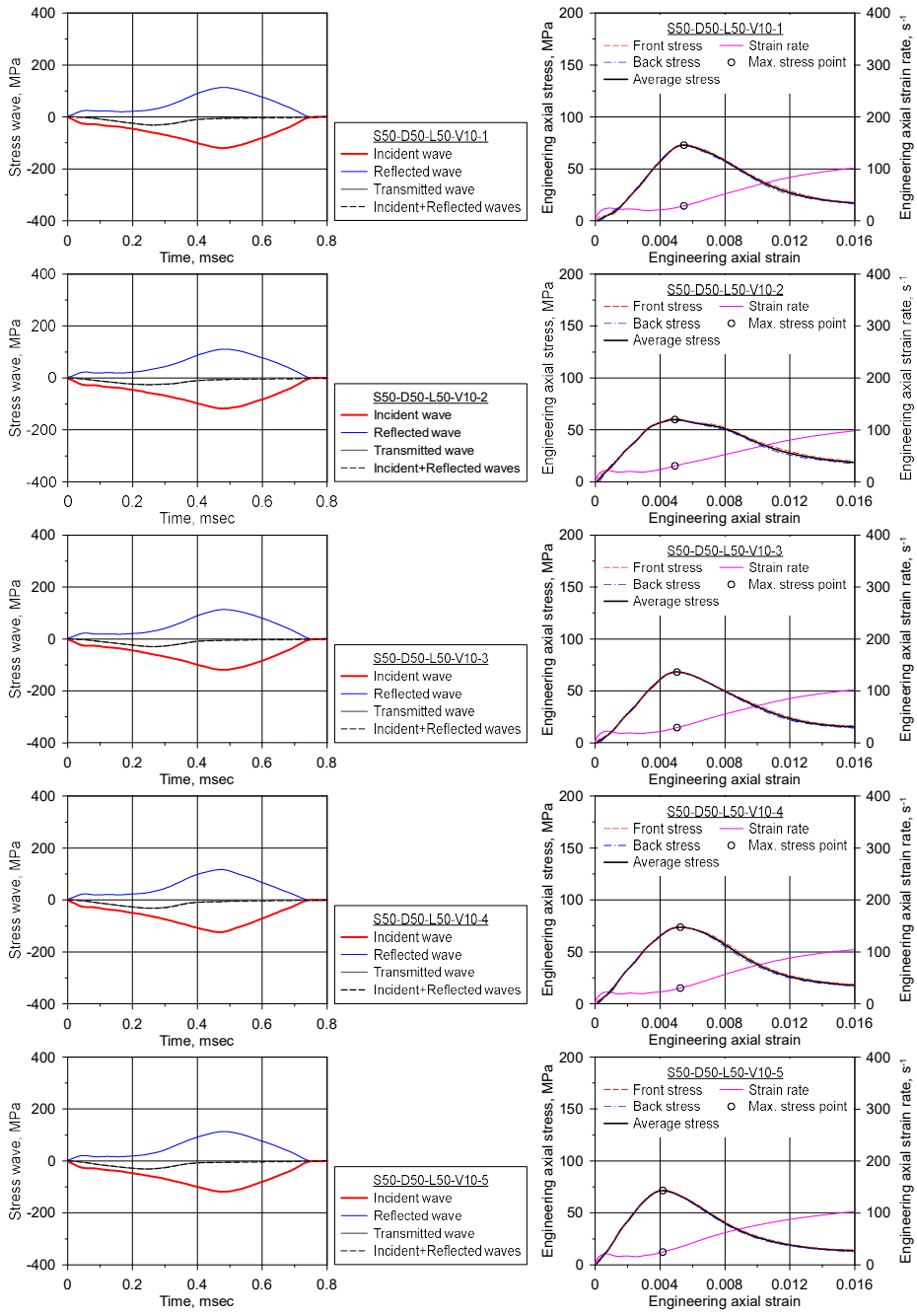

Figure D.26 Stress waves and the axial stress–strain curve of S50-D50-L50-V10

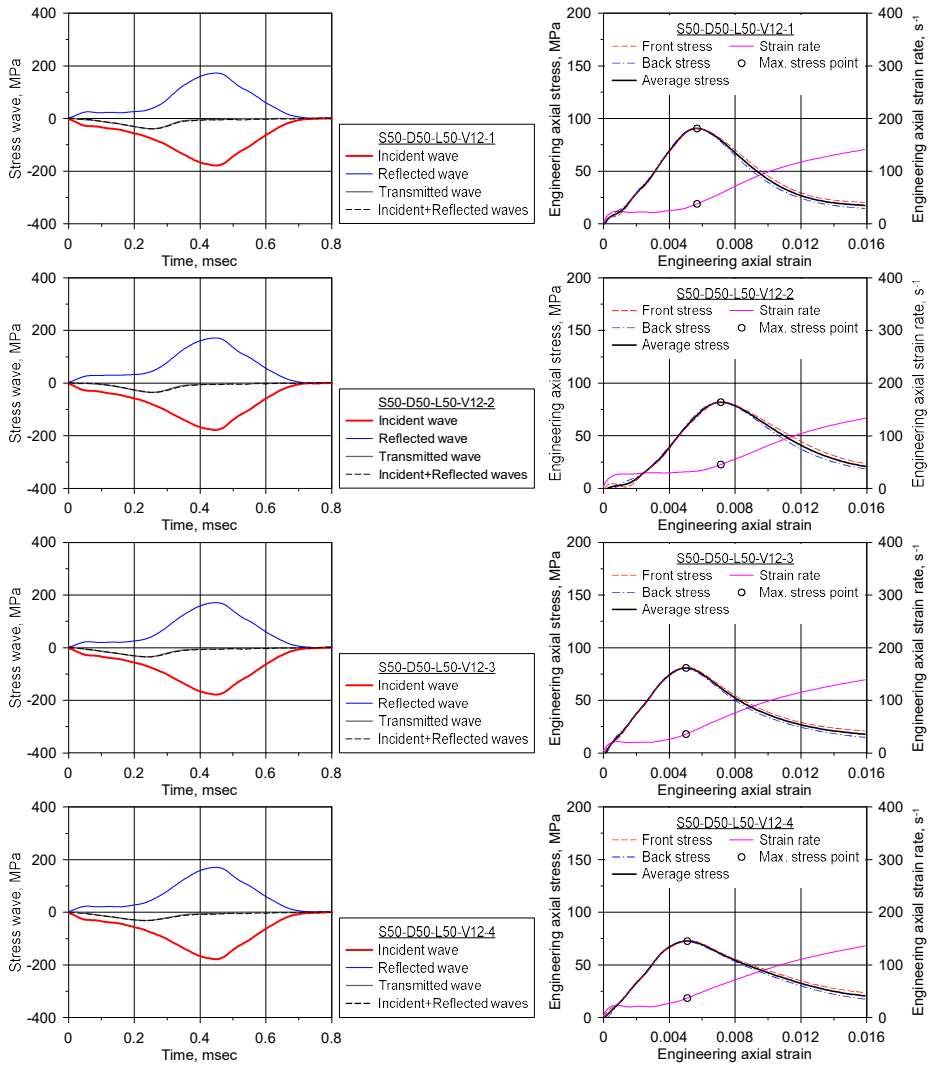

Figure D.27 Stress waves and the axial stress–strain curve of S50-D50-L50-V12

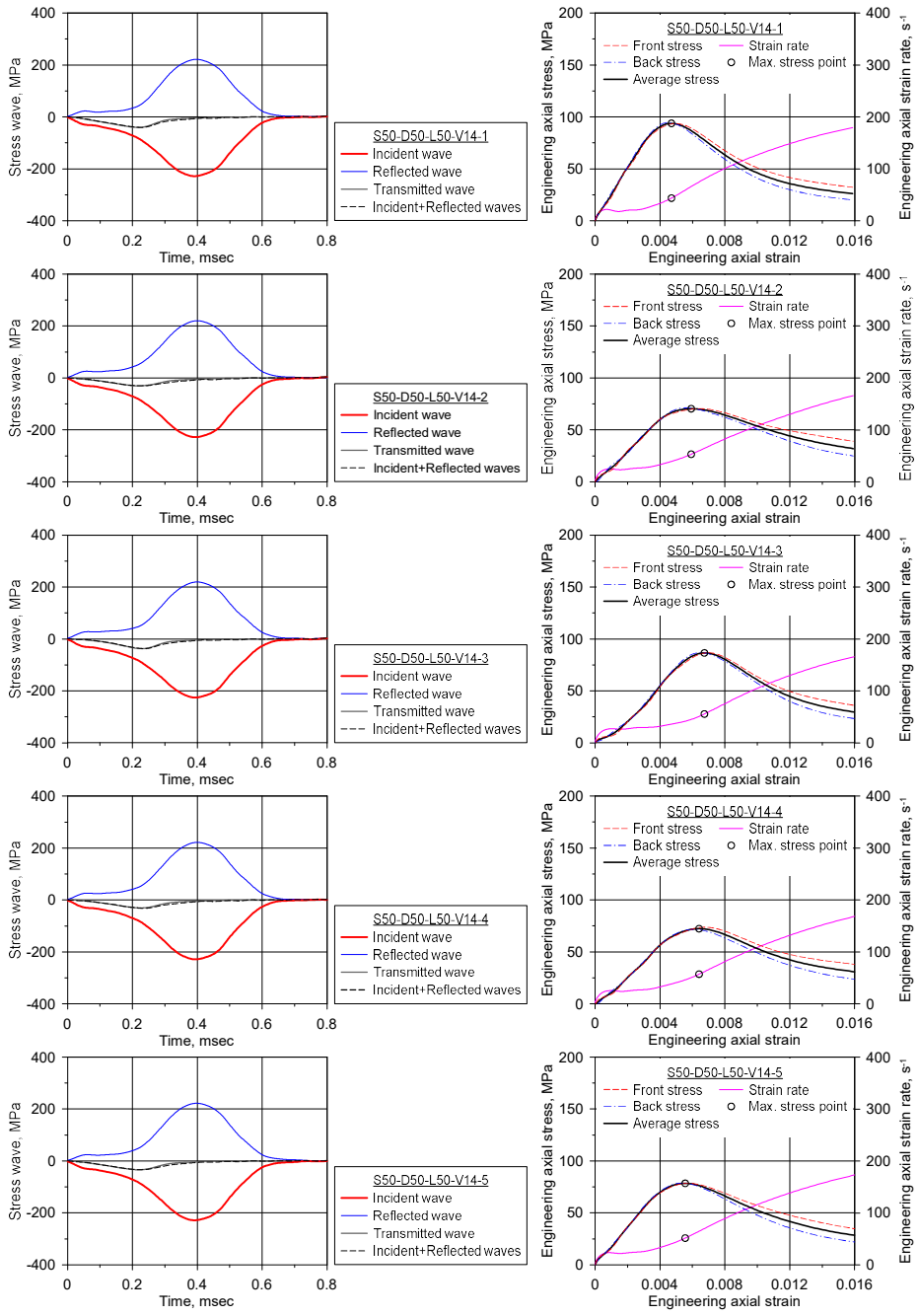

Figure D.28 Stress waves and the axial stress–strain curve of S50-D50-L50-V14

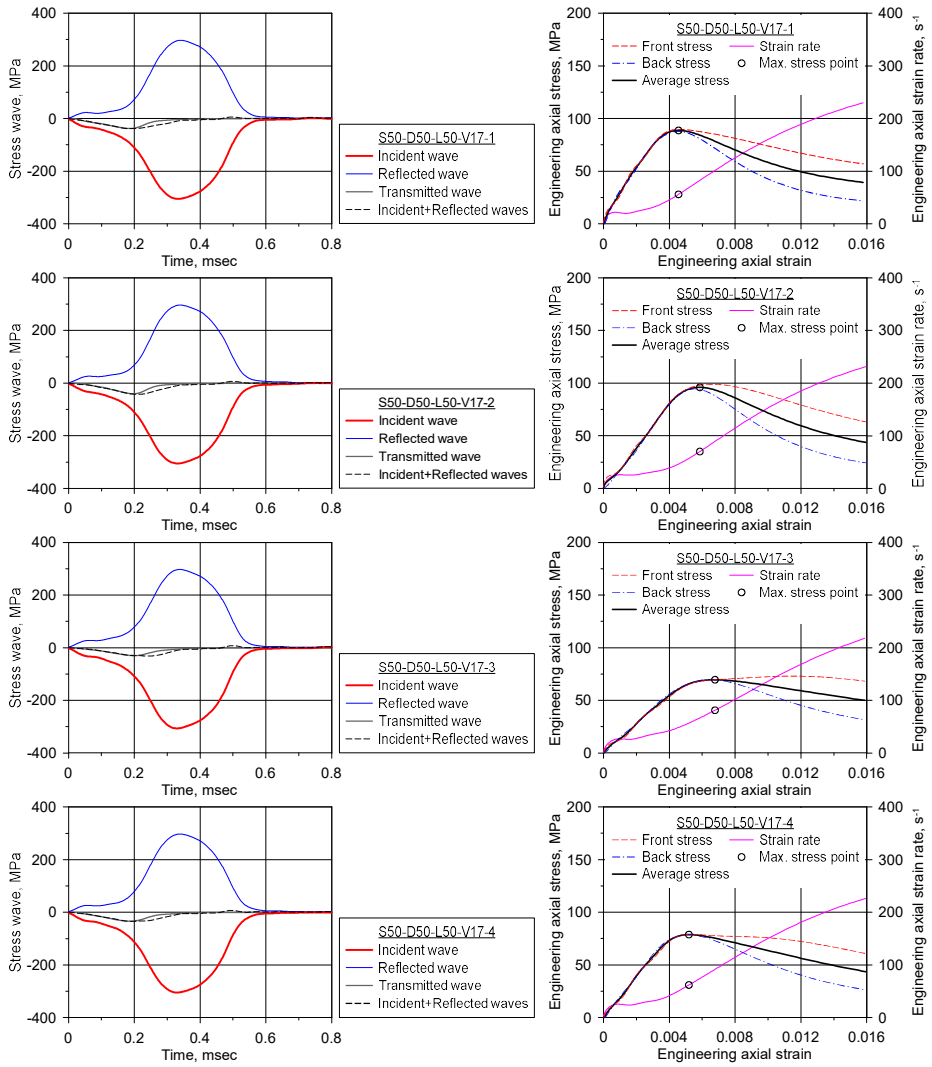

Figure D.29 Stress waves and the axial stress–strain curve of S50-D50-L50-V17

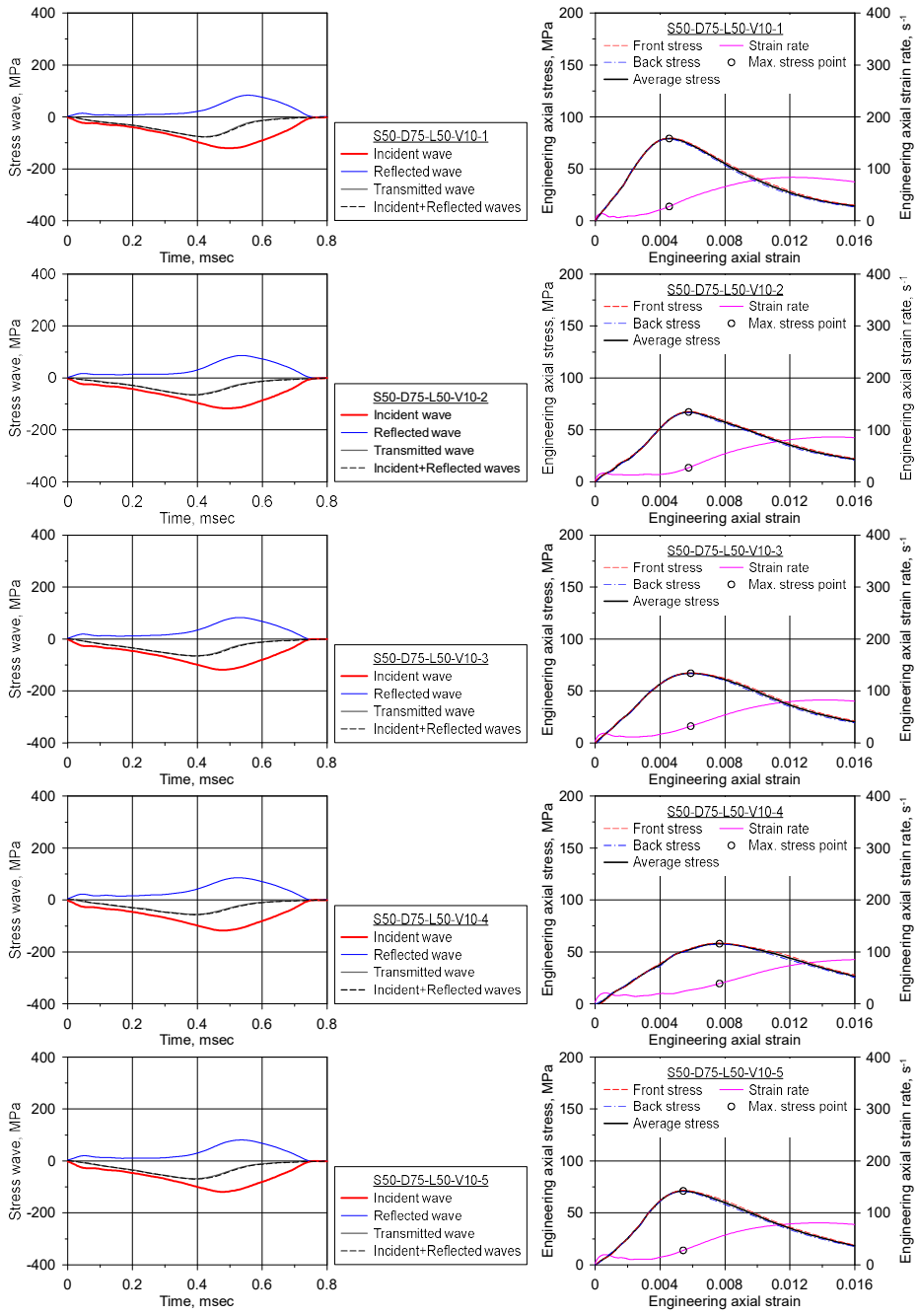

Figure D.30 Stress waves and the axial stress–strain curve of S50-D75-L50-V10

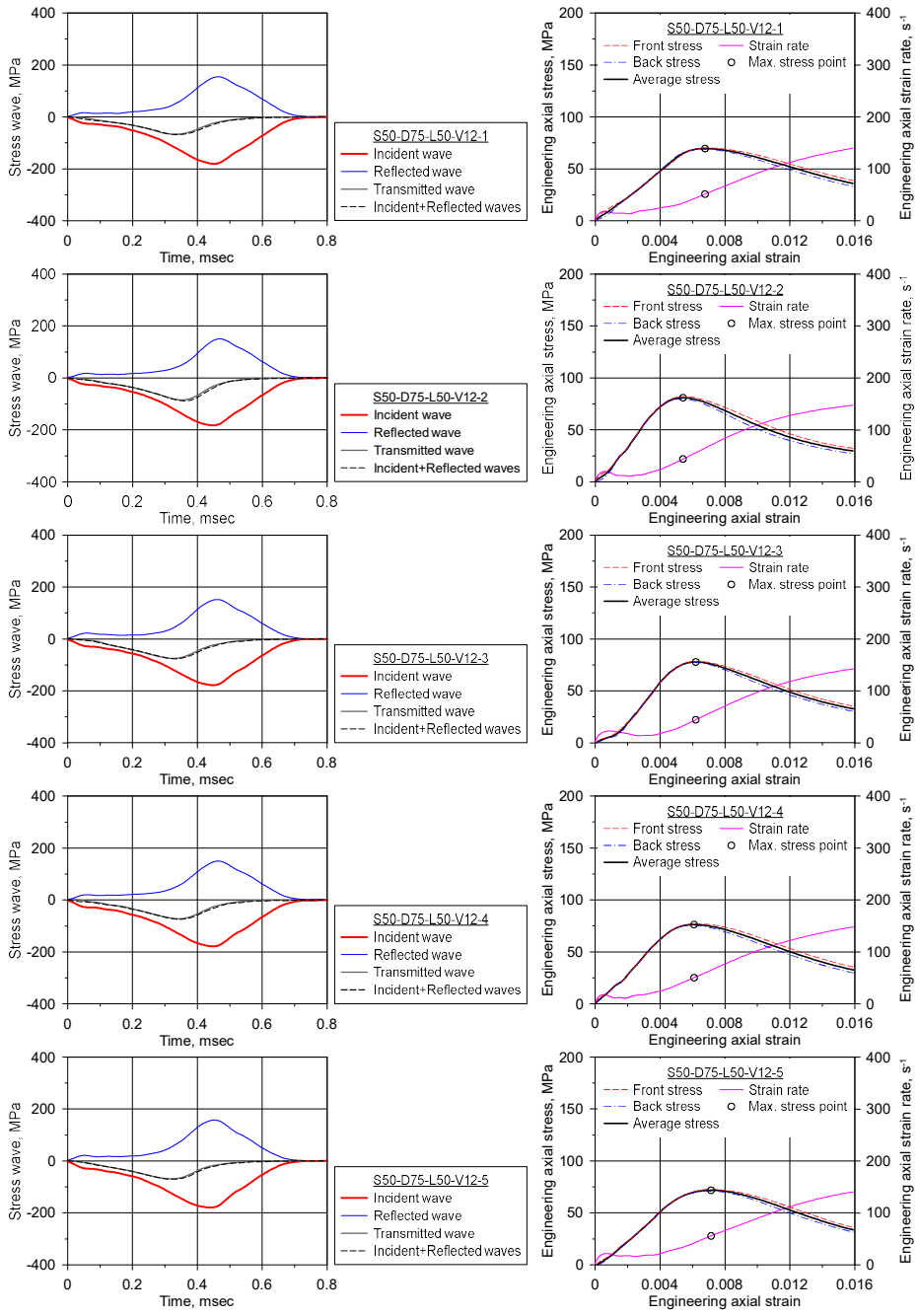

Figure D.31 Stress waves and the axial stress–strain curve of S50-D75-L50-V12

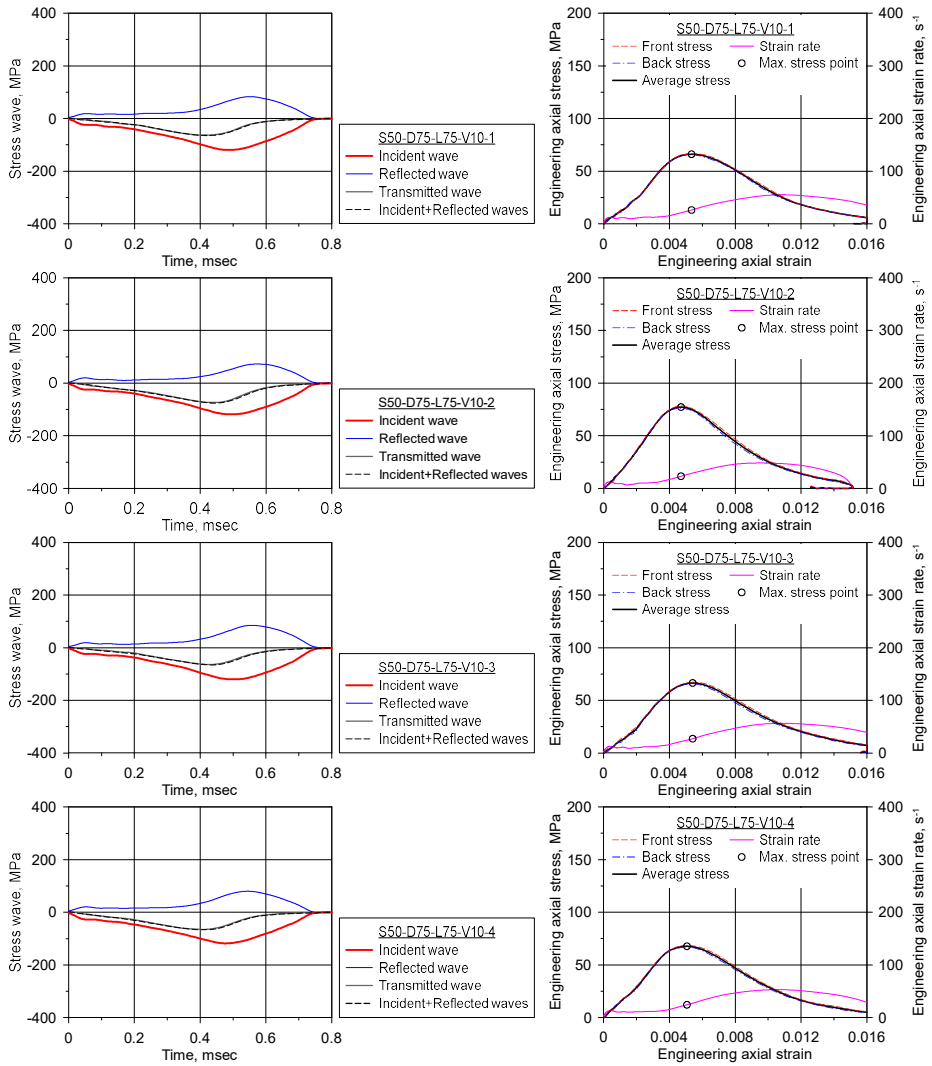

Figure D.32 Stress waves and the axial stress–strain curve of S50-D75-L75-V10

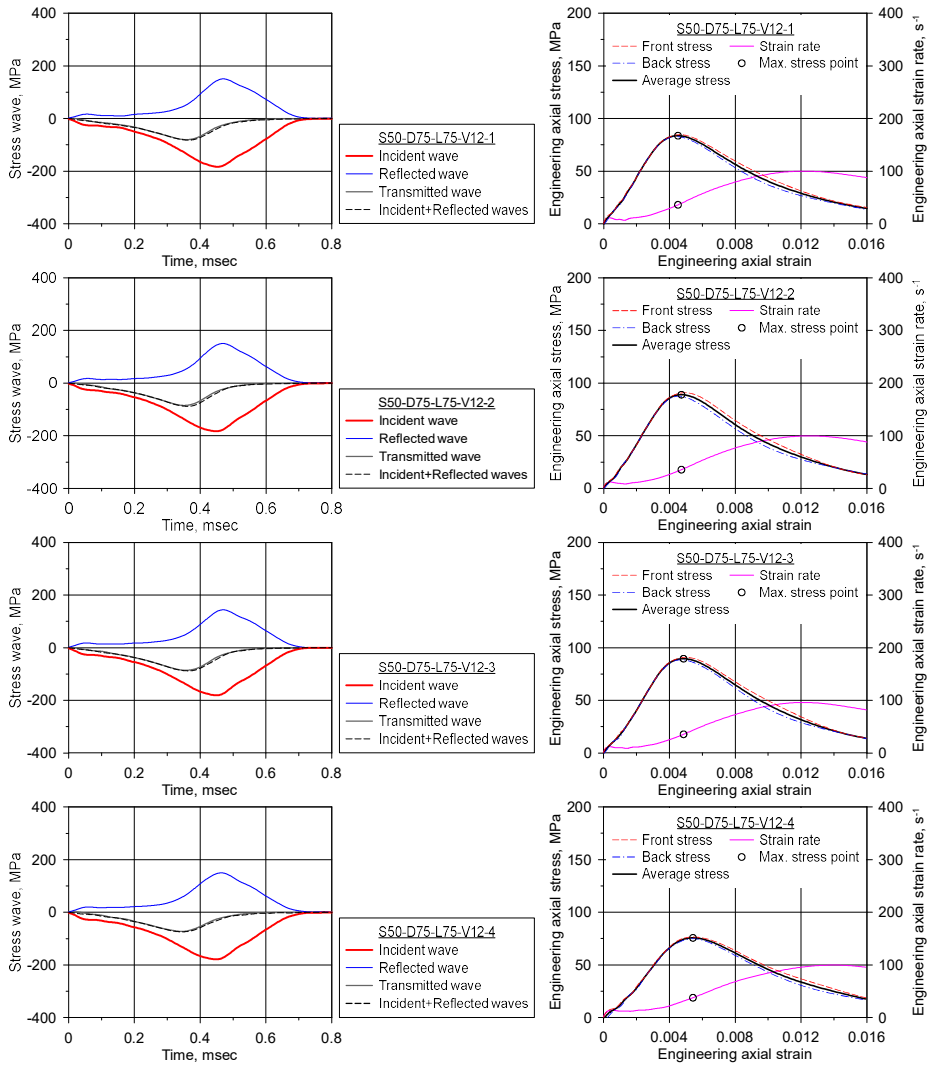

Figure D.33 Stress waves and the axial stress–strain curve of S50-D75-L75-V12

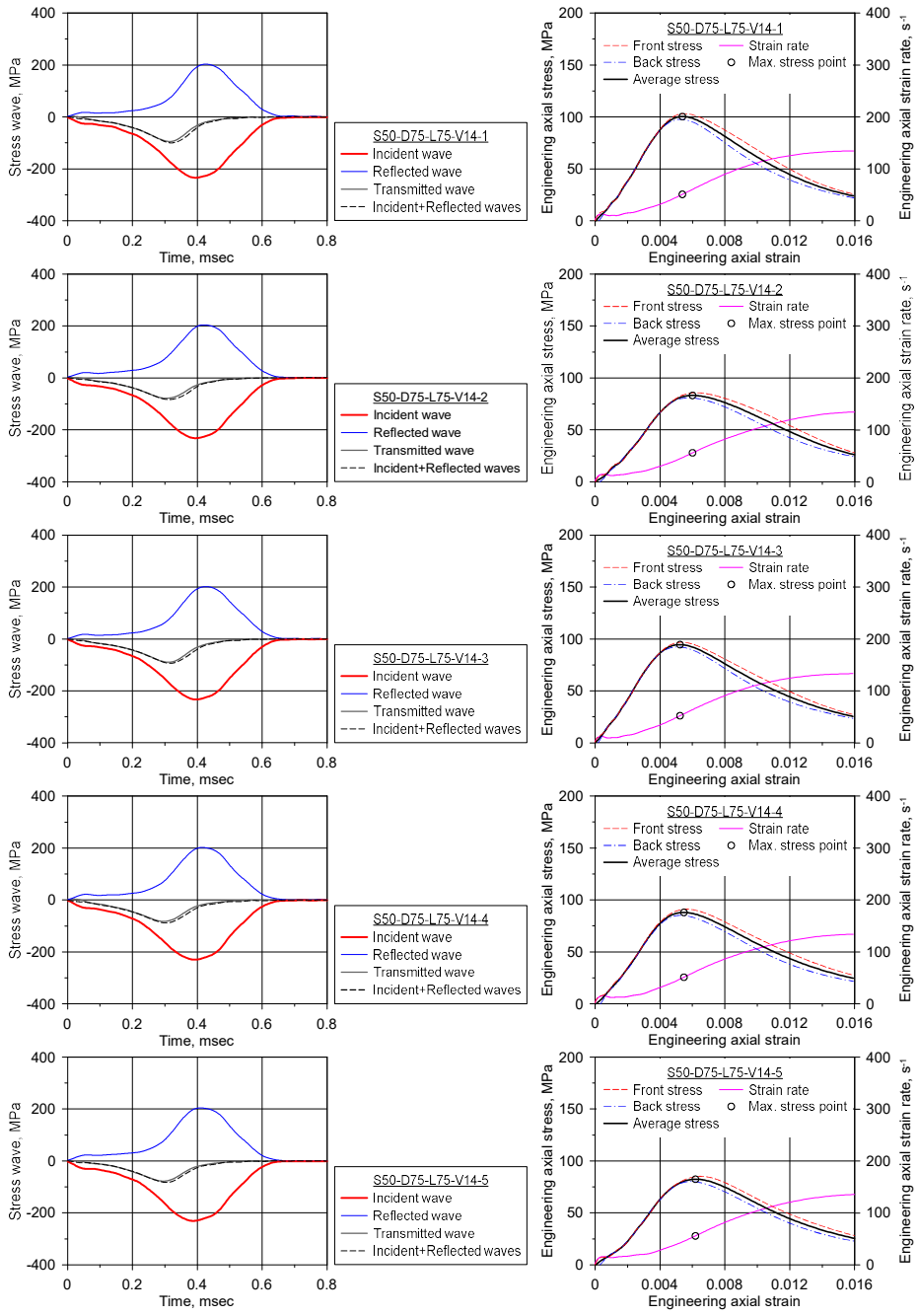

Figure D.34 Stress waves and the axial stress–strain curve of S50-D75-L75-V14

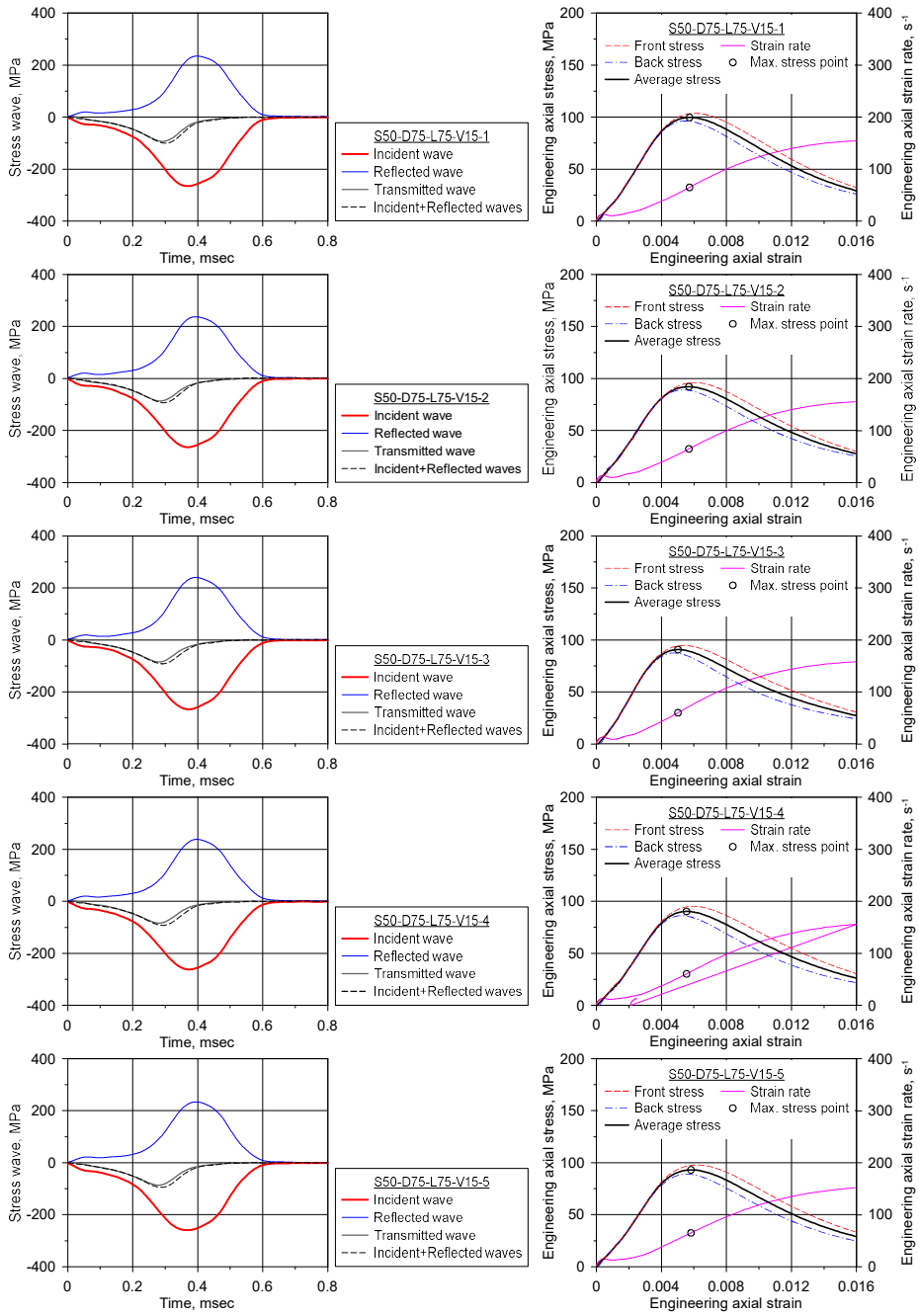

Figure D.35 Stress waves and the axial stress–strain curve of S50-D75-L75-V15

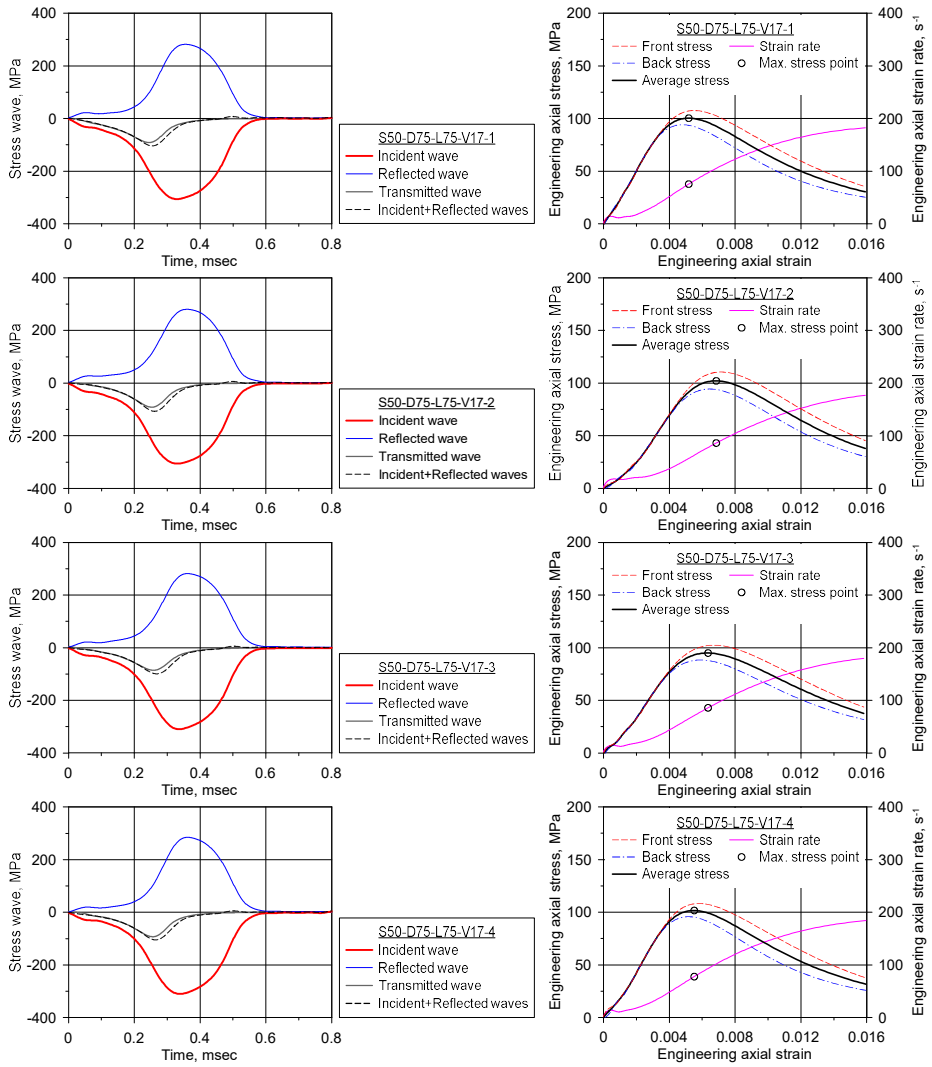

Figure D.36 Stress waves and the axial stress–strain curve of S50-D75-L75-V17

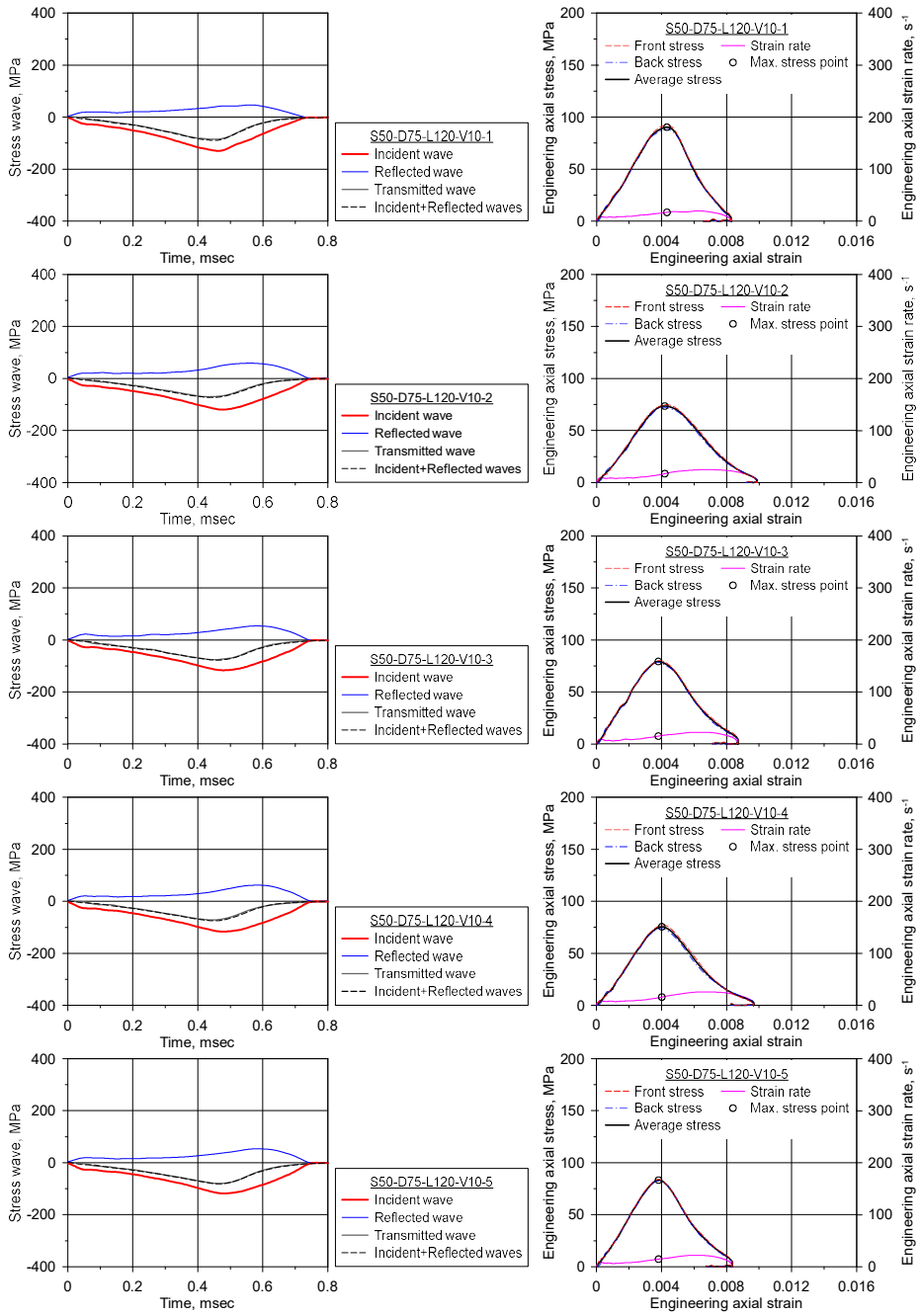

Figure D.37 Stress waves and the axial stress–strain curve of S50-D75-L120-V10

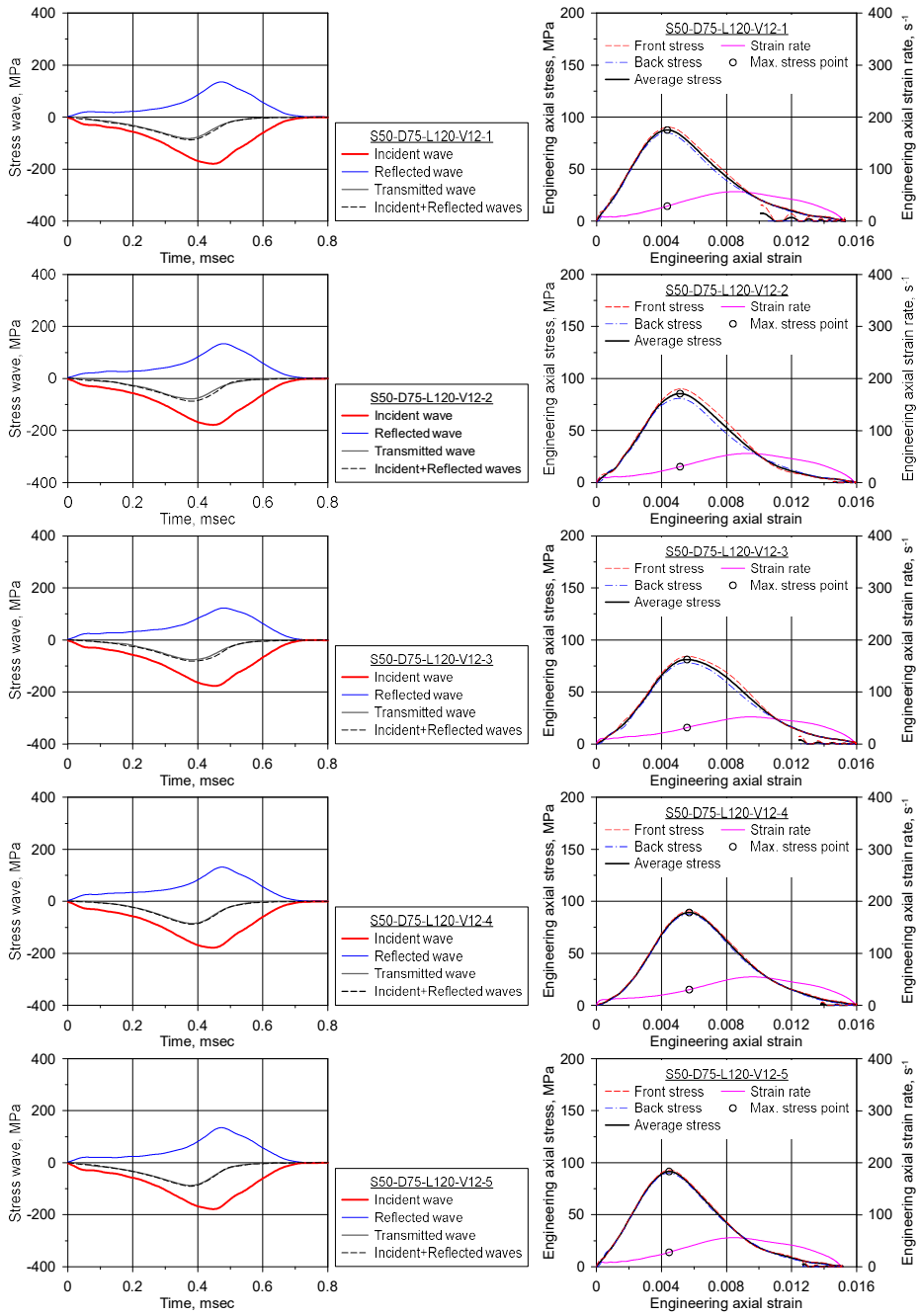

Figure D.38 Stress waves and the axial stress–strain curve of S50-D75-L120-V12

국문초록

콘크리트 Split Hopkinson Pressure Bar 실험절차의 표준화

김 경 민

최근 플랜트 폭발, 차량 및 선박 충돌, 낙석, 그리고 항공기 또는 미사일 충돌과 같은 극한상황의 발생 빈도가 높아지고 있다. 이에 따라 사회기반시설의 안전을 위하여 극한하중 하 구조물의 내충격 성능평가 등 극한하중과 관련된 연구의 필요성 또한 증대되고 있다. 특히, 사회기반시설의 필수 재료인 콘크리트는 변형률 속도 의존 특성을 지닌 재료이다. 콘크리트 압축강도는 변형률 속도 효과에 의하여 변형률 속도가 높아짐에 따라 증진되며, 일상적인 범주의 하중을 받는 경우와 다른 거동을 보인다. 따라서, 극한하중을 받는 구조물의 정확한 성능 평가와 경제적인 설계를 위해서는 콘크리트의 동적압축특성의 파악이 필수적이다. 특히 콘크리트의 동적압축강도는 다양한 동적재료실험을 통해 획득할 수 있으며, split Hopkinson pressure bar (SHPB) 실험이 주로 수행되고 있다.

그러나 콘크리트 SHPB 실험의 가장 큰 한계점은 표준실험절차가 정립되지 않았다는 것이다. 콘크리트는 굵은골재 및 잔골재 같이 입자의 크기가 다른 성분들로 이루어진 비균질 재료로,

금속과 같은 균질 재료에 비해 상대적으로 실험결과의 분산성이 크게 나타난다. 또한 SHPB 실험에서는 마찰효과에 의해 변형률 속도 효과에 의해 증진된 동적압축강도를 과대평가할 수 있다. 그렇기 때문에 표준화된 SHPB 실험절차가 없다면 일관되고 정확하게 동적압축강도를 평가하기 어렵다. 따라서 SHPB 실험을 통해 정확하고 일관된 콘크리트의 동적압축강도를 획득하기 위해서는 시편 제작부터 실험결과의 획득까지 표준화된 실험방법의 개발이 필요하다.

이 연구의 주 목적은 콘크리트 동적압축강도 평가의 일관성을 향상시키기 위한 SHPB 실험절차 정립이다. 이를 위해 SHPB 실험절차에 포함되어야 할 항목들을 선정하였다. 여러 항목들 중 시편 치수, 윤활 방법, 그리고 하중 조건의 세 가지 주요 주제를 선정하였다. 각 주제에 대해 적절한 가이드라인 제시를 위해 선행 실험 및 수치해석 연구들을 분석하였으며, 일련의 실험 및 수치해석 연구를 수행하였다.

첫번째로, 콘크리트 시편 치수를 결정하기 위한 가이드라인 제시를 위해 240 개의 시편에 대해 SHPB 실험을 수행하였다. 굵은골재 최대치수와 시편 치수를 주요 변수로 설정하였으며, 특히 실제 건설 현장에서 사용되는 크기의 굵은골재를 포함하였다. 콘크리트는 비균질성 재료이므로 굵은골재의 크기가 실험결과의 분산성에 영향을 미칠 수 있다. 따라서 굵은골재 최대치수가 실험결과의 분산성에 미치는 영향을 확인하였으며, 각각의 굵은골재

크기에 따른 동적증가계수(DIF)를 획득하고 비교하였다. 실험결과를 바탕으로 일관된 실험결과의 확보를 위한 콘크리트 SHPB 실험 시편 치수 결정 가이드라인을 다음과 같이 제시하였다: (1) 시편 치수는 굵은골재 최대치수의 최소 3 배여야 하며 (2) 실제로 사용되는 굵은골재를 콘크리트 SHPB 실험에 사용해야 한다.

다음으로, 적절한 윤활방법을 제시하기 위한 수치해석 및 실험연구를 수행하였다. 콘크리트 SHPB 실험에서는 장비와 시편 사이의 마찰이 구속효과를 야기한다. 이러한 마찰효과는 변형률 속도 효과에 의한 압축강도 증진 외에 추가적으로 압축강도를 증진시키므로 동적압축강도의 과대평가를 유발한다. 따라서 정확한 동적압축강도 평가를 위해 SHPB 실험 시 장비와 시편 사이의 마찰을 최소화할 수 있는 적절한 윤활방법이 필요하다. 이 연구에서는 적절한 윤활 방법 제시를 위해 윤활제 종류와 윤활제 도포량을 주요 변수로 설정하여 52 회의 콘크리트 SHPB 실험을 수행하였다. 그리고 다양한 치수를 갖는 75 개의 콘크리트 시편에 대한 후속 SHPB 실험을 수행하여 제시한 윤활방법을 검증하였다. 실험결과들을 바탕으로 콘크리트 SHPB 실험에서 마찰효과를 제거하기 위한 윤활방법을 다음과 같이 제시하였다: 시편은 고진공 그리스, 페트롤륨 젤리, 또는 테플론 윤활제를 12 mg/cm^2 이상 도포하여야 한다.

마지막으로, 유효한 실험결과를 확보할 수 있도록 하는 입사응력파 결정방법 제시를 위한 연구를 수행하였다. 콘크리트

SHPB 실험 시 유효한 실험결과를 획득하기 위해서는 시편의 동적응력평형이 만족되어야 한다. 시편의 동적응력평형은 시편의 특성 및 SHPB 실험의 중인 입사응력파의 영향을 받는다. 따라서 시편의 특성을 고려하였을 때 사용 가능한 입사응력파 범위가 정의되어야 한다. 이 연구에서는 선행된 콘크리트 SHPB 실험결과들을 바탕으로 시편이 동적응력평형을 만족할 수 있도록 하는 시편 특성을 고려한 입사응력파 변화율 범위를 제시하였다. 제시한 입사응력파 변화율의 범위는 시편 치수 및 정적압축강도와 같이 다양한 시편 특성을 지닌 184 개의 시편에 대한 콘크리트 SHPB 실험을 통해 검증되었다. 또한 추가된 실험결과를 활용하여 제시한 범위를 수정하였다.

최종적으로 각각의 연구결과들을 바탕으로 콘크리트 동적압축강도를 일관되게 평가할 수 있도록 하는 SHPB 실험절차를 개발하였다. 또한 개발한 실험절차서의 적용성을 검증하였다.

이와 같이 개발한 콘크리트 SHPB 실험절차는 극한하중 하 콘크리트의 동적재료특성 획득과 관련하여 양질의 데이터베이스를 구축할 수 있게 한다. 또한 이 연구를 통해 개발한 콘크리트 SHPB 실험절차는 표준실험절차로 활용될 수 있으며 구조물 및 재료의 극한성능평가의 신뢰도를 향상시킬 수 있다.

주요어: 콘크리트 동적압축강도, split Hopkinson pressure bar, 표준시편 제작법, 표준실험절차, 동적재료실험

학번: 2018-31976